Pierre Sagaut

Large Eddy Simulation for Incompressible Flows

Scientific Computation

An Introduction

Springer

Scientific Computation

A Computational Method in Plasma Physics
F. Bauer, O. Betancourt, P. Garabechan

Implementation of Finite Element Methods for Navier-Stokes Equations
F. Thomasset

Finite-Different Techniques for Vectorized Fluid Dynamics Calculations
Edited by D. Book

Unsteady Viscous Flows
D. P. Telionis

Computational Methods for Fluid Flow
R. Peyret, T. D. Taylor

Computational Methods in Bifurcation Theory and Dissipative Structures
M. Kubicek, M. Marek

Optimal Shape Design for Elliptic Systems
O. Pironneau

The Method of Differential Approximation
Yu. I. Shokin

Computational Galerkin Methods
C. A. J. Fletcher

Numerical Methods for Nonlinear Variational Problems
R. Glowinski

Numerical Methods in Fluid Dynamics
Second Edition M. Holt

Computer Studies of Phase Transitions and Critical Phenomena O. G. Mouritsen

Finite Element Methods in Linear Ideal Magnetohydrodynamics
R. Gruber, J. Rappaz

Numerical Simulation of Plasmas
Y. N. Dnestrovskii, D. P. Kostomarov

Computational Methods for Kinetic Models of Magnetically Confined Plasmas
J. Killeen, G. D. Kerbel, M. C. McCoy, A. A. Mirin

Spectral Methods in Fluid Dynamics
Second Edition C. Canuto, M. Y. Hussaini, A. Quarteroni, T. A. Zang

Computational Techniques for Fluid Dynamics 1
Fundamental and General Techniques
Second Edition C. A. J. Fletcher

Computational Techniques for Fluid Dynamics 2
Specific Techniques for Different Flow Categories
Second Edition C. A. J. Fletcher

Methods for the Localization of Singularities in Numerical Solutions of Gas Dynamics Problems
E. V. Vorozhtsov, N. N. Yanenko

Classical Orthogonal Polynomials of a Discrete Variable
A. F. Nikiforov, S. K. Suslov, V. B. Uvarov

Flux Coordinates and Magnetic Filed Structure: A Guide to a Fundamental Tool of Plasma Theory
W. D. D'haeseleer, W. N. G. Hitchon, J. D. Callen, J. L. Shohet

Monte Carlo Methods in Boundary Value Problems
K. K. Sabelfeld

The Least-Squares Finite Element Method
Theory and Applications in Computational Fluid Dynamics and Electromagnetics
Bo-nan Jiang

Computer Simulation of Dynamic Phenomena
M. L. Wilkins

Grid Generation Methods
V. D. Liseikin

Radiation in Enclosures
A. Mbiock, R. Weber

Large Eddy Simulation for Incompressible Flows
An Introduction
P. Sagaut

Series homepage – http://www.springer.de/phys/books/sc/

Pierre Sagaut

Large Eddy Simulation for Incompressible Flows

An Introduction

With 53 Figures and 11 Tables

Springer

Scientific Computation

Springer
Berlin
Heidelberg
New York
Barcelona
Hong Kong
London
Milan
Paris
Singapore
Tokyo

Physics and Astronomy ONLINE LIBRARY
http://www.springer.de/phys/

and oceans are concerned, because it dissipates the large-scale motions too much. It was an immense success, though, with users interested in industrial-flow applications, which shows that the outcomes of research are as unpredictable as turbulence itself! A little later, in the 1970s, the theoretical physicist Kraichnan[5] developed the important concept of spectral eddy viscosity, which allows us to go beyond the separation-scale assumption inherent in the typical eddy-viscosity concept of Smagorinsky. From then on, the history of large-eddy simulations developed, first in the wake of two schools: Stanford–Torino, where a dynamic version of Smagorinsky's model was developed; and Grenoble, which followed Kraichnan's footsteps. Then researchers, including industrial researchers, all around the world became infatuated with these techniques, being aware of the limits of classical modeling methods based on the averaged equations of motion (Reynolds equations).

It is a complete account of this young but very rich discipline, the large-eddy simulation of turbulence, which is presented to us by the young ONERA researcher Pierre Sagaut, in a book whose reading brings pleasure and interest. *Introduction to Large-Eddy Simulation* very wisely limits itself to the case of incompressible fluids, which is a suitable starting point if one wants to avoid multiplying difficulties. Let us point out, however, that compressible flows quite often exhibit near-incompressible properties in boundary layers, once the variation of the molecular viscosity with the temperature has been taken into account, as predicted by Morkovin in his famous hypothesis.[6] Pierre Sagaut shows an impressive culture, describing exhaustively all the subgrid-modeling methods for simulating the large scales of turbulence, without hesitating to give the mathematical details needed for a proper understanding of the subject.

After a general introduction, he presents and discusses the various filters used, in cases of statistically homogeneous and inhomogeneous turbulence, and their applications to Navier–Stokes equations. He very aptly describes the representation of various tensors in Fourier space, Germano-type relations obtained by double filtering, and the consequences of Galilean invariance of the equations. He then goes into the various ways of modeling isotropic turbulence. This is done first in Fourier space, with the essential wave-vector triad idea, and a discussion of the transfer-localness concept. An excellent review of spectral-viscosity models is provided, with developments sometimes beyond the original papers. Then he goes to physical space, with a discussion of the structure-function models and the dynamic procedures (Eulerian and Lagrangian, with energy equations and so forth). The study is then generalized to the anisotropic case. Finally, functional approaches based on Taylor series expansions are discussed, along with non-linear models, homogenization techniques, and simple and dynamic mixed models.

[5] He worked as a postdoctoral student with Einstein at Princeton.

[6] M.V. Morkovin, in *Mécanique de la Turbulence*, A. Favre et al. (eds.), CNRS, pp. 367–380 (1962).

Pierre Sagaut also discusses the importance of numerical errors, and proposes a very interesting review of the different wall models in the boundary layers. The last chapter gives a few examples of applications carried out at ONERA and a few other French laboratories. These examples are well chosen in order of increasing complexity: isotropic turbulence, with the non-linear condensation of vorticity into the "worms" vortices discovered by Siggia[7]; planar Poiseuille flow with ejection of "hairpin" vortices above low-speed streaks; the round jet and its alternate pairing of vortex rings; and, finally, the backward-facing step, the unavoidable test case of computational fluid dynamics. Also on the menu: beautiful visualizations of the separation behind a wing at high incidence, with the shedding of superb longitudinal vortices. Completing the work are two appendices on the statistical and spectral analysis of turbulence, as well as isotropic and anisotropic EDQNM modeling.

A bold explorer, Pierre Sagaut had the daring to plunge into the jungle of multiple modern techniques of large-scale simulation of turbulence. He came back from his trek with an extremely complete synthesis of all the models, giving us a very complete handbook that novices can use to start off on this enthralling adventure, while specialists can discover models different from those they use every day. *Introduction to Large-Eddy Simulation* is a thrilling work in a somewhat austere wrapping. I very warmly recommend it to the broad public of postgraduate students, researchers, and engineers interested in fluid mechanics and its applications in numerous fields such as aerodynamics, combustion, energetics, and the environment.

Grenoble, March 2000

Marcel Lesieur

[7] E.D. Siggia, J. Flu[illegible] Mech., **107**, pp. 375–406 (1981).

Dr. Pierre Sagaut
ONERA (Office National d'Etudes et de Recherches Aerospatiale)
DSNA/ETRI
29, av. Div. Leclerc
92320 Chatillon, France
e-mail: sagaut@onera.fr

Title of the original French edition: Introduction à la simulation des grandes échelles pour les écoulements de fluide incompressible, Mathématique & Applications.

Library of Congress Cataloging-in-Publication Data: Sagaut, Pierre, 1967– . Large eddy simulation for incompressible flows: an introduction/ Pierre Sagaut. p. cm.– (Scientific computation, ISSN 1434-8322) Includes bibliographical references and index. ISBN 3540678905 (alk. paper) 1. Turbulence–Mathematical models. 2. Eddies–Mathematical models. I. Title. II. Series. TA357.5.T87 S27 2000 532'.0527–dc21 00-059563

ISSN 1434-8322
ISBN 3-540-67890-5 Springer-Verlag Berlin Heidelberg New York

Springer-Verlag Berlin Heidelberg New York
a member of BertelsmannSpringer Science+Business Media GmbH

Printed in Germany

Typesetting: Data conversion: LE-TeX, Leipzig
Cover design: *design & production* GmbH, Heidelberg
Printed on acid-free paper SPIN: 10776849 55/3141/ba - 5 4 3 2 1 0

Foreword

Still today, turbulence in fluids is considered as one of the most difficult problems of modern physics. Yet we are quite far from the complexity of microscopic molecular physics, since we only deal with Newtonian mechanics laws applied to a continuum, in which the effect of molecular fluctuations has been smoothed out and is represented by molecular-viscosity coefficients. Such a system has a dual behaviour of determinism in the Laplacian sense, and extreme sensitivity to initial conditions because of its very strong non-linear character. One does not know, for instance, how to predict the critical Reynolds number of transition to turbulence in a pipe, nor how to compute precisely the drag of a car or an aircraft, even with today's largest computers.

We know, since the meteorologist Richardson,[1] numerical schemes allowing us to solve in a deterministic manner the equations of motion, starting with a given initial state and with prescribed boundary conditions. They are based on momentum and energy balances. However, such a resolution requires formidable computing power, and is only possible for low Reynolds numbers. These Direct-Numerical Simulations may involve calculating the interaction of several million interacting sites. Generally, industrial, natural, or experimental configurations involve Reynolds numbers that are far too large to allow direct simulations,[2] and the only possibility then is Large-Eddy Simulation, where the small-scale turbulent fluctuations are themselves smoothed out and modelled via eddy-viscosity and diffusivity assumptions. The history of large-eddy simulation began in the 1960s with the famous Smagorinsky model. Smagorinsky, also a meteorologist, wanted to represent the effects upon large synoptic quasi-two-dimensional atmospheric or oceanic motions[3] of a three-dimensional subgrid turbulence cascading toward small scales according to mechanisms described by Richardson in 1926 and formalized by the famous mathematician Kolmogorov in 1941.[4] It is interesting to note that Smagorinsky's model was a total failure as far as the atmosphere

[1] L.F. Richardson, *Weather Prediction by Numerical Process*, Cambridge University Press (1922).
[2] More than 10^{15} modes should be necessary for a supersonic-plane wing!
[3] Subject to vigorous inverse-energy cascades.
[4] L.F. Richardson, Proc. Roy. Soc. London, Ser A, **110**, pp. 709–737 (1926); A. Kolmogorov, Dokl. Akad. Nauk SSSR, **30**, pp. 301–305 (1941).

Preface

While giving lectures dealing with Large-Eddy Simulation (LES) to students or senior scientists, I have found difficulties indicating published references which can serve as general and complete introductions to this technique.

I have tried therefore to write a textbook which can be used by students or researchers showing theoretical and practical aspects of the Large-Eddy Simulation technique, with the purpose of presenting the main theoretical problems and ways of modeling. It assumes that the reader possesses a basic knowledge of fluid mechanics and applied mathematics.

Introducing Large-Eddy Simulation is not an easy task, since no unified and universally accepted theoretical framework exists for it. It should be remembered that the first LES computations were carried out in the early 1960s, but the first rigorous derivation of the LES governing equations in general coordinates was published in 1995! Many reasons can be invoked to explain this lack of a unified framework. Among them, the fact that LES stands at the crossroads of physical modeling and numerical analysis is a major point, and only a few really successful interactions between physicists, mathematicians and practitioners have been registered over the past thirty years, each community sticking to its own language and center of interest. Each of these three communities, though producing very interesting work, has not yet provided a complete theoretical framework for LES by its own means. I have tried to gather these different contributions in this book, in an understandable form for readers having a basic background in applied mathematics.

Another difficulty is the very large number of existing physical models, referred to as subgrid models. Most of them are only used by their creators, and appear in a very small number of publications. I made the choice to present a very large number of models, in order to give the reader a good overview of the ways explored. The distinction between functional and structural models is made in this book, in order to provide a general classification; this was necessary in order to produce an integrated presentation.

In order to provide a useful synthesis of forty years of LES development, I had to make several choices. Firstly, the subject is restricted to incompressible flows, as the theoretical background for compressible flow is less evolved. Secondly, it was necessary to make a unified presentation of a large number

of works issued from many research groups, and very often I have had to change the original proof and to reduce it. I hope that the authors will not feel betrayed by the present work. Thirdly, several thousand journal articles and communications dealing with LES can be found, and I had to make a selection. I have deliberately chosen to present a large number of theoretical approaches and physical models to give the reader the most general view of what has been done in each field. I think that the most important contributions are presented in this book, but I am sure that many new physical models and results dealing with theoretical aspects will appear in the near future.

A typical question of people who are discovering LES is "what is the best model for LES?". I have to say that I am convinced that this question cannot be answered nowadays, because no extensive comparisons have been carried out, and I am not even sure that the answer exists, because people do not agree on the criterion to use to define the "best" model. As a consequence, I did not try to rank the model, but gave very generally agreed conclusions on the model efficiency.

A very important point when dealing with LES is the numerical algorithm used to solve the governing equations. It has always been recognized that numerical errors could affect the quality of the solution, but new emphasis has been put on this subject during the last decade, and it seems that things are just beginning. This point appeared as a real problem to me when writing this book, because many conclusions are still controversial (e.g. the possibility of using a second-order accurate numerical scheme or an artificial diffusion). So I chose to mention the problems and the different existing points of view, but avoided writing a part dealing entirely with numerical discretization and time integration, discretization errors, etc. This would have required writing a companion book on numerical methods, and that was beyond the scope of the present work. Many good textbooks on that subject already exist, and the reader should refer to them.

Another point is that the analysis of the coupling of LES with typical numerical techniques which should greatly increase the range of applications, such as Arbitrary Lagrangian–Eulerian methods, Adaptive Mesh-Refinement or embedded grid techniques, is still to be developed.

I am indebted to a large number of people, but I would like to express special thanks to Dr. P. Le Quére, Prof. O. Daube, who gave me the opportunity to write my first manuscript on LES, and to Prof. J.M. Ghidaglia who offered me the possiblity of publishing the first version of this book (in French). I would also like to thank ONERA for helping me to write this new, augmented and translated version of the book. Mrs. J. Ryan is gratefully acknowledged for her help in writing the English version.

Paris, September 2000 *Pierre Sagaut*

Contents

1. Introduction

1.1 Computational Fluid Dynamics

Computational Fluid Dynamics (CFD) is the study of fluids in flow by numerical simulation, and is a field advancing by leaps and bounds. The basic idea is to use appropriate algorithms to find solutions to the equations describing the fluid motion.

Numerical simulations are used for two types of purposes.

The first is to accompany research of a fundamental kind. By describing the basic physical mechanisms governing fluid dynamics better, numerical simulation helps us understand, model, and later control these mechanisms. This kind of study requires that the numerical simulation produce data of very high accuracy, which implies that the physical model chosen to represent the behavior of the fluid must be pertinent and that the algorithms used, and the way they are used by the computer system, must introduce no more than a low level of error. The quality of the data generated by the numerical simulation also depends on the level of resolution chosen. For the best possible precision, the simulation has to take into account all the space-time scales affecting the flow dynamics. When the range of scales is very large, as it is in turbulent flows, for example, the problem becomes a stiff one, in the sense that the ratio between the largest and smallest scales becomes very large.

Numerical simulation is also used for another purpose: engineering analyses, where flow characteristics need to be predicted in equipment design phase. Here, the goal is no longer to produce data for analyzing the flow dynamics itself, but rather to predict certain of the flow characteristics or, more precisely, the values of physical parameters that depend on the flow, such as the stresses exerted on an immersed body, the production and propagation of acoustic waves, or the mixing of chemical species. The purpose is to reduce the cost and time needed to develop a prototype. The desired predictions may be either of the mean values of these parameters or their extremes. If the former, the characteristics of the system's normal operating regime are determined, such as the fuel an aircraft will consume per unit of time in cruising flight. The question of study here is mainly the system's performance. When extreme parameter values are desired, the question is rather the system's characteristics in situations that have a little probability of ever existing, *i.e.* in the presence of rare or critical phenomena, such as

rotating stall in aeronautical engines. Studies like this concern system safety at operating points far from the cruising regime for which they were designed.

The constraints on the quality of representation of the physical phenomena differ here from what is required in fundamental studies, because what is wanted now is evidence that certain phenomena exist, rather than all the physical mechanisms at play. In theory, then, the description does not have to be as detailed as it does for fundamental studies. However, it goes without saying that the quality of the prediction improves with the richness of the physical model.

The various levels of approximation going into the physical model are discussed in the following.

1.2 Levels of Approximation: General

A mathematical model for describing a physical system cannot be defined before we have determined the *level of approximation* that will be needed for obtaining the required precision on a fixed set of parameters (see [136] for a fuller discussion). This set of parameters, associated with the other variables characterizing the evolution of the model, contain the necessary information for describing the system completely.

The first decision that is made concerns the scale of reality considered. That is, physical reality can be described at several levels: in terms of particle physics, atomic physics, or micro- and macroscopic descriptions of phenomena. This latter level is the one used by classical mechanics, especially continuum mechanics, which will serve as the framework for the explanations given here.

A system description at a given scale can be seen as a statistical averaging of the detailed descriptions obtained at the previous (lower) level of description. In fluid mechanics, which is essentially the study of systems consisting of a great many interacting elements, the choice of a level of description, and thus a level of averaging, is fundamental. A description at the molecular level would call for a definition of a discrete system governed by Boltzmann equations, whereas the continuum paradigm would be called for in a macroscopic description corresponding to a scale of representation larger than the mean free path of the molecules. The system will then be governed by the Navier–Stokes equations, if the fluid is Newtonian.

After deciding on a level of reality, several other levels of approximation have to be considered in order to obtain the desired information concerning the evolution of the system:

- *Level of space-time resolution.* This is a matter of determining the time and space scales characteristic of the system evolution. The smallest pertinent scale is taken as the resolution reference so as to capture all the dynamic mechanisms. The system spatial dimension (zero to three dimensions) has to be determined in addition to this.
- *Level of dynamic description.* Here we determine the various forces exerted on the system components, and their relative importance. In the continuum mechanics framework, the most complete model is that of the Navier–Stokes equations, complemented by empirical laws for describing the dependency of the diffusion coefficients as a function of the other variables, and the state law. This can first be simplified by considering that the elliptic character of the flow is due only to the pressure, while the other variables are considered to be parabolic, and we then refer to the parabolic Navier–Stokes equations. Other possible simplifications are, for example, Stokes equations, which account only for the pressure and diffusion effects, and the Euler equations, which neglect the viscous mechanisms.

The different choices made at each of these levels make it possible to develop a mathematical model for describing the physical system. In all of the following, we restrict ourselves to the case of a Newtonian fluid of a single species, of constant volume, isothermal, and isochoric in the absence of any external forces. The mathematical model consists of the unsteady Navier–Stokes equations. The numerical simulation then consists in finding solutions of these equations using algorithms for Partial Differential Equations. Because of the way computers are structured, the numerical data thus generated is a discrete set of degrees of freedom, and of finite dimensions. We therefore assume that the behavior of the discrete dynamical system represented by the numerical result will approximate that of the exact, continuous solution of the Navier–Stokes equations with adequate accuracy.

1.3 Statement of the Scale Separation Problem

Solving the unsteady Navier–Stokes equations implies that we must take into account all the space-time scales of the solution if we want to have a result of maximum quality. The discretization has to be fine enough to represent all these scales numerically. That is, the simulation is discretized in steps Δx in space and Δt in time that must be smaller, respectively, than the characteristic length and the characteristic time associated with the smallest dynamically active scale of the exact solution. This is equivalent to saying that the space-time resolution scale of the numerical result must be at least as fine as that of the continuous problem. This solution criterion may turn out to be extremely constrictive when the solution to the exact problem contains scales of very different sizes, which is the case for turbulent flows.

This is illustrated by taking the case of the simplest turbulent flow, *i.e.* one that is statistically homogeneous and isotropic (see Appendix A for a more precise definition). For this flow, the ratio between the characteristic

length of the most energetic scale, L, and that of the smallest dynamically active scale, η, is evaluated by the relation:

$$\frac{L}{\eta} = O\left(Re^{3/4}\right) \quad , \tag{1.1}$$

in which Re is the Reynolds number, which is a measure of the ratio of the forces of inertia and the molecular viscosity effect, ν. We therefore need $O\left(Re^{9/4}\right)$ degrees of freedom in order to be able to represent all the scales in a cubic volume of edge L. The ratio of characteristic times also varies as $O\left(Re^{3/4}\right)$. So in order to calculate the evolution of the solution in a volume L^3 for a duration equal to the characteristic time of the most energetic scale, we have to solve the Navier–Stokes equations numerically $O\left(Re^3\right)$ times!

This type of computation for large Reynolds numbers (applications in the aeronautical field deal with Reynolds numbers of as much as 10^8) requires computer resources very much greater than currently available supercomputer capacities, and is therefore not practicable.

In order to be able to compute the solution, we need to reduce the number of operations, so we no longer solve the dynamics of all the scales of the exact solution directly. To do this, we have to introduce a new, coarser level of description of the fluid system. This comes down to picking out certain scales that will be represented directly in the simulation while others will not be. The non-linearity of the Navier–Stokes equations reflects the dynamic coupling that exists among all the scales of the solution, which implies that these scales cannot be calculated independently of each other. So if we want a quality representation of the scales that are resolved, their interactions with the scales that are not have to be considered in the simulation. This is done by introducing an additional term in the equations governing the evolution of the resolved scales, to model these interactions. Since these terms represent the action of a large number of other scales with those that are resolved (without which there would be no effective gain), they reflect only the global or average action of these scales. They are therefore only statistical models: an individual deterministic representation of the inter-scale interactions would be equivalent to a direct numerical simulation.

Such modeling offers a gain only to the extent that it is universal, *i.e.* if it can be used in cases other than the one for which it is established. This means there exists a certain universality in the dynamic interactions the models reflect. This universality of the assumptions and models will be discussed all through the text.

1.4 Usual Levels of Approximation

There are several common ways of reducing the number of degrees of freedom in the numerical solution:

– By calculating the statistical average of the solution directly. This is called the Reynolds Averaged Numerical Simulation (RANS)[179], which is used mostly for engineering calculations. The exact solution $\mathbf{u}$ splits into the sum of its statistical average $\langle\mathbf{u}\rangle$ and a fluctuation $\mathbf{u}'$ (see Appendix A):

$$\mathbf{u}(\mathbf{x},t) = \langle\mathbf{u}(\mathbf{x},t)\rangle + \mathbf{u}'(\mathbf{x},t) \quad .$$

This splitting, or "decomposition", is illustrated by Fig. 1.1. The fluctuation $\mathbf{u}'$ is not represented directly by the numerical simulation, and is included only by way of a turbulence model. The statistical averaging operation is in practice often associated with a time averaging:

$$\langle\mathbf{u}(\mathbf{x},t)\rangle \approx \overline{\mathbf{u}}(\mathbf{x}) = \lim_{T\to\infty}\frac{1}{T}\int_0^T \mathbf{u}(\mathbf{x},t)dt \quad .$$

The mathematical model is then that of the steady Navier–Stokes equations. This averaging operation makes it possible to reduce the number of scales in the solution considerably, and therefore the number of degrees of freedom of the discrete system. The statistical character of the solution prevents a fine description of the physical mechanisms, so that this approach is not usable for studies of a fundamental character, especially so when the statistical average is combined with a time average. Nor is it possible to isolate rare events. On the other hand, it is an appropriate approach for analyzing performance as long as the turbulence models are able to reflect the existence of the turbulent fluctuation $\mathbf{u}'$ effectively.

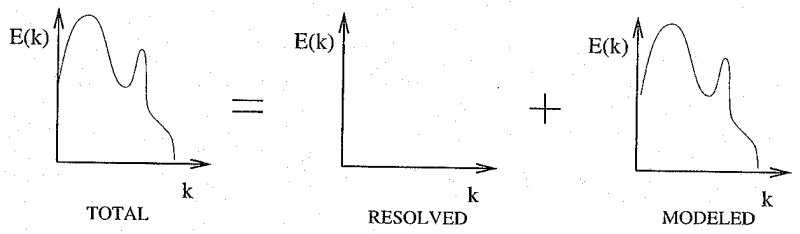

Fig. 1.1. Decomposition of the energy spectrum of the solution associated with the Reynolds Averaged Numerical Simulation (symbolic representation).

– By calculating directly only certain low-frequency modes in time (of the order of a few hundred hertz) and the average field. This approach goes by a number of names: *Unsteady Reynolds Averaged Numerical Simulation* (URANS) , *Semi-Deterministic Simulation* (SDS), *Very Large-Eddy Simulation* (VLES), and sometimes *Coherent Structure Capturing* (CSC) [16, 331]. The field $\mathbf{u}$ appears here as the sum of three contributing terms:

$$\mathbf{u}(\mathbf{x},t) = \overline{\mathbf{u}}(\mathbf{x}) + \langle\mathbf{u}(\mathbf{x},t)\rangle_c + \mathbf{u}'(\mathbf{x},t) \quad .$$

The first term is the time average of the exact solution, the second its conditional statistical average, and the third the turbulent fluctuation.

This decomposition is illustrated in Fig. 1.2. The conditional average is associated with a predefined class of events. When these events occur at a set time period, this is a phase average. The $\langle \mathbf{u}(\mathbf{x},t)\rangle_c$ term is interpreted as the contribution of the coherent modes to the flow dynamics, while the $\mathbf{u}'$ term, on the other hand, is supposed to represent the random part of the turbulence. The variable described by the mathematical model is now the sum $\overline{\mathbf{u}}(\mathbf{x}) + \langle \mathbf{u}(\mathbf{x},t)\rangle_c$, with the random part being represented by a turbulence model. It should be noted that, in the case where there exists a deterministic low-frequency forcing of the solution, the conditional average is conventionally interpreted as a phase average of the solution, for a frequency equal to that of the forcing term; but if this does not exist, the interpretation of the results is still open to debate. Since this is an unsteady approach, it contains more information than the previous one; but it still precludes a deterministic description of a particular event. It is of use for analyzing the performance characteristics of systems in which the unsteady character is forced by some external action (such as periodically pulsed flows).

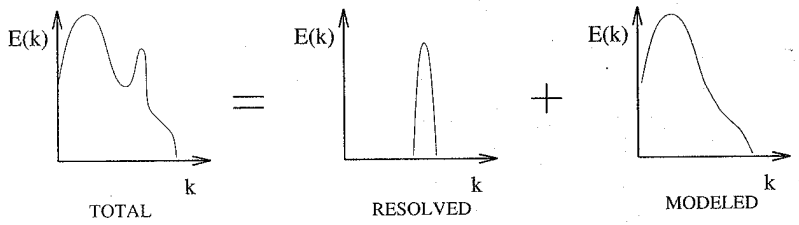

Fig. 1.2. Decomposition of the energy spectrum of the solution associated with the Unsteady Reynolds Averaged Numerical Simulation approach, when a predominant frequency exists (symbolic representation).

– By projecting the solution on the *ad hoc* function basis and retaining only a minimum number of modes, to get a dynamical system with fewer degrees of freedom. The idea here is to find an optimum decomposition base for representing the phenomenon, in order to minimize the number of degrees of freedom in the discrete dynamical system. There is no averaging done here, so the space-time and dynamics resolution of the numerical model is still as fine as that of the continuum model, but is now optimized. Several approaches are encountered in practice.
The first is to use standard basis function (Fourier modes in the spectral space or polynomials in the physical space, for example) and distribute the degrees of freedom as best possible in space and time to minimize the number of them, *i.e.* adapt the space-time resolution of the simulation to the nature of the solution. We thus adapt the topology of the discrete dynamical system to that of the exact solution. This approach results in the use of self-adapting grids and time steps in the physical space. It is not associated with an operation to reduce the complexity by switching to a higher level of statistical description of the system. It leads to a much less reduction of the discrete system than those techniques based on statistical averaging, and is limited by the complexity of the continuous solution.
Another approach is to use optimal basis functions, a small number of which will suffice for representing the flow dynamics. The problem is then to determine what these base functions are. One example is the Proper Orthogonal Decomposition (POD) mode basis, which is optimum for representing kinetic energy (see [20] for a survey). This technique allows very high data compression, and generates a dynamical system of very small dimensions (a few dozen degrees of freedom at most, in practice). The approach is very seldom used because it requires very complete information concerning the solution in order to be able to determine the base functions. The various approaches above all return complete information concerning the solutions of the exact problem, so they are perfectly suited to studies of a fundamental nature. They may not, on the other hand, be optimal in terms of reducing the complexity for certain engineering analyses that do not require such complete data.
– By calculating only the low-frequency modes in space directly. This is what is done in *Large-Eddy Simulation* (LES). It is this approach that is discussed in the following. It is illustrated in Fig. 1.3.

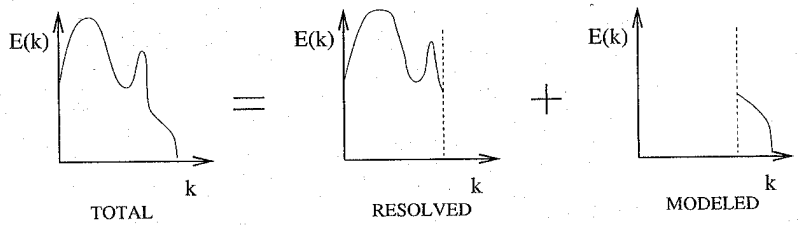

Fig. 1.3. Decomposition of the energy spectrum in the solution associated with large-eddy simulation (symbolic representation).

1.5 Large-Eddy Simulation

The scale selection that the large-eddy simulation technique is based on [97, 190, 220, 280, 285] is a separation between large and small scales. In order to define these two categories, a reference or cutoff length first has to be determined. Those scales that are of a characteristic size greater than the cutoff length are called large or resolved scales, and others are called small

or subgrid scales. The latter are included by way of a statistical model called a subgrid model. It should be remembered that this separation between different scales is not associated with a statistical averaging operation, as are some of the techniques mentioned above.

On the mathematical level, this scale separation is formalized in the form of a frequency low-pass filter, discussed in Chap. 2. The application of this filter to the Navier–Stokes equations, described in Chap. 3, yields the constitutive mathematical model for the large-eddy simulation. The convection term, because it is non-linear, has to be decomposed. Part of the resultant terms can be calculated directly from the resolved scales, the rest have to be modeled.

Two modeling approaches are spoken of here: functional modeling, based on representing kinetic energy transfers (covered in Chaps. 4 and 5), and structural modeling, which aims to reproduce the eigenvectors of the statistical correlation tensors of the subgrid modes (presented in Chap. 6). The basic assumptions and the subgrid models corresponding to each of these approaches are presented.

Chapter 7 is devoted to the theoretical problems arising from the effects of the numerical method used in the simulation. The representation of the numerical error in the form of an additional filter is introduced, along with the problem of the relative weight of the various filters used in the numerical simulation. Question concerning the analysis and validation of the large-eddy simulation calculations are dealt with in Chap. 8.

The boundary conditions used for large-eddy simulation are discussed in Chap. 9, where the main cases treated are solid walls and inflow conditions.

The practical aspects concerning the implementation of subgrid models are described in Chap. 10. Lastly, the discussion is illustrated by examples of large-eddy simulation applications for different categories of flows, in Chap. 11.

2. Formal Introduction to Scale Separation: Band-Pass Filtering

The idea of scale separation introduced in the preceding chapter will now be formalized on the mathematical level, to show how to handle the equations and derive the subgrid models. The representation of the filtering as a convolution product is first presented in the ideal case of a filter of uniform cutoff length in space over an infinite domain. Extensions to the cases of a bounded domain and a filter of variable cutoff length are then discussed.

2.1 Definition and Properties of the Filter in the Homogeneous Case

The framework is restricted here to the case of homogeneous isotropic filters, for the sake of easier analysis, and to allow a better understanding of the physics of the phenomena. The filter considered is *isotropic*. This means that its properties are independent of the position and orientation of the reference system in space, which implies that it is applied to an unbounded domain and that the cutoff scale is constant and identical in all directions of space. This is the framework in which subgrid modeling developed historically. The extension to anisotropic and inhomogeneous[1] filters, which researchers have only more recently begun to look into, is described in Sect. 2.2.

2.1.1 Definition

Scales are separated by applying a scale high-pass filter, *i.e.* low-pass in frequency, to the exact solution. This filtering is represented mathematically in physical space as a convolution product. The resolved part $\overline{\phi}(\mathbf{x},t)$ of a space-time variable $\phi(\mathbf{x},t)$ is defined formally by the relation:

$$\overline{\phi}(\mathbf{x},t) = \int_{-\infty}^{+\infty}\int_{-\infty}^{+\infty} \phi(\boldsymbol{\xi},t')G(\mathbf{x}-\boldsymbol{\xi},t-t')dt'd^3\boldsymbol{\xi} \quad , \tag{2.1}$$

[1] That is, whose characteristics, such as the mathematical form or cutoff frequency, are not invariant by translation or rotation of the reference system in which they are defined.

in which the convolution kernel G is characteristic of the filter used, which is associated with the cutoff scales in space and time, $\overline{\Delta}$ and $\overline{\tau}_c$, respectively. This relation is denoted symbolically by:

$$\overline{\phi} = G \star \phi \quad . \tag{2.2}$$

The dual definition in the Fourier space is obtained by multiplying the spectrum $\widehat{\phi}(\mathbf{k},\omega)$ of $\phi(\mathbf{x},t)$ by the spectrum $\widehat{G}(\mathbf{k},\omega)$ of the kernel $G(\mathbf{x},t)$:

$$\overline{\widehat{\phi}}(\mathbf{k},\omega) = \widehat{\phi}(\mathbf{k},\omega)\widehat{G}(\mathbf{k},\omega) \quad , \tag{2.3}$$

or, in symbolic form:

$$\overline{\widehat{\phi}} = \widehat{G}\widehat{\phi} \quad , \tag{2.4}$$

where k and ω are the spatial wave number and time frequency, respectively.

The function $\widehat{G}$ is the transfer function associated with the kernel G. The spatial cutoff length $\overline{\Delta}$ is associated with the cutoff wave number k_c and time $\overline{\tau}_c$ with the cutoff frequency ω_c. The unresolved part of $\phi(\mathbf{x},t)$, denoted $\phi'(\mathbf{x},t)$, is defined operationally as:

$$\phi'(\mathbf{x},t) = \phi(\mathbf{x},t) - \overline{\phi}(\mathbf{x},t) \tag{2.5}$$

$$= \phi(\mathbf{x},t) - \int_{-\infty}^{+\infty}\int_{-\infty}^{+\infty} \phi(\boldsymbol{\xi},t')G(\mathbf{x}-\boldsymbol{\xi},t-t')dt'd^3\boldsymbol{\xi}, \tag{2.6}$$

or:

$$\phi' = (1-G)\star\phi \quad . \tag{2.7}$$

The corresponding form in spectral space is:

$$\widehat{\phi}'(\mathbf{k},\omega) = \widehat{\phi}(\mathbf{k},\omega) - \overline{\widehat{\phi}}(\mathbf{k},\omega) = \left(1-\widehat{G}(\mathbf{k},\omega)\right)\widehat{\phi}(\mathbf{k},\omega) \quad , \tag{2.8}$$

i.e.

$$\widehat{\phi}' = (1-\widehat{G})\widehat{\phi} \quad . \tag{2.9}$$

2.1.2 Fundamental Properties

In order to be able to manipulate the Navier–Stokes equations after applying a filter, we require that the filter verify the three following properties:

1. Conservation of constants

$$\overline{a} = a \Longleftrightarrow \int_{-\infty}^{+\infty}\int_{-\infty}^{+\infty} G(\boldsymbol{\xi},t')d^3\boldsymbol{\xi}dt' = 1 \tag{2.10}$$

2. Linearity

$$\overline{\phi+\psi} = \overline{\phi}+\overline{\psi} \quad . \tag{2.11}$$

This property is automatically satisfied, since the product of convolution verifies it independently of the characteristics of the kernel G.

3. Commutation with derivation

$$\overline{\frac{\partial\phi}{\partial s}} = \frac{\partial\overline{\phi}}{\partial s}, \quad s = \mathbf{x}, t \quad . \tag{2.12}$$

Introducing the commutator $[f,g]$ of two operators f and g applied to the dummy variable ϕ

$$[f,g]\phi \equiv f\circ g(\phi) - g\circ f(\phi) = f(g(\phi)) - g(f(\phi)) \quad , \tag{2.13}$$

the relation (2.12) can be re-written symbolically

$$\left[G\star, \frac{\partial}{\partial s}\right] = 0 \quad . \tag{2.14}$$

The commutator defined by relation (2.13) has the following properties[2]:

$$[f,g] = -[g,f] \quad \text{Skew-symmetry} \quad , \tag{2.15}$$

$$[f\circ g, h] = [f,h]\circ g + f\circ[g,h] \quad , \tag{2.16}$$

$$[f,[g,h]] + [g,[h,f]] + [h,[f,g]] = 0 \quad \text{Jacobi's identity} \quad . \tag{2.17}$$

The filters that verify these three properties are not, in the general case, Reynolds operators (see Appendix A), *i.e.*

$$\overline{\overline{\phi}} = G\star G\star\phi = G^2\star\phi \neq \overline{\phi} = G\star\phi \quad , \tag{2.18}$$

$$\overline{\phi'} = G\star(1-G)\star\phi \neq 0 \quad , \tag{2.19}$$

which is equivalent to saying that G is not a projector (excluding the trivial case of the identity application). Let us recall that an application P is defined as being a projector if $P\circ P = P$. Such an application is idempotent because it verifies the relation

$$P^n \equiv \underbrace{P\circ P\circ\ldots\circ P}_{n \text{ times}} = P, \ \forall n\in\mathbb{N}^+ \quad . \tag{2.20}$$

[2] In the linear case, the commutator satisfies all the properties of the Poisson-bracket operator, defined in classical mechanics.

When G is not a projector, the filtering can be interpreted as a change of variable, and can be inverted, so there is no loss of information[3] [112]. The kernel of the application is reduced to the null element, *i.e.* $\ker(G) = \{0\}$.

If the filter is a Reynolds operator, we get

$$G^2 = 1 \quad , \tag{2.21}$$

or, remembering the property of conservation of constants:

$$G = 1 \quad . \tag{2.22}$$

In the spectral space, the idempotency property implies that the transfer function takes the following form:

$$\widehat{G}(\mathbf{k}, \omega) = \begin{cases} 0 \\ 1 \end{cases} \qquad \forall \mathbf{k}, \ \forall \omega \quad . \tag{2.23}$$

The convolution kernel $\widehat{G}$ therefore takes the form of a sum of Dirac functions and Heaviside functions associated with non-intersecting domains. The conservation of constants implies that $\widehat{G}$ is 1 for the modes that are constant in space and time. The application can no longer be inverted because its kernel $\ker(G) = \{\phi'\}$ is no longer reduced to the zero element; and consequently, the filtering induces an irremediable loss of information.

A filter is said to be positive if:

$$G(\mathbf{x}, t) > 0, \forall \mathbf{x} \text{ and } \forall t \quad . \tag{2.24}$$

2.1.3 Characterization of Different Approximations

The various methods mentioned in the previous section for reducing the number of degrees of freedom will now be explained. We now assume that the space-time convolution kernel $G(\mathbf{x}-\boldsymbol{\xi}, t-t')$ in $\mathbb{R}^4$ is obtained by tensorizing mono-dimensional kernels:

$$G(\mathbf{x} - \boldsymbol{\xi}, t - t') = G(\mathbf{x} - \boldsymbol{\xi}) G_t(t - t') = G_t(t - t') \prod_{i=1,3} G_i(x_i - \xi_i) \quad . \tag{2.25}$$

The Reynolds time average over a time interval T is found by taking:

$$G_t(t - t') = \frac{\mathcal{H}_T}{T}, \quad G_i(x_i - \xi_i) = \delta(x_i - \xi_i), \quad i = 1, 2, 3 \quad , \tag{2.26}$$

[3] The reduction of the number of degrees of freedom comes from the fact that the new variable, *i.e.* the filtered variable, is more regular than the original one in the sense that it contains fewer high frequencies. Its characteristic scale in space is therefore larger, which makes it possible to use a coarser solution to describe it, and therefore fewer degrees of freedom.

in which δ is a Dirac function and $\mathcal{H}_T$ the Heaviside function corresponding to the interval chosen. This average is extended to the ith direction of space by letting $G_i(x_i - \xi_i) = \mathcal{H}_L/L$, in which L is the desired integration interval.

The phase average corresponding to the frequency ω_c is obtained by letting:

$$\widehat{G}_t(\omega) = \delta(\omega - \omega_c), \quad G_i(x_i - \xi_i) = \delta(x_i - \xi_i), \quad i = 1, 2, 3 \quad . \tag{2.27}$$

In all of the following, only the large-eddy simulation technique based on spatial filtering will be described, because it is the only approach actually used, with very rare exceptions [71, 72]. This is expressed by:

$$G_t(t - t') = \delta(t - t') \quad . \tag{2.28}$$

Different forms of the kernel $G_i(x_i - \xi_i)$ in common use are described in the following section. It should nonetheless be noted that, when a spatial filtering is imposed, it automatically induces an implicit time filtering, since the dynamics of the Navier–Stokes equations makes it possible to associate a characteristic time with each characteristic length scale[4]. We nonetheless assume that the description with a spatial filtering along is pertinent.

2.1.4 Differential Filters

A subset of the filters defined in the previous section is the set of *differential filters* [111, 112, 114, 117]. These filters are such that the kernel G is the Green's function associated to an inverse linear differential operator F:

[4] This time scale is evaluated as follows. Let $\overline{\Delta}$ be the cutoff length associated with the filter, and $k_c = \pi/\overline{\Delta}$ the associated wave number. Let $E(k)$ be the energy spectrum of the exact solution (see Appendix A for a definition). The kinetic energy associated with the wave number k_c is $k_c E(k_c)$. The velocity scale v_c associated with this same wave number is estimated as:

$$v_c = \sqrt{k_c E(k_c)} \quad .$$

The characteristic time t_c associated with the length $\overline{\Delta}$ is calculated by dimensional arguments as follows:

$$t_c = \overline{\Delta}/v_c \quad .$$

The corresponding frequency is $\omega_c = 2\pi/t_c$. The physical analysis shows that for spectrum forms $E(k)$ considered in the large-eddy simulation framework, v_c is a monotonic decreasing function of k_c (resp. monotonic increasing function of $\overline{\Delta}$), so that ω_c is a monotonic increasing function of k_c (resp. monotonic decreasing function of $\overline{\Delta}$). Suppressing the spatial scales corresponding to wave numbers higher than k_c induces the disappearance of the time frequencies higher than ω_c.

$$\begin{aligned}\phi &= F(G\star\phi) = F(\overline{\phi}) \\ &= \overline{\phi} + \theta\frac{\partial\overline{\phi}}{\partial t} + \overline{\Delta}_l\frac{\partial\overline{\phi}}{\partial x_l} + \overline{\Delta}_{lm}\frac{\partial^2\overline{\phi}}{\partial x_{lm}} + \dots \quad ,\end{aligned} \tag{2.29}$$

where θ and $\overline{\Delta}_l$ are some time and space scales, respectively. Differential filters can be grouped into several classes: elliptic, parabolic or hyperbolic filters. In the framework of a generalized space-time filtering, Germano [111, 112, 114] recommends using a parabolic or hyperbolic time filter and an elliptic space filter, for reasons of physical consistency with the nature of the Navier–Stokes equations. It is recalled that a filter is said to be elliptic (resp. parabolic or hyperbolic) if F is an elliptic (resp. parabolic, hyperbolic) operator. Examples are given below [117].

Time Low-Pass Filter. A first example is the time low-pass filter. The associated inverse differential relation is :

$$\phi = \overline{\phi} + \theta\frac{\partial\overline{\phi}}{\partial t} \quad . \tag{2.30}$$

The corresponding convolution filter is:

$$\overline{\phi} = \frac{1}{\theta}\int_{-\infty}^{t}\phi(x,t')\exp\left(-\frac{t-t'}{\theta}\right)dt' \quad . \tag{2.31}$$

It is easily seen that this filter commutes with time and space derivatives. This filter is causal, because it incorporates no future information, and therefore is applicable to real-time or post-processing of the data.

Elliptic Filter. An elliptic filter is obtained by taking:

$$\phi = \overline{\phi} - \overline{\Delta}^2\frac{\partial^2\overline{\phi}}{\partial x_l^2} \quad . \tag{2.32}$$

It corresponds to a second-order elliptic operator, which depends only on space. The convolutional integral form is:

$$\overline{\phi} = \frac{1}{4\pi\overline{\Delta}^2}\int\frac{\phi(\xi,t)}{|x-\xi|}\exp\left(-\frac{|x-\xi|}{\overline{\Delta}}\right)d\xi \quad . \tag{2.33}$$

This filter satisfies the three previously mentionned basic properties.

Parabolic Filter. A parabolic filter is obtained taking

$$\phi = \overline{\phi} + \theta\frac{\partial\overline{\phi}}{\partial t} - \overline{\Delta}^2\frac{\partial^2\overline{\phi}}{\partial x_l^2} \quad , \tag{2.34}$$

yielding

$$\overline{\phi} = \frac{\sqrt{\theta}}{(4\pi)^{3/2}\overline{\Delta}^3}\int_{-\infty}^{t}\int\frac{\phi(\xi,t)}{(t-t')^{3/2}}\exp\left(-\frac{(x-\xi)^2\theta}{4\overline{\Delta}^2(t-t')} - \frac{t-t'}{\theta}\right)d\xi dt' \quad . \tag{2.35}$$

It is easily verified that the parabolic filter satistifies the three required properties.

Convective and Lagrangian Filters. A convective filter is obtained by adding a convective part to the parabolic filter, leading to:

$$\phi = \overline{\phi} + \theta\frac{\partial\overline{\phi}}{\partial t} + \theta V_l\frac{\partial\overline{\phi}}{\partial x_l} - \overline{\Delta}^2\frac{\partial^2\overline{\phi}}{\partial x_l^2} \quad , \tag{2.36}$$

where $\mathbf{V}$ is an arbitrary velocity field. This filter is linear and constant preserving, but commutes with derivatives if and only if $\mathbf{V}$ is uniform. A Lagrangian filter is obtained when $\mathbf{V}$ is taken equal to $\mathbf{u}$, the velocity field. In this last case, the commutation property is obviously lost.

2.1.5 Three Classical Filters for Large-Eddy Simulation

Three convolution filters are ordinarily used for performing the spatial scale separation. For a cutoff length $\overline{\Delta}$, in the mono-dimensional case, these are written:

– Box or top-hat filter:

$$G(x-\xi) = \begin{cases}\dfrac{1}{\overline{\Delta}} \text{ if } |x-\xi| \le \dfrac{\overline{\Delta}}{2} \\ 0 \quad \text{otherwise}\end{cases} \quad , \tag{2.37}$$

$$\widehat{G}(k) = \frac{\sin(k\overline{\Delta}/2)}{k\overline{\Delta}/2} \quad . \tag{2.38}$$

The convolution kernel G and the transfer function $\widehat{G}$ are represented in Figs. 2.1 and 2.2, respectively.

– Gaussian filter:

$$G(x-\xi) = \left(\frac{\gamma}{\pi\overline{\Delta}^2}\right)^{1/2}\exp\left(\frac{-\gamma|x-\xi|^2}{\overline{\Delta}^2}\right) \quad , \tag{2.39}$$

$$\widehat{G}(k) = \exp\left(\frac{-\overline{\Delta}^2k^2}{4\gamma}\right) \quad , \tag{2.40}$$

in which γ is a constant generally taken to be equal to 6. The convolution kernel G and the transfer function $\widehat{G}$ are represented in Figs. 2.3 and 2.4, respectively.

– Spectral or sharp cutoff filter:

$$G(x-\xi) = \frac{\sin\left(k_c(x-\xi)\right)}{k_c(x-\xi)}, \text{ avec } k_c = \frac{\pi}{\overline{\Delta}} \quad , \tag{2.41}$$

$$\widehat{G}(k) = \begin{cases}1 \text{ if } |k| \le k_c \\ 0 \quad \text{otherwise}\end{cases} \quad . \tag{2.42}$$

The convolution kernel G and the transfer function $\widehat{G}$ are represented in Figs. 2.5 and 2.6, respectively.

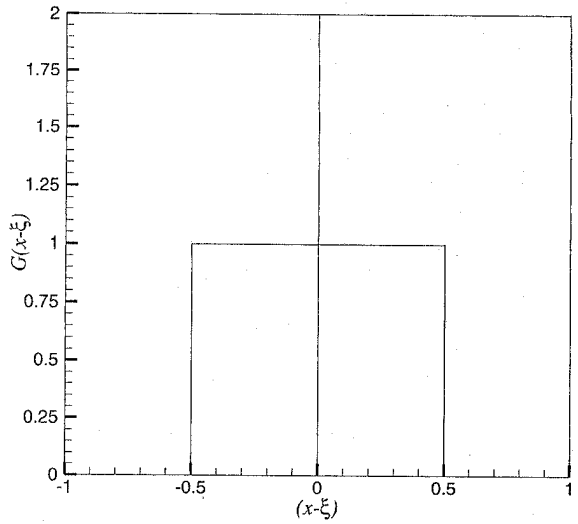

Fig. 2.1. Top-hat filter. Convolution kernel in the physical space normalized by $\overline{\Delta}$.

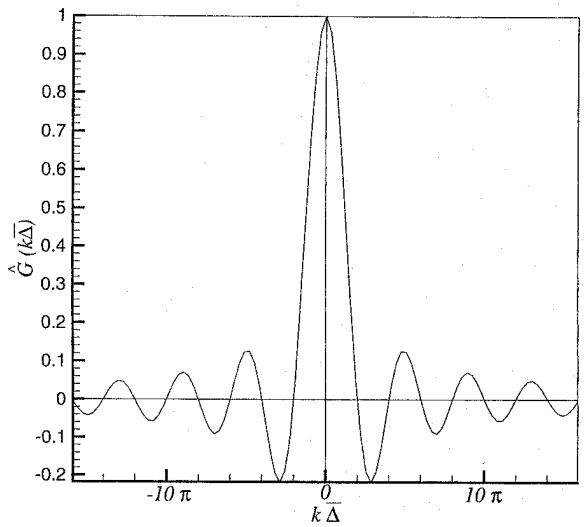

Fig. 2.2. Top-hat filter. Associated transfer function.

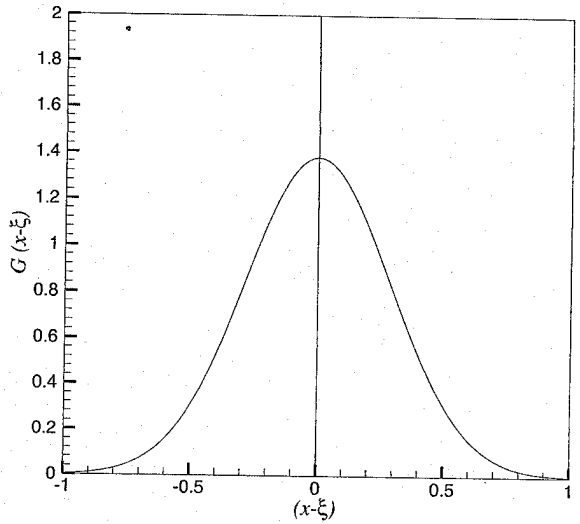

Fig. 2.3. Gaussian filter. Convolution kernel in the physical space normalized by $\overline{\Delta}$.

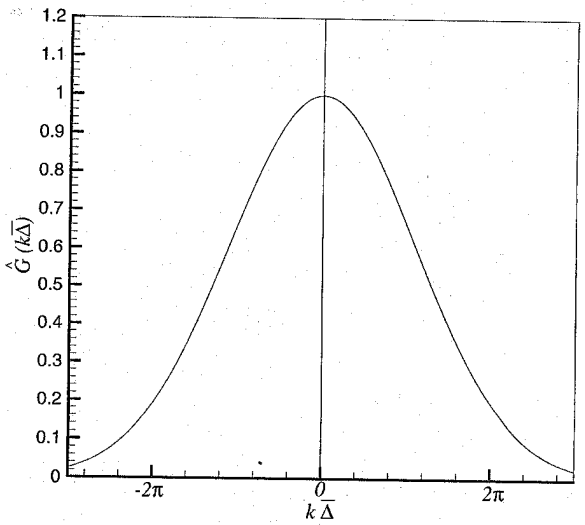

Fig. 2.4. Gaussian filter. Associated transfer function.

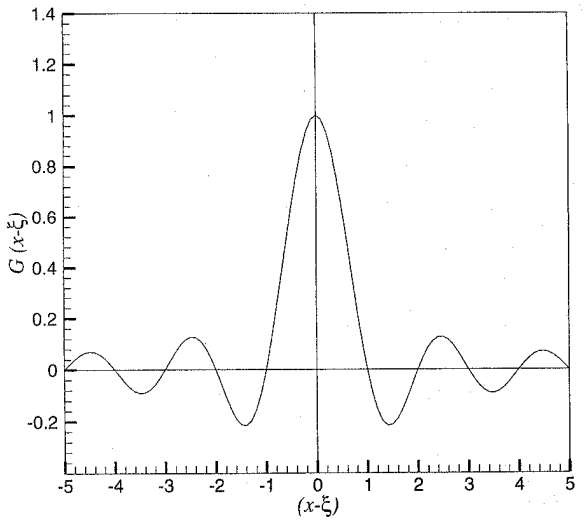

Fig. 2.5. Sharp cutoff filter. Convolution kernel in the physical space.

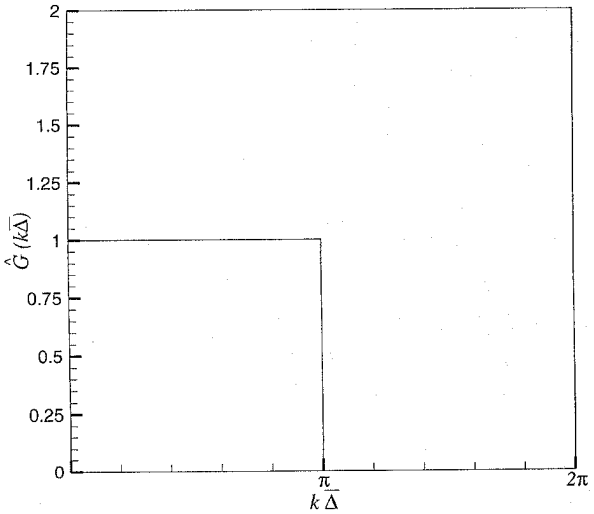

Fig. 2.6. Sharp cutoff filter. Associated transfer function.

It is trivially verified that the first two filters are positive while the sharp cutoff filter is not. The top-hat filter is local in the physical space (its support is compact) and non-local in the Fourier space, inversely from the sharp cutoff filter, which is local in the spectral space and non-local in the physical space. As for the Gaussian filter, it is non-local both in the spectral and physical spaces. Of all the filters presented, only the sharp cutoff has the property:

$$\underbrace{\widehat{G}\cdot\widehat{G}\ldots\cdot\widehat{G}}_{n \text{ times}} = \widehat{G}^n = \widehat{G} \quad ,$$

and is therefore idempotent in the spectral space. Lastly, the top-hat and Gaussian filters are said to be smooth because there is a frequency overlap between the quantities $\overline{\mathbf{u}}$ and $\mathbf{u}'$.

2.2 Extension to the Inhomogeneous Case

2.2.1 General

In the above explanations, it was assumed that the filter is homogeneous and isotropic. These assumptions are at time too restrictive for the resulting conclusions to be usable. For example, the definition of bounded fluid domains forbids the use of filters that are non-local in space, since these would no longer be defined. The problem then arises of defining filters near the domain boundaries. At the same time, there may be some advantage in varying the filter cutoff length to adapt the structure of the solution better and thereby ensure optimum gain in terms of reducing the number of degrees of freedom in the system to be resolved.

From relation (2.1), we get the following general form of the commutation error for a convolution filter $G(y, \overline{\Delta}(x,t))$ on a domain Ω [105, 121]:

$$\left[\frac{\partial}{\partial x}, G\star\right]\phi = \frac{\partial}{\partial x}(G\star\phi) - G\star\frac{\partial\phi}{\partial x} \,. \tag{2.43}$$

The first term of the right hand side of (2.43) can be expanded as

$$\frac{\partial}{\partial x}(G\star\phi) = \frac{\partial}{\partial x}\int_\Omega G(x-\xi,\overline{\Delta}(x,t))\phi(\xi,t)d\xi \tag{2.44}$$

$$= \left(\frac{\partial G}{\partial\overline{\Delta}}\star\phi\right)\frac{\partial\overline{\Delta}}{\partial x} + \int_{\partial\Omega} G(x-\xi,\overline{\Delta}(x,t))\phi(\xi,t)n(\xi)ds + G\star\frac{\partial\phi}{\partial x} \quad , \tag{2.45}$$

where $n(\xi)$ is the outward unit normal vector to the boundary of Ω, $\partial\Omega$, yielding

$$\left[\frac{\partial}{\partial x}, G\star\right]\phi = \left(\frac{\partial G}{\partial \overline{\Delta}} \star \phi\right)\frac{\partial \overline{\Delta}}{\partial x} + \int_{\partial\Omega} G(x-\xi, \overline{\Delta}(x,t))\phi(\xi,t)n(\xi)ds \ . \quad (2.46)$$

The first term appearing in the right hand side of relation (2.46) is due to spatial variation of the filtering length, while a domain boundary generates the second one. A similar development leads to:

$$\left[\frac{\partial}{\partial t}, G\star\right]\phi = \left(\frac{\partial G}{\partial \overline{\Delta}} \star \phi\right)\frac{\partial \overline{\Delta}}{\partial t} \ . \quad (2.47)$$

These error terms must be eliminated, or bounded, in order to be able to define a controlled and consistent filtering process for large-eddy simulation. This is done by deriving new filtering operators. Several alternatives to the classical convolution products have been proposed, which are described in the following.

2.2.2 Non-uniform Filtering Over an Arbitrary Domain

This section presents the findings concerning the extension of the filtering to the case where the filter cutoff length varies in space and where the domain over which it applies is bounded or infinite.

New Definition of Filters and Properties: Mono-dimensional Case. Alternative proposals in the homogeneous case. Ghosal and Moin [123] propose to define the filtering of a variable $\phi(\xi)$, defined over the interval $]-\infty, +\infty[$, as

$$\overline{\phi}(\xi) = G\star\phi = \frac{1}{\overline{\Delta}}\int_{-\infty}^{+\infty} G\left(\frac{\xi-\eta}{\overline{\Delta}}\right)\phi(\eta)d\eta \ , \quad (2.48)$$

in which the cutoff length $\overline{\Delta}$ is constant. The convolution kernel G is made to verify the following four properties:

1. Symmetry

$$G(-\xi) = G(\xi) \ . \quad (2.49)$$

We note that this property was not explicitly required before, but that it is verified by the three filters described in Sect. 2.1.5.

2. Conservation of constants

$$\int_{-\infty}^{+\infty} aG(\xi)d\xi, \quad a = \text{const.} \quad (2.50)$$

3. Fast decay. $G(\xi) \to 0$ as $|\xi| \to \infty$ fast enough for all of its moments to be finite, *i.e.*

$$\int_{-\infty}^{+\infty} G(\xi)\xi^n d\xi < \infty, \quad \forall n \geq 0 \ . \quad (2.51)$$

4. Quasi-local in physical space. $G(\xi)$ is localized (in a sense to be specified) in the interval $[-1/2, 1/2]$.

Extension of the Top-Hat Filter to the Inhomogeneous Case: Properties. Considering definition (2.48), the top-hat filter (2.37) is expressed:

$$G(\xi) = \begin{cases} 1 & \text{if } |\xi| \leq \frac{1}{2} \\ 0 & \text{otherwise} \end{cases} \ . \quad (2.52)$$

There are a number of ways of extending this filter to the inhomogeneous case. The problem posed is strictly analogous to that of extending finite volume type schemes to the case of inhomogeneous structured grids: the control volumes can be defined directly on the computational grid or in a reference space carrying a uniform grid, after a change of variable. Two extensions of the box filter are discussed in the following, each based on a different approach.

Direct extension. If the cutoff length varies in space, one solution is to say:

$$\overline{\phi}(\xi) = \frac{1}{\Delta_+(\xi)+\Delta_-(\xi)}\int_{\xi-\Delta_-(\xi)}^{\xi+\Delta_+(\xi)} \phi(\eta)d\eta \ , \quad (2.53)$$

in which $\Delta_+(\xi)$ and $\Delta_-(\xi)$ are positive functions and $(\Delta_+(\xi)+\Delta_-(\xi))$ is the cutoff length at point ξ. These different quantities are represented in Fig. 2.7. If the domain is finite or semi- infinite, the functions $\Delta_+(\xi)$ and $\Delta_-(\xi)$ must decrease fast enough near the domain boundaries for the integration interval $[\xi-\Delta_-(\xi), \xi+\Delta_+(\xi)]$ to remain defined. The box filter is extended intuitively here, as an average over the control cell $[\xi-\Delta_-(\xi), \xi+\Delta_+(\xi)]$. This approach is similar to the finite volume techniques based on control volumes defined directly on the computational grid.

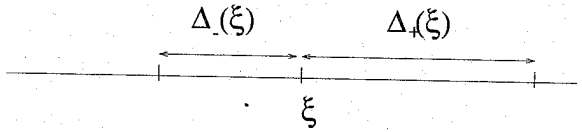

Fig. 2.7. Direct extension of the top-hat filter. Representation of the integration cell at point ξ.

It is shown that this expression does not ensure the commutation property with derivation in space. Relation (2.12) becomes (the dependency of the functions Δ_+ and Δ_- as a function of ξ is not explicitly state, to streamline the notation):

$$\left[G\star, \frac{d}{d\xi}\right]\phi = \frac{(d/d\xi)(\Delta_- + \Delta_+)}{\Delta_- + \Delta_+}\overline{\phi} - \frac{1}{\Delta_+ + \Delta_-}\left[\phi(\xi+\Delta_+)\frac{d\Delta_+}{d\xi} + \phi(\xi-\Delta_-)\frac{d\Delta_-}{d\xi}\right] \ . \quad (2.54)$$

The amplitude of the error committed cannot be evaluated *a priori*, and thus cannot be neglected. Also, when (2.53) is applied to the Navier–Stokes equations, all the terms, including the linear ones, will introduce unknown terms that will require a closure.

Extension by Variable Change. SOCF. To remedy this problem, a more general alternative description than relation (2.53) is proposed by Ghosal and Moin [123]. This new definition consists of defining filters that commute at the second order with the derivation in space (Second Order Commuting Filter, or SOCF). This is based on a change of variable that allows the use of a homogeneous filter. The function ϕ is assumed to be defined over a finite or infinite interval $[a,b]$. Any regular monotonic function defined over this interval can be related to a definite function over the interval $[-\infty,+\infty]$ by performing the variable change:

$$\xi = f(x) \quad , \tag{2.55}$$

in which f is a strictly monotonic differentiable function such that:

$$f(a) = -\infty, \quad f(b) = +\infty \quad . \tag{2.56}$$

The constant cutoff length $\overline{\Delta}$ defined over the reference space $[-\infty,+\infty]$ is associated with the variable cutoff length $\overline{\delta}(x)$ over the starting interval by the relation:

$$\overline{\delta}(x) = \frac{\overline{\Delta}}{f'(x)} \quad . \tag{2.57}$$

In the case of a finite or semi-infinite domain, the function f' takes infinite values at the bounds and the convolution kernel becomes a Dirac function. The filtering of a function $\psi(x)$ is defined in the inhomogeneous case in three steps:

1. We perform the variable change $x = f^{-1}(\xi)$, which leads to the definition of the function $\phi(\xi) = \psi(f^{-1}(\xi))$.
2. The function $\phi(\xi)$ is then filtered by the usual homogeneous filter (2.48):

$$\overline{\psi}(x) \equiv \overline{\phi}(\xi) = \frac{1}{\overline{\Delta}} \int_{-\infty}^{+\infty} G\left(\frac{f(x)-\eta}{\overline{\Delta}}\right) \phi(\eta) d\eta \quad . \tag{2.58}$$

3. The filtered quantity is then re-expressed in the original space:

$$\overline{\psi}(x) = \frac{1}{\overline{\Delta}} \int_a^b G\left(\frac{f(x)-f(y)}{\overline{\Delta}}\right) \psi(y) f'(y) dy \quad . \tag{2.59}$$

This new expression of the filter modifies the commutation error with the spatial derivation. Using (2.58) and integrating by parts, we get:

$$\frac{d\overline{\psi}}{dx} = -\frac{f'(x)}{\overline{\Delta}} \left[G\left(\frac{f(x)-f(y)}{\overline{\Delta}}\right) \psi(y) \right]_{y=a}^{y=b} + \frac{1}{\overline{\Delta}} \int_a^b G\left(\frac{f(x)-f(y)}{\overline{\Delta}}\right) f'(x)\psi'(y) dy \quad . \tag{2.60}$$

The fast decay property of the kernel G makes it possible to cancel the first term of the rigth-hand side. The commutation error is:

$$\left[G\star, \frac{d}{d\xi}\right] \phi = \frac{1}{\overline{\Delta}} \int_a^b G\left(\frac{f(x)-f(y)}{\overline{\Delta}}\right) f'(y)\psi'(y) \times \left[1 - \frac{f'(x)}{f'(y)}\right] dy \quad . \tag{2.61}$$

In order to simplify this expression, we introduce a new variable ζ such that:

$$f(y) = f(x) + \overline{\Delta}\zeta \quad . \tag{2.62}$$

The variable y is then re-expressed as a series as a function of $\overline{\Delta}$:

$$y = y_0(\zeta) + \overline{\Delta} y_1(\zeta) + \overline{\Delta}^2 y_2(\zeta) + ... \tag{2.63}$$

Then, combining relations (2.62) and (2.63), we get (the dependence of the functions according to the variable x is not explicitly shown, to streamline the notation):

$$y = x + \frac{\overline{\Delta}\zeta}{f'} - \frac{\overline{\Delta}^2 f''\zeta}{2f'^3} + ... \quad , \tag{2.64}$$

which allows us to re-write relation (2.61) as:

$$\left[G\star, \frac{d}{d\xi}\right] \phi = \int_{-\infty}^{+\infty} G(\zeta)\psi'(y(\zeta)) \left[1 - \frac{f'(x)}{f'(y(\zeta))}\right] d\zeta \tag{2.65}$$

$$= C_1\overline{\Delta} + C_2\overline{\Delta}^2 + ... \quad , \tag{2.66}$$

in which the coefficients C_1 and C_2 are expressed as:

$$C_1 = \frac{f''\psi'}{f'^2} \int_{-\infty}^{+\infty} \zeta G(\zeta) d\zeta \quad , \tag{2.67}$$

$$C_2 = \frac{2f'f''\psi'' + f'f'''\psi' - 3f''^2\psi'}{2f'^4} \int_{-\infty}^{+\infty} \zeta^2 G(\zeta) d\zeta \quad . \tag{2.68}$$

The symmetry property of the kernel G implies $C_1 = 0$, which ensures that the filter commutation error with the spatial derivation is of the second order as a function of the cutoff length $\overline{\Delta}$. The authors call this Second-Order Commuting Filter (SOCF).

A study of the spectral distribution of the commutation error is available in reference [123]. Rather than detailing this analysis here, only the major results will be explained. Considering a function of the form:

$$\psi(x) = \widehat{\psi}_k^{\mathrm{i}kx}, \quad \mathrm{i}^2 = -1 \quad , \tag{2.69}$$

the two derivation operations are written:

$$\overline{\frac{d\psi}{dx}} = \mathrm{i}k\overline{\psi}, \quad \frac{d\overline{\psi}}{dx} = \mathrm{i}k\overline{\psi} \quad . \tag{2.70}$$

The commutation error can be measured by comparing the two wave numbers k and k', the latter being such that $\overline{\mathrm{i}k\psi} = \mathrm{i}k'\overline{\psi}$. The commutation error is zero if $k = k'$. Algebraic manipulations lead to the relation:

$$\frac{k'}{k} = 1 - \mathrm{i}\overline{\Delta}\frac{f''}{f'^2}\frac{\displaystyle\int_{-\infty}^{+\infty}\zeta G(\zeta)\sin(k\overline{\Delta}\zeta/f')d\zeta}{\displaystyle\int_{-\infty}^{+\infty}G(\zeta)\cos(k\overline{\Delta}\zeta/f')d\zeta} \quad . \tag{2.71}$$

Using the modal decomposition (2.69), the commutation error can be expressed in differential form. The calculations lead to:

$$\left[G\star, \frac{d}{dx}\right]\psi = \alpha^{(2)}\frac{f''}{f'^3}\overline{\Delta}^2\frac{d^2\overline{\psi}}{dx^2} + O(k\overline{\Delta})^4 \tag{2.72}$$

$$= -\alpha^{(2)}\overline{\delta}^2\left(\frac{\overline{\delta}'}{\overline{\delta}}\right)\frac{d^2\overline{\psi}}{dx^2} + O(k\overline{\delta})^4 \quad , \tag{2.73}$$

in which $\overline{\delta}(x)$ is the local cutoff length and $\alpha^{(2)}$ the second-order moment of G, *i.e.*

$$\alpha^{(2)} = \int_{-\infty}^{+\infty}\zeta^2 G(\zeta)d\zeta \quad . \tag{2.74}$$

Van der Ven's Filters. Commuting filters can be defined with the spatial derivation at an order higher than 2, at least in the case of an infinite domain. To obtain such filters, Van der Ven [330] proposes defining the filtering for the case of a variable cutoff length $\overline{\delta}(x)$ by direct extension of the form (2.48):

$$\overline{\phi}(x) = \frac{1}{\overline{\delta}(x)}\int_{-\infty}^{+\infty}G\left(\frac{x-y}{\overline{\delta}(x)}\right)\phi(y)dy \quad . \tag{2.75}$$

The function G is assumed here to be class C^1, symmetrical, and must conserve the constants. Also, the function $\overline{\delta}(x)$ is also assumed to be class C^1. This definition is achieved by linearizing the general formula (2.59) around x, that is by letting $\phi'(y) = \phi'(x)$ and $\phi(x) - \phi(y) = \phi'(x)(x-y)$ and including relation (2.57). This linearization operation is equivalent to considering that the function ϕ is linear in a neighbourhood of x containing the support of the convolution kernel. By introducing the variable change $y = x - \zeta\overline{\delta}(x)$, the corresponding commutation error is expressed:

$$\left[G\star, \frac{d}{dx}\right]\phi = \frac{\overline{\delta}'}{\overline{\delta}}\int\left(G(\zeta) + \zeta G'(\zeta)\right)\phi(x - \zeta\delta(x))d\zeta \quad . \tag{2.76}$$

To increase the order of the commutation error, we look for functions G that are solutions to the equation

$$G + \zeta G' = aG^{(n)}, \quad n > 1 \quad , \tag{2.77}$$

in which a is a real and $G^{(n)}$ designates the n-th derivative of the kernel G. For such functions, the commutation error becomes:

$$\left[G\star, \frac{d}{dx}\right]\phi = a\frac{\overline{\delta}'}{\overline{\delta}}(-1)^n\int G(\zeta)\left(\frac{\partial}{\partial\zeta}\right)^n\phi(x - \zeta\overline{\delta}(x))d\zeta \tag{2.78}$$

$$= a\overline{\delta}'(x)\overline{\delta}(x)^{n-1}\overline{\phi^{(n)}}(x) \quad , \tag{2.79}$$

and is thus formally of order $n-1$. Simple analysis shows that the Fourier transform $\widehat{G}$ of the solution to problem (2.77) verifying the constant conservation property is of the form:

$$\widehat{G}(k) = \exp\left(\frac{-a\mathrm{i}^n}{n}k^n\right) \quad . \tag{2.80}$$

The symmetry property of G implies that $n = 2m$ is even, and therefore:

$$\widehat{G}(k) = \exp\left(\frac{-a(-1)^m}{2m}k^{2m}\right) \quad . \tag{2.81}$$

The fast decay property is recovered for $a = b(-1)^m, b > 0$. It can be seen that the Gaussian filter then occurs again by letting $m = 1$. It is important to note that this analysis is valid only for infinite domains, because when the bounds of the fluid domain are included they bring out additional error terms with which it is no longer possible to be sure of the order of the commutation error. The transfer function obtained for various values of the parameter m is represented in Fig. 2.8.

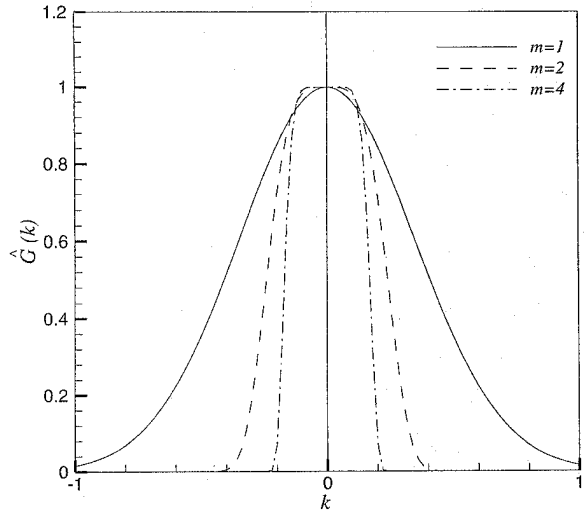

Fig. 2.8. High-order commuting filter. Graph of the associated transfer function for different values of the parameter m.

High-Order Commuting Filters. Van der Ven's analysis has been generalized by Vasilyev *et al.* [332] so as to contain previous works (SOCF and Van der Ven's filters) as special cases. As for SOCF, the filtering process is defined thanks to the use of a reference space. We now consider that the physical domain $[a, b]$ is mapped into the domain $[\alpha, \beta]$. Ghosal and Moin used $\alpha = -\infty$ and $\beta = +\infty$. The correspondances between the two domains are summarized in Table 2.1.

Table 2.1. Correspondances for Vasilyev's high-order commuting filters.

Domain	$[a, b]$	$[\alpha, \beta]$
Coordinate	$x = f^{-1}(\xi)$	$\xi = f(x)$
Filter length	$\overline{\delta}(x) = \overline{\Delta}/f'(x)$	$\overline{\Delta}$
Function	$\psi(x)$	$\phi(\xi) = \psi(f^{-1}(\xi))$

Considering this new mapping, relation (2.58) is transformed as

$$\overline{\phi}(\xi) = \frac{1}{\overline{\Delta}} \int_{\beta}^{\alpha} G\left(\frac{\xi - \eta}{\overline{\Delta}}\right) \phi(\eta) d\eta \quad , \tag{2.82}$$

and using the change of variables (2.62), we get

$$\overline{\phi}(\xi) = \int_{\frac{\xi-\beta}{\overline{\Delta}}}^{\frac{\xi-\alpha}{\overline{\Delta}}} G(\zeta)\, \phi(\xi - \overline{\Delta}\zeta) d\zeta \quad . \tag{2.83}$$

The next step consists in performing a Taylor expansion of $\phi(\xi - \overline{\Delta}\zeta)$ in powers of $\overline{\Delta}$:

$$\phi(\xi - \overline{\Delta}\zeta) = \sum_{k=0,+\infty} \frac{(-1)^k}{k!} \overline{\Delta}^k \zeta^k \frac{\partial^k \phi}{\partial \xi^k}(\xi) \quad . \tag{2.84}$$

Substituting (2.84) into (2.83), we get

$$\overline{\phi}(\xi) = \sum_{k=0,+\infty} \frac{(-1)^k}{k!} \overline{\Delta}^k \alpha^{(k)}(\xi) \frac{\partial^k \phi}{\partial \xi^k}(\xi) \quad , \tag{2.85}$$

where the kth moment of the filter kernel is now defined as

$$\alpha^{(k)}(\xi) = \int_{\frac{\xi-\beta}{\overline{\Delta}}}^{\frac{\xi-\alpha}{\overline{\Delta}}} G(\zeta)\, \zeta^k d\zeta \quad . \tag{2.86}$$

Using the relation (2.85), the space derivative of the filtered variable expressed in the physical space can be evaluated as follows:

$$\frac{d\overline{\psi}}{dx}(x) = f'(x) \frac{d\overline{\phi}}{d\xi}(\xi) \tag{2.87}$$

$$= f'(x) \sum_{k=0,+\infty} \frac{(-1)^k}{k!} \overline{\Delta}^k \left(\frac{d\alpha^{(k)}}{d\xi}(\xi) \frac{\partial^k \phi}{\partial \xi^k}(\xi) + \alpha^{(k)}(\xi) \frac{\partial^{k+1} \phi}{\partial \xi^{k+1}}(\xi) \right) . \tag{2.88}$$

A similar procedure is used to evaluate the second part of the commutation error. Using (2.87) and the same change of variables, we get:

$$\frac{\overline{d\psi}}{dx}(x) = \frac{1}{\overline{\Delta}} \int_{\alpha}^{\beta} G\left(\frac{\xi - \eta}{\overline{\Delta}}\right) \frac{d\phi}{d\eta}(\eta) f'(f^{-1}(\eta)) d\eta \quad , \tag{2.89}$$

with

$$f'(f^{-1}(\eta)) = \sum_{l=1,+\infty} \frac{1}{(l-1)!} \left(\sum_{k=1,+\infty} \frac{(-1)^k}{k!} \overline{\Delta}^k \zeta^k \frac{\partial^k f^{-1}}{\partial \xi^k}(\xi) \right)^{l-1} \frac{\partial^l f}{\partial x^l}(x) \quad , \tag{2.90}$$

and

$$\frac{d\phi}{d\eta}(\eta) = \sum_{k=0,+\infty} \frac{(-1)^k}{k!} \overline{\Delta}^k \zeta^k \frac{\partial^{k+1} \phi}{\partial \xi^{k+1}}(\xi) \quad . \tag{2.91}$$

Making the assumptions that all the Taylor expansion series are convergent[5], the commutation error in the physical space is equal to

$$\left[G\star, \frac{d}{dx}\right]\psi = \sum_{k=1,+\infty} A_k \alpha^{(k)}(\xi)\overline{\Delta}^k + \sum_{k=0,+\infty} B_k \frac{d\alpha^{(k)}}{d\xi}(\xi)\overline{\Delta}^k \quad , \tag{2.92}$$

where A_k and B_k are real non-zero coefficients. It is easily seen from relation (2.92) that the commutation error is determined by the filter moments and the mapping function. The order of the commutation error can then be governed by chosing an adequate filter kernel. Vasilyev proposes to use a function G such that:

$$\alpha^{(0)} = 1 \quad \forall \xi \in [\alpha, \beta] \quad , \tag{2.93}$$

$$\alpha^{(k)} = 0 \quad 1 \leq k \leq n-1, \quad \forall \xi \in [\alpha, \beta] \quad , \tag{2.94}$$

$$\alpha^{(k)} < \infty \quad k \geq n, \quad \forall \xi \in [\alpha, \beta] \quad . \tag{2.95}$$

An immediate consequence is

$$\frac{d\alpha^{(k)}}{d\xi}(\xi) = 0, \quad 0 \leq k \leq n-1, \quad \forall \xi \in [\alpha, \beta] \quad , \tag{2.96}$$

leading to

$$\left[G\star, \frac{d}{dx}\right]\psi = O(\overline{\Delta}^n) \quad . \tag{2.97}$$

The commutation error can be controlled by choosing a kernel G with desired moment values. It is important noting that conditions (2.93) - (2.95) do not require that the filter kernel be symmetric. Discrete filters verifying theses properties will be discussed in Sect. 10.2.

Extension to the Multidimensional Case

SOCF Filters. SOCF filters are extensible to the three-dimensional case for finite or infinite domains. Let (x_1, x_2, x_3) be a Cartesian system, and (X_1, X_2, X_3) the reference axis system associated with a uniform isotropic grid with a mesh size $\overline{\Delta}$. The two systems are related by the relations:

$$X_1 = H_1(x_1, x_2, x_3), \quad x_1 = h_1(X_1, X_2, X_3) \quad , \tag{2.98}$$

$$X_2 = H_2(x_1, x_2, x_3), \quad x_2 = h_2(X_1, X_2, X_3) \quad , \tag{2.99}$$

$$X_3 = H_3(x_1, x_2, x_3), \quad x_3 = h_3(X_1, X_2, X_3) \quad , \tag{2.100}$$

[5] Vasilyev *et al.* [332] show that this is always true for practical numerical simulations.

or, in vectorial form:

$$\mathbf{X} = \mathbf{H}(\mathbf{x}), \quad \mathbf{x} = \mathbf{h}(\mathbf{X}), \quad \mathbf{h} = \mathbf{H}^{-1} \quad . \tag{2.101}$$

The filtering of a function $\psi(\mathbf{x})$ is defined analogously to the mono-dimensional case. We first make a variable change to work in the reference coordinate system, in which a homogeneous filter is applied, and then perform the inverse transformation. The three-dimensional convolution kernel is defined by tensorizing homogeneous mono-dimensional kernels.

After making the first change of variables, we get:

$$\overline{\psi}(\mathbf{h}(\mathbf{X})) = \frac{1}{\overline{\Delta}^3} \int \prod_{i=1,3} G\left(\frac{X_i - X_i'}{\overline{\Delta}}\right) \psi(\mathbf{h}(\mathbf{X}'))d^3\mathbf{X}' \quad , \tag{2.102}$$

or, in the original space:

$$\overline{\psi}(\mathbf{x}) = \frac{1}{\overline{\Delta}^3} \int \prod_{i=1,3} G\left(\frac{H_i(\mathbf{x}) - X_i'}{\overline{\Delta}}\right) \psi(\mathbf{h}(\mathbf{X}'))d^3\mathbf{X}' \tag{2.103}$$

$$= \frac{1}{\overline{\Delta}^3} \int \prod_{i=1,3} G\left(\frac{H_i(\mathbf{x}) - H_i(\mathbf{x}')}{\overline{\Delta}}\right) \psi(\mathbf{x}')J(\mathbf{x}')d^3\mathbf{x}', \tag{2.104}$$

where $J(\mathbf{x})$ is the Jacobian of the transformation $\mathbf{X} = \mathbf{H}(\mathbf{x})$. Analysis of the error shows that, for filters defined this way, the commutation error with the derivation in space is always of the second order, *i.e.*

$$\overline{\frac{\partial\psi}{\partial x_k}} - \frac{\partial\overline{\psi}}{\partial x_k} = O(\overline{\Delta}^2) \quad , \tag{2.105}$$

where the second term of the left-hand side is written:

$$\frac{\partial\overline{\psi}}{\partial x_k} = \frac{1}{\overline{\Delta}^3} \int \frac{1}{\overline{\Delta}} G'\left(\frac{H_j(\mathbf{x}) - X_j'}{\overline{\Delta}}\right) \times \prod_{i=1,3;i\neq j} G\left(\frac{H_i(\mathbf{x}) - X_i'}{\overline{\Delta}}\right) H_{j,k}(\mathbf{x})\psi(\mathbf{h}(\mathbf{X}'))d^3\mathbf{X}', \tag{2.106}$$

with the notation:

$$H_{j,k}(\mathbf{x}) = \frac{\partial H_j(\mathbf{x})}{\partial x_k} \quad . \tag{2.107}$$

Differential analysis of the commutation error is performed by considering the solutions of the form:

$$\psi(\mathbf{x}) = \widehat{\psi_\mathbf{k}} \exp(i\mathbf{k}\cdot\mathbf{x}) \quad . \tag{2.108}$$

An analogous approach to the one already made in the mono-dimensional case leads to the relation:

$$\left[G\star, \frac{\partial}{\partial x_k}\right]\psi = -\alpha^{(2)}\overline{\Delta}^2\Gamma_{kmp}\frac{\partial^2\overline{\psi}}{\partial x_m \partial x_p} + O(k\overline{\Delta})^4 \quad , \tag{2.109}$$

where the function Γ_{kmp} is defined as:

$$\Gamma_{kmp} = h_{m,jq}(\mathbf{H}(\mathbf{x}))h_{p,q}(\mathbf{H}(\mathbf{x}))H_{j,k}(\mathbf{x}) \quad . \tag{2.110}$$

Van der Ven's Filters. Van der Ven's simplified filtering naturally extends to the three-dimensional case in Cartesian coordinates by letting:

$$\overline{\phi}(\mathbf{x}) = \frac{1}{\prod\limits_{i=1,3}\overline{\delta}_i(\mathbf{x})}\int_{R^3}\prod_{i=1,3} G\left(\frac{x_i - x_i'}{\overline{\delta}_i(\mathbf{x})}\right)\phi(\mathbf{x}')d^3\mathbf{x}' \quad , \tag{2.111}$$

in which $\overline{\delta}_i(\mathbf{x})$ is the filter cutoff length in the ith direction of space at point x. For a kernel G verifying (2.77), the commutation error is expressed:

$$\left[G\star, \frac{\partial}{\partial x_j}\right]\phi = a\sum_{i=1,3}\frac{\partial\overline{\delta}_i(\mathbf{x})}{\partial x_j}\overline{\delta}_i(\mathbf{x})^{n-1}\overline{\frac{\partial^n\phi(\mathbf{x})}{\partial x_i^n}} \quad , \tag{2.112}$$

and is formally of order $n-1$.

High-Order Commuting Filters. Vasilyev's filters are generalized to the multiple dimension case in the same way as SOCF.

3. Application to Navier–Stokes Equations

This chapter is devoted to the derivation of the constitutive equations of the large-eddy simulation technique, which is to say the filtered Navier–Stokes equations. Our interest here is in the case of an incompressible viscous Newtonian fluid of constant mass density and temperature.

We first describe the application of an isotropic spatial filter[1] to the Navier–Stokes equations expressed in Cartesian coordinates[2]. It should be noted that this ideal framework, which implies that the fluid domain is unbounded, is the one nearly all authors use because it is only in this framework that the theory on which the subgrid modeling is based can be fully developed. The commutation errors between the filter and the derivation in space are then ignored. Section 3.4 is on the application of an inhomogeneous filter to the basic equations.

We begin by deriving the filtered Navier–Stokes equations. The various decompositions of the non-linear term as a function of the filtered quantities are then discussed. We lastly introduce the closure problem, *i.e.* the representation of the unknowns as a function of the variables in the filtered problem.

3.1 Navier–Stokes Equations

We recall here the equations governing the evolution of an incompressible Newtonian fluid, first in the physical space, and then in the spectral space.

3.1.1 Formulation in Physical Space

In the physical space, the velocity field $\mathbf{u} = (u_1, u_2, u_3)$ expressed in a reference Cartesian coordinate system $\mathbf{x} = (x_1, x_2, x_3)$ is a solution of the system comprising the momentum and continuity equations:

$$\frac{\partial u_i}{\partial t} + \frac{\partial}{\partial x_j}(u_i u_j) = -\frac{\partial p}{\partial x_i} + \nu\frac{\partial}{\partial x_j}\left(\frac{\partial u_i}{\partial x_j} + \frac{\partial u_j}{\partial x_i}\right), \quad i = 1,2,3 \quad , \tag{3.1}$$

[1] Refer to the definition given in Chap. 2.

[2] The case of the Navier–Stokes equation written in generalized coordinates will not be considere ere. It has been treated by Jordan [154].

$$\frac{\partial u_i}{\partial x_i} = 0 \quad , \tag{3.2}$$

in which $p = P/\rho$ and ν are, respectively, the static pressure and the assumedly constant, uniform kinematic viscosity. To obtain a well-posed problem, we have to add initial and boundary conditions to this system.

3.1.2 Formulation in Spectral Space

The dual system in spectral space is obtained by applying a Fourier transform to equations (3.1) and (3.2). By making use of the fact that the incompressibility constraint is reflected geometrically by the orthogonality[3] of the wave vector $\mathbf{k}$ and of the mode $\widehat{\mathbf{u}}(\mathbf{k})$, defined as (see Appendix A for greater detail on the spectral analysis of turbulence) :

$$\widehat{\mathbf{u}}(\mathbf{k}) = \frac{1}{(2\pi)^3} \int\int\int \mathbf{u}(\mathbf{x})^{-\mathrm{i}\mathbf{k}\cdot\mathbf{x}} d^3\mathbf{x}, \quad \mathrm{i}^2 = -1 \quad , \tag{3.3}$$

the system (3.1) - (3.2) can be reduced to a single equation:

$$\left(\frac{\partial}{\partial t} + 2\nu k^2\right) \widehat{u}_i(\mathbf{k}) = T_i(\mathbf{k}) \quad , \tag{3.4}$$

in which the non-linear term $T_i(\mathbf{k})$ is of the form:

$$T_i(\mathbf{k}) = M_{ijm}(\mathbf{k}) \int\int \widehat{u}_j(\mathbf{p}) \widehat{u}_m(\mathbf{q}) \delta(\mathbf{k}-\mathbf{p}-\mathbf{q}) d^3\mathbf{p} d^3\mathbf{q} \quad , \tag{3.5}$$

with:

$$M_{ijm}(\mathbf{k}) = -\frac{\mathrm{i}}{2} \left(k_m P_{ij}(\mathbf{k}) + k_j P_{im}(\mathbf{k})\right) \quad , \tag{3.6}$$

in which δ is the Kronecker symbol and $P_{ij}(\mathbf{k})$ is the projection operator on the plane orthogonal to the vector $\mathbf{k}$. This operator is written:

$$P_{ij}(\mathbf{k}) = \left(\delta_{ij} - \frac{k_i k_j}{k^2}\right) \quad . \tag{3.7}$$

[3] This orthogonality relation is demonstrated by re-writing the incompressibility constraint of the velocity field in the spectral space as:

$$\frac{\partial u_i}{\partial x_i} = 0 \iff k_i \widehat{u}_i(k) \equiv \mathbf{k} \cdot \widehat{\mathbf{u}}(\mathbf{k}) = 0 \quad .$$

3.2 Filtered Navier–Stokes Equations (Homogeneous Case)

This section describes the equations of large-eddy simulation such as they are obtained by applying a homogeneous filter verifying the properties of linearity, conservation of constants, and commutation with derivation, to the Navier–Stokes equations. These are the equations that will be resolved in the numerical simulation.

3.2.1 Formulation in Physical Space

In light of the commutation with derivation property, the application of a filter to equations (3.1) and (3.2) is expressed:

$$\frac{\partial \overline{u}_i}{\partial t} + \frac{\partial}{\partial x_j}\left(\overline{u_i u_j}\right) = -\frac{\partial \overline{p}}{\partial x_i} + \nu \frac{\partial}{\partial x_j}\left(\frac{\partial \overline{u}_i}{\partial x_j} + \frac{\partial \overline{u}_j}{\partial x_i}\right) \quad , \tag{3.8}$$

$$\frac{\partial \overline{u}_i}{\partial x_i} = 0 \quad , \tag{3.9}$$

where $\overline{p}$ is the filtered pressure. The filtered momentum equation brings out the non-linear term $\overline{u_i u_j}$ which, in order for this equation to be usable, will have to be expressed as a function of $\overline{\mathbf{u}}$ and $\mathbf{u}'$, which are now the only unknowns left in the problem and where:

$$\mathbf{u}' = \mathbf{u} - \overline{\mathbf{u}} \quad . \tag{3.10}$$

This decomposition is not unique, and will be discussed in the following section.

3.2.2 Formulation in Spectral Space

Using the equivalence $\overline{\widehat{u}}_i(\mathbf{k}) = \widehat{G}(\mathbf{k})\widehat{u}_i(\mathbf{k})$, the momentum equation in the spectral space obtained by multiplying equation (3.4) by the transfer function $\widehat{G}(\mathbf{k})$ is expressed:

$$\left(\frac{\partial}{\partial t} + 2\nu k^2\right) \widehat{G}(\mathbf{k})\widehat{u}_i(\mathbf{k}) = \widehat{G}(\mathbf{k}) T_i(\mathbf{k}) \quad , \tag{3.11}$$

in which the filtered non-linear term $\widehat{G}(\mathbf{k})T_i(\mathbf{k})$ is written:

$$\widehat{G}(\mathbf{k})T_i(\mathbf{k}) = M_{ijm}(\mathbf{k}) \int\int \widehat{G}(\mathbf{k})\widehat{u}_j(\mathbf{p})\widehat{u}_m(\mathbf{q}) \delta(\mathbf{k}-\mathbf{p}-\mathbf{q}) d^3\mathbf{p} d^3\mathbf{q} \quad . \tag{3.12}$$

The filtered non-linear term (3.12) brings out the contributions of the modes $\widehat{\mathbf{u}}(\mathbf{p})$ and $\widehat{\mathbf{u}}(\mathbf{q})$. To complete the decomposition, these modes also have to be expressed as the sum of a filtered part and a fluctuation. This is the same problem as the one encountered when writing the equations in the physical space. This operation is described in the following section.

3.3 Decomposition of the Non-linear Term. Associated Equations

This section details the various existing decompositions of the non-linear term and the associated equations.

3.3.1 Leonard's Decomposition

Expression in Physical Space. Leonard [186] expresses the non-linear term in the form of a triple summation:

$$\overline{u_i u_j} = \overline{(\overline{u}_i + u_i')(\overline{u}_j + u_j')} \tag{3.13}$$

$$= \overline{\overline{u}_i \overline{u}_j} + \overline{\overline{u}_i u_j'} + \overline{\overline{u}_j u_i'} + \overline{u_i' u_j'} \quad . \tag{3.14}$$

The non-linear term is now written entirely as a function of the filtered quantity $\overline{\mathbf{u}}$ and the fluctuation $\mathbf{u}'$. We then have two versions of this [347].

The first considers that all the terms appearing in the evolution equations of a filtered quantity must themselves be filtered quantities, because the simulation solution has to be the same for all the terms. The filtered momentum equation is then expressed:

$$\frac{\partial \overline{u}_i}{\partial t} + \frac{\partial}{\partial x_j}\left(\overline{\overline{u}_i \overline{u}_j}\right) = -\frac{\partial \overline{p}}{\partial x_i} + \nu \frac{\partial}{\partial x_j}\left(\frac{\partial \overline{u}_i}{\partial x_j} + \frac{\partial \overline{u}_j}{\partial x_i}\right) - \frac{\partial \tau_{ij}}{\partial x_j} \quad , \tag{3.15}$$

in which the subgrid tensor τ, grouping together all the terms that are not exclusively dependent on the large scales, is defined as:

$$\tau_{ij} = C_{ij} + R_{ij} = \overline{u_i u_j} - \overline{\overline{u}_i \overline{u}_j} \quad , \tag{3.16}$$

where the cross-stress tensor, C, which represents the interactions between large and small scales, and the Reynolds subgrid tensor, R, which reflects the interactions between subgrid scales, are expressed:

$$C_{ij} = \overline{\overline{u}_i u_j'} + \overline{\overline{u}_j u_i'} \quad , \tag{3.17}$$

$$R_{ij} = \overline{u_i' u_j'} \quad . \tag{3.18}$$

In the following, this decomposition will be called double decomposition.

The other point of view consists of considering that it must be possible to evaluate the terms directly from the filtered variables. But the $\overline{\overline{u}_i \overline{u}_j}$ term cannot be calculated directly because it requires a second application of the filter. To remedy this, Leonard proposes a further decomposition:

$$\overline{\overline{u}_i \overline{u}_j} = \left(\overline{\overline{u}_i \overline{u}_j} - \overline{u}_i \overline{u}_j\right) + \overline{u}_i \overline{u}_j$$

$$= L_{ij} + \overline{u}_i \overline{u}_j \quad . \tag{3.19}$$

The new L term, called Leonard tensor, represents interactions among the large scales. Using this new decomposition, the filtered momentum equation becomes:

$$\frac{\partial \overline{u}_i}{\partial t} + \frac{\partial}{\partial x_j}\left(\overline{u}_i \overline{u}_j\right) = -\frac{\partial \overline{p}}{\partial x_i} + \nu \frac{\partial}{\partial x_j}\left(\frac{\partial \overline{u}_i}{\partial x_j} + \frac{\partial \overline{u}_j}{\partial x_i}\right) - \frac{\partial \tau_{ij}}{\partial x_j} \quad . \tag{3.20}$$

The subgrid tensor τ, which now groups all the terms that are not expressed directly from $\overline{u}$, takes the form:

$$\tau_{ij} = L_{ij} + C_{ij} + R_{ij} = \overline{u_i u_j} - \overline{u}_i \overline{u}_j \quad . \tag{3.21}$$

This decomposition will be designated hereafter the Leonard or triple decomposition. Equation (3.20) and the subgrid term τ_{ij} defined by (3.21) can be obtained directly from the Navier–Stokes equations without using the Leonard decomposition for this. It should be noted that the term $\overline{u}_i \overline{u}_j$ is a quadratic term and that it contains frequencies that are in theory higher than each of the terms composing. So in order to represent it completely, more degrees of freedom are needed than for each of the terms $\overline{u}_i$ and $\overline{u}_j$[4].

We may point out that, if the filter is a Reynolds operator, then the tensors C_{ij} and L_{ij} are identically zero[5] and the two decompositions are then equivalent, since the subgrid tensor is reduced to the tensor R_{ij}.

---

[4] In practice, if the large-eddy simulation filter is associated with a given computational grid on which the Navier–Stokes equations are resolved, this means that the grid used for composing the $\overline{u}_i \overline{u}_j$ product has to be twice as fine (in each direction of space) as the one used to represent the velocity field. If the product is composed on the same grid, then only the $\overline{\overline{u}_i \overline{u}_j}$ term can be calculated.

[5] It is recalled that if the filter is a Reynolds operator, then we have the three following properties (see Appendix A):

$$\overline{\overline{\mathbf{u}}} = \overline{\mathbf{u}}, \ \overline{\mathbf{u}'} = 0, \ \overline{\overline{\mathbf{u}}\mathbf{u}} = \overline{\mathbf{u}}\,\overline{\mathbf{u}} \quad ,$$

whence

$$C_{ij} = \overline{\overline{u}_i u_j'} + \overline{\overline{u}_j u_i'}$$

$$= \overline{\overline{u}_i \overline{u}_j'} + \overline{\overline{u}_j \overline{u}_i'}$$

$$= 0 \quad ,$$

$$L_{ij} = \overline{\overline{u}_i \overline{u}_j} - \overline{u}_i \overline{u}_j$$

$$= \overline{\overline{u}_i \overline{u}_j} - \overline{u}_i \overline{u}_j$$

$$= 0 \quad .$$

Writing the Navier–Stokes equations (3.1) in the symbolic form

$$\frac{\partial \mathbf{u}}{\partial t} = \mathcal{NS}(\mathbf{u}) \quad , \tag{3.22}$$

the filtered Navier–Stokes equations are expressed

$$G\star \frac{\partial \mathbf{u}}{\partial t} = \frac{\partial \overline{\mathbf{u}}}{\partial t} = G\star \mathcal{NS}(\mathbf{u}) \tag{3.23}$$

$$= \mathcal{NS}(\overline{\mathbf{u}}) + [G\star, \mathcal{NS}](\mathbf{u}) \quad , \tag{3.24}$$

where $[.,.]$ is the commutator operator introduced in Sect. 2.1.2. We note that the subgrid tensor corresponds to the commutation error between the filter and the non-linear term. Introducing the bilinear form $B(\cdot,\cdot)$:

$$B(u_i, u_j) \equiv u_i u_j \quad , \tag{3.25}$$

we get

$$\tau_{ij} = [G\star, B](u_i, u_j) \quad . \tag{3.26}$$

Double decomposition (3.16) leads to the following equation for the resolved kinetic energy $q_r^2 = \overline{u}_i\overline{u}_i/2$:

$$\begin{aligned}\frac{\partial q_r^2}{\partial t} = & \underbrace{\overline{\overline{u}_i\overline{u}_j}\frac{\partial \overline{u}_i}{\partial x_j}}_{I} + \underbrace{\tau_{ij}\frac{\partial \overline{u}_i}{\partial x_j}}_{II} - \underbrace{\nu\frac{\partial \overline{u}_i}{\partial x_j}\frac{\partial \overline{u}_i}{\partial x_j}}_{III} \\ & \underbrace{-\frac{\partial}{\partial x_i}(\overline{u}_i\overline{p})}_{IV} + \underbrace{\frac{\partial}{\partial x_i}\left(\nu\frac{\partial q_r^2}{\partial x_i}\right)}_{V} \\ & \underbrace{-\frac{\partial}{\partial x_j}\left(\overline{u}_i\overline{\overline{u}_i\overline{u}_j}\right)}_{VI} \underbrace{-\frac{\partial}{\partial x_j}(\overline{u}_i\tau_{ij})}_{VII} \quad .\end{aligned} \tag{3.27}$$

This equation shows the existence of several mechanisms exchanging kinetic energy at the resolved scales:

- *I* - production
- *II* - subgrid dissipation
- *III* - dissipation by viscous effects
- *IV* - diffusion by pressure effect
- *V* - diffusion by viscous effects
- *VI* - diffusion by interaction among resolved scales
- *VII* - diffusion by interaction with subgrid modes.

Leonard's decomposition (3.21) can be used to obtain the similar form:

$$\begin{aligned}\frac{\partial q_r^2}{\partial t} = & \underbrace{-\frac{\partial q_r^2\overline{u}_j}{\partial x_j}}_{VIII} + \underbrace{\tau_{ij}\frac{\partial \overline{u}_i}{\partial x_j}}_{IX} \underbrace{-\nu\frac{\partial \overline{u}_i}{\partial x_j}\frac{\partial \overline{u}_i}{\partial x_j}}_{X} \\ & \underbrace{-\frac{\partial}{\partial x_i}(\overline{u}_i\overline{p})}_{XI} + \underbrace{\frac{\partial}{\partial x_i}\left(\nu\frac{\partial q_r^2}{\partial x_i}\right)}_{XII} \\ & + \underbrace{\overline{u}_i\overline{u}_j\frac{\partial \overline{u}_i}{\partial x_j}}_{XIII} \underbrace{-\frac{\partial}{\partial x_j}(\overline{u}_i\tau_{ij})}_{XIV} \quad .\end{aligned} \tag{3.28}$$

This equation differs from the previous one only in the first and sixth terms of the right-hand side, and in the definition of tensor τ:

- *VIII* - advection
- *IX* - *idem II*
- *X* - *idem III*
- *XI* - *idem IV*
- *XII* - *idem V*
- *XIII* - production
- *XIV* - *idem VII*

The momentum equation for the small scales is obtained by subtracting the large scale equation from the unfiltered momentum equation (3.1), making, for the double decomposition:

$$\begin{aligned}\frac{\partial u_i'}{\partial t} + \frac{\partial}{\partial x_j}\left((\overline{u}_i + u_i')(\overline{u}_j + u_j') - \overline{\overline{u}_i\overline{u}_j} - \tau_{ij}\right) = & -\frac{\partial p'}{\partial x_i} \\ & + \nu\frac{\partial}{\partial x_j}\left(\frac{\partial u_i'}{\partial x_j} + \frac{\partial u_j'}{\partial x_i}\right) \quad ,\end{aligned} \tag{3.29}$$

and, for the triple decomposition:

$$\begin{aligned}\frac{\partial u_i'}{\partial t} + \frac{\partial}{\partial x_j}\left((\overline{u}_i + u_i')(\overline{u}_j + u_j') - \overline{u}_i\overline{u}_j - \tau_{ij}\right) = & -\frac{\partial p'}{\partial x_i} \\ & + \nu\frac{\partial}{\partial x_j}\left(\frac{\partial u_i'}{\partial x_j} + \frac{\partial u_j'}{\partial x_i}\right) \quad .\end{aligned} \tag{3.30}$$

The subgrid kinetic energy $q_{sgs}^2 = \overline{u_k'u_k'}/2$ equation obtained by multiplying (3.30) by u_i' and filtering the relation thus derived is expressed:

$$\frac{\partial q^2_{\rm sgs}}{\partial t} = \underbrace{-\frac{\partial}{\partial x_j}\left(q^2_{\rm sgs}\overline{u}_j\right)}_{XV} \underbrace{-\frac{1}{2}\frac{\partial}{\partial x_j}\left(\overline{u_i u_i u_j} - \overline{u}_j\overline{u_i u_i}\right)}_{XVI} \underbrace{-\frac{\partial}{\partial x_j}\left(\overline{p u_j} - \overline{p}\,\overline{u}_j\right)}_{XVII}$$
$$+ \underbrace{\frac{\partial}{\partial x_j}\left(\nu\frac{\partial q^2_{\rm sgs}}{\partial x_j}\right)}_{XVIII} + \underbrace{\frac{\partial}{\partial x_j}\left(\tau_{ij}\overline{u}_i\right)}_{XIX}$$
$$\underbrace{-\nu\left(\overline{\frac{\partial u_i}{\partial x_j}\frac{\partial u_i}{\partial x_j}} - \frac{\partial\overline{u}_i}{\partial x_j}\frac{\partial\overline{u}_i}{\partial x_j}\right)}_{XX} \underbrace{-\tau_{ij}\frac{\partial\overline{u}_i}{\partial x_j}}_{XXI} \qquad (3.31)$$

- XV - advection
- XVI - turbulent transport
- $XVII$ - diffusion by pressure effects
- $XVIII$ - diffusion by viscous effects
- XIX - diffusion by subgrid modes
- XX - dissipation by viscous effects
- XXI - subgrid dissipation.

For the double decomposition, equation (3.29) leads to:

$$\frac{\partial q^2_{\rm sgs}}{\partial t} = \underbrace{-\frac{\partial}{\partial x_j}\left(\overline{u_i u_i u_j} - \overline{\overline{u}_i\overline{u_i u_j}}\right)}_{XXII} + \underbrace{\overline{u_i u_j}\frac{\partial u_i}{\partial x_j} - \overline{\overline{u}_i\overline{u}_j}\frac{\partial\overline{u}_i}{\partial x_j}}_{XXIII}$$
$$\underbrace{-\frac{\partial}{\partial x_j}\left(\overline{p u_j} - \overline{\overline{p}\,\overline{u}_j}\right)}_{XXIV} + \underbrace{\nu\left(\overline{u_i\frac{\partial^2 u_i}{\partial x_j^2}} - \overline{\overline{u}_i\frac{\partial^2\overline{u}_i}{\partial x_j^2}}\right)}_{XXV}$$
$$+ \underbrace{\frac{\partial}{\partial x_j}\left(\overline{\tau_{ij}\overline{u}_i}\right) - \overline{\tau_{ij}\frac{\partial\overline{u}_i}{\partial x_j}}}_{XXVI} \quad , \qquad (3.32)$$

with:

- $XXII$ - turbulent transport
- $XXIII$ - production
- $XXIV$ - diffusion by pressure effects
- XXV - viscous effects
- $XXVI$ - subgrid dissipation and diffusion

It is recalled that, if the filter used is not positive, the generalized subgrid kinetic energy $q^2_{\rm gsgs}$ defined as the half-trace of the subgrid tensor,

$$q^2_{\rm gsgs} = \tau_{kk}/2 \quad ,$$

can admit negative values locally (see Sect. 3.3.5). If the filter is a Reynolds operator, the subgrid tensor is then reduced to the subgrid Reynolds tensor and the generalized subgrid kinetic energy is equal to the subgrid kinetic energy, *i.e.*

$$q^2_{\rm sgs} \equiv \frac{1}{2}\overline{u'_i u'_i} = q^2_{\rm gsgs} \equiv \tau_{kk}/2 \quad . \qquad (3.33)$$

Expression in Spectral Space. Both versions of the Leonard decomposition can be transcribed in the spectral space. Using the definition of the fluctuation $\widehat{\mathbf{u}}'(\mathbf{k})$ as

$$\widehat{u}'_i(\mathbf{k}) = (1 - \widehat{G}(\mathbf{k}))\widehat{u}_i(\mathbf{k}) \quad , \qquad (3.34)$$

the filtered non-linear term $\widehat{G}(\mathbf{k})T_i(\mathbf{k})$ is expressed, for the triple decomposition:

$$\begin{aligned}\widehat{G}(\mathbf{k})T_i(\mathbf{k}) &= M^{\bullet}_{ijm}(\mathbf{k})\int\int \widehat{G}(\mathbf{p})\widehat{G}(\mathbf{q})\widehat{u}_j(\mathbf{p})\widehat{u}_m(\mathbf{q})\delta(\mathbf{k}-\mathbf{p}-\mathbf{q})d^3\mathbf{p}d^3\mathbf{q}\\
&- M_{ijm}(\mathbf{k})\int\int(1-\widehat{G}(\mathbf{k}))\widehat{G}(\mathbf{p})\widehat{G}(\mathbf{q})\\
&\times\widehat{u}_j(\mathbf{p})\widehat{u}_m(\mathbf{q})\delta(\mathbf{k}-\mathbf{p}-\mathbf{q})d^3\mathbf{p}d^3\mathbf{q}\\
&+ M_{ijm}(\mathbf{k})\int\int\widehat{G}(\mathbf{k})\left(\widehat{G}(\mathbf{p})(1-\widehat{G}(\mathbf{q}))+\widehat{G}(\mathbf{q})(1-\widehat{G}(\mathbf{p}))\right)\\
&\times\widehat{u}_j(\mathbf{p})\widehat{u}_m(\mathbf{q})\delta(\mathbf{k}-\mathbf{p}-\mathbf{q})d^3\mathbf{p}d^3\mathbf{q}\\
&+ M_{ijm}(\mathbf{k})\int\int\widehat{G}(\mathbf{k})\left((1-\widehat{G}(\mathbf{q}))(1-\widehat{G}(\mathbf{p}))\right)\\
&\times\widehat{u}_j(\mathbf{p})\widehat{u}_m(\mathbf{q})\delta(\mathbf{k}-\mathbf{p}-\mathbf{q})d^3\mathbf{p}d^3\mathbf{q} \quad . \qquad (3.35)\end{aligned}$$

The first term of the right-hand side corresponds to the contribution $\overline{u}_i\overline{u}_j$, the second to the Leonard tensor L, the third to the cross stresses represented by the tensor C, and the fourth to the subgrid Reynolds tensor R. This is illustrated by Fig. 3.1.

The double decomposition is derived by combination of the first two terms of the right-hand side of (3.35):

$$\begin{aligned}\widehat{G}(\mathbf{k})T_i(\mathbf{k}) &= M_{ijm}(\mathbf{k})\int\int\widehat{G}(\mathbf{p})\widehat{G}(\mathbf{q})\widehat{G}(\mathbf{k})\\
&\times\widehat{u}_j(\mathbf{p})\widehat{u}_m(\mathbf{q})\delta(\mathbf{k}-\mathbf{p}-\mathbf{q})d^3\mathbf{p}d^3\mathbf{q}\\
&+ M_{ijm}(\mathbf{k})\int\int\widehat{G}(\mathbf{k})\left(\widehat{G}(\mathbf{p})(1-\widehat{G}(\mathbf{q}))+\widehat{G}(\mathbf{q})(1-\widehat{G}(\mathbf{p}))\right)\\
&\times\widehat{u}_j(\mathbf{p})\widehat{u}_m(\mathbf{q})\delta(\mathbf{k}-\mathbf{p}-\mathbf{q})d^3\mathbf{p}d^3\mathbf{q}\\
&+ M_{ijm}(\mathbf{k})\int\int\widehat{G}(\mathbf{k})\left((1-\widehat{G}(\mathbf{q}))(1-\widehat{G}(\mathbf{p}))\right)\\
&\widehat{u}_m(\mathbf{q})\delta(\mathbf{k}-\mathbf{p}-\mathbf{q})d^3\mathbf{p}d^3\mathbf{q} \quad . \qquad (3.36)\end{aligned}$$

The first term of the right-hand side corresponds to the contribution $\overline{\overline{u_i}\overline{u_j}}$ in the physical space, and the last two remain unchanged with respect to the triple decomposition. Let us note that the sum of the contributions of the cross tensor and the subgrid Reynolds tensor simplifies to the form:

$$C_{ij} + R_{ij} = M_{ijm}(\mathbf{k}) \int\int (1 - \widehat{G}(\mathbf{p})\widehat{G}(\mathbf{q}))\widehat{G}(\mathbf{k}) \times \widehat{u}_j(\mathbf{p})\widehat{u}_m(\mathbf{q})\delta(\mathbf{k}-\mathbf{p}-\mathbf{q})d^3\mathbf{p}d^3\mathbf{q} \quad . \tag{3.37}$$

The momentum equations corresponding to these two decompositions are found by replacing the right-hand side of equation (3.11) with the desired terms. For the double decomposition, we get:

$$\begin{aligned}\left(\frac{\partial}{\partial t} + 2\nu k^2\right)\widehat{G}(\mathbf{k})\widehat{u}_i(\mathbf{k}) &= M_{ijm}(\mathbf{k}) \int\int \widehat{G}(\mathbf{p})\widehat{G}(\mathbf{q})\widehat{G}(\mathbf{k}) \\ &\quad \times \widehat{u}_j(\mathbf{p})\widehat{u}_m(\mathbf{q})\delta(\mathbf{k}-\mathbf{p}-\mathbf{q})d^3\mathbf{p}d^3\mathbf{q} \\ &\quad + M_{ijm}(\mathbf{k}) \int\int (1 - \widehat{G}(\mathbf{p})\widehat{G}(\mathbf{q}))\widehat{G}(\mathbf{k}) \\ &\quad \times \widehat{u}_j(\mathbf{p})\widehat{u}_m(\mathbf{q})\delta(\mathbf{k}-\mathbf{p}-\mathbf{q})d^3\mathbf{p}d^3\mathbf{q} \quad ,\end{aligned} \tag{3.38}$$

and for the triple decomposition:

$$\begin{aligned}\left(\frac{\partial}{\partial t} + 2\nu k^2\right)\widehat{G}(\mathbf{k})\widehat{u}_i(\mathbf{k}) &= M_{ijm}(\mathbf{k}) \int\int \widehat{G}(\mathbf{p})\widehat{G}(\mathbf{q}) \\ &\quad \times \widehat{u}_j(\mathbf{p})\widehat{u}_m(\mathbf{q})\delta(\mathbf{k}-\mathbf{p}-\mathbf{q})d^3\mathbf{p}d^3\mathbf{q} \\ &\quad - M_{ijm}(\mathbf{k}) \int\int (1 - \widehat{G}(\mathbf{k}))\widehat{G}(\mathbf{p})\widehat{G}(\mathbf{q}) \\ &\quad \times \widehat{u}_j(\mathbf{p})\widehat{u}_m(\mathbf{q})\delta(\mathbf{k}-\mathbf{p}-\mathbf{q})d^3\mathbf{p}d^3\mathbf{q} \\ &\quad + M_{ijm}(\mathbf{k}) \int\int \widehat{G}(\mathbf{k}) \Big(\widehat{G}(\mathbf{p})(1 - \widehat{G}(\mathbf{q})) \\ &\quad + \widehat{G}(\mathbf{q})(1 - \widehat{G}(\mathbf{p}))\Big) \\ &\quad \times \widehat{u}_j(\mathbf{p})\widehat{u}_m(\mathbf{q})\delta(\mathbf{k}-\mathbf{p}-\mathbf{q})d^3\mathbf{p}d^3\mathbf{q} \\ &\quad + M_{ijm}(\mathbf{k}) \int\int \widehat{G}(\mathbf{k}) \Big((1 - \widehat{G}(\mathbf{q}))(1 - \widehat{G}(\mathbf{p}))\Big) \\ &\quad \times \widehat{u}_j(\mathbf{p})\widehat{u}_m(\mathbf{q})\delta(\mathbf{k}-\mathbf{p}-\mathbf{q})d^3\mathbf{p}d^3\mathbf{q} \quad .\end{aligned} \tag{3.39}$$

For both decompositions, the momentum equation can be expressed in the symbolic form:

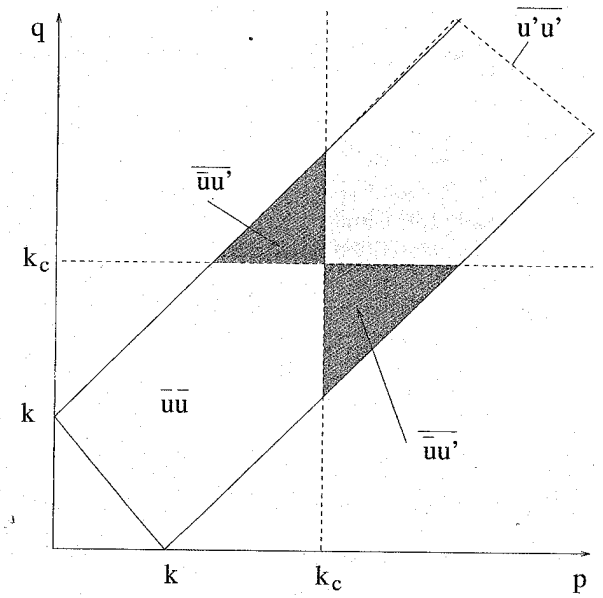

Fig. 3.1. Representation of the various Leonard decomposition terms in the spectral space, when using a sharp cutoff filter with a cutoff frequency k_c.

$$\left(\frac{\partial}{\partial t} + 2\nu k^2\right)\widehat{G}(\mathbf{k})\widehat{u}_i(\mathbf{k}) = T_r(\mathbf{k}) + T_{sgs}(\mathbf{k}) \quad , \tag{3.40}$$

in which $T_r(\mathbf{k})$ designates the transfer terms calculated directly from the resolved modes, and is therefore equivalent to the contribution of the $\overline{u_i}\overline{u_j}$ term in the case of the triple decomposition, and that of the $\overline{\overline{u_i}\overline{u_j}}$ term for the double decomposition. The $T_{sgs}(k)$ term designates the other non-linear terms, and therefore corresponds to the contribution of the subsidiary term such as defined above. Let $E(k)$ be the energy contained on the sphere of radius k. It is calculated as:

$$E(k) = \frac{1}{2}k^2 \int \widehat{\mathbf{u}}(\mathbf{k}) \cdot \widehat{\mathbf{u}}^*(\mathbf{k}) dS(\mathbf{k}) \quad , \tag{3.41}$$

where $dS(\mathbf{k})$ is the surface element of the sphere, and where the asterisk designates a conjugate complex number. The kinetic energy of the resolved modes contained on this same sphere, denoted $\overline{E}_r(k)$, is defined by the relation

$$\overline{E}_r(k) = \frac{1}{2}k^2 \int \widehat{G}(\mathbf{k})\widehat{\mathbf{u}}(\mathbf{k}) \cdot \widehat{G}(\mathbf{k})\widehat{\mathbf{u}}^*(\mathbf{k}) dS(\mathbf{k}) \tag{3.42}$$

$$= \widehat{G}^2(k)E(k) \quad . \tag{3.43}$$

We return to the kinetic energy of the resolved modes, $q_r^2 = \overline{u}_i\overline{u}_i/2$, by summation on all the wave numbers:

$$q_r^2 = \int_0^\infty \overline{E}_r(k)dk \quad . \tag{3.44}$$

It is important to note that $\overline{E}_r(k)$ is related to the energy of the resolved modes, which is generally not equal to the filtered part of the kinetic energy which, for its part, is associated with the quantity denoted $\overline{E}(k)$, defined as

$$\overline{E}(k) = \widehat{G}(k)E(k) \quad . \tag{3.45}$$

The identity of these two quantities is verified when the transfer function is such that $\widehat{G}^2(k) = \widehat{G}(k)$, $\forall k$, *i.e.* when the filter used is a projector. The evolution equation for $\overline{E}_r(k)$ is obtained by multiplying the filtered momentum equation (3.11) by $k^2\widehat{G}(\mathbf{k})\widehat{\mathbf{u}}^*(\mathbf{k})$, and then integrating the result on the sphere of radius k. Using the double decomposition we get the following equation:

$$\begin{aligned}\left(\frac{\partial}{\partial t} + 2\nu k^2\right)\overline{E}_r(k) &= \frac{1}{2}\int\int_\Delta \widehat{G}(\mathbf{p})\widehat{G}(\mathbf{q})\widehat{G}^2(\mathbf{k})S(\mathbf{k}|\mathbf{p},\mathbf{q})d\mathbf{p}d\mathbf{q} \\ &+ \frac{1}{2}\int\int_\Delta (1-\widehat{G}(\mathbf{p})\widehat{G}(\mathbf{q}))\widehat{G}^2(\mathbf{k})S(\mathbf{k}|\mathbf{p},\mathbf{q})d\mathbf{p}d\mathbf{q} \quad ,\end{aligned} \tag{3.46}$$

and the triple decomposition:

$$\begin{aligned}\left(\frac{\partial}{\partial t} + 2\nu k^2\right)\overline{E}_r(k) &= \frac{1}{2}\int\int_\Delta \widehat{G}(\mathbf{p})\widehat{G}(\mathbf{q})\widehat{G}(\mathbf{k})S(\mathbf{k}|\mathbf{p},\mathbf{q})d\mathbf{p}d\mathbf{q} \\ &- \frac{1}{2}\int\int \widehat{G}(\mathbf{k})(1-\widehat{G}(\mathbf{k}))\widehat{G}(\mathbf{p})\widehat{G}(\mathbf{q})S(\mathbf{k}|\mathbf{p},\mathbf{q})d\mathbf{p}d\mathbf{q} \\ &+ \frac{1}{2}\int\int_\Delta \widehat{G}^2(\mathbf{k})\Big(\widehat{G}(\mathbf{p}) \\ &\quad \times(1-\widehat{G}(\mathbf{q})) + \widehat{G}(\mathbf{q})(1-\widehat{G}(\mathbf{p}))\Big)S(\mathbf{k}|\mathbf{p},\mathbf{q})d\mathbf{p}d\mathbf{q} \\ &+ \frac{1}{2}\int\int_\Delta \widehat{G}^2(\mathbf{k})\Big((1-\widehat{G}(\mathbf{q}))(1-\widehat{G}(\mathbf{p}))\Big) \\ &\quad \times S(\mathbf{k}|\mathbf{p},\mathbf{q})d\mathbf{p}d\mathbf{q} \quad ,\end{aligned} \tag{3.47}$$

in which

$$S(\mathbf{k}|\mathbf{p},\mathbf{q}) = 16\pi^2 kpq M_{ijm}(\mathbf{k})\widehat{u}_j(\mathbf{p})\widehat{u}_m(\mathbf{q})\widehat{u}_i(-\mathbf{k})\delta(\mathbf{k}-\mathbf{p}-\mathbf{q}) \quad , \tag{3.48}$$

and where the symbol $\int\int_\Delta$ designates integration over the interval $|k-p| < q < k+p$.

Following the example of what was done for the momentum equations, the kinetic energy evolution equation for the resolved modes can be expressed in the abbreviated form

$$\left(\frac{\partial}{\partial t} + 2\nu k^2\right)\overline{E}_r(\mathbf{k}) = T_r^e(\mathbf{k}) + T_{sgs}^e(\mathbf{k}) \quad . \tag{3.49}$$

The terms $T_r^e(\mathbf{k})$ and $T_{sgs}^e(\mathbf{k})$ represent, respectively, the energy transfers of mode $\mathbf{k}$ with all the other modes associated with the terms that can be calculated directly from the resolved modes, and the subgrid terms. The kinetic energy conservation property for inviscid fluids, *i.e.* in the case of zero viscosity, implies:

$$\int (T_r^e(\mathbf{k}) + T_{sgs}^e(\mathbf{k}))d^3\mathbf{k} = 0 \quad . \tag{3.50}$$

The momentum equations for the unresolved scales are obtained by algebraic manipulations strictly analogous to those used for obtaining the equations for the resolved scales, except that this time equation (3.4) is multiplied by $(1-\widehat{G}(\mathbf{k}))$ instead of $\widehat{G}(\mathbf{k})$. These equations are written:

$$\left(\frac{\partial}{\partial t} + 2\nu k^2\right)(1-\widehat{G}(\mathbf{k}))\widehat{u}_i(\mathbf{k}) = (1-\widehat{G}(\mathbf{k}))T_i(\mathbf{k}) \quad . \tag{3.51}$$

Calculations similar to those explained above lead to:

$$\begin{aligned}\left(\frac{\partial}{\partial t} + 2\nu k^2\right)\widehat{u}_i'(\mathbf{k}) &= M_{ijm}(\mathbf{k})\int\int \widehat{G}(\mathbf{p})\widehat{G}(\mathbf{q})(1-\widehat{G}(\mathbf{k})) \\ &\quad \times\widehat{u}_j(\mathbf{p})\widehat{u}_m(\mathbf{q})\delta(\mathbf{k}-\mathbf{p}-\mathbf{q})d^3\mathbf{p}d^3\mathbf{q} \\ &+ M_{ijm}(\mathbf{k})\int\int(1-\widehat{G}(\mathbf{k}))\Big(\widehat{G}(\mathbf{p})(1-\widehat{G}(\mathbf{q})) \\ &\quad +\widehat{G}(\mathbf{q})(1-\widehat{G}(\mathbf{p}))\Big) \\ &\quad \times\widehat{u}_j(\mathbf{p})\widehat{u}_m(\mathbf{q})\delta(\mathbf{k}-\mathbf{p}-\mathbf{q})d^3\mathbf{p}d^3\mathbf{q} \\ &+ M_{ijm}(\mathbf{k})\int\int(1-\widehat{G}(\mathbf{k}))\Big((1-\widehat{G}(\mathbf{q}))(1-\widehat{G}(\mathbf{p}))\Big) \\ &\quad \times\widehat{u}_j(\mathbf{p})\widehat{u}_m(\mathbf{q})\delta(\mathbf{k}-\mathbf{p}-\mathbf{q})d^3\mathbf{p}d^3\mathbf{q} \quad .\end{aligned} \tag{3.52}$$

The first term of the right-hand side represents the contribution of the interactions between large scale modes, the second the contribution of the cross interactions, and the last the interactions among the subgrid modes.

Let $\overline{E}_{sgs}$ be the energy contained in the subgrid modes. This energy is defined as:

$$\overline{E}_{\rm sgs}(k) = \frac{1}{2}k^2 \int (1-\widehat{G}(\mathbf{k}))\widehat{\mathbf{u}}(\mathbf{k})\cdot(1-\widehat{G}(\mathbf{k}))\widehat{\mathbf{u}}^*(\mathbf{k})dS(\mathbf{k}) \quad (3.53)$$

$$= (1-\widehat{G})^2(k)E(k) \quad , \quad (3.54)$$

and is different, in the general case, from the kinetic energy fluctuation $E'(k) = (1-\widehat{G})(k)E(k)$, though the equality of these two quantities is verified when the filter is a Reynolds operator. Simple calculations give us the following evolution equation for $\overline{E}_{\rm sgs}(k)$:

$$\left(\frac{\partial}{\partial t}+2\nu k^2\right)\overline{E}_{\rm sgs}(k) = \frac{1}{2}\int\int_\Delta \widehat{G}(\mathbf{p})\widehat{G}(\mathbf{q})(1-\widehat{G}(\mathbf{k}))^2 S(\mathbf{k}|\mathbf{p},\mathbf{q})d\mathbf{p}d\mathbf{q}$$
$$+\frac{1}{2}\int\int_\Delta (1-\widehat{G}(\mathbf{k}))\Big(\widehat{G}(\mathbf{p})(1-\widehat{G}(\mathbf{q}))$$
$$+\widehat{G}(\mathbf{q})(1-\widehat{G}(\mathbf{p}))\Big) S(\mathbf{k}|\mathbf{p},\mathbf{q})d\mathbf{p}d\mathbf{q}$$
$$+\frac{1}{2}\int\int_\Delta (1-\widehat{G}(\mathbf{k}))^2(1-\widehat{G}(\mathbf{q}))(1-\widehat{G}(\mathbf{p}))$$
$$\times S(\mathbf{k}|\mathbf{p},\mathbf{q})d\mathbf{p}d\mathbf{q} \quad , \quad (3.55)$$

where the notation used is the same as for the kinetic energy evolution equation of the resolved modes. The subgrid kinetic energy $q^2_{\rm sgs}$ is obtained by summation over the entire spectrum:

$$q^2_{\rm sgs} = \int_0^\infty \overline{E}_{\rm sgs}(k)dk \quad . \quad (3.56)$$

3.3.2 Germano Consistent Decomposition

This section presents the Germano consistent decomposition, which is a generalization of the Leonard decomposition.

Definition and Properties of Generalized Central Moments. For convenience, we use $[\phi]_{\rm G}$ to denote the resolved part of the field ϕ, defined as in the first chapter, where G is the convolution kernel, *i.e.*:

$$[\phi]_{\rm G}(\mathbf{x}) \equiv G\star\phi(\mathbf{x}) \equiv \int_{-\infty}^{+\infty} G(\mathbf{x}-\boldsymbol{\xi})\phi(\boldsymbol{\xi})d^3\boldsymbol{\xi} \quad . \quad (3.57)$$

We define the generalized central moments with the filter G, denoted $\tau_{\rm G}$, as [113, 115–117]:

$$\tau_{\rm G}(\phi_1,\phi_2) = [\phi_1\phi_2]_{\rm G} - [\phi_1]_{\rm G}[\phi_2]_{\rm G} \quad , \quad (3.58)$$

$$\tau_{\rm G}(\phi_1,\phi_2,\phi_3) = [\phi_1\phi_2\phi_3]_{\rm G} - [\phi_1]_{\rm G}\tau_{\rm G}(\phi_2,\phi_3) - [\phi_2]_{\rm G}\tau_{\rm G}(\phi_1,\phi_3)$$
$$-[\phi_3]_{\rm G}\tau_{\rm G}(\phi_1,\phi_2) - [\phi_1]_{\rm G}[\phi_2]_{\rm G}[\phi_3]_{\rm G} \quad , \quad (3.59)$$

$$\tau_{\rm G}(\phi_1,\phi_2,\phi_3,\phi_4) = ... \quad (3.60)$$

The generalized central moments thus defined verify the following properties:

$$\tau_{\rm G}(\phi,\psi) = \tau_{\rm G}(\psi,\phi) \quad , \quad (3.61)$$

$$\tau_{\rm G}(\phi,a) = 0, \quad \text{for a = const.} \quad , \quad (3.62)$$

$$\tau_{\rm G}(\phi,\psi,a) = 0, \quad \text{for a = const.} \quad , \quad (3.63)$$

$$\partial\tau_{\rm G}(\phi,\psi)/\partial s = \tau_{\rm G}(\partial\phi/\partial s,\psi) + \tau_{\rm G}(\phi,\partial\psi/\partial s), \ s=\mathbf{x},t \quad . \quad (3.64)$$

If we perform the decomposition $\phi=\phi_1+\phi_2, \psi=\psi_1+\psi_2$, we get:

$$\tau_{\rm G}(\psi_1+\psi_2,\phi_1+\phi_2) = \tau_{\rm G}(\psi_1,\phi_1)+\tau_{\rm G}(\psi_1,\phi_2)$$
$$+\tau_{\rm G}(\psi_2,\phi_1)+\tau_{\rm G}(\psi_2,\phi_2) \quad . \quad (3.65)$$

The generalized central moments also appear as the coefficients of the following formal Taylor expansion [116]:

$$[\phi(a_1,...,a_n)]_G = \phi([a_1]_G,...,[a_n]_G) + \sum_{l,m}\frac{\tau_G(a_l,a_m)}{2!}y_{lm}$$
$$+\sum_{l,m,k}\frac{\tau_G(a_l,a_m,a_k)}{3!}y_{lmk}+... \quad , \quad (3.66)$$

with

$$y_{lm} = \frac{\partial^2\phi([a_1]_G,...,[a_n]_G)}{\partial[a_l]_G\partial[a_m]_G}, \quad y_{lmk} = \frac{\partial^3\phi([a_1]_G,...,[a_n]_G)}{\partial[a_l]_G\partial[a_m]_G\partial[a_k]_G} \quad ,$$

and where the a_i are generic turbulent quantities. The relation (3.66) establishes a link between the filtered value of the functional ϕ and its unfiltered counterpart applied to the filtered variables $[a_i]_G$.

Consistent Decomposition: Associated Equations. By applying the property (3.65) to the decomposition $\phi=[\phi]_{\rm G}+\phi', \psi=[\psi]_{\rm G}+\psi'$, we get:

$$\tau_{\rm G}([\phi]_{\rm G}+\phi',[\psi]_{\rm G}+\psi') = \tau_{\rm G}([\phi]_{\rm G},[\psi]_{\rm G})+\tau_{\rm G}(\phi',[\psi]_{\rm G})$$
$$+\tau_{\rm G}([\phi]_{\rm G},\psi')+\tau_{\rm G}(\phi',\psi') \quad . \quad (3.67)$$

This decomposition is said to be *consistent* because it is consistent with the definition of the generalized central moments, ensuring that all the terms in it are of the same form, which is not true of the Leonard decomposition. The various terms of the right-hand side of equation (3.67) can be interpreted as generalizations of the terms of the Leonard triple decomposition. By applying this definition to the components of the velocity fields, the subgrid tensor (3.21) appears in a double form:

$$\begin{aligned}\tau_{\mathrm{G}}(u_i,u_j) &= [u_iu_j]_{\mathrm{G}} - [u_i]_{\mathrm{G}}[u_j]_{\mathrm{G}} \\ &= L_{ij} + C_{ij} + R_{ij} \\ &= \mathcal{L}_{ij} + \mathcal{C}_{ij} + \mathcal{R}_{ij} \quad , \end{aligned} \tag{3.68}$$

in which the tensors $\mathcal{L}$, $\mathcal{C}$ and $\mathcal{R}$ are defined as:

$$\mathcal{L}_{ij} = \tau_{\mathrm{G}}([u_i]_{\mathrm{G}},[u_j]_{\mathrm{G}}) \quad , \tag{3.69}$$

$$\mathcal{C}_{ij} = \tau_{\mathrm{G}}([u_i]_{\mathrm{G}},u_j') + \tau_{\mathrm{G}}(u_i',[u_j]_{\mathrm{G}}) \quad , \tag{3.70}$$

$$\mathcal{R}_{ij} = \tau_{\mathrm{G}}(u_i',u_j') \quad , \tag{3.71}$$

and represent, respectively, the interactions between the large scales, the cross interactions, and the interactions among subgrid scales. They therefore represent tensors defined by Leonard, but are not the same as them in the general case.

By bringing out the generalized central moments, the filtered momentum equations are written in the form:

$$\frac{\partial [u_i]_{\mathrm{G}}}{\partial t} + \frac{\partial}{\partial x_j}\left([u_i]_{\mathrm{G}}[u_j]_{\mathrm{G}}\right) = -\frac{\partial [p]_{\mathrm{G}}}{\partial x_i} + \nu\frac{\partial}{\partial x_j}\left(\frac{\partial [u_i]_{\mathrm{G}}}{\partial x_j} + \frac{\partial [u_j]_{\mathrm{G}}}{\partial x_i}\right) - \frac{\partial \tau_{\mathrm{G}}(u_i,u_j)}{\partial x_j} \quad . \tag{3.72}$$

This equation is equivalent to the one derived from the triple Leonard decomposition. Similarly, the subgrid kinetic energy evolution equation (3.31) is re-written as:

$$\frac{\partial q_{\mathrm{sgs}}^2}{\partial t} = \frac{\partial}{\partial x_j}\left(\frac{1}{2}\tau_{\mathrm{G}}(u_i,u_i,u_j) + \tau_{\mathrm{G}}(p,u_j) - \nu\frac{\partial q_{\mathrm{sgs}}^2}{\partial x_j}\right) - \nu\tau_{\mathrm{G}}(\partial u_i/\partial x_j,\partial u_i/\partial x_j) - \tau_{\mathrm{G}}(u_i,u_j)\frac{\partial [u_i]_{\mathrm{G}}}{\partial x_j} \quad . \tag{3.73}$$

It is easy to check that the structure of the filtered equations is, in terms of generalized central moments, independent of the filter used. This is called the *filtering (or averaging) invariance property.*

3.3.3 Germano Identity

Basic Germano Identity. Subgrid tensors corresponding to two different filtering levels can be related by an exact relation derived by Germano [115].

A sequential application of two filters, F and G, is denoted:

$$[u_i]_{\mathrm{FG}} = [[u_i]_{\mathrm{F}}]_{\mathrm{G}} = [[u_i]_{\mathrm{G}}]_{\mathrm{F}} \quad , \tag{3.74}$$

or equivalently:

$$[u_i]_{\mathrm{FG}}(\mathbf{x}) = \int_{-\infty}^{+\infty} G(\mathbf{x}-\mathbf{y})d^3\mathbf{y}\int_{-\infty}^{+\infty} F(\mathbf{y}-\boldsymbol{\xi})u_i(\boldsymbol{\xi})d^3\boldsymbol{\xi} \quad . \tag{3.75}$$

Here, $[u_i]_{\mathrm{FG}}$ corresponds to the resolved field for the double filtering FG. The subgrid tensor associated with the level FG is defined as the following generalized central moment:

$$\tau_{\mathrm{FG}}(u_i,u_j) = [u_iu_j]_{\mathrm{FG}} - [u_i]_{\mathrm{FG}}[u_j]_{\mathrm{FG}} \quad . \tag{3.76}$$

This expression is a trivial extension of the definition of the subgrid tensor associated with the G filtering level. By definition, the subgrid tensor $\tau_{\mathrm{G}}([u_i]_{\mathrm{F}},[u_j]_{\mathrm{F}})$ calculated from the scales resolved for the F filtering level, is written:

$$\tau_{\mathrm{G}}([u_i]_{\mathrm{F}},[u_j]_{\mathrm{F}}) = [[u_i]_{\mathrm{F}}[u_j]_{\mathrm{F}}]_{\mathrm{G}} - [u_i]_{\mathrm{FG}}[u_j]_{\mathrm{FG}} \quad . \tag{3.77}$$

These two subgrid tensors are related by the following exact relation, called the Germano identity:

$$\tau_{\mathrm{FG}}(u_i,u_j) = [\tau_{\mathrm{F}}(u_i,u_j)]_{\mathrm{G}} + \tau_{\mathrm{G}}([u_i]_{\mathrm{F}},[u_j]_{\mathrm{F}}) \quad . \tag{3.78}$$

This relation can be interpreted physically as follows. The subgrid tensor at the FG filtering level is equal to the sum of the subgrid tensor at the F level filtered at the G level and the subgrid tensor at the G level calculated from the field resolved at the F level. This relation is local in space and time and is independent of the filter used.

It is interesting noting that re-writing the subgrid tensor as

$$\tau_{FG}(u_i,u_j) = [F\star G\star, B](u_i,u_j) \quad ,$$

where $[.,.]$ is the commutator operator (see equation (2.13)) and $B(.,.)$ the bilinear form defined by relation (3.25), the Germano identity (3.78) is strictly equivalent to relation (2.16):

$$[F\star G\star, B](u_i,u_j) = [F\star,B]\circ(G\star)(u_i,u_j) + (F\star)\circ[G\star,B](u_i,u_j) \; . \tag{3.79}$$

Multilevel Germano Identity. The Germano Identity can be extended to the case of N filtering levels, $G_i, i = 1, N$, with associated characteristic lengths $\overline{\Delta}_1 \leq \overline{\Delta}_2 \leq ... \leq \overline{\Delta}_N$ [117, 290, 327].

We define the nth level filtered variable $\overline{\phi}^n$ as

$$\overline{\phi}^n = G_n \star G_{n-1} \star ... \star G_1 \star \phi = \mathcal{G}_1^n \star \phi \quad , \tag{3.80}$$

with

$$\mathcal{G}_m^n \equiv G_n \star G_{n-1} \star ... \star G_m, \mathcal{G}_n^n = Id, \quad \forall m \in [1, n] \quad . \tag{3.81}$$

Let $\tau_{ij}^n = \overline{u_i u_j}^n - \overline{u}_i^n \overline{u}_j^n$ be the subgrid tensor associated to the nth filtering level. The classical two-level Germano identity (3.78) reads

$$\tau_{ij}^{n+1} = \overline{\tau_{ij}^n}^{n+1} + L_{ij}^{n+1}, \quad L_{ij}^{n+1} = \overline{\overline{u}_i^n \overline{u}_j^n}^{n+1} - \overline{u}_i^{n+1} \overline{u}_j^{n+1} \quad . \tag{3.82}$$

Simple algebraic developments lead to the following relation between two filtering levels n and m, with $m < n$:

$$\tau_{ij}^n = L_{ij}^n + \sum_{k=m+1,n-1} \mathcal{G}_{k+1}^n L_{ij}^k + \mathcal{G}_{m+1}^n \tau_{ij}^m \quad , \tag{3.83}$$

resulting in a fully general mutilevel identity.

Generalized Germano Identity. A more general identity is obtained by applying an arbitrary operator $\mathcal{L}$ to the basic identity (3.79) [287], yielding

$$\begin{aligned} \mathcal{L}\{[F \star G\star, B](u_i, u_j)]\} &= \mathcal{L}\{[F\star, B] \circ (G\star)(u_i, u_j) \\ &+ (F\star) \circ [G\star, B](u_i, u_j)\} \quad . \end{aligned} \tag{3.84}$$

For linear operators, we get

$$\begin{aligned} \mathcal{L}\{[F \star G\star, B](u_i, u_j)]\} &= \mathcal{L}\{[F\star, B] \circ (G\star)(u_i, u_j)\} \\ &+ \mathcal{L}\{(F\star) \circ [G\star, B](u_i, u_j)\} \quad . \end{aligned} \tag{3.85}$$

Application to the multilevel identity (3.83) is straightforward.

3.3.4 Invariance Properties

One of the basic principles of modeling in mechanics is to conserve the generic properties of the starting equations [105, 121, 259, 313].

We consider in the present section the analysis of some invariance/symmetry properties of the filtered Navier–Stokes equations, and the resulting constraints for subgrid models. It is remembered that a differential equation will be said to be invariant under a transformation if it is left unchanged by this transformation. It is important to note that these properties are not shared by the boundary conditions. It is shown that properties of the filtered Navier–Stokes equations depend on the filter used to operate the scale separation. The preservation of the symmetry properties of the original Navier–Stokes equations will then lead to the definition of specific requirements for the filter kernel[6] $G(x, \xi)$. The properties considered below are:

- Galilean invariance.
- Time invariance.
- Rotation invariance.
- Reflection invariance.
- Material indifference.

Galilean Invariance. This section is devoted to the analysis by Speziale [313] of the preservation of the Galilean invariance property for translations of the Navier–Stokes equations, first by applying a filter, then by using the different decompositions presented above.

Let us take the Galilean transformation (translation):

$$\mathbf{x}^\bullet = \mathbf{x} + \mathbf{V}t + \mathbf{b}, \quad t^\bullet = t \quad , \tag{3.86}$$

in which $\mathbf{V}$ and $\mathbf{b}$ are arbitrary uniform vectors in space and constant in time. If the $(\mathbf{x}, t)$ reference system is associated with an inertial reference system, then so is $(\mathbf{x}^\bullet, t^\bullet)$. Let $\mathbf{u}$ and $\mathbf{u}^\bullet$ be the velocity vectors expressed in the base coordinate system and the new translated one, respectively. The passage from one system to the other is defined by the relations:

$$\mathbf{u}^\bullet = \mathbf{u} + \mathbf{V} \quad , \tag{3.87}$$

$$\frac{\partial}{\partial x_i^\bullet} = \frac{\partial}{\partial x_i} \quad , \tag{3.88}$$

$$\frac{\partial}{\partial t^\bullet} = \frac{\partial}{\partial t} - V_i \frac{\partial}{\partial x_i} \quad . \tag{3.89}$$

The proof of the invariance of the Navier–Stokes equations for the transformation (3.86) is trivial and is not reproduced here. With this property in

[6] We will only consider filters with constant and uniform cutoff length, i.e. $\overline{\Delta}$ is independent on both space and time. Variable length filters are anisotropic or nonhomogeneous, and violate the following properties in the most general case.

hand, what remains to be shown in order to prove the invariance of the filtered equations by such a transformation is that the filtering process preserves this property.

Let there be a variable ϕ such that

$$\phi^\bullet = \phi \quad . \tag{3.90}$$

The filtering in the translated coordinate system is expressed:

$$\overline{\phi}^\bullet = \int G(\mathbf{x}^\bullet - \mathbf{x}^{\bullet\prime})\phi^\bullet(\mathbf{x}^{\bullet\prime})d^3\mathbf{x}^{\bullet\prime} \quad . \tag{3.91}$$

By using the previous relations, we get:

$$\mathbf{x}^\bullet - \mathbf{x}^{\bullet\prime} = (\mathbf{x} + \mathbf{V}t + \mathbf{b}) - (\mathbf{x}' + \mathbf{V}t + \mathbf{b}) = \mathbf{x} - \mathbf{x}' \quad , \tag{3.92}$$

$$d^3\mathbf{x}^{\bullet\prime} = \left|\frac{\partial x^{\bullet\prime}_i}{\partial x'_j}\right| d^3\mathbf{x}' = d^3\mathbf{x}' \quad , \tag{3.93}$$

and thus, by substitution, the equality:

$$\overline{\phi}^\bullet = \int G(\mathbf{x} - \mathbf{x}')\phi(\mathbf{x}')d^3\mathbf{x}' = \overline{\phi} \quad , \tag{3.94}$$

which completes the proof[7]. The invariance of the Navier–Stokes equations for the transformation (3.86) implies that the sum of the subgrid terms and the convection term, calculated directly from the large scales, is also invariant, but not that each term taken individually is invariant. In the following, we study the properties of each term arising from the Leonard and Germano decompositions.

The above relations imply:

$$\overline{\mathbf{u}^\bullet} = \overline{\mathbf{u}} + \mathbf{V}, \quad \mathbf{u}^{\bullet\prime} = \mathbf{u}', \quad \overline{\mathbf{u}^{\bullet\prime}} = \overline{\mathbf{u}'} \quad , \tag{3.95}$$

which reflects the fact that the velocity fluctuations are invariant by Galilean transformation, while the total velocity is not. In the spectral space, this corresponds to the fact that only the constant mode does not remain invariant by this type of transformation since, with the V field being uniform, it alone is affected by the change of coordinate system[8].

[7] A sufficient condition is that the filter kernel appears as a function of $\mathbf{x} - \mathbf{x}'$.

[8] This is expressed:

$$\mathbf{V} = \text{cste} \Longrightarrow \widehat{\mathbf{V}}(\mathbf{k}) = 0 \ \forall \mathbf{k} \neq 0 \quad ,$$

and thus

$$\widehat{\mathbf{u}^\bullet}(\mathbf{k}) = \widehat{\mathbf{u}}(\mathbf{k}) \ \forall \mathbf{k} \neq 0 \quad ,$$
$$\widehat{\mathbf{u}^\bullet}(0) = \widehat{\mathbf{u}}(0) + \widehat{\mathbf{V}}(0) \quad .$$

In the translated system, the Leonard tensor takes the form:

$$L^\bullet_{ij} = \overline{\overline{u^\bullet_i}\,\overline{u^\bullet_j}} - \overline{u^\bullet_i}\,\overline{u^\bullet_j} \tag{3.96}$$
$$= L_{ij} + \left(\overline{V_i\overline{u}_j + V_j\overline{u}_i}\right) - \left(V_i\overline{u}_j + V_j\overline{u}_i\right) \tag{3.97}$$
$$= L_{ij} - \left(V_i\overline{u}'_j + V_i\overline{u}'_j\right) \quad . \tag{3.98}$$

So this tensor is not invariant. Similar analyses show that:

$$C^\bullet_{ij} = C_{ij} + \left(V_i\overline{u}'_j + V_i\overline{u}'_j\right) \quad , \tag{3.99}$$
$$R^\bullet_{ij} = R_{ij} \quad , \tag{3.100}$$
$$L^\bullet_{ij} + C^\bullet_{ij} = L_{ij} + C_{ij} \quad . \tag{3.101}$$

The tensor C is thus not invariant in the general case, while the tensor R and the groups L+C and L+C+R are. A difference can be seen to appear here between the double and triple decompositions: the double retains groups of terms (subgrid tensor and terms computed directly) that are not individually invariant, while the groups in the triple decomposition are.

The generalized central moments are invariant by construction. That is, by combining relations (3.65) and (3.61), we immediately get:

$$\tau^\bullet_G(u^\bullet_i, u^\bullet_j) = \tau_G(u_i, u_j) \quad . \tag{3.102}$$

This property results in all the terms in Germano's consistent decomposition being invariant by Galilean transformation, which is all the more true for the tensors $\mathcal{L}$, $\mathcal{C}$ and $\mathcal{R}$.

Time Invariance. A time shift of the amount t_0 yields the following change of coordinates:

$$t^\bullet = t + t_0, \quad \mathbf{x}^\bullet = \mathbf{x}, \quad \mathbf{u}^\bullet = \mathbf{u} \quad . \tag{3.103}$$

Since we are considering space dependent filters only, the filtered Navier–Stokes equations are automatically time-invariant, without any restriction on the filter kernel. We have:

$$\overline{\mathbf{u}}^\bullet = \overline{\mathbf{u}}, \quad \mathbf{u}^{\bullet\prime} = \mathbf{u}' \quad , \tag{3.104}$$

and

$$\tau^\bullet_{ik} = \tau_{ik} \quad , \tag{3.105}$$
$$L^\bullet_{ik} = L_{ik} \quad , \tag{3.106}$$
$$R^\bullet_{ik} = R_{ik} \quad , \tag{3.107}$$
$$C^\bullet_{ik} = C_{ik} \quad . \tag{3.108}$$

All the subgrid terms are invariant.

Rotation Invariance. We now consider the following change of reference system:

$$t^\bullet = t, \quad \mathbf{x}^\bullet = A\mathbf{x}, \quad \mathbf{u}^\bullet = A\mathbf{u} \quad , \tag{3.109}$$

where A is the rotation matrix with $A^TA = AA^T = Id$ and $|A| = 1$. Simple calculations similar to those shown for in the section devoted to Galilean invariance lead to the following relations:

$$\overline{\mathbf{u}}^\bullet = A\overline{\mathbf{u}}, \quad \mathbf{u}'^\bullet = A\mathbf{u}' \quad , \tag{3.110}$$

if and only if the filter kernel $G(x,\xi)$ satisfies

$$G(A(x-\xi)) = G(x-\xi) \Longrightarrow G(x,\xi) = G(|x-\xi|) \quad , \tag{3.111}$$

meaning that the filter must be spherically symmetric. The subgrid terms are transformed as:

$$\tau^\bullet_{ik} = A_{im}A_{kn}\tau_{mn} \quad , \tag{3.112}$$
$$L^\bullet_{ik} = A_{im}A_{kn}L_{mn} \quad , \tag{3.113}$$
$$R^\bullet_{ik} = A_{im}A_{kn}R_{mn} \quad , \tag{3.114}$$
$$C^\bullet_{ik} = A_{im}A_{kn}C_{mn} \quad , \tag{3.115}$$

and are seen to be invariant.

Reflection Invariance. We now consider a reflection in the lth direction of space:

$$t^\bullet = t;\ x^\bullet_l = -x_l; x^\bullet_i = x_i, i \neq l; u^\bullet_l = -u_l; u^\bullet_i = u_i, i \neq l \quad . \tag{3.116}$$

If the filter is such that $G(x-\xi) = G(-x+\xi)$, i.e. is symmetric, then

$$\overline{u}^\bullet_l = -\overline{u}_l; \overline{u}^\bullet_i = \overline{u}_i, i \neq l; u'^\bullet_l = -u'_l; u'^\bullet_i = u'_i, i \neq l \quad , \tag{3.117}$$

yielding

$$\tau^\bullet_{ik} = \beta\tau_{ik} \quad , \tag{3.118}$$
$$L^\bullet_{ik} = \beta L_{ik} \quad , \tag{3.119}$$
$$R^\bullet_{ik} = \beta R_{ik} \quad , \tag{3.120}$$
$$C^\bullet_{ik} = \beta C_{ik} \quad , \tag{3.121}$$

with $\beta = -1$ if $i = l$ or $k = l$ and $i \neq l$, and $\beta = 1$ otherwise. We can see that the subgrid tensor and all the terms appearing in both the double and triple decomposition are invariant.

Material Indifference. The last symmetry considered in the present section is the material indifference, which is a generalization of the preceding cases. The change of frame is expressed as:

$$t^\bullet = t, \quad \mathbf{x}^\bullet = A(t)\mathbf{x} + c(t), \quad \mathbf{u}^\bullet = A\mathbf{u} + d(t), \quad d(t) = \dot{c} + \dot{A}\mathbf{x} \quad , \tag{3.122}$$

where the rotation matrix A is such that $A^TA = AA^T = Id$, $|A| = 1$ and $c(t)$ is a vector.

The resulting changes of the subgrid and resolved velocity field are:

$$\overline{\mathbf{u}}^\bullet = A\overline{\mathbf{u}} + d, \quad \mathbf{u}'^\bullet = A\mathbf{u}' \quad , \tag{3.123}$$

yielding

$$\tau^\bullet_{ik} = A_{im}\tau_{mn}A_{kn} \quad , \tag{3.124}$$
$$L^\bullet_{ik} = A_{im}\tau_{mn}L_{kn} - B_{ik} \quad , \tag{3.125}$$
$$C^\bullet_{ik} = A_{im}\tau_{mn}C_{kn} + B_{ik} \quad , \tag{3.126}$$
$$R^\bullet_{ik} = A_{im}R_{mn}A_{kn} \quad , \tag{3.127}$$

with

$$B_{ij} = u'_i d_j + u'_j d_i \quad .$$

These properties are subjected to the condition $G(x,\xi) = G(|x-\xi|)$. We can see that the properties of the subgrid tensors are the same as in the case of the Galilean invariance case.

Table 3.1 summarizes the results dealing with the symmetry properties.

Table 3.1. Invariance properties of convolution filters and subgrid tensors

Symmetry	$G(x,\xi)$	L	C	$L+C$	R
Galilean translation	$G(x-\xi)$	no	no	yes	yes
Time shift	$G(x,\xi)$	yes	yes	yes	yes
Rotation	$G(\|x-\xi\|)$	yes	yes	yes	yes
Reflection	$G(x-\xi) = G(\xi-x)$	yes	yes	yes	yes
Material indifference	$G(\|x-\xi\|)$	no	no	yes	yes

3.3.5 Realizability Conditions

A second-rank tensor τ is realizable or semi-positive definite, if the following inequalities are verified (without summation on the repeated greek indices) [121, 340]:

$$\tau_{\alpha\alpha} \geq 0, \quad \alpha = 1,2,3 \quad , \tag{3.128}$$

$$|\tau_{\alpha\beta}| \leq \sqrt{\tau_{\alpha\alpha}\tau_{\beta\beta}}, \quad \alpha,\beta = 1,2,3 \quad , \tag{3.129}$$

$$\det(\tau) \geq 0 \quad . \tag{3.130}$$

These conditions can be written in several equivalent forms [121]. Some of these are listed below.

1. The quadratic form

$$Q = x_i \tau_{ij} x_j \tag{3.131}$$

is positive semidefinite.

2. The three principal invariants of τ are nonnegative:

$$I_1 = \sum \tau_{\alpha\beta} \geq 0 \quad , \tag{3.132}$$

$$I_2 = \sum_{\alpha\neq\beta} (\tau_{\alpha\alpha}\tau_{\beta\beta} - \tau_{\alpha\beta}^2) \geq 0 \quad , \tag{3.133}$$

$$I_3 = \det(\tau) \geq 0 \quad . \tag{3.134}$$

The positiveness of the filter as defined by relation (2.24) is a necessary and sufficient condition to ensure the realizability of the subgrid tensor τ. Below, we reproduce the demonstration given by Vreman *et al.* [340], which is limited to the case of a spatial filter $G(\mathbf{x}-\boldsymbol{\xi})$ without restricting the general applicability of the result.

Let us first assume that $G \geq 0$. To prove that the tensor τ is realizable at any position $\mathbf{x}$ of the fluid domain Ω, we define the sub-domain Ω_x representing the support of the application $\boldsymbol{\xi} \to G(\mathbf{x}-\boldsymbol{\xi})$. Let F_x be the space of real functions defined on Ω_x. Since G is positive, for $\phi, \psi \in F_x$, the application

$$(\phi,\psi)_x = \int_{\Omega_x} G(\mathbf{x}-\boldsymbol{\xi})\phi(\boldsymbol{\xi})\psi(\boldsymbol{\xi})d\boldsymbol{\xi} \tag{3.135}$$

defines an inner product on F_x. Using the definition of the filtering, the subgrid tensor can be re-written in the form:

$$\begin{aligned}
\tau_{ij}(\mathbf{x}) &= \overline{u_iu_j}(\mathbf{x}) - \overline{u}_i(\mathbf{x})\overline{u}_j(\mathbf{x}) \\
&= \overline{u_iu_j}(\mathbf{x}) - \overline{u}_i(\mathbf{x})\overline{u}_j(\mathbf{x}) - \overline{u}_j(\mathbf{x})\overline{u}_i(\mathbf{x}) + \overline{u}_i(\mathbf{x})\overline{u}_j(\mathbf{x}) \\
&= \int_{\Omega_x} G(\mathbf{x}-\boldsymbol{\xi})u_i(\boldsymbol{\xi})u_j(\boldsymbol{\xi})d^3\boldsymbol{\xi} - \overline{u}_i(\mathbf{x})\int_{\Omega_x} G(\mathbf{x}-\boldsymbol{\xi})u_j(\boldsymbol{\xi})d^3\boldsymbol{\xi} \\
&- \overline{u}_j(\mathbf{x})\int_{\Omega_x} G(\mathbf{x}-\boldsymbol{\xi})u_i(\boldsymbol{\xi})d^3\boldsymbol{\xi} - \overline{u}_i(\mathbf{x})\overline{u}_j(\mathbf{x})\int_{\Omega_x} G(\mathbf{x}-\boldsymbol{\xi})d^3\boldsymbol{\xi} \\
&= \int_{\Omega_x} G(\mathbf{x}-\boldsymbol{\xi})\left(u_i(\boldsymbol{\xi}) - \overline{u}_i(\mathbf{x})\right)\left(u_j(\boldsymbol{\xi}) - \overline{u}_j(\mathbf{x})\right) \\
&= (u_i^x, u_j^x)_x \quad ,
\end{aligned} \tag{3.136}$$

where the difference $u_i^x(\boldsymbol{\xi}) = u_i(\boldsymbol{\xi}) - \overline{u}_i(\mathbf{x})$ is defined on Ω_x. The tensor τ thus appears as a Grammian 3×3 matrix of inner products, and is consequently always defined as semi-positive. This shows that the stated condition is sufficient.

Let us now assume that the condition $G \geq 0$ is not verified for a piecewise continuous kernel. There then exists a pair $(\mathbf{x},\mathbf{y}) \in \Omega \times \Omega$, an $\epsilon \in \mathbb{R}^+$, $\epsilon > 0$, and a neighbourhood $V = \{\boldsymbol{\xi} \in \Omega, |\boldsymbol{\xi}-\mathbf{y}| < \epsilon\}$, such that $G(\mathbf{x}-\boldsymbol{\xi}) < 0$, $\forall \boldsymbol{\xi} \in V$. For a function u_1 defined on Ω such that $u_1(\boldsymbol{\xi}) \neq 0$ if $\boldsymbol{\xi} \in V$ et $u_1(\boldsymbol{\xi}) = 0$ everywhere else, then the component τ_{11} is negative:

$$\tau_{11}(x) = \overline{u_1^2}(x) - (\overline{u}_1(x))^2 \leq \int_V G(\mathbf{x}-\boldsymbol{\xi})\left(u_1(\boldsymbol{\xi})\right)^2 d^3\boldsymbol{\xi} < 0 \quad . \tag{3.137}$$

The tensor τ is thus not semi-positive definite, which concludes the demonstration. The properties of the three usual analytical filter presented in Sect. 2.1.5 are summarized in Table 3.2.

Table 3.2. Positiveness property of convolution filters

Filter	Eq.	Positiveness
Box	(2.37)	yes
Gaussian	(2.39)	yes
Sharp cutoff	(2.41)	no

3.4 Extension to the Inhomogeneous Case

The results of the previous sections were obtained by applying isotropic homogeneous filters on an unbounded domain. What is presented here are the equations obtained by applying non-homogeneous convolution filters on

bounded domains. Using the commutator (2.13), the most general form of the filtered Navier–Stokes equations is:

$$\frac{\partial \overline{u}_i}{\partial t} + \frac{\partial}{\partial x_j}(\overline{u}_i\overline{u}_j) + \frac{\partial \overline{p}}{\partial x_i} - \nu\frac{\partial}{\partial x_j}\left(\frac{\partial \overline{u}_i}{\partial x_j} + \frac{\partial \overline{u}_j}{\partial x_i}\right) = -\frac{\partial \tau_{ij}}{\partial x_j} - \left[G\star, \frac{\partial}{\partial t}\right](u_i) - \left[G\star, \frac{\partial}{\partial x_j}\right](u_iu_j) - \left[G\star, \frac{\partial}{\partial x_i}\right](p) + \nu\left[G\star, \frac{\partial^2}{\partial x_k \partial x_k}\right](u_i) \quad , \tag{3.138}$$

$$\frac{\partial \overline{u}_i}{\partial x_i} = -\left[G\star, \frac{\partial}{\partial x_i}\right](u_i) \quad . \tag{3.139}$$

All the terms appearing in the right hand side of equations (3.138) and (3.139) are commutation errors. The first term of the right hand side of the filtered momentum equation is the subgrid force, and is subject to modeling. The other terms are artefacts due to the filter, and escape subgrid modeling.

The governing equations obtained using second-order commuting filters (SOCF), as well as the technique proposed by Ghosal and Moin [123] to reduce the commutation error and Vasilyev's high-order commuting filters [332], are presented in the following.

3.4.1 Second-Order Commuting Filter

Here we propose to generalize Leonard's approach by applying SOCF filters. The decomposition of the non-linear term considered here as an example is the triple decomposition; but the double decomposition is also usable. For convenience in writing the filtered equations, we introduce the operator $\mathcal{D}_i$ such that:

$$\overline{\frac{\partial \psi}{\partial x_i}} = \mathcal{D}_i\psi \quad . \tag{3.140}$$

According to the results of Sect. 2.2.2, the operator $\mathcal{D}_i$ is of the form:

$$\mathcal{D}_i = \frac{\partial}{\partial x_i} - \alpha^{(2)}\overline{\Delta}^2\Gamma_{ijk}\frac{\partial^2}{\partial x_i^2} + O(\overline{\Delta}^4) \quad , \tag{3.141}$$

in which the term Γ is defined by the relation (2.110). By applying the filter and bringing out the subgrid tensor $\tau_{ij} = \overline{u_iu_j} - \overline{u}_i\overline{u}_j$, we get for the momentum equation:

$$\frac{\partial \overline{u}_i}{\partial t} + \mathcal{D}_j(\overline{u}_i\overline{u}_j) = -\mathcal{D}_i\overline{p} + \nu\mathcal{D}_j\mathcal{D}_j\overline{u}_i - \mathcal{D}_j\tau_{ij} \quad . \tag{3.142}$$

To measure the errors, we introduce the expansion as a function of $\overline{\Delta}$:

$$\overline{p} = \overline{p}^{(0)} + \overline{\Delta}^2\overline{p}^{(1)} + \ldots \quad , \tag{3.143}$$

$$\overline{\mathbf{u}} = \overline{\mathbf{u}}^{(0)} + \overline{\Delta}^2\overline{\mathbf{u}}^{(1)} + \ldots \tag{3.144}$$

The terms corresponding to the odd powers of $\overline{\Delta}$ are identically zero because of the symmetry of the convolution kernel. By substituting this decomposition in (3.142), at the first order we get:

$$\frac{\partial \overline{u}_i^{(0)}}{\partial t} + \frac{\partial}{\partial x_j}\left(\overline{u}_i^{(0)}\overline{u}_j^{(0)}\right) = -\frac{\partial \overline{p}^{(0)}}{\partial x_i} + \nu\frac{\partial}{\partial x_j}\left(\frac{\partial \overline{u}_i^{(0)}}{\partial x_j} + \frac{\partial \overline{u}_j^{(0)}}{\partial x_i}\right) - \frac{\partial \tau_{ij}^{(0)}}{\partial x_j} \quad , \tag{3.145}$$

in which $\tau_{ij}^{(0)}$ is the subgrid term calculated from the field $\overline{\mathbf{u}}^{(0)}$. The associated continuity equation is:

$$\frac{\partial \overline{u}_i^{(0)}}{\partial x_i} = 0 \quad . \tag{3.146}$$

These equations are identical to those obtained in the homogeneous case, but relate to a variable containing an error in $O(\overline{\Delta}^2)$ with respect to the exact solution.

To reduce the error, the problem of the term in $\overline{\Delta}^2$ has to be resolved, *i.e.* solve the equations that use the variables $\overline{\mathbf{u}}^{(1)}$ and $\overline{p}^{(1)}$. Simple expansions lead to the system:

$$\frac{\partial \overline{u}_i^{(1)}}{\partial t} + \frac{\partial}{\partial x_j}\left(\overline{u}_i^{(1)}\overline{u}_j^{(0)} + \overline{u}_i^{(0)}\overline{u}_j^{(1)}\right) = -\frac{\partial \overline{p}^{(1)}}{\partial x_i} + \nu\frac{\partial}{\partial x_j}\left(\frac{\partial \overline{u}_i^{(1)}}{\partial x_j} + \frac{\partial \overline{u}_j^{(1)}}{\partial x_i}\right) - \frac{\partial \tau_{ij}^{(1)}}{\partial x_j} + \alpha^{(2)}f_i^{(1)} \quad , \tag{3.147}$$

in which the coupling term $f_i^{(1)}$ defined as:

$$f_i^{(1)} = \Gamma_{jmn}\frac{\partial^2(\overline{u}_i^{(0)}\overline{u}_j^{(0)})}{\partial x_m \partial x_n} + \Gamma_{imn}\frac{\partial^2 \overline{p}^{(0)}}{\partial x_m \partial x_n} + \Gamma_{jmn}\frac{\partial^2 \tau_{ij}^{(0)}}{\partial x_m \partial x_n} - \nu\frac{\partial \Gamma_{kmn}}{\partial x_k}\frac{\partial^2 \overline{u}_i^{(0)}}{\partial x_m \partial x_n} - 2\Gamma_{kmn}\frac{\partial^3 \overline{u}_i^{(0)}}{\partial x_k \partial x_m \partial x_n} \quad , \tag{3.148}$$

$$\frac{\partial \overline{u}_i^{(1)}}{\partial x_i} = 0 \quad . \tag{3.149}$$

By solving this second problem, we can ensure the accuracy of the solution up to the order $O(\overline{\Delta}^4)$.

3.4.2 High-Order Commuting Filters

The use of Vasilyev's filters (see Sect. 2.2.2) instead of SOCF yields a set of governing filtered equations formally equivalent to (3.142), but with:

$$\mathcal{D}_i = \frac{\partial}{\partial x_i} + O(\overline{\Delta}^n) \quad , \tag{3.150}$$

where the order of accuracy n is fixed by the number of vanishing moments of the filter kernel. The classical filtered equations, without extra-terms accounting for the commutation errors, relate to a variable containing an error scaling as $O(\overline{\Delta}^n)$ with respect to the exact filtered solution.

3.5 Closure Problem

3.5.1 Statement of the Problem

As was already said in the first chapter, large-eddy simulation is a technique for reducing the number of degrees of freedom of the solution. This is done by separating the scales in the exact solution into two categories: resolved scales and subgrid scales. The selection is made by the filtering technique described above.

The complexity of the solution is reduced by retaining only the large scales in the numerical solution process, which entails reducing the number of degrees of freedom in the solution in space and time. The information concerning the small scales is consequently lost, and none of the terms that use these scales, *i.e.* the terms in $\mathbf{u}'$ in the physical space and in $(1 - \widehat{G})$ in the spectral space, can be calculated directly. They are grouped into the subgrid tensor τ. This scale selection determines the level of resolution of the mathematical model.

Nonetheless, in order for the dynamics of the resolved scales to remain correct, the subgrid terms have to be taken into consideration, and thus have to be modeled. The modeling consists of approximating the coupling terms on the basis of the information contained in the resolved scales alone. The modeling problem is twofold:

1. Since the subgrid scales are lacking in the simulation, their existence is unknown and cannot be decided locally in space and time. The problem thus arises of knowing if the exact solution contains, at each point in space and time, any smaller scales than the resolution established by the filter. In order to answer this question, additional information has to be introduced, in either of two ways. The first is to use additional assumptions derived from acquired knowledge in fluid mechanics to link the existence of subgrid modes to certain properties of the resolved scales. The second way is to enrich the simulation by introduc new unknowns directly related to the subgrid modes, such as their kinetic energy, for example.
2. Once the existence of the subgrid modes is determined, their interactions with the resolved scales have to be reflected. The quality of the simulation will depend on the fidelity with which the subgrid model reflects these interactions.

Various modeling strategies and models that have been developed are presented in the following.

Other techniques exist for minimizing the algorithmic complexity of the simulation. One of them consists in optimizing the number of degrees of freedom used for representing the flow by adapting the space-time resolution, *i.e.* the space and time cutoff scales, to the structure of the solution in such a way as to capture all the scales making it up. Among these techniques, we may mention the methods of Incremental Unknowns [55, 90] and of Adaptive Mesh Refinement (AMR) [275]. The choice here is the dual of the choice on which large-eddy simulation is based: in AMR methods the resolution is variable and all the scales are resolved, while for Large-eddy simulation the cut-off scale determines the resolution and certain scales are parametrized.

All these approaches are confronted with the same problem of determining the existence of unresolved scales. This point is crucial because it represents a prerequisite for the application of a subgrid model or the enrichment of the grid, and requires that indicators be determined. Let us recall that since the exact solution is in theory unknown, these indictors incorporate information external to the simulation in implicit form (assumption concerning the solution) or explicit form (adding degrees of freedom).

These techniques can be interpreted as techniques for controlling the dynamical system of finite dimension represented by the computed solution. The subgrid models are then the actuators of the control loop.

3.5.2 Postulates

So far, we have assumed nothing concerning the type of flow at hand, aside from those assumptions that allowed us to demonstrate the momentum and continuity equations. Subgrid modeling usually assumes the following hypothesis

Hypothesis 3.1. *If subgrid scales exist, then the flow is locally (in space and time) turbulent.*

Consequently, the subgrid models will be built on the known properties of the turbulence.

It should be noted that theories exist that use other basic hypotheses. We may mention as an example the description of suspensions in the form of a fluid with modified properties [178]: the solid particles are assumed to have predefined charac stics (mass, form, spatial distribution, and so forth) and

have a characteristic size very much less than the filter cutoff length, *i.e.* at the scale at which we want to describe the flow dynamics directly. Their actions are taken into account globally, which means a very high saving compared with an individual description of each particle. The different descriptions obtained by homogenization techniques also enter into this framework.

3.5.3 Functional and Structural Modeling

Preliminary Remarks. Before discussing the various ways of modeling the subgrid terms, we have to set some constraints in order to orient the choices [285]. The subgrid modeling must be done in compliance with two constraints:

1. Physical constraint. The model must be consistent from the viewpoint of the phenomenon being modeled, *i.e.*:
   - Conserve the basic properties of the starting equation, such as Galilean invariance;
   - Be zero wherever the exact solution exhibits no small scales corresponding to the subgrid scales;
   - Induce an effect of the same kind (dispersive or dissipative, for example) as the modeled terms;
   - Not destroy the dynamics of the solve scales, and thus especially not inhibit the flow driving mechanisms.
2. Numerical constraint. A subgrid model can only be thought of as included in a numerical simulation method, and must consequently:
   - Be of acceptable algorithmic cost, and especially be local in time and space;
   - Not destabilize the numerical simulation;
   - Be insensitive to discretization, *i.e.* the physical effects induced theoretically by the model must not be inhibited by the discretization.

Modeling Strategies. The problem of subgrid modeling consists in taking the interaction with the fluctuating field $\mathbf{u}'$, represented by the term $\nabla \cdot \tau$, into account in the evolution equation of the filtered field $\overline{\mathbf{u}}$. Two modeling strategies exist [285]:

- *Structural modeling* of the subgrid term, which consists in making the best approximation of the tensor τ by constructing it from an evaluation of $\overline{\mathbf{u}}$ or a formal series expansion. The modeling assumption therefore consists in using a relation of the form $\mathbf{u}' = \mathcal{H}(\overline{\mathbf{u}})$ or $\tau = \mathcal{H}(\overline{\mathbf{u}})$.
- *Functional modeling*, which consists in modeling the action of the subgrid terms on the quantity $\overline{\mathbf{u}}$ and not the tensor τ itself, *i.e.* introducing a dissipative or dispersive term, for example, that has a similar effect but not necessarily the same structure (not the same proper axes, for example). The closure hypothesis can then be expressed in the form $\nabla \cdot \tau = \mathcal{H}(\overline{\mathbf{u}})$.

These two modeling approaches do not require the same foreknowledge of the dynamics of the equations treated and theoretically do not offer the same potential in terms of the quality of results obtained.

The structural approach requires no knowledge of the nature of the inter-scale interaction, but does require enough knowledge of the structure of the small scales of the solution in order to be able to determine one of the relations $u' = \mathcal{H}(\overline{\mathbf{u}})$ or $\tau = \mathcal{H}(\overline{\mathbf{u}})$ to be possible, one of the two following conditions has to be met:

- The dynamics of the equation being computed leads to a universal form of the small scales (and therefore to their total structural independence from the resolved motion, as all that remains to be determined is their energy level).
- The dynamics of the equation induces a sufficiently strong and simple inter-scale correlation for the structure of the subgrid scales to be deduced from the information contained in the resolved field.

As concerns the modeling of the inter-scale interaction by just taking its effect into account, this requires no foreknowledge of the subgrid scale structure, but does require knowing the nature of the interaction [81] [166]. Moreover, in order for such an approach to be practical, the effect of the small scales on the large must be universal in character, and therefore independent of the large scales of the flow.

4. Functional Modeling (Isotropic Case)

It would be illusory to try to describe the structure of the scales of motion and the interactions in all imaginable configurations, in light of the very large disparity of physical phenomena encountered. So we have to restrict this description to cases which by nature include scales that are too small for today's computer facilities to solve them entirely, and which are at the same time accessible to theoretical analysis. This description will therefore be centered on the inter-scale interactions in the case of fully developed isotropic homogeneous turbulence[1], which is moreover the only case accessible by theoretical analysis and is consequently the only theoretical framework used today for developing subgrid models. Attempts to extend this theory to anisotropic and/or inhomogeneous cases are discussed in Chap. 5. The text will mainly be oriented toward the large-eddy simulation aspects. For a detailed description of the isotropic homogeneous turbulence properties, which are reviewed in Appendix A, the reader may refer to the works of Lesieur [189] and Batchelor [17].

4.1 Phenomenology of Inter-Scale Interactions

It is important to note here the framework of restrictions that apply to the results we will be presenting. These results concern three-dimensional flows and thus do not cover the physics of two-dimensional flows (in the sense of flows with two directions[2], and not two-component[3] flows), which have a totally different dynamics [168–170, 188, 216]. The modeling in the two-dimensional case leads to specific models [14, 282, 283] which will not be

[1] That is, whose statistical properties are invariant by translation, rotation, or symmetry.

[2] These are flows such that there exists a direction x for which we have the property:

$$\frac{\partial \mathbf{u}}{\partial x} \equiv 0 \quad .$$

[3] These are flows such that there exists a framework in which the velocity field has an identical' ero component.

presented. For details on two-dimensional turbulence, the reader may also refer to [189].

4.1.1 Local Isotropy Assumption: Consequences

In the case of fully developed turbulence, Kolmogorov's statistical description of the small scales of the flow, based on the assumption of local isotropy, has been the one most used for a very long time.

By introducing the idea of local isotropy, Kolmogorov assumes that the small scales belonging to the inertial range of the energy spectrum of a fully developed inhomogeneous turbulent flow are:

- *Statistically isotropic*, and therefore entirely characterized by a characteristic velocity and time;
- *Without time memory*, therefore in energy equilibrium with the large scales of the flow by instantaneous re-adjustment.

This isotropy of the small scales implies that they are statistically independent of the large energetic scales, which are characteristic of each flow and are therefore anisotropic. Experimental work [234] has shown that this assumption is not valid in shear flows for all the scales belonging to the inertial area, but only for those whose size is of the order of the Kolmogorov scale. Numerical experiments [10] show that turbulent stresses are nearly isotropic for wave numbers k such that $kL_\varepsilon > 50$, where L_ε is the integral dissipation length[4]. These experiments have also shown that the existence of an inertial region does not depend on the local isotropy hypothesis. The causes of this persistence of the anisotropy in the inertial range due to interactions existing between the various scales of the flow will be mentioned in Chap. 5. Works based on direct numerical simulations have also shown that the assumption of equilibrium between the resolved and subgrid scales may be faulted, at least temporarily, when the flow is subject to unsteady forcing [199, 226, 258, 266]. This is due to the fact that the relaxation times of these two scale ranges are different. In the case of impulsively accelerated flows (plane channel, boundary layer, axisymmetric straining) the subgrid scales react more quickly than the resolved ones, and then also relax more quickly toward an equilibrium solution.

The existence of a zone of the spectrum, corresponding to the higher frequencies, where the scales of motion are statistically isotropic, justifies the study of the inter-modal interactions in the ideal case of isotropic homogeneous turbulence. Strictly speaking, the results can be used for determining

[4] The integral dissipation length is defined as

$$L_\varepsilon = \frac{\langle u_i u_i \rangle^{3/2}}{\varepsilon} \quad ,$$

where ε is the energy dissipation rate.

subgrid models only if the cutoff associated with the filter is in this region, because the dynamics of the unresolved scales then corresponds well to that of the isotropic homogeneous turbulence. It should be noted that this last condition implies that the representation of the dynamics, while incomplete, is nonetheless very fine, which theoretically limits the gain in complexity that can be expected from large-eddy simulation technique.

Another point is that the local isotropy hypothesis is formulated for fully developed turbulent flows at very high Reynolds numbers. As it affirms the universal character of the small scales' behavior for these flows, it ensures the possibility using the large-eddy simulation technique strictly, if the filter cutoff frequency is set sufficiently high. There is no theoretical justification, though, for applying the results of this analysis to other flows, such as those in transition.

4.1.2 Interactions Between Resolved and Subgrid Scales

In order to study the interactions between the resolved and subgrid scales, we adopt an isotropic filter by a cutoff wave number k_c. The subgrid scales are those represented by the $\mathbf{k}$ modes such that $k \geq k_c$.

In the case of fully developed isotropic homogeneous turbulence, the statistical description of the inter-scale interactions is reduced to that of the kinetic energy transfers. Consequently, only the information associated with the amplitude of the fluctuations is conserved, and none concerning the phase is taken into account.

These transfers are analyzed using several tools:

- Analytical theories of turbulence, also called two-point closures, which describe triadic interactions on the basis of certain assumptions. They will therefore express the non- linear term $S(\mathbf{k}|\mathbf{p},\mathbf{q})$, defined by relation (3.48) completely. For a description of these theories, the reader may refer to Lesieur's book [189], and we also mention Waleffe's analysis [342, 343], certain conclusions of which are presented in the following.
- Direct numerical simulations, which provide a complete description of the dynamics.

Typology of the Triadic Interactions. It appears from the developments of Sect. 3.1.2 (also see Appendix A) that the $\widehat{\mathbf{u}}(\mathbf{k})$ mode interacts only with those modes whose wave vectors $\mathbf{p}$ and $\mathbf{q}$ form a closed triangle with $\mathbf{k}$. The wave vector triads $(\mathbf{k},\mathbf{p},\mathbf{q})$ thus defined are classified in several groups [369] which are represented in Fig. 4.1:

- *Local triads* for which

$$\frac{1}{a} \leq \max\left\{\frac{p}{k}, \frac{q}{k}\right\} \leq a, \qquad a = O(1) \quad ,$$

which correspond to interactions among wave vectors of neighboring modules, and therefore to interactions among scales of slightly different sizes;

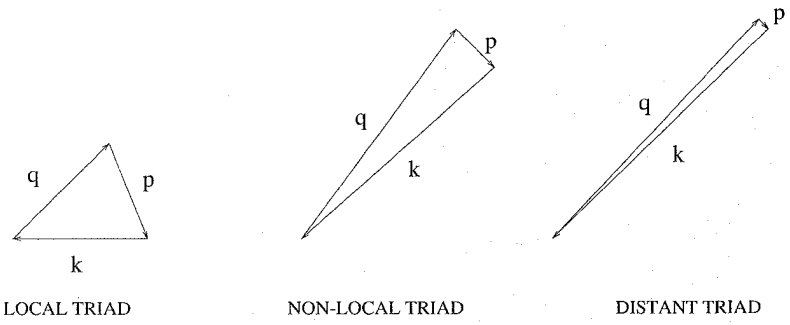

Fig. 4.1. Different types of triads.

– *Non-local triads*, which are all those interactions that do not fall within the first category, *i.e.* interactions among scales of widely differing sizes. Here, we adopt the terminology proposed in [35], which distinguishes between two sub-classes of non-local triads, one being distant triads of interactions in which $k \ll p \sim q$ or $k \sim q \gg p$. It should be noted that these terms are not unequivocal, as certain authors [189, 192] refer to these "distant" triads as being just "non-local".

By extension, a phenomenon will be called local if it involves wave vectors $\mathbf{k}$ and $\mathbf{p}$ such that $1/a \leq p/k \leq a$, and otherwise non-local or distant.

Canonical Analysis. This section presents the results from analysis of the simplest theoretical case, which we call here canonical analysis. This consists of assuming the following two hypotheses:

1. Hypothesis concerning the flow. The energy spectrum $E(\mathbf{k})$ of the exact solution is a Kolmogorov spectrum, *i.e.*

$$E(\mathbf{k}) = K_0 \varepsilon^{2/3} k^{-5/3}, \quad k \in [0, \infty] \quad , \tag{4.1}$$

   where K_0 is the Komogorov constant and ε the kinetic energy dissipation rate. We point out that this spectrum is not integrable since its corresponds to an infinite kinetic energy.
2. Hypothesis concerning the filter. The filter is a sharp cutoff type. The subgrid tensor is thus reduced to the subgrid Reynolds tensor.

In analyzing the energy transfers $T^{e}_{sgs}(k)$ (see relation (3.49)) between the modes to either side of a cutoff wave number k_c located in the inertial range of the spectrum, Kraichnan [170] uses the Test Field Model (TFM) to bring out the existence of two spectral bands (see Fig. 4.2) for which the interactions with the small scales (p and/or $q \geq k_c$) are of different kinds.

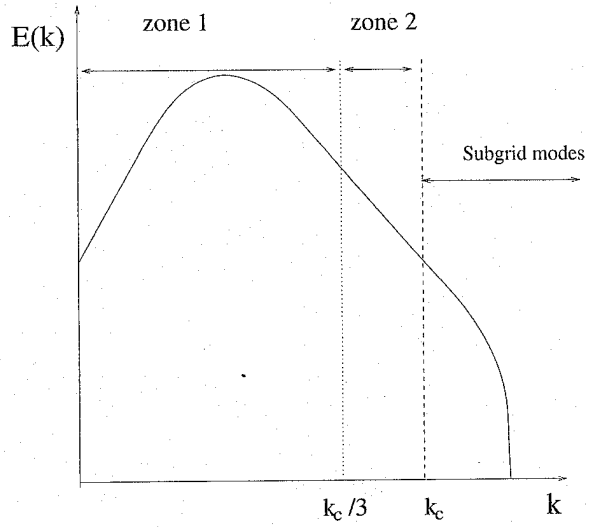

Fig. 4.2. Interaction regions between resolved and subgrid scales.

1. In the first region (1 in Fig. 4.2), which corresponds to the modes such that $k \ll k_c$, the dominant dynamic mechanism is a random displacement of the momentum associated with $\mathbf{k}$ by disturbances associated with $\mathbf{p}$ and $\mathbf{q}$. This phenomenon, analogous to the effects of the molecular viscosity, entails a kinetic energy decay associated with $\mathbf{k}$ and, since the total kinetic energy is conserved, a resulting increase of it associated with $\mathbf{p}$ and $\mathbf{q}$. So here it is a matter of a non-local transfer of energy associated with non-local triadic interactions. These transfers, which induce a damping of the fluctuations, are associated with what Waleffe [342, 343] classifies as type F triads (represented in Fig. 4.3).

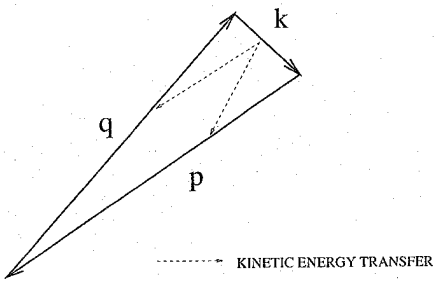

Fig. 4.3. Non-local triad $(\mathbf{k}, \mathbf{p}, \mathbf{q})$ of the F type according to Waleffe's classification, and the associated non-local energy transfers. The kinetic energy of the mode corresponding to the smallest wave vector $\mathbf{k}$ is distributed to the other two modes $\mathbf{p}$ and $\mathbf{q}$, creating ward energy cascade in the region where $k \ll k_c$.

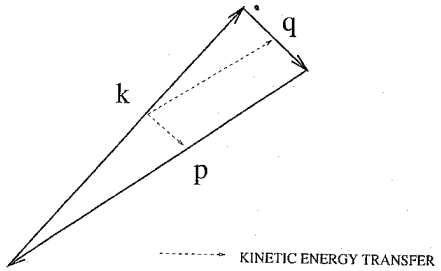

Fig. 4.4. Non-local $(\mathbf{k}, \mathbf{p}, \mathbf{q})$ triad of the R type according to Waleffe's classification, and the associated energy transfers in the case $q \ll k_c$. The kinetic energy of the mode corresponding to the intermediate wave vector $\mathbf{k}$ is distributed locally to the largest wave vector $\mathbf{p}$ and non-locally to the smallest wave vector, $\mathbf{q}$. The former transfer originates the intensification of the coupling in the $(k_c - k) \ll k_c$ spectral band, while the latter originates the backward kinetic energy cascade.

Subsequent analyses using the Direct Interaction Approximation (DIA) and the Eddy Damped Quasi-Normal Markovian (EDQNM) models [54, 61, 192, 193] or Waleffe's analyses [342, 343] have refined this representation by showing the existence of two competitive mechanisms in the region where $k \ll k_c$. The first region is where the energy of the large scales is drained by the small, as already shown by Kraichnan. The second mechanism, of much lesser intensity, is a return of energy from the small scales $\mathbf{p}$ and $\mathbf{q}$ to the large scale $\mathbf{k}$. This mechanism also corresponds to a non-local energy transfer associated with non-local triadic interactions that Waleffe classifies as type R (see Fig. 4.4). It represents a backward stochastic energy cascade associated with an energy spectrum in k^4 for very small wave numbers. This phenomenon has been predicted analytically [192] and verified by numerical experimentation [54, 191]. The analytical studies and numerical simulations show that this backward cascade process is dominant for very small wave numbers. On the average, these modes receive more energy from the subgrid modes than they give to them.

2. In the second region (region 2 in Fig. 4.2), which corresponds to the $\mathbf{k}$ modes such that $(k_c - k) \ll k_c$, the mechanisms already present in region 1 persist. The energy transfer to the small scales is at the origin of the forward kinetic energy cascade.
   Moreover, another mechanism appears involving triads such that p or $q \ll k_c$, which is that the interactions between the scales of this region and the subgrid scales are much more intense than in the first. Let us take $q \ll k_c$. This mechanism is a coherent straining of the small scales $\mathbf{k}$ and $\mathbf{p}$ by the shear associated with $\mathbf{q}$, resulting in a wave number diffusion process between $\mathbf{k}$ and $\mathbf{p}$ through the cutoff, with one of the structures being stretched (vortex stretching phenomenon) and the other unstretched.

What we are observing here is a local energy transfer between $\mathbf{k}$ and $\mathbf{p}$ associated with non-local triadic interactions due to the type R triads (see Fig. 4.4). Waleffe refines the analysis of this phenomenon: a very large part of the energy is transferred locally from the intermediate wave number located just ahead of the cutoff toward the larger wave number just after it, and the remaining fraction of energy is transferred to the smaller wave number. These findings have been corroborated by numerical data [54, 82, 84] and other theoretical analyses [61, 193].

The energy transfers $T^e_{sgs}(k)$ (see relation (3.49)) between mode $\mathbf{k}$ and the subgrid modes can be represented in a form analogous to molecular dissipation. To do this, by following Heisenberg (see [317] for a description of Heisenberg's theory), we define an effective viscosity $\nu_e(k|k_c)$, which represents the energy transfers between the $\mathbf{k}$ mode and the modes located beyond the k_c cutoff such that:

$$T^e_{sgs}(k) = -2\nu_e(k|k_c)k^2E(k) \quad . \tag{4.2}$$

It should be pointed out that this viscosity is real, *i.e.* $\nu_e(k|k_c) \in \mathbb{R}$, and that if any information related to the phase were included, it would lead the definition of a complex term having an a priori non-zero imaginary part, which may seem to be more natural for representing a dispersive type of coupling. Such a term is obtained not by starting with the kinetic energy equation, but with the momentum equation[5].

The two energy cascades, forward and backward, can be introduced separately by introducing distinct effective viscosities, constructed in such a way as to ensure energy transfers equivalent to those of these cascades. We get the following two forms:

$$\nu_e^+(k|k_c,t) = -\frac{T^+_{sgs}(k|k_c,t)}{2k^2E(k,t)} \quad , \tag{4.3}$$

$$\nu_e^-(k|k_c,t) = -\frac{T^-_{sgs}(k|k_c,t)}{2k^2E(k,t)} \quad , \tag{4.4}$$

in which $T^+_{sgs}(k|k_c,t)$ (resp. $T^-_{sgs}(k|k_c,t)$) is the energy transfer term from the k mode to the subgrid modes (resp. from the subgrid modes to the k mode). This leads to the decomposition:

$$T^e_{sgs}(k) = T^+_{sgs}(k|k_c,t) + T^-_{sgs}(k|k_c,t) \tag{4.5}$$

$$= -2k^2E(k,t)\left(\nu_e^+(k|k_c,t) + \nu_e^-(k|k_c,t)\right) \quad . \tag{4.6}$$

[5] This possibility is only mentioned here, because no works have been published on it to date.

These two viscosities depend explicitly on the wave number k and the cutoff wave vector k_c, as well as the shape of the spectrum. The result of these dependencies on the flow is that the viscosities are not, because they characterize the flow and not the fluid. They are of opposite sign: $\nu_e^+(k|k_c,t)$ ensures a loss of energy of the resolved scales and is consequently positive, like the molecular viscosity, whereas $\nu_e^-(k|k_c,t)$, which represents an energy gain in the resolved scales, is negative.

The conclusions of the theoretical analyses [170, 193] and numerical studies [54] are in agreement on the form of these two viscosities. Their behavior is presented in Fig. 4.5 in the canonical case.

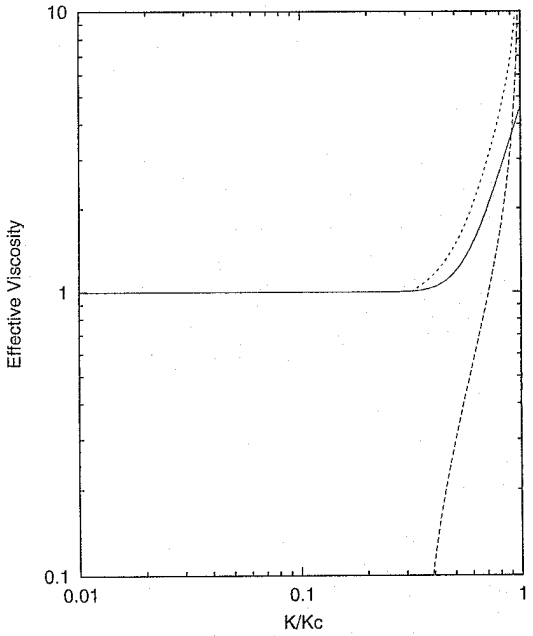

Fig. 4.5. Representation of effective viscosities in the canonical case. – *Short dashes:* $\nu_e^+(k|k_c,t)$; *long dashes:* $-\nu_e^-(k|k_c,t)$; *solid:* $\nu_e^+(k|k_c,t)+\nu_e^-(k|k_c,t)$.

We may note that these two viscosities become very high for wave numbers close to the cutoff. These two effective viscosities diverge as $(k_c-k)^{-2/3}$ as k tends toward k_c. However, their sum $\nu_e(k|k_c,t)$ remains finite and Leslie *et al.* [193] proposes the estimation:

$$\nu_e(k_c|k_c,t) = 5.24\nu_e^+(0|k_c,t) \quad . \tag{4.7}$$

The interactions with the subgrid scales is therefore especially important in the dynamics of the smallest resolved scales. More precisely, Kraichnan's theoretical analysis leads to the conclusion that about 7 of the energy

transfers of a k mode occur with the modes located in the $[k/2, 2k]$ spectral band. No transfers outside this spectral band have been observed in direct numerical simulations at low Reynolds numbers [82, 368, 369]. The difference with the theoretical analysis stems from the fact that this analysis is performed in the limit of the infinite Reynolds numbers.

In the limit of the very small wave numbers, we have the asymptotic behaviors:

$$2k^2E(k,t)\nu_e^+(k|k_c,t) \propto k^{1/3} \quad , \tag{4.8}$$

$$2k^2E(k,t)\nu_e^-(k|k_c,t) \propto k^4 \quad . \tag{4.9}$$

The effective viscosity associated with the energy cascade takes the constant asymptotic value:

$$\nu_e^+(0|k_c,t) = 0.292\varepsilon^{1/3}k_c^{-4/3} \quad . \tag{4.10}$$

Dependency According to the Filter. Leslie and Quarini [193] extended the above analysis to the case of the Gaussian filter. The spectrum considered is always of the Kolmogorov type. The Leonard term is now non-zero. The results of the analysis show very pronounced differences from the canonical analysis. Two regions of the spectrum are still distinguishable, though, with regard to the variation of the effective viscosities ν_e^+ and ν_e^-, which are shown in Fig. 4.6:

- In the first region, where $k \ll k_c$, the transfer terms still observe a constant asymptotic behavior, independent of the wave number considered, as in the canonical case. The backward cascade term is negligible compared with the forward cascade term.
- In the second region, on the other hand, when approaching cutoff, the two transfer terms do not have divergent behavior, contrary to what is observed in the canonical case. The forward cascade term decreases monotonically and cancels out after the cutoff for wave numbers more than a decade beyond it. The backward cascade term increases up to cutoff and exhibits a decreasing behavior analogous to that of the forward cascade term. The maximum intensity of the backward cascade is encountered for modes just after the cutoff.

In contrast to the sharp cutoff filter used for the canonical analysis, the Gaussian filter makes it possible to define Leonard terms and non-identically zero cross terms. The effective viscosity associated with these terms is shown in Fig. 4.7, where it can be seen that it is negligible for all the modes more than a decade away from the cutoff. In the same way as for the backward cascade term, the maximum amplitude is observed for modes located just after the cutoff. This term remains smaller than the forward and backward cascade terms for all the wavenumbers.

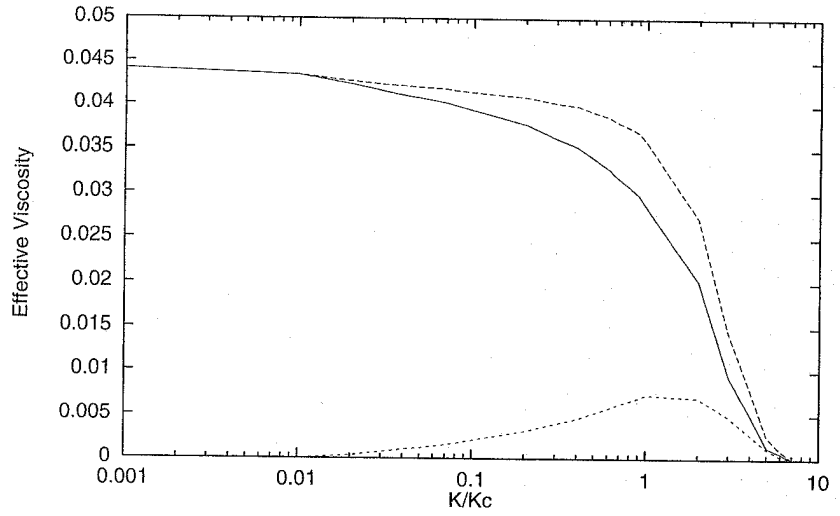

Fig. 4.6. Effective viscosities in the application of a Gaussian filter to a Kolmogorov spectrum. *Long dots* $\nu_e^+(k|k_c,t)$; *dots:* $-\nu_e^-(k|k_c,t)$; *solid:* $\nu_e^+(k|k_c,t)+\nu_e^-(k|k_c,t)$.

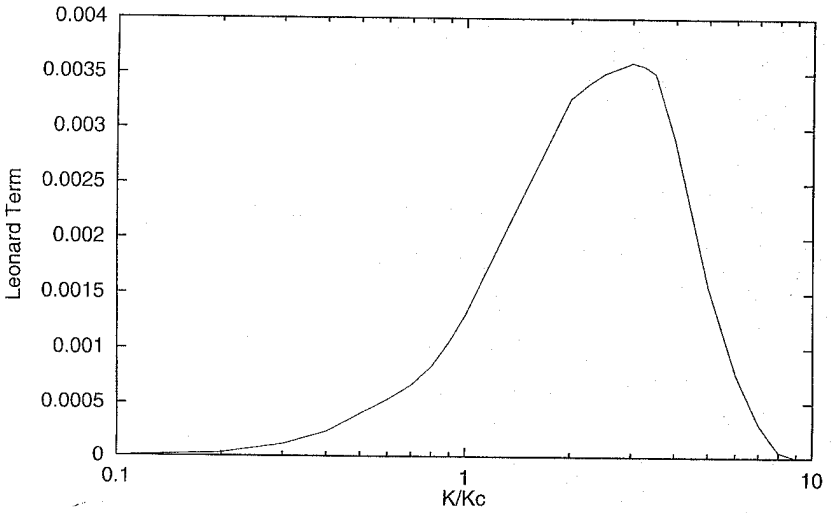

Fig. 4.7. Effective viscosity corresponding to the Leonard term in the case of the application of a Gaussian filter to a Kolmogorov spectrum.

Dependency According to Spectrum Shape. The results of the canonical analysis are also dependent on the shape of the spectrum considered. The analysis is repeated for the case of the application of the sharp cutoff filter to a production spectrum of the form:

$$E(\mathbf{k}) = A_s(k/k_p)K_0\varepsilon^{2/3}k^{-5/3} \quad , \tag{4.11}$$

with

$$A_s(x) = \frac{x^{s+5/3}}{1+x^{s+5/3}} \quad , \tag{4.12}$$

and where k_p is the wave number that corresponds to the maximum of the energy spectrum [193]. The shape of the spectrum thus defined is illustrated in Fig. 4.8 for several values of the s parameter.

The variation of the total effective viscosity ν_e for different values of the quotient k_c/k_p is diagrammed in Fig. 4.9. For low values of this quotient, *i.e.* when the cutoff is located at the beginning of the inertial range, we observe that the viscosity may decrease at the approach to the cutoff, while it is strictly increasing in the canonical case. This difference is due to the fact that the asymptotic reasoning that was applicable in the canonical case is no longer valid, because the non-localness of the triadic interactions involved relay the difference in spectrum shape to the whole of it. For higher values of this quotient, *i.e.* when the cutoff is located *sufficiently far* into the inertial range (for large values of the ratio k_c/k_p), a behavior that is qualitatively similar to that observed in the canonical case is once again found[6].

[6] In practice, k_c/k_p=8 seems appropriate.

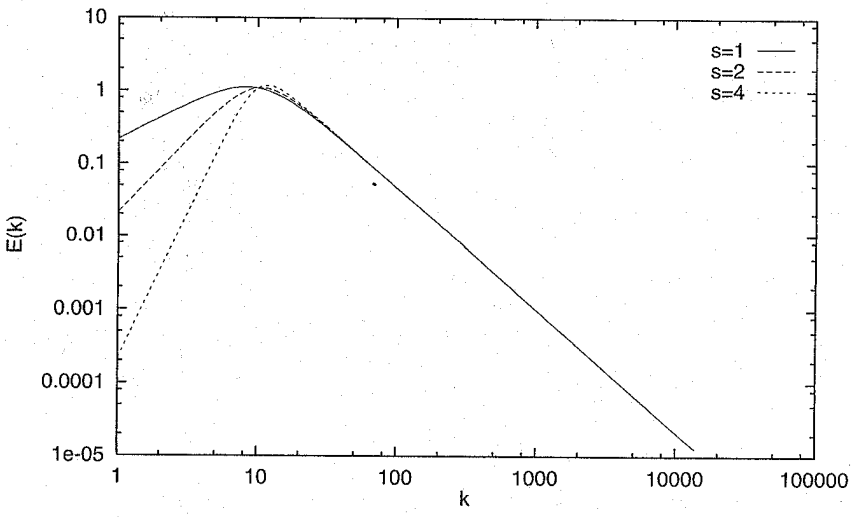

Fig. 4.8. Production spectrum for different values of the shape parameter s.

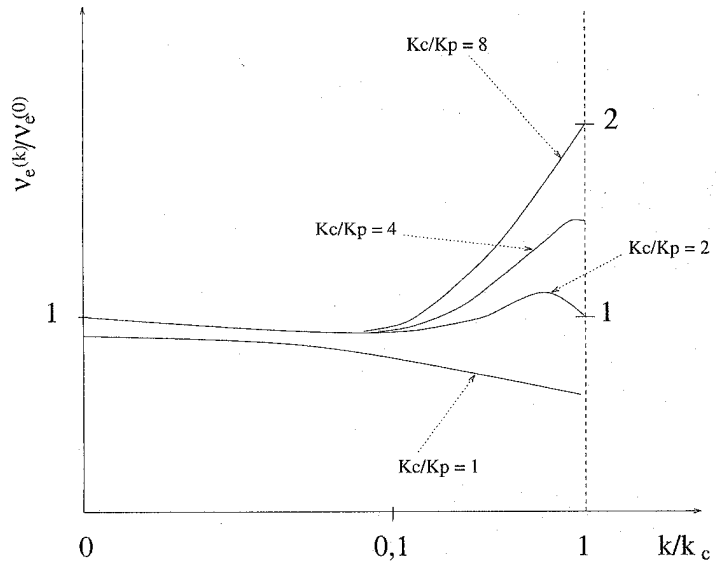

Fig. 4.9. Total effective viscosity $\nu_e(k|k_c)$ in the case of the application of a sharp cutoff filter to a production spectrum for different values of the quotient k_c/k_p, normalized by its value at the origin.

For $k_c = k_p$, no increase is observed in the energy transfers as k tends toward k_c. The behavior approximates that observed for the canonical analysis as the ratio k_p/k_c decreases.

4.1.3 A View in Physical Space

Analyses described in the preceding section were all performed in the Fourier space, and do not give any information about the location of the subgrid transfer in the physical space and its correlation with the resolved scale features[7]. Complementary informations on the subgrid transfer in the physical space have been found by several authors using direct numerical simulation. Kerr *et al.* [166] propose to use the rotational form of the non-linear term of the momentum equation:

$$N(x) = u(x) \times \omega(x) - \nabla p_h(x) \quad , \tag{4.13}$$

where $\omega = \nabla \times u$ and p_h the pressure term. By splitting the velocity and vorticity field into a resolved and a subgrid contribution, we get:

[7] This is a prerequisite for designing functional subgrid mode physical space.

$$\underbrace{u \times \omega - \overline{u} \times \overline{\omega}}_{I} = \underbrace{\overline{u} \times \omega'}_{II} + \underbrace{u' \times \overline{\omega}}_{III} + \underbrace{u' \times \omega'}_{IV} \quad . \tag{4.14}$$

The four terms represent different coupling mechanisms between the resolved motion and the subgrid scales:

- I - exact subgrid term,
- II - interaction between resolved velocity and subgrid vorticity,
- III - interaction between subgrid velocity and resolved vorticity,
- IV - interaction between subgrid velocity and subgrid vorticity.

The corresponding complete non-linear terms $N^I, ..., N^{IV}$ are built by adding the specific pressure term. The associated subgrid kinetic energy transfer terms are computed as $\varepsilon^l = \overline{u} \cdot N^l$. The authors made three significant observations for isotropic turbulence:

- Subgrid kinetic energy transfer is strongly correlated with the boundaries of regions of large vorticity production (stretching), i.e. regions where $\overline{\omega}_i \overline{S}_{ij} \overline{\omega}_j$ is large;
- Term II, $\overline{u} \times \omega'$, has a correlation with subgrid non-linear term I up to 0.9. This term dominates the backward energy cascade;
- Up to 90 % of the subgrid kinetic energy transfer comes from term III, i.e. from the interaction of subgrid velocity with resolved vorticity. This term mostly contributes to the forward energy cascade.

Additional results of Borue and Orszag [33] show that the subgrid transfer takes place in regions where the vorticity stretching term is positive or in regions with negative skewness of the resolved strain rate tensor, $\mathrm{Tr}(\overline{S}^3)$. These authors also found that there is only a very poor local correlation between the subgrid transfer $\tau_{ij}\overline{S}_{ij}$ and the local strain $\overline{S}_{ij}\overline{S}_{ij}$, where $\overline{S}_{ij}$ is the resolved strain rate tensor.

4.1.4 Summary

The different analyses performed in the framework of fully developed isotropic turbulence show that:

1. Interactions between the small and large scales is reflected by two main mechanisms:
   - A drainage of energy from the resolved scales by the subgrid scales (forward energy cascade phenomenon);
   - A weak feedback of energy, proportional to k^4 to the resolved scales (backward energy cascade phenomenon).

2. The interactions between the subgrid scales and the smallest of the resolved scales depend on the filter used and on the shape of the spectrum. In certain cases, the coupling with the subgrid scales is strengthened for wave numbers close to the cutoff and the energy toward the subgrid modes is intensified.
3. These cascade mechanisms are associated to specific features of the velocity and vorticity field in physical space.

4.2 Basic Functional Modeling Hypothesis

All the subgrid models entering into this category make more or less implicit use of the following hypothesis:

Hypothesis 4.1. *The action of the subgrid scales on the resolved scales is essentially an energetic action, so that the balance of the energy transfers alone between the two scale ranges is sufficient to describe the action of the subgrid scales.*

Using this hypothesis as a basis for modeling, then, we neglect a part of the information contained in the small scales, such as the structural information related to the anisotropy. As was seen above, the energy transfers between subgrid scales and resolved scales mainly exhibit two mechanisms: a forward energy transfer toward the subgrid scales and a backward transfer to the resolved scales which, it seems, is much weaker in intensity. All the approaches existing today for numerical simulation at high Reynolds numbers consider the energy lost by the resolved scales, while only a few rare attempts have been made to consider the backward energy cascade.

Once hypothesis 4.1 is assumed, the modeling consists in modifying the different evolution equations of the system in such a way as to integrate the desired dissipation or energy production effects into them. To do this, two different approaches can be found in today's works:

- *Explicit modeling* of the desired effects, *i.e.* including them by adding additional terms to the equations: the actual subgrid models;
- *Implicit inclusion* by the numerical scheme used, by arranging it so the truncation error induces the desired effects.

Let us note that while the explicit approach is what would have to be called the classical modeling approach, the implicit one appears generally only as an a posteriori interpretation of dissipative properties for certain numerical methods used.

4.3 Modeling of the Forward Energy Cascade Process

This section describes the main functional models of the energy cascade mechanism. Those derived in the Fourier space, conceived for simulations based on spectral numerical methods, and models derived in the physical space, suited to the other numerical methods, are presented separately.

4.3.1 Spectral Models

The models belonging to this category are all effective viscosity models drawing upon the analyses of Kraichnan for the canonical case presented above. The following models are described:

1. The Chollet–Lesieur model (p.78) which, based on the results of the canonical analysis (inertial range of the spectrum with a slope of $-5/3$, sharp cutoff filter, no effects associated with a production type spectrum) yields an analytical expression for the effective viscosity as a function of the wave number considered and the cutoff wave number. It will reflect the local effects at the cutoff, *i.e.* the increase in the energy transfer toward the subgrid scales. This model explicitly brings out a dependency of the effective viscosity as a function of the kinetic energy at the cutoff. This guarantees that, when all the modes of the exact solution are resolved, the subgrid model automatically cancels out. The fact that this information is local in frequency allows the model to consider (at least partially) the spectral disequilibrium phenomena that occur at the level of the resolved scales[8], though without relaxing the hypotheses underlying the canonical analysis. Only the amplitude of the transfers is variable, and not their pre-supposed shape.
2. The effective viscosity model (p.79), which is a simplification of the previous one and is based on the same assumptions. The effective viscosity is then independent of the wave number and is calculated so as to ensure the same average value as the Chollet–Lesieur model. It is simpler to compute, but does not reflect the local effects at the cutoff.
3. The dynamic spectral model (p.79), which is an extension of the Chollet–Lesieur model for spectra having a slope different from that of the canonical case (*i.e.* $-5/3$). Richer information is considered here: while the Chollet–Lesieur model is based only on the energy level at the cutoff, the dynamic spectral model also incorporates the spectrum slope at the cutoff. With this improvement, we can cancel the subgrid model in certain cases for which the kinetic energy at cutoff is non-zero but where the kinetic energy transfer to the subgrid modes is zero[9]. This model

[8] This is by their action on the transfers between resolved scales and the variations induced on the energy level at cutoff.

[9] As is the case, for example, for two-dimensional flows.

$$\nu_e^+(k|k_c) = \nu_e(k|k_m,k_c)\sqrt{\frac{k_c}{E(k_c)}} + \nu_e^+(0)\left(\frac{k_m}{k_c}\right)^{4/3} \quad . \tag{4.23}$$

The factor $\nu_e^+(0)$ is evaluated by considering that we have the relations

$$\nu_e^+(k|k_m) \approx \nu_e^+(0), \quad \nu_e(k|k_m,k_c) \approx \nu_e(0|k_m,k_c) \quad , \tag{4.24}$$

for $k \ll k_m$, which leads to:

$$\nu_e^+(0) = \nu_e(0|k_m,k_c)\sqrt{\frac{k_c}{E(k_c)}}\left[1-\left(\frac{k_m}{k_c}\right)^{4/3}\right]^{-1} \quad . \tag{4.25}$$

Models Based on Analytical Theories of Turbulence. The effective viscosity models presented above are all based on an approximation of the effective viscosity profile obtained in the canonical case, and are therefore intrinsically linked to the underlying hypotheses, especially those concerning the shape of the energy spectrum. One way of relaxing this constraint is to compute the effective viscosity directly from the computed spectrum using analytical theories of turbulence. This approach has been used by Aupoix [7], Chollet [57, 58], and Bertoglio [21–23].

More recently, following the recommendations of Leslie and Quarini, which are to model the forward and backward cascade mechanisms separately, Chasnov [54] in 1991 proposed an effective viscosity model considering only the energy draining effects, with the backward cascade being modeled separately (see Sect. 4.4). Starting with an EDQNM analysis, Chasnov proposes computing the effective viscosity $\nu_e(k|k_c)$ as:

$$\nu_e(k|k_c) = \frac{1}{2k^2}\int_{k_c}^{\infty} dp \int_{p-k}^{p} dq \Theta_{kpq}\left(\frac{p^2}{q}(xy+z^3)E(q) + \frac{q^2}{p}(xz+y^3)E(p)\right), \tag{4.26}$$

in which x, y and z are geometric factors associated with the $(\mathbf{k},\mathbf{p},\mathbf{q})$ triads and Θ_{kpq} a relaxation time. These terms are explained in Appendix B. To compute this integral, the shape of the energy spectrum beyond the cutoff k_c must be known. As it is not known *a priori*, it must be specified elsewhere. In practice, Chasnov uses a Kolmogorov spectrum extending from the cutoff to infinity. To simplify the computations, the relation (4.26) is not used outside the interval $[k_c \le p \le 3k_c]$. For wave numbers $p > 3k_c$, the following simplified asymptotic form already proposed by Kraichnan is used:

$$\nu_e(k|k_c) = \frac{1}{15}\int_{k_c}^{\infty} dp \Theta_{kpq}\left(5E(p) + p\frac{\partial E(p)}{\partial p}\right) \quad . \tag{4.27}$$

4.3.2 Physical Space Models

Subgrid Viscosity Concept. The forward energy cascade mechanism to the subgrid scales is modeled explicitly using the following hypothesis:

Hypothesis 4.2. *The energy transfer mechanism from the resolved to the subgrid scales is analogous to the molecular mechanisms represented by the diffusion term, in which the viscosity ν appears.*

This hypothesis is equivalent to assuming that the behavior of the subgrid scales is analogous to the Brownian motion superimposed on the motion of the resolved scales. In gaskinetics theory, molecular agitation draws energy from the flow by way of molecular viscosity. So the energy cascade mechanism will be modeled by a term having a mathematical structure similar to that of molecular diffusion, but in which the molecular viscosity will be replaced by a subgrid viscosity denoted ν_{sgs}. As Boussinesq proposed, this choice of mathematical form of the subgrid model is written:

$$-\nabla\cdot\tau^d = \nabla\cdot\left(\nu_{sgs}(\nabla\overline{\mathbf{u}} + \nabla^T\overline{\mathbf{u}})\right) \quad , \tag{4.28}$$

in which τ^d is the deviator of τ, *i.e.*:

$$\tau_{ij}^d \equiv \tau_{ij} - \frac{1}{3}\tau_{kk}\delta_{ij} \quad . \tag{4.29}$$

The complementary spherical tensor $\frac{1}{3}\tau_{kk}\delta_{ij}$ is added to the filtered static pressure term and consequently requires no modeling. This decomposition is necessary since the tensor $(\nabla\overline{\mathbf{u}} + \nabla^T\overline{\mathbf{u}})$ has a zero trace, and we can only model a tensor that also has a zero trace. This leads to the definition of the modified pressure Π:

$$\Pi = \overline{p} + \frac{1}{3}\tau_{kk} \quad . \tag{4.30}$$

It is important to note that the modified pressure and filtered pressure $\overline{p}$ may take very different values when the generalized subgrid kinetic energy becomes large [163]. The closure thus now consists in determining the relation:

$$\nu_{sgs} = \mathcal{N}(\overline{\mathbf{u}}) \quad . \tag{4.31}$$

The use of hypothesis (4.2) and of a model structured as above calls for a few comments.

Obtaining a scalar subgrid viscosity requires the adoption of the following hypothesis:

Hypothesis 4.3. *A characteristic length l_0 and a characteristic time t_0 are sufficient for describing the subgrid scales.*

Then, by dimensional reasoning similar to Prandtl's, we arrive at:

$$\nu_{\text{sgs}} \propto \frac{l_0^2}{t_0} \quad . \tag{4.32}$$

Models of the form (4.28) are local in space and time, which is a necessity if they are to be used in practice. This local character, similar to that of the molecular diffusion terms, implies [9, 170, 370]:

Hypothesis 4.4 (Scale Separation Hypothesis). *There exists a total separation between the subgrid and resolved scales.*

A spectrum verifying this hypothesis is presented in Fig. 4.10.

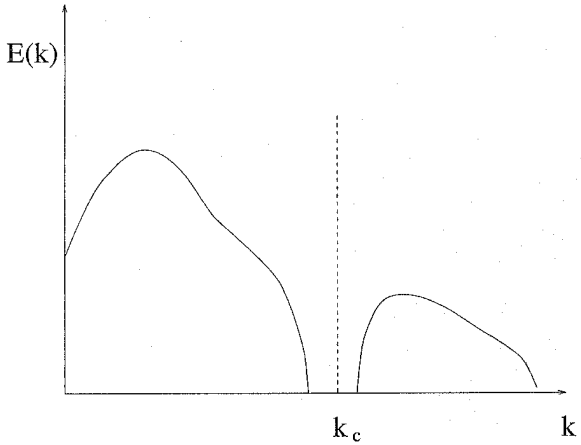

Fig. 4.10. Energy spectrum corresponding to a total scale separation for cutoff wave number k_c.

Using L_0 and T_0 to denote the characteristic scales, respectively, of the resolved field in space and time, this hypothesis can be reformulated as:

$$\frac{l_0}{L_0} \ll 1, \quad \frac{t_0}{T_0} \ll 1 \quad . \tag{4.33}$$

This hypothesis is verified in the case of molecular viscosity. The ratio between the size of the smallest dynamically active scale, η_{K}, and the mean free path ξ_{fp} of the molecules of a gas is evaluated as:

$$\frac{\xi_{\text{fp}}}{\eta_{\text{K}}} \simeq \frac{\text{Ma}}{Re^{1/4}} \quad , \tag{4.34}$$

where Ma is the Mach number, defined as the ratio of the fluid velocity to the speed of sound, and Re the Reynolds number [326]. In most of the cases encountered, this ratio is less than 10^3, which ensu the pertinence

of using a continuum model. For applications involving rarefied gases, this ratio can take on much higher values of the order of unity, and the Navier–Stokes equations are then no longer an adequate model for describing the fluid dynamics.

Filtering associated to large-eddy simulation does not introduce such a separation between resolved and subgrid scales because the turbulent energy spectrum is continuous. The characteristic scales of the smallest resolved scales are consequently very close to those of the largest subgrid scales[10]. This continuity originates the existence of the spectrum region located near the cutoff, in which the effective viscosity varies rapidly as a function of the wave number. The result of this difference in nature with the molecular viscosity is that the subgrid viscosity is not a characteristic of the fluid but of the flow. Let us not that Yoshizawa [357, 359], using a re-normalization technique, has shown that the subgrid viscosity is defined as a fourth-order non-local tensor in space and time, in the most general case. The use of the scale separation hypothesis therefore turns out to be indispensable for constructing local models, although it is contrary to the scale similar hypothesis of Bardina *et al.* [13], which is discussed in Chap. 6.

The modeling problem consists in determining the characteristic scales l_0 and t_0.

Model Types. The subgrid viscosity models can be classified in three categories according to the quantities they bring into play [9]:

1. Models based on the resolved scales (p.85): the subgrid viscosity is evaluated using global quantities related to the resolved scales. The existence of subgrid scales at a given point in space and time will therefore be deduced from the global characteristics of the resolved scales, which requires the introduction of assumptions.
2. Models based on the energy at the cutoff (p.87): the subgrid viscosity is calculated from the energy of the highest resolved frequency. Here, it is a matter of information contained in the resolved field, but localized in frequency and therefore theoretically more pertinent for describing the phenomena at cutoff than the quantities that are global and thus not localized in frequency, which enter into the models of the previous class. The existence of subgrid scales is associated with a non-zero value of the energy at cutoff[11].

[10] This is all the more true for smooth filters such as the Gaussian and box filters, which allow a frequency overlapping between the resolved and subgrid scales.

[11] This hypothesis is based on the fact that the energy spectrum $E(k)$ of an isotropic turbulent flow in spectral equilibrium corresponding to a Kolmogorov spectrum is a monotonic continuous decreasing function of the wave number k. If there exists a wave number k^* such that $E(k^*) = 0$, then $E(k) = 0$, $\forall k > k^*$. Also, if the energy is non-zero at the cutoff, then subgrid modes exist, *i.e.* if $E(k_c) \neq 0$, then there exists a neighbourhood $\Omega_{k_c} = [k_c, k_c + \epsilon_c]$, $\epsilon_c > 0$ such that $E(k_c) \geq E(k) \geq 0 \forall k \in \Omega_k$

3. Models based on the subgrid scales (p.88), which use information directly related to the subgrid scales. The existence of the subgrid scales is no longer determined on the basis of assumptions concerning the characteristics of the resolved scales as it is in the previous cases, but rather directly from this additional information. These models, because they are richer, also theoretically allow a better description of these scales than the previous models.

These model classes are presented in the following. All the developments are based on the analysis of the energy transfers in the canonical case. In order to be able to apply the models formulated from these analyses to more realistic flows, such as the homogeneous isotropic flows associated with a production type spectrum, we adopt the assumption that the filter cutoff frequency is located sufficiently far into the inertial range for these analyses to remain valid (refer to Sect. 4.1.2). The use of these subgrid models for arbitrary developed turbulent flows (anisotropic, inhomogeneous) is justified by the local isotropy hypothesis: we assume then that the cutoff occurs in the scale range that verifies this hypothesis.

The case corresponding to an isotropic homogeneous flow associated with a production spectrum is represented in Fig. 4.11. Three energy fluxes are defined: the injection rate of turbulent kinetic energy into the flow by the driving mechanisms (forcing, instabilities), denoted ε_I; the kinetic energy transfer rate through the cutoff, denoted $\tilde{\varepsilon}$; and the kinetic energy dissipation rate by the viscous effects, denoted ε.

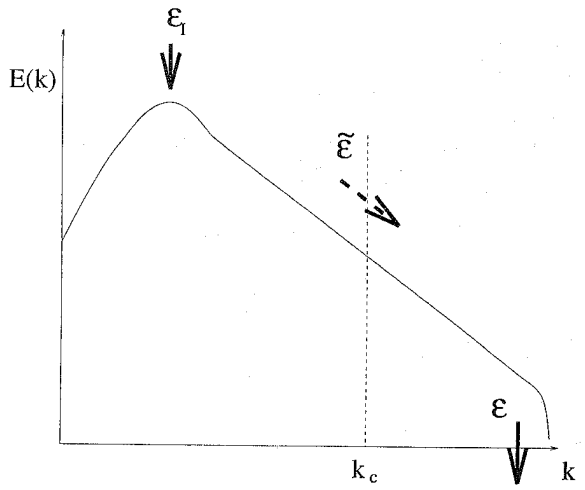

Fig. 4.11. Dynamics of the kinetic energy in the spectral space. The energy is injected at the rate ε_I. The transfer rate through the cutoff, located wave number k_c, is denoted $\tilde{\varepsilon}$. The dissipation rate due to viscous effects is denoted ε. The local equilibrium hypothesis is expressed by the equality $\varepsilon_I = \tilde{\varepsilon} = \varepsilon$.

Models Based on the Resolved Scales. These models are of the generic form:

$$\nu_{\text{sgs}} = \nu_{\text{sgs}}\left(\overline{\Delta}, \tilde{\varepsilon}\right) \quad , \tag{4.35}$$

in which $\overline{\Delta}$ is the characteristic cutoff length of the filter and $\tilde{\varepsilon}$ the instantaneous energy flux through the cutoff. We implicitly adopt the assumption here, then, that the subgrid modes exist, *i.e.* that the exact solution is not entirely represented by the filtered field when this flux is non-zero.

First Method. Simple dimensional analysis shows that:

$$\nu_{\text{sgs}} \propto \tilde{\varepsilon}^{1/3}\,\overline{\Delta}^{4/3} \quad . \tag{4.36}$$

Reasoning as in the framework of Kolmogorov's hypotheses for isotropic homogeneous turbulence, for the case of an infinite inertial spectrum of the form

$$E(k) = K_0\,\langle\varepsilon\rangle^{2/3} k^{-5/3}, \quad K_0 \sim 1.4 \quad , \tag{4.37}$$

in which ε is the kinetic energy dissipation rate, we get the equation:

$$\langle\nu_{\text{sgs}}\rangle = \frac{A}{K_0 \pi^{4/3}} \langle\tilde{\varepsilon}\rangle^{1/3}\,\overline{\Delta}^{4/3} \quad , \tag{4.38}$$

in which the constant A is evaluated as $A = 0.438$ with the TFM model and as $A = 0.441$ by the EDQNM theory [9]. The angle brackets operator $\langle\,\rangle$, designates a statistical average. This statistical averaging operation is intrinsically associated with a spatial mean by the fact of the flow's spatial homogeneity and isotropy hypotheses. This notation is used in the following to symbolize the fact that the reasoning followed in the framework of isotropic homogeneous turbulence applies only to the statistical averages and not to the local values in the physical space. The problem is then to evaluate the average flux $\langle\tilde{\varepsilon}\rangle$. In the isotropic homogeneous case, we have:

$$\langle 2|\overline{S}|^2\rangle = \langle 2\overline{S}_{ij}\overline{S}_{ij}\rangle = \int_0^{k_c} 2k^2 E(k)dk, \quad k_c = \frac{\pi}{\overline{\Delta}} \quad . \tag{4.39}$$

If the cutoff k_c is located far enough into the inertial range, the above relation can be expressed solely as a function of this region's characteristic quantities. Using a spectrum of the shape (4.37), we get:

$$\langle 2|\overline{S}|^2\rangle = \pi^{4/3} K_0 \frac{3}{2} \langle\varepsilon\rangle^{2/3}\,\overline{\Delta}^{-4/3} \quad . \tag{4.40}$$

Using the hypothesis[12] [194] :

$$\langle |\overline{S}|^{3/2} \rangle \simeq \langle |\overline{S}| \rangle^{3/2} \quad , \tag{4.41}$$

we get the equality:

$$\langle \varepsilon \rangle = \frac{1}{\pi^2} \left(\frac{3K_0}{2} \right)^{-3/2} \overline{\Delta}^2 \langle 2|\overline{S}|^2 \rangle^{3/2} \quad . \tag{4.42}$$

In order to evaluate the dissipation rate $\langle \varepsilon \rangle$ from the information contained in the resolved scales, we assume the following:

Hypothesis 4.5 (Local Equilibrium Hypothesis). *The flow is in constant spectral equilibrium, so there is no accumulation of energy at any frequency and the shape of the energy spectrum remains invariant with time.*

This implies an instantaneous adjustment of all the scales of the solution to the turbulent kinetic energy production mechanism, and therefore equality between the production, dissipation, and energy flux through the cutoff:

$$\langle \varepsilon_I \rangle = \langle \tilde{\varepsilon} \rangle = \langle \varepsilon \rangle \quad . \tag{4.43}$$

Using this equality and relations (4.38) and (4.42), we get the closure relation:

$$\langle \nu_{\text{sgs}} \rangle = \left(C\overline{\Delta} \right)^2 \langle 2|\overline{S}|^2 \rangle^{1/2} \quad , \tag{4.44}$$

where the constant C is evaluated as:

$$C = \frac{\sqrt{A}}{\pi \sqrt{K_0}} \left(\frac{3K_0}{2} \right)^{-1/4} \sim 0.148 \quad . \tag{4.45}$$

Second Method. The local equilibrium hypothesis allows:

$$\langle \varepsilon \rangle = \langle \tilde{\varepsilon} \rangle \equiv \langle -\overline{S}_{ij} \tau_{ij} \rangle = \langle \nu_{\text{sgs}} 2\overline{S}_{ij} \overline{S}_{ij} \rangle \quad . \tag{4.46}$$

The idea is then to assume that:

$$\langle \nu_{\text{sgs}} 2\overline{S}_{ij} \overline{S}_{ij} \rangle = \langle \nu_{\text{sgs}} \rangle \langle 2\overline{S}_{ij} \overline{S}_{ij} \rangle \quad . \tag{4.47}$$

By stating at the outset that the subgrid viscosity is of the form (4.44) and using relation (4.40), a new value is found for the constant C:

$$C = \frac{1}{\pi} \left(\frac{3K_0}{2} \right)^{-3/4} \sim 0.18 \quad . \tag{4.48}$$

We note that the value of this constant is independent of the cutoff wave number k_c, but because of the way it is calculated, we can expect a dependency as a function of the spectrum shape.

[12] The error margin measured in direct numerical simulations of isotropic homogeneous turbulence is of the order of 20 % [229].

Alternate Form. This modeling induces a dependency as a function of the cutoff length $\overline{\Delta}$ and the strain rate tensor $\overline{S}$ of the resolved velocity field. In the isotropic homogeneous case, we have the equality:

$$\langle 2|\overline{S}|^2 \rangle = \langle \overline{\omega} \cdot \overline{\omega} \rangle, \quad \overline{\omega} = \nabla \times \overline{\mathbf{u}} \quad . \tag{4.49}$$

By substitution, we get the equivalent form [218]:

$$\langle \nu_{\text{sgs}} \rangle = \left(C\overline{\Delta} \right)^2 \langle \overline{\omega} \cdot \overline{\omega} \rangle^{1/2} \quad . \tag{4.50}$$

These two versions bring in the gradients of the resolved velocity field. This poses a problem of physical consistency since the subgrid viscosity is non-zero as soon as the velocity field exhibits spatial variations, even if it is laminar and all the scales are resolved. The hypothesis that links the existence of the subgrid modes to that of the mean field gradients therefore prevents us from considering the large scale intermittency and thereby requires us to develop models which by nature can only be effective for dealing with flows that are completely turbulent and under-resolved everywhere[13]. Poor behavior can therefore be expected when treating intermittent or weakly developed turbulent flows (*i.e.* in which the inertial range does not appear in the spectrum) due to too strong an action by the model.

Models Based on the Energy at Cutoff. The models of this category are based on the intrinsic hypothesis that if the energy at the cutoff is non-zero, then subgrid modes exist.

First Method. Using relation (4.38) and supposing that the cutoff occurs within an inertial region, *i.e.*:

$$E(k_c) = K_0 \langle \varepsilon \rangle^{2/3} k_c^{-5/3} \quad , \tag{4.51}$$

by substitution, we get:

$$\langle \nu_{\text{sgs}} \rangle = \frac{A}{\sqrt{K_0}} \sqrt{\frac{E(k_c)}{k_c}}, \; k = \pi/\overline{\Delta} \quad . \tag{4.52}$$

This model raises the problem of determining the energy at the cutoff in the physical space, but on the other hand ensures that the subgrid viscosity will be null if the flow is well resolved, *i.e.* if the highest-frequency mode captured by the grid is zero. This type of model thus ensures a better physical consistency than those models based on the large scales. It should be noted that it is equivalent to the spectral model of constant effective viscosity.

[13] In the sense that the subgrid modes exist at each point in space and at each time step.

Second Method. As in the case of models based on the large scales, there is a second way of determining the model constant. By combining relations (4.46) and (4.51), we get:

$$\langle \nu_{\text{sgs}} \rangle = \frac{2}{3K_0^{3/2}} \sqrt{\frac{E(k_c)}{k_c}} \quad . \tag{4.53}$$

Models Based on Subgrid Scales. Here we considers models of the form:

$$\langle \nu_{\text{sgs}} \rangle = \langle \nu_{\text{sgs}} \rangle \left(\overline{\Delta}, \langle q_{\text{sgs}}^2 \rangle, \langle \varepsilon \rangle \right) \quad , \tag{4.54}$$

in which $\langle q_{\text{sgs}}^2 \rangle$ is the kinetic energy of the subgrid scales and $\langle \varepsilon \rangle$ the kinetic energy dissipation rate[14]. These models contain more information about the subgrid modes than those belonging to the two categories described above, and thereby make it possible to do without the local equilibrium hypothesis (4.5) by introducing characteristic scales specific to the subgrid modes by way of $\langle q_{\text{sgs}}^2 \rangle$ and $\langle \varepsilon \rangle$. This capacity to handle the energy disequilibrium is expressed by the relation:

$$\langle \widetilde{\varepsilon} \rangle \equiv \langle -\tau_{ij} \overline{S}_{ij} \rangle \neq \langle \varepsilon \rangle \quad , \tag{4.55}$$

which should be compared with (4.43). In the case of an inertial range extending to infinity beyond the cutoff, we have the relation:

$$\langle q_{\text{sgs}}^2 \rangle \equiv \langle \frac{1}{2} \overline{u_i' u_i'} \rangle = \int_{k_c}^{\infty} E(k) dk = \frac{3}{2} K_0 \langle \varepsilon \rangle^{2/3} k_c^{-2/3} \quad , \tag{4.56}$$

from which we deduce:

$$\langle \varepsilon \rangle = \frac{k_c}{(3K_0/2)^{3/2}} \langle q_{\text{sgs}}^2 \rangle^{3/2} \quad . \tag{4.57}$$

By introducing this last equation into relation (4.38), we come to the general form:

$$\langle \nu_{\text{sgs}} \rangle = C_\alpha \langle \varepsilon \rangle^{\alpha/3} \langle q_{\text{sgs}}^2 \rangle^{(1-\alpha)/2} \overline{\Delta}^{1+\alpha/3} \quad , \tag{4.58}$$

in which

$$C_\alpha = \frac{A}{K_0 \pi^{4/3}} \left(\frac{3K_0}{2} \right)^{(\alpha-1)/2} \pi^{(1-\alpha)/3} \quad , \tag{4.59}$$

and in which α is a real weighting parameter. Interesting forms of ν_{sgs} have been found for certain values:

[14] Other models are of course possible using other subgrid scale quantities like a length or time scale, but we limit ourselves here to classes of models for which practical results exist.

– For $\alpha = 1$, we get

$$\langle \nu_{\text{sgs}} \rangle = \frac{A}{K_0 \pi^{4/3}} \overline{\Delta}^{4/3} \langle \varepsilon \rangle^{1/3} \quad . \tag{4.60}$$

This form uses only the dissipation and is analogous to that of the models based on the resolved scales. If the local equilibrium hypothesis is used, these two types of models are formally equivalent.

– For $\alpha = 0$, we get

$$\langle \nu_{\text{sgs}} \rangle = \sqrt{\frac{2}{3}} \frac{A}{\pi K_0^{3/2}} \overline{\Delta} \left(\langle q_{\text{sgs}}^2 \rangle \right)^{1/2} \quad . \tag{4.61}$$

This model uses only the kinetic energy of the subgrid scales. As such, it is formally analogous to the definition of the diffusion coefficient of an ideal gas in the framework of gaskinetics theory. In the case of an inertial spectrum extending to infinity beyond the cutoff, this model is strictly equivalent to the model based on the energy at cutoff, since in this precise case we have the relation:

$$\frac{3}{2} k_c E(k_c) = \langle q_{\text{sgs}}^2 \rangle \quad . \tag{4.62}$$

– For $\alpha = -3$, we have:

$$\langle \nu_{\text{sgs}} \rangle = \frac{4A}{9K_0^3} \frac{\left(\langle q_{\text{sgs}}^2 \rangle \right)^2}{\langle \varepsilon \rangle} \quad . \tag{4.63}$$

This model is formally analogous to the $k-\varepsilon$ statistical model of turbulence for the Reynolds Averaged Navier–Stokes equations, and does not bring in the filter cutoff length explicitly.

The closure problem consists in determining the quantities $\langle \varepsilon \rangle$ and $\langle q_{\text{sgs}}^2 \rangle$. To do this, we can introduce one or more equations for the evolution of these quantities or we can deduce them from the information contained in the resolved field. As these quantities represent the subgrid scales, we are justified in thinking that, if they are correctly evaluated, the subgrid viscosity will be negligible when the flow is well resolved numerically. However, it should be noted that these models in principle require more computation than those based on the resolved scales, because they produce more information concerning the subgrid scales.

Extension to Other Spectrum Shapes. The above developments are based on a Kolmogorov spectrum, which reflects only the existence of a region of similarity of the real spectra. This approach can be extended to other more realistic spectrum shapes, mainly including the viscous effects. Several extensions of the models based on the large scales were proposed by Voke [337] for this. The total dissipation $\langle \varepsilon \rangle$ can be decomposed into the sum of the dissipation

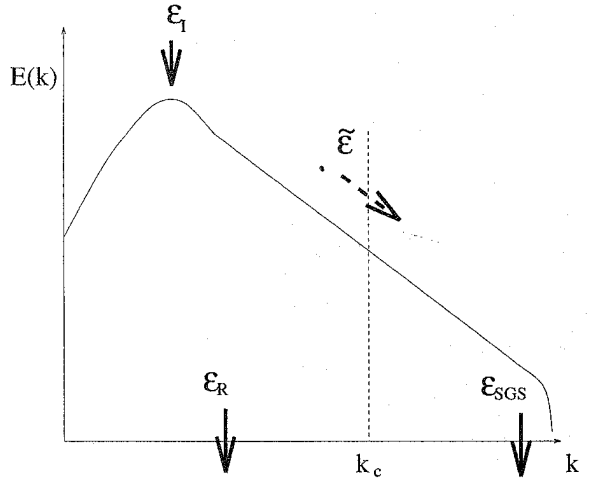

Fig. 4.12. Kinetic energy dynamics in the spectral space. The energy is injected at the rate ε_I. The transfer rate through the cutoff located at the wave number k_c is denoted $\tilde{\varepsilon}$. The dissipation rate in the form of heat by the viscous effects associated with the scales located before and after the cutoff k_c are denoted ε_r and ε_{sgs}, respectively.

associated with the large scales, denoted $\langle\varepsilon_r\rangle$, and the dissipation associated with the subgrid scales, denoted $\langle\varepsilon_{sgs}\rangle$, (see Fig. 4.12):

$$\langle\varepsilon\rangle = \langle\varepsilon_r\rangle + \langle\varepsilon_{sgs}\rangle \quad . \tag{4.64}$$

These three quantities can be evaluated as:

$$\langle\varepsilon\rangle = \langle 2(\nu_{sgs}+\nu)|\overline{S}|^2\rangle \quad , \tag{4.65}$$

$$\langle\varepsilon_r\rangle = 2\nu\langle|\overline{S}|^2\rangle = 2\nu\int_0^{k_c} k^2 E(k)dk \quad , \tag{4.66}$$

$$\langle\varepsilon_{sgs}\rangle = 2\langle\nu_{sgs}|\overline{S}|^2\rangle = C_s\overline{\Delta}^2\left(2\langle|\overline{S}|^2\rangle\right)^{3/2} \quad , \tag{4.67}$$

from which we get:

$$\frac{\langle\varepsilon_r\rangle}{\langle\varepsilon\rangle} = \frac{1}{1+\tilde{\nu}}, \quad \tilde{\nu} = \frac{\langle\nu_{sgs}\rangle}{\nu} \quad . \tag{4.68}$$

This ratio is evaluated by calculating the $\langle\varepsilon_r\rangle$ term analytically from the chosen spectrum shapes, which provides a way of then computing the subgrid viscosity $\langle\nu_{sgs}\rangle$.

We define the three following parameters:

$$\kappa = \frac{k}{k_d} = k\left(\frac{\nu^3}{\langle\varepsilon\rangle}\right)^{1/4}, \quad \kappa_c = \frac{k_c}{k_d} \quad , \tag{4.69}$$

$$Re_{\overline{\Delta}} = \frac{\overline{\Delta}^2\sqrt{2|\overline{S}|^2}}{\nu} \quad , \tag{4.70}$$

in which k_d is the wave number associated with the Kolmogorov scale (see Appendix A), and $Re_{\overline{\Delta}}$ is the mesh-Reynolds number. Algebraic substitutions lead to:

$$\kappa = \pi Re_{\overline{\Delta}}^{-1/2}(1+\tilde{\nu})^{-1/4} \quad . \tag{4.71}$$

The spectra studied here are of the generic form:

$$E(k) = K_0\varepsilon^{2/3}k^{-5/3}f(\kappa) \quad , \tag{4.72}$$

in which f is a damping function for large wave numbers. The following are some commonly used forms of this function:

– Heisenberg–Chandrasekhar spectrum:

$$f(\kappa) = \left[1+\left(\frac{3K_0}{2}\right)^3\kappa^4\right]^{-4/3} \quad . \tag{4.73}$$

– Kovasznay spectrum:

$$f(\kappa) = \left(1-\frac{K_0}{2}\kappa^{4/3}\right)^2 \quad . \tag{4.74}$$

Note that this function cancels out for $\kappa = (2/K_0)^{3/4}$, which requires that the spectrum be forced to zero for wave numbers beyond this limit.

– Pao spectrum:

$$f(\kappa) = \exp\left(-\frac{3K_0}{2}\kappa^{4/3}\right) \quad . \tag{4.75}$$

These three spectrum shapes are graphed in Fig. 4.13. An analytical integration leads to:

– For the Heisenberg–Chandrasekhar spectrum:

$$\frac{\langle\varepsilon_r\rangle}{\langle\varepsilon\rangle} = \kappa_c^{4/3}\left[\left(\frac{2}{3K_0}\right)^3+\kappa_c^4\right]^{-1/3} \quad , \tag{4.76}$$

or:

$$\langle\nu_{sgs}\rangle = \nu\left\{\kappa_c^{-4/3}\left[\left(\frac{2}{3K_0}\right)^3+\kappa_c^4\right]^{1/3}-1\right\} \quad . \tag{4.77}$$

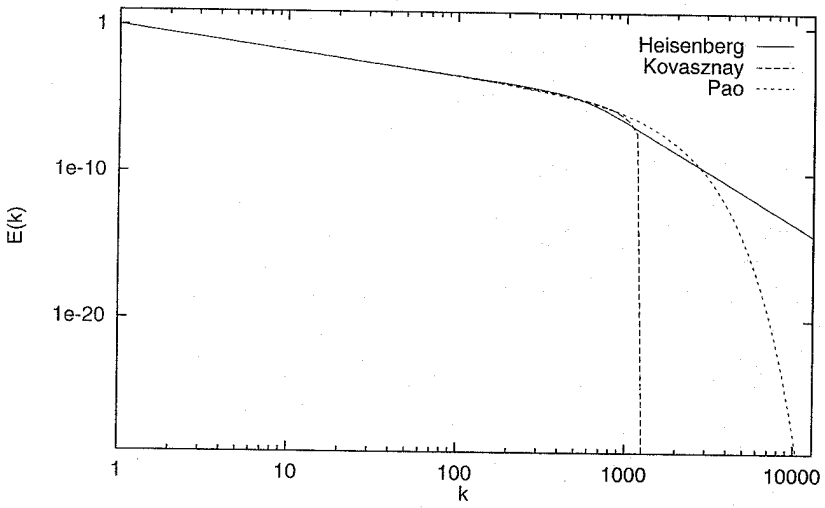

Fig. 4.13. Graph of Heisenberg–Chandrasekhar, Kovasznay, and Pao spectra, for $k_d = 1000$.

– For the Kovazsnay spectrum:

$$\frac{\langle \varepsilon_r \rangle}{\langle \varepsilon \rangle} = 1 - \left(1 - \frac{K_0}{2}\kappa_c^{4/3}\right)^3 \quad , \tag{4.78}$$

or:

$$\langle \nu_{sgs} \rangle = \nu \left\{ \left[1 - \left(1 - \frac{K_0}{2}\kappa_c^{4/3}\right)^3 \right]^{-1} - 1 \right\} \quad . \tag{4.79}$$

– For the Pao spectrum:

$$\frac{\langle \varepsilon_r \rangle}{\langle \varepsilon \rangle} = 1 - \exp\left(\frac{3K_0}{2}\kappa_c^{4/3}\right)^3 \quad , \tag{4.80}$$

or:

$$\langle \nu_{sgs} \rangle = \nu \left\{ \left[1 - \exp\left(\frac{3K_0}{2}\kappa_c^{4/3}\right)^3 \right]^{-1} - 1 \right\} \quad . \tag{4.81}$$

These new estimates of the subgrid viscosity $\langle \nu_{sgs} \rangle$ make it possible to take the viscous effects into account, but requires that the spectrum shape be set *a priori*, as well as the value of the ratio κ_c between the cutoff wave number k_c and the wave number k_d associated with the Kolmogorov scale.

Inclusion of the Local Effects at Cutoff. The subgrid viscosity models in the physical space, such as they have been developed, do not reflect the increase in the coupling intensity with the subgrid modes when we consider modes near the cutoff. These models are therefore analogous to that of constant effective viscosity. To bring out these effects in the proximity of the cutoff, Chollet [59], Ferziger [98], Lesieur and Métais [190], Deschamps [80], Borue and Orszag [29–32], Winckelmans *et al.* [347] and Layton [181] propose introducing high-order dissipation terms that will have a strong effect on the high frequencies of the resolved field without affecting the low frequencies.

Chollet [59], when pointing out that the energy transfer term T^e_{sgs} can be written in the general form

$$T^e_{sgs}(k|k_c) = -2\nu_e^{(n)}(k|k_c)k^{2n}E(k) \quad , \tag{4.82}$$

in which $\nu_e^{(n)}(k|k_c)$ is a hyper-viscosity, proposes modeling the subgrid term in the physical space as the sum of an ordinary subgrid viscosity model and a sixth-order dissipation. This new model is expressed:

$$\nabla \cdot \tau = -\langle \nu_{sgs} \rangle \left(C_1 \nabla^2 + C_2 \nabla^6 \right) \overline{\mathbf{u}} \quad , \tag{4.83}$$

in which C_1 and C_2 are constants. Ferziger proposes introducing a fourth-order dissipation by adding to the subgrid tensor τ the tensor $\tau^{(4)}$, defined as:

$$\tau_{ij}^{(4)} = \frac{\partial}{\partial x_j}\left(\nu_{sgs}^{(4)}\frac{\partial^2 \overline{u}_i}{\partial x_k \partial x_k}\right) + \frac{\partial}{\partial x_i}\left(\nu_{sgs}^{(4)}\frac{\partial^2 \overline{u}_j}{\partial x_k \partial x_k}\right) \quad , \tag{4.84}$$

or as

$$\tau_{ij}^{(4)} = \frac{\partial^2}{\partial x_k \partial x_k}\left(\nu_{sgs}^{(4)}\left(\frac{\partial \overline{u}_i}{\partial x_j} + \frac{\partial \overline{u}_j}{\partial x_i}\right)\right) \quad , \tag{4.85}$$

in which the hyper-viscosity $\nu_{sgs}^{(4)}$ is defined by dimensional arguments as

$$\nu_{sgs}^{(4)} = C_m \overline{\Delta}^4 |\overline{S}| \quad . \tag{4.86}$$

The full subgrid term that appears in the momentum equations is then written:

$$\tau_{ij} = \tau_{ij}^{(2)} + \tau_{ij}^{(4)} \quad , \tag{4.87}$$

in which $\tau_{ij}^{(2)}$ is a subgrid viscosity model described above. A similar form is proposed by Lesieur and Métais: after defining the velocity field $\mathbf{u}^\diamond$ as

$$\mathbf{u}^\diamond = \nabla^{2p}\overline{\mathbf{u}} \quad , \tag{4.88}$$

the two authors propose the composite form:

$$\tau_{ij} = -\nu_{sgs}\overline{S}_{ij} + (-1)^{p+1}\nu_{sgs}^\diamond S_{ij}^\diamond \quad , \tag{4.89}$$

in which $\nu^{\diamond}_{\text{sgs}}$ hyper-viscosity obtained by applying a subgrid viscosity model to the $\mathbf{u}^{\diamond}$ field, and $S^{\diamond}$ the strain rate tensor computed from this same field. The constant of the subgrid model used should be modified to verify the local equilibrium relation, which is

$$\langle -\tau_{ij}\overline{S}_{ij}\rangle = \langle \varepsilon \rangle \quad .$$

It is worth noting that subgrid dissipations defined thusly, as the sum of second- and fourth-order dissipations, are similar in form to certain numerical schemes designed for capturing strong gradients, like that of Jameson *et al.* [150].

Borue and Orszag [29–32] propose to eliminate the molecular and the subgrid viscosities by replacing them by a higher power of the Laplacian operator. Numerical tests show that three-dimensional inertial-range dynamics is relatively independent of the form of the hyperviscosity. It was also shown that for a given numerical resolution, hyperviscous dissipations increase the extent of the inertial range of three-dimensional turbulence by an order of magnitude. It is worth noting that this type of iterated Laplacian is commonly used for two-dimensional simulations. Borue and Orszag used a height-time iterated Laplacian to get these conclusions. Such operators are easily defined when using spectral methods, but are of poor interest when dealing with finite difference of finite volume techniques.

Subgrid-Viscosity Models. Various subgrid viscosity models belonging to the three categories defined above will now be described. These are the following:

1. The Smagorinsky model (p.95), which is based on the resolved scales. This model, though very simple to implant, suffers from the defects already mentioned for the models based on the large scales.
2. The Structure Function model (p.95), which is an extension into physical space of the models based on the energy at cutoff. Theoretically based on local frequency information, this model should be capable of treating large-scale intermittency better than the Smagorinsky model. However, the impossibility of localizing the information in both space and frequency (see discussion further on) reduces its efficiency.
3. A model based on the kinetic energy of the subgrid modes (p.97). This energy is considered as an additional variable of the problem, and is evaluated by solving a evolution equation. Since it contains information relative to the subgrid scales, it is theoretically more capable of handling large-scale intermittency than the previous model. Moreover, the local equilibrium hypothesis can be relaxed, so that the spectral nonequilibrium can be integrated better. The model requires additional hypotheses, though (modeling, boundary conditions).
4. The Yoshizawa model (p.98), which includes an additional evolution equation for a quantity linked to a characteristic subg scale, by which it can be classed among models based on the subgrid scales. It has the same advantages and disadvantages as the previous model.
5. The Mixed Scale Model (p.99), which uses information related both to the subgrid modes and to the resolved scales, though without incorporating additional evolution equations. The subgrid scale data is deduced from that contained in the resolved scales by extrapolation in the frequency domain. This model is of intermediate level of complexity (and quality) between those based on the large scales and those that use additional variables.

Smagorinsky Model. The Smagorinsky model [312] is based on the large scales. It is generally used in a local form the physical space, *i.e.* variable in space, in order to be more adaptable to the flow being calculated. It is obtained by space and time localization of the statistical relations given in the previous section. There is no particular justification for this local use of relations that are on average true for the whole, since they only ensure that the energy transfers through the cutoff are expressed correctly on the average, and not locally.

This model is expressed:

$$\nu_{\text{sgs}}(\mathbf{x},t) = \left(C_{\text{s}}\overline{\Delta}\right)^2 \left(2|\overline{S}(\mathbf{x},t)|^2\right)^{1/2} \quad . \tag{4.90}$$

The constant theoretical value C_{s} is evaluated by the relations (4.45) or (4.48). It should nonetheless be noted that the value of this constant is, in practice, adjusted to improve the results. Clark *et al.* [65] use $C_{\text{s}} = 0.2$ for a case of isotropic homogeneous turbulence, while Deardorff [76] uses $C_{\text{s}} = 0.1$ for a plane channel flow. Studies of shear flows using experimental data yield similar evaluations ($C_{\text{s}} \simeq 0.1 - 0.12$) [225, 258]. This decrease in the value of the constant with respect to its theoretical value is due to the fact that the field gradient is now non-zero and that it contributes to the $|\overline{S}(\mathbf{x},t)|$ term. To enforce the local equilibrium relation, the value of the constant has to be reduced. It should be noted that this new value ensures only that the right quantity of resolved kinetic energy will be dissipated on the whole throughout the field, but that the quality of the level of local dissipation is uncontrolled.

Structure Function Model. This model is a transposition of Métais and Lesieur's constant effective viscosity model into the physical space, and can consequently be interpreted as a model based on the energy at cutoff, expressed in physical space. The authors [235] propose evaluating the energy at cutoff $E(k_{\text{c}})$ by means of the second-order velocity structure function. This is defined as:

$$F_2(\mathbf{x},r,t) = \int_{|\mathbf{x}'|=r} \left[\mathbf{u}(\mathbf{x},t) - \mathbf{u}(\mathbf{x}+\mathbf{x}',t)\right]^2 d^3\mathbf{x}' \quad . \tag{4.91}$$

In the case of isotropic homogeneous turbulence, we have the relation:

$$F_2(r,t) = \int F_2(\mathbf{x},r,t)d^3\mathbf{x} = 4\int_0^\infty E(k,t)\left(1-\frac{\sin(kr)}{kr}\right)dk \quad . \tag{4.92}$$

Using a Kolmogorov spectrum, the calculation of (4.92) leads to:

$$F_2(r,t) = \frac{9}{5}\Gamma(1/3)K_0\varepsilon^{2/3}r^{2/3} \quad , \tag{4.93}$$

or, expressing the dissipation ε, as a function of $F_2(r,t)$ in the expression for the Kolmogorov spectrum:

$$E(k) = \frac{5}{9\Gamma(1/3)}F_2(r,t)r^{-2/3}k^{-5/3} \quad . \tag{4.94}$$

To derive a subgrid model, we now have to evaluate the second-order structure function from the resolved scales alone. To do this, we decompose by:

$$F_2(r,t) = \overline{F}_2(r,t) + C_0(r,t) \quad , \tag{4.95}$$

in which $\overline{F}_2(r,t)$ is computed from the resolved scales and $C_0(r,t)$ corresponds to the contribution of the subgrid scales:

$$C_0(r,t) = 4\int_{k_c}^\infty E(k,t)\left(1-\frac{\sin(kr)}{kr}\right)dk \quad . \tag{4.96}$$

By replacing the quantity $E(k,t)$ in equation (4.96) by its value (4.94), we get:

$$C_0(r,t) = F_2(r,t)\left(\frac{r}{\overline{\Delta}}\right)^{-2/3} H_{sf}(r/\overline{\Delta}) \quad , \tag{4.97}$$

in which $H_{\rm sf}$ is the function

$$H_{\rm sf}(x) = \frac{20}{9\Gamma(1/3)}\left[\frac{3}{2\pi^{2/3}} + x^{2/3}\mathrm{Im}\left\{\exp(i5\pi/6)\Gamma(-5/3,i\pi x)\right\}\right] \quad . \tag{4.98}$$

Once it is substituted in (4.95), this equation makes it possible to evaluate the energy at the cutoff. The Structure Function model takes the form:

$$\langle\nu_{\rm sgs}(r)\rangle = A(r/\overline{\Delta})\overline{\Delta}\sqrt{\overline{F}_2(r,t)} \quad , \tag{4.99}$$

in which

$$A(x) = \frac{2K_0^{-3/2}}{3\pi^{4/3}\sqrt{(9/5)\Gamma(1/3)}}x^{-4/3}\left(1-x^{-2/3}H_{\rm sf}(x)\right)^{-1/2} \quad . \tag{4.100}$$

In the same way as for the Smagorinsky model, a local model in space can be had by using relation (4.94) locally in order to include the local intermittency of the turbulence. The model is then written:

$$\nu_{\rm sgs}(\mathbf{x},r) = A(r/\overline{\Delta})\overline{\Delta}\sqrt{\overline{F}_2(\mathbf{x},r,t)} \quad . \tag{4.101}$$

In the case where $r = \overline{\Delta}$, the model takes the simplified form:

$$\nu_{\rm sgs}(\mathbf{x},\overline{\Delta},t) = 0.105\overline{\Delta}\sqrt{\overline{F}_2(\mathbf{x},\overline{\Delta},t)} \quad . \tag{4.102}$$

A link can be established with the models based on the resolved scale gradients by noting that:

$$\mathbf{u}(\mathbf{x},t) - \mathbf{u}(\mathbf{x}+\mathbf{x}',t) = -\mathbf{x}'\cdot\nabla\mathbf{u}(\mathbf{x},t) + O(|\mathbf{x}'|^2) \quad . \tag{4.103}$$

This last relation shows that the function $\overline{F}_2$ is homogeneous to a norm of the resolved velocity field gradient. If this function is evaluated in the simulation in a way similar to how the resolved strain rate tensor is computed for the Smagorinsky model, we can in theory expect the Structure Function model to suffer some of the same weaknesses: the information contained in the model will be local in space, therefore non-local in frequency, which induces a poor estimation of the kinetic energy at cutoff and a loss of precision of the model in the treatment of large-scale intermittency and spectral nonequilibrium.

Model Based on the Subgrid Kinetic Energy. One model, of the form (4.61), based on the subgrid scales, was developed independently by a number of authors [137,242,298,318,361,362]. The subgrid viscosity is computed from the kinetic energy of the subgrid modes $q^2_{\rm sgs}$:

$$\nu_{\rm sgs}(\mathbf{x},t) = C_{\rm m}\overline{\Delta}\sqrt{q^2_{\rm sgs}(\mathbf{x},t)} \quad , \tag{4.104}$$

where, for reference:

$$q^2_{\rm sgs}(\mathbf{x},t) = \frac{1}{2}\overline{(u_i(\mathbf{x},t)-\overline{u}_i(\mathbf{x},t))^2} \quad . \tag{4.105}$$

The constant $C_{\rm m}$ is evaluated by the relation (4.61). This energy constitutes another variable of the problem and is evaluated by solving an evolution equation. This equation is obtained from the exact evolution equation (3.31), whose unknown terms are modeled according to Lilly's proposals [194], or by a re-normalization method. The various terms are modeled as follows (refer to the work of McComb [207], for example):

- The diffusion term is modeled by a gradient hypothesis, by stating that the non-linear term is proportional to the kinetic energy $q^2_{\rm sgs}$ gradient (Kolmogorov-Prandtl relation):

$$\frac{\partial}{\partial x_j}\left(\frac{1}{2}\overline{u_i'u_i'u_j'} + \overline{u_j'p}\right) = C_2\frac{\partial}{\partial x_j}\left(\overline{\Delta}\sqrt{q^2_{\rm sgs}}\frac{\partial q^2_{\rm sgs}}{\partial x_j}\right) \quad . \tag{4.106}$$

– The dissipation term is modeled using dimensional reasoning, by:

$$\varepsilon = \frac{\nu}{2}\overline{\frac{\partial u_i'}{\partial x_j}\frac{\partial u_i'}{\partial x_j}} = C_1\frac{(q_{\rm sgs}^2)^{3/2}}{\overline{\Delta}} \quad . \tag{4.107}$$

The resulting evolution equation is:

$$\frac{\partial q_{\rm sgs}^2}{\partial t} + \underbrace{\frac{\partial \overline{u}_j q_{\rm sgs}^2}{\partial x_j}}_{I} = \underbrace{-\tau_{ij}\overline{S}_{ij}}_{II} - \underbrace{C_1\frac{q_{\rm sgs}^{2\ 3/2}}{\overline{\Delta}}}_{III} + \underbrace{C_2\frac{\partial}{\partial x_j}\left(\overline{\Delta}\sqrt{q_{\rm sgs}^2}\frac{\partial q_{\rm sgs}^2}{\partial x_j}\right)}_{IV} + \underbrace{\nu\frac{\partial^2 q_{\rm sgs}^2}{\partial x_j \partial x_j}}_{V} \quad , \tag{4.108}$$

in which C_1 and C_2 are two positive constants and the various terms represent:

– I - advection by the resolved modes,
– II - production by the resolved modes,
– III - turbulent dissipation,
– IV - turbulent diffusion,
– V - viscous dissipation.

Using an analytical theory of turbulence, Yoshizawa [361, 362] and Horiuti [137] propose $C_1 = 1$ and $C_2 = 0.1$.

Yoshizawa Model. The filter cutoff length, $\overline{\Delta}$, is the only length scale used in deriving models based on the large scales, as this derivation has been explained above. The characteristic length associated with the subgrid scales, denoted $\Delta_{\rm f}$, is assumed to be proportional to this length, and the developments of Sect. 4.3.2 show that:

$$\Delta_{\rm f} = C_{\rm s}\overline{\Delta} \quad . \tag{4.109}$$

The variations in the structure of the subgrid modes cannot be included by setting a constant value for the coefficient $C_{\rm s}$, as is done in the case of the Smagorinsky model, for example. To remedy this, Yoshizawa [358, 360] proposes differentiating these two characteristic scales and introducing an additional evolution equation to evaluate $\Delta_{\rm f}$. This length can be evaluated from the dissipation ε and the subgrid kinetic energy $q_{\rm sgs}^2$ by the relation:

$$\Delta_{\rm f} = C_1\frac{(q_{\rm sgs}^2)^{3/2}}{\varepsilon} + C_2\frac{(q_{\rm sgs}^2)^{3/2}}{\varepsilon^2}\frac{Dq_{\rm sgs}^2}{Dt} - C_3\frac{(q_{\rm sgs}^2)^{5/2}}{\varepsilon^3}\frac{D\varepsilon}{Dt} \quad , \tag{4.110}$$

in which D/Dt is the material derivative associated with the resolved velocity field. The values of the constants appearing in equation (4.110) can be determined by an analysis conducted with the TSDIA technique [360] : $C_1 = 1.84$, $C_2 = 4.95$ et $C_3 = 2.91$. We now express the proportionality relation between the two lengths as:

$$\Delta_{\rm f} = (1 + r(\mathbf{x}, t))\overline{\Delta} \quad . \tag{4.111}$$

By evaluating the subgrid kinetic energy as:

$$q_{\rm sgs}^2 = \left(\overline{\Delta}\varepsilon/C_1\right)^{2/3} \quad , \tag{4.112}$$

relations (4.110) and (4.111) lead to:

$$r = C_4\overline{\Delta}^{2/3}\varepsilon^{-4/3}\frac{D\varepsilon}{Dt} \quad , \tag{4.113}$$

with $C_4 = 0.04$. Using the local equilibrium hypothesis, we get:

$$\varepsilon = -\tau_{ij}\overline{S}_{ij} \simeq C_5\Delta_{\rm f}^2|\overline{S}|^3 \quad , \tag{4.114}$$

in which $C_5 = 6.52.10^{-3}$. This definition completes the calculation of the factor r and the length $\Delta_{\rm f}$. This variation of the characteristic length $\Delta_{\rm f}$ can be re-interpreted as a variation of the constant in the Smagorinsky model:

$$C_{\rm s} = C_{\rm s0}\left(1 - C_{\rm a}|\overline{S}|^{-2}\frac{D|\overline{S}|}{Dt} + C_{\rm b}\overline{\Delta}^2|\overline{S}|^{-2}\frac{\partial}{\partial x_j}\left(|\overline{S}|^{-2}\frac{\partial|\overline{S}|}{\partial x_j}\right)\right) \quad . \tag{4.115}$$

The constants $C_{\rm s0}$, $C_{\rm a}$ and $C_{\rm b}$ are evaluated at 0.16, 1.8, and 0.047, respectively, by Yoshizawa [360] and Murakami [253]. In practice, $C_{\rm b}$ is taken to be equal to zero and the constant $C_{\rm s}$ is bounded in order to ensure the stability of the simulation: $0.1 \leq C_{\rm s} \leq 0.27$. Morinishi and Kobayashi [247] recommend using the values $C_{\rm a} = 32$ and $C_{\rm s0} = 0.1$.

Mixed Scale Model. Ta Phuoc Loc and Sagaut [284, 285] defined models having a triple dependency on the large and small structures of the resolved field as a function of the cutoff length. These models, which make up the one-parameter Mixed Scale Model family, are derived by taking a weighted geometric average of the models based on the large scales and those based on the energy at cutoff:

$$\nu_{\rm sgs}(\alpha)(\mathbf{x}, t) = C_{\rm m}\left|\mathcal{F}(\overline{\mathbf{u}}(\mathbf{x}, t))\right|^{\alpha}\left(q_{\rm c}^2\right)^{\frac{1-\alpha}{2}}(\mathbf{x}, t)\ \overline{\Delta}^{1+\alpha} \quad , \tag{4.116}$$

with

$$\mathcal{F}(\overline{\mathbf{u}}(\mathbf{x}, t)) = \overline{S}(\mathbf{x}, t) \text{ or } \nabla \times \overline{\mathbf{u}}(\mathbf{x}, t) \quad . \tag{4.117}$$

It should be noted that localized versions of the models are used here, so that any flows that do not verify the spatial homogeneity property can be

processed better. The kinetic energy q_c^2 is evaluated in the physical space by the formula:

$$q_c^2(\mathbf{x},t) = \frac{1}{2}(\overline{u}_i(\mathbf{x},t))'\,(\overline{u}_i(\mathbf{x},t))' \quad . \tag{4.118}$$

The *test field* $(\overline{\mathbf{u}})'$ represents the high-frequency part of the resolved velocity field, defined using a second filter, referred to as the *test filter*, designated by the *tilde* symbol and associated with the cutoff length $\widetilde{\overline{\Delta}} > \overline{\Delta}$ (see Fig. 4.14):

$$(\overline{\mathbf{u}})' = \overline{\mathbf{u}} - \widetilde{\overline{\mathbf{u}}} \quad . \tag{4.119}$$

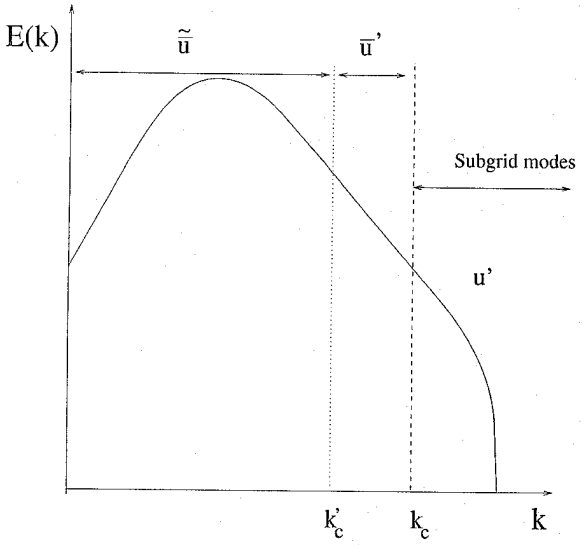

Fig. 4.14. Spectral subdivisions for double sharp-cutoff filtering. $\widetilde{\overline{u}}$ is the resolved field in the sense of the test filter, $(\overline{u})'$ the test field, and u' the unresolved scales in the sense of the initial filter.

The resulting model can be interpreted in two ways:

- As a model based on the kinetic energy of the subgrid scales, *i.e.* the second form of the models based on the subgrid scales in Sect. 4.3.2, if we use Bardina's hypothesis of scale similarity (described in Chap. 6), which allows us to set:

$$q_c^2 \simeq q_{sgs}^2 \quad , \tag{4.120}$$

in which q_{sgs}^2 is the kinetic energy of the subgrid scales. This assumption can be refined in the framework of the canonical analysis. Assuming that the two cutoffs occur in the inertial range of the spectrum, we get:

$$q_c^2 = \int_{k_c'}^{k_c} E(k)dk = \frac{3}{2}K_0\varepsilon^{2/3}\left(k_c'^{-2/3} - k_c^{-2/3}\right) \quad , \tag{4.121}$$

in which k_c and k_c' are wave numbers associated with $\overline{\Delta}$ and $\widetilde{\overline{\Delta}}$, respectively. We then define the relation:

$$q_c^2 = \beta q_{sgs}^2, \quad \beta = \left[\left(\frac{k_c'}{k_c}\right)^{-2/3} - 1\right] \quad . \tag{4.122}$$

It can be seen that the approximation is exact if $\beta = 1$, *i.e.* if:

$$k_c' = \frac{1}{\sqrt{8}}k_c \quad . \tag{4.123}$$

This approximation is also used by Bardina *et al.* [13] and Yoshizawa *et al.* [363] to derive models based on the subgrid kinetic energy without using any additional transport equation.

- As a model based on the energy at cutoff, and therefore as a generalization of the spectral model of constant effective viscosity into the physical space. That is, using the same assumptions as before, we get:

$$q_c^2 = \frac{3}{2}\beta k_c E(k_c) \quad . \tag{4.124}$$

Here, the approximation is exact if $k_c' = k_c/\sqrt{8}$.

It is important to note that the Mixed Scale Model makes no use of any commutation property between the test filter and the derivation operators. Also, we note that for $\alpha \in [0,1]$ the subgrid viscosity $\nu_{sgs}(\alpha)$ is always defined, whereas the model appears in the form of a quotient for other values of α can then raise problems of numerical stability once it is discretized, because the denominator may cancel out.

The model constant can be evaluated theoretically by analytical theories of turbulence in the canonical case. Resuming the results of Sect. 4.3.2, we get:

$$C_m = C_q^{1-\alpha} C_s^{2\alpha} \quad , \tag{4.125}$$

in which $C_s \sim 0.18$ or $C_s \sim 0.148$ and $C_q \sim 0.20$.

4.3.3 Improvement of Models in the Physical Space

Statement of the Problem. Experience shows that the various models yield good results when they are applied to homogeneous turbulent flows and that the cutoff is placed sufficiently far into the inertial range of the spectrum, *i.e.* when a large part of the total kinetic energy is contained in the resolved scales[15].

In other cases, as in transitional flows, highly anisotropic flows, highly under-resolved flows, or those in high energetic disequilibrium, the subgrid models behave much less satisfactorily. Aside from the problem stemming from numerical errors, there are mainly two reasons for this:

1. The characteristics of these flows does not correspond to the hypotheses on which the models are derived, which means that the models are at fault. We then have two possibilities: deriving models from new physical hypotheses or adjusting existing ones, more or less empirically. The first choice is theoretically more exact, but there is a lack of descriptions of turbulence for frameworks other than that of isotropic homogeneous turbulence. Still, a few attempts have been made to consider the anisotropy appearing in this category. These are discussed in Chap. 5. The other solution, if the physics of the models is put to fault, consists in reducing their importance, *i.e.* increasing the cutoff frequency to capture a larger part of the flow physics directly. This means increasing the number of degrees of freedom and striking a compromise between the grid enrichment techniques and subgrid modeling efforts.
2. Deriving models based on the energy at cutoff or the subgrid scales (with no additional evolution equation) for simulations in the physical space runs up against Gabor-Heisenberg's generalized principle of uncertainty [91, 285], which stipulates that the precision of the information cannot be improved in space and in frequency at the same time. This is illustrated by Fig. 4.15. Very good frequency localization implies high non-localization in space, which reduces the possibilities of taking the intermittency[16] into account and precludes the treatment of highly inhomogeneous flows. Inversely, very good localization of the information in space prevents any good spectral resolution, which leads to high errors, e.g. in computing the energy at the cutoff. Yet this frequency localization is very important, since it alone can be used to detect the presence of the subgrid scales. It is important to recall here that large-eddy simulation is based on a selection in frequency of modes making up the exact solution. Problems arise here, induced by the localization of statistical average relations that are exact, as this localization may correspond to a statistical average. Two solutions may be considered: developing an acceptable compromise between the precision in space and frequency, or enriching the information contained in the simulation, which is done either by adding variables to it as in the case of models based on the kinetic energy of the subgrid modes, or by assuming further hypotheses when deriving models.

[15] Certain authors estimate this share to be between 80 % and 90 % [53]. Another criterion sometimes mentioned is that the cutoff scale should be of the order of Taylor's microscale. Bagget *et al.* [10] propose to define the cutoff length in such a way that the subgrid scales will be quasi-isotropic, leading to $\overline{\Delta} \approx L_\varepsilon/10$, where L_ε is the integral dissipation length.

[16] Direct numerical simulations and experimental data show that the true subgrid dissipation and its surrogates do not have the same scaling s [52, 232].

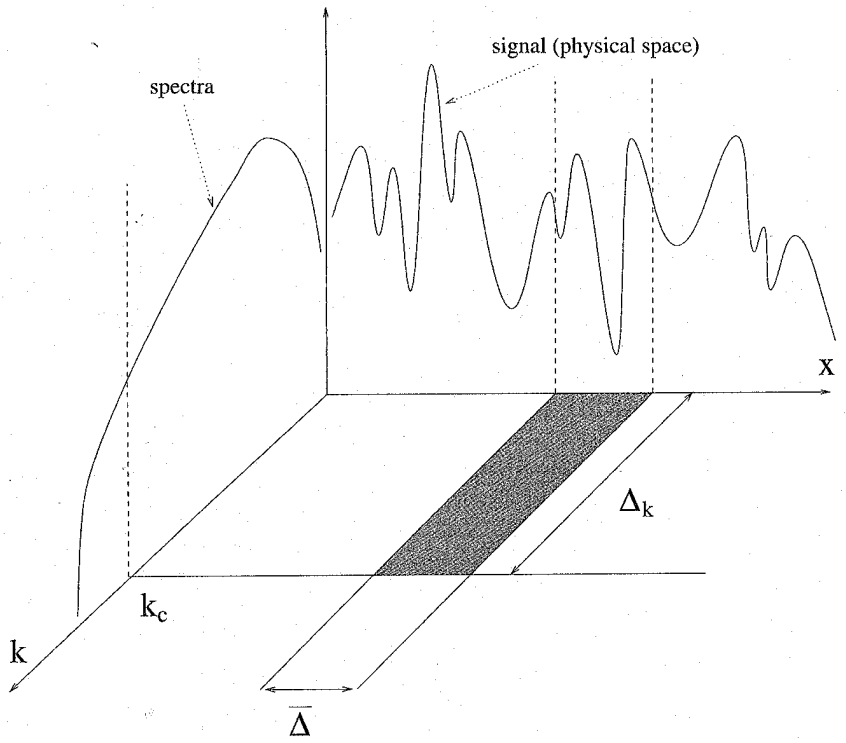

Fig. 4.15. Representation of the resolution in the space-frequency plane. The spat ial resolution $\overline{\Delta}$ is associated with frequency resolution Δ_k. Gabor-Heisenberg's uncertainty principle stipulates that the product $\overline{\Delta} \times \Delta_k$ remains constant, *i.e.* that the area of the gray domain keeps the same value (from [91], with the permission of F. Ducros).

In the following, we present techniques developed to improve the simulation results, though without modifying the structure of the subgrid models deeply. The purpose of all these modifications is to adapt the subgrid model

better to the local state of the flow and remedy the lack of frequency localization of the information.

We will be describing:

1. Dynamic procedures for computing subgrid model constants (p.105). These constants are computed in such a way as to reduce an a priori estimate of the error committed with the model considered, locally in space and time, in the least squares sense. This estimation is made using the Germano identity, and requires the use of an analytical filter. It should be noted that the dynamic procedures do not change the model in the sense that its form (e.g. subgrid viscosity) remains the same. All that is done here is to minimize a norm of the error associated with the form of the model considered. The errors committed intrinsically[17] by adopting an a priori form of the subgrid tensor are not modified. These procedures, while theoretically very attractive, do pose problems of numerical stability and can induce non-negligible extra computational costs. This variation of the constant at each point and each time step makes it possible to minimize the error locally for each degree of freedom, while determining a constant value offers only the less efficient possibility of an overall minimization. This is illustrated by the above discussion of the constant in the Smagorinsky model.
2. Structural sensors (p.118), which condition the existence of the subgrid scales to the verification of certain constraints by the highest frequencies of the resolved scales. More precisely, we consider here that the subgrid scales exist if the highest resolved frequencies verify topological properties that are expected in the case of isotropic homogeneous turbulence. When these criteria are verified, we adopt the hypothesis that the highest resolved frequencies have a dynamics close to that of the scales contained in the inertial range. On the basis of energy spectrum continuity (see the note of page p.83), we then deduce that unresolved scales exist, and the subgrid model is then used, but is otherwise canceled.
3. The accentuation technique (p.120), which consists in artificially increasing the contribution of the highest resolved frequencies when evaluating the subgrid viscosity. This technique allows a better frequency localization of the information included in the model, and therefore a better treatment of the intermittence phenomena, as the model is sensitive only to the higher resolved frequencies. This result is obtained by applying a frequency high-pass filter to the resolved field.
4. The damping functions for the near-wall region (p.123), by which certain modifications in the turbulence dynamics and characteristic scales of the subgrid modes in the boundary layers can be taken into account. These functions are established in such a way as to cancel the subgrid viscosity models in the near-wall region so that they will not inhibit the driving mechanisms occurring in this area. These models are of limited generality as they presuppose a particular form of the flow dynamics in the region considered. They also require that the relative position of each point with respect to the solid wall be known, which can raise problems in practice such as when using multidomain techniques or when several surfaces exist. And lastly, they constitute only an amplitude correction of the subgrid viscosity models for the forward energy cascade: they are not able to include any changes in the form of this mechanism, or the emergence of new mechanisms.

[17] For example, the subgrid viscosity models described above all induce a linear dependency between the subgrid tensor and the resolved-scale tensor:

$$\tau_{ij}^{\mathrm{d}} = -\nu_{\mathrm{sgs}} \overline{S}_{ij} \quad .$$

The three "generalist" techniques (dynamic procedure, structural sensor, accentuation) for adapting the subgrid viscosity models are all based on extracting a test field from the resolved scales by applying a test filter to these scales. This field corresponds to the highest frequencies catured by the simulation, so we can see that all these techniques are based on a frequency localization of the information contained in the subgrid models. The loss of localness in space is reflected by the fact that the number of neighbors involved in the subgrid model computation is increased by using the test filter.

Dynamic Procedures for Computing the Constants. Dynamic Models

Germano–Lilly Dynamic Procedure. In order to adapt the models better to the local structure of the flow, Germano *et al.* [118] proposed an algorithm for adapting the Smagorinsky model by automatically adjusting the constant at each point in space and at each time step. This procedure, described below, is applicable to any model that makes explicit use of an arbitrary constant C_{d}, such that the constant now becomes time- and space-dependent: C_{d} becomes $C_{\mathrm{d}}(\mathbf{x}, t)$.

The dynamic procedure is based on the Germano identity (3.78), now written in the form:

$$L_{ij} = T_{ij} - \tilde{\tau}_{ij} \quad , \tag{4.126}$$

in which

$$\tau_{ij} \equiv L_{ij} + C_{ij} + R_{ij} = \widetilde{\overline{u_i u_j}} - \widetilde{\overline{u}_i}\,\widetilde{\overline{u}_j} \quad , \tag{4.127}$$

$$T_{ij} \equiv \widetilde{\overline{u_i u_j}} - \widetilde{\overline{u}_i}\,\widetilde{\overline{u}_j} \quad , \tag{4.128}$$

$$L_{ij} \equiv \widetilde{\overline{u_i}\,\overline{u_j}} - \widetilde{\overline{u}_i}\,\widetilde{\overline{u}_j} \quad , \tag{4.129}$$

in which the tilde symbol *tilde* designates the test filter. The tensors τ and T are the subgrid tensors corresponding, respectively, to the first and second

filtering levels. The latter filtering level is associated with the characteristic length $\widetilde{\overline{\Delta}}$, with $\widetilde{\overline{\Delta}} > \overline{\Delta}$. Numerical tests show that an optimal value is $\widetilde{\overline{\Delta}} = 2\overline{\Delta}$. The tensor L can be computed directly from the resolved field.

We then assume that the two subgrid tensors τ and T can be modeled by the same constant C_d for both filtering levels. Formally, this is expressed:

$$\tau_{ij} - \frac{1}{3}\tau_{kk}\delta_{ij} = C_\mathrm{d}\beta_{ij} \quad , \tag{4.130}$$

$$T_{ij} - \frac{1}{3}T_{kk}\delta_{ij} = C_\mathrm{d}\alpha_{ij} \quad , \tag{4.131}$$

in which the tensors α and β designate the deviators of the subgrid tensors obtained using the subgrid model deprived of its constant. It is important noting that the use of the same subgrid model with the same constant is equivalent to a scale-invariance assumption on both the subgrid fluxes and the filter, to be discussed in the following.

Some examples of subgrid model kernels for α_{ij} and β_{ij} are given in Table 4.1.

Table 4.1. Examples of subgrid model kernels for the dynamic procedure.

Model	β_{ij}	α_{ij}
(4.90)	$-2\overline{\Delta}^2\lvert\overline{S}\rvert\overline{S}_{ij}$	$-2\widetilde{\overline{\Delta}}^2\lvert\widetilde{\overline{S}}\rvert\widetilde{\overline{S}}_{ij}$
(4.102)	$-2\overline{\Delta}\sqrt{\overline{F}(\overline{\Delta})}\overline{S}_{ij}$	$-2\widetilde{\overline{\Delta}}\sqrt{\widetilde{\overline{F}}(\widetilde{\overline{\Delta}})}\widetilde{\overline{S}}_{ij}$
(4.116)	$-2\overline{\Delta}^{1+\alpha}\lvert\mathcal{F}(\overline{\mathbf{u}})\rvert^\alpha(q_c^2)^{\frac{1-\alpha}{2}}\overline{S}_{ij}$	$-2\widetilde{\overline{\Delta}}^{1+\alpha}\lvert\mathcal{F}(\widetilde{\overline{\mathbf{u}}})\rvert^\alpha(\tilde{q}_c^2)^{\frac{1-\alpha}{2}}\widetilde{\overline{S}}_{ij}$

Introducing the above two formulas in the relation (4.126), we get[18]:

$$L_{ij} - \frac{1}{3}L_{kk}\delta_{ij} \equiv L_{ij}^\mathrm{d} = C_\mathrm{d}\alpha_{ij} - \widetilde{C_\mathrm{d}\beta_{ij}} \quad . \tag{4.132}$$

We cannot use this equation directly for determining the constant C_d because the second term uses the constant only through a filtered product [281]. In order to continue modeling, we need to make the approximation:

$$\widetilde{C_\mathrm{d}\beta_{ij}} = C_\mathrm{d}\widetilde{\beta}_{ij} \quad , \tag{4.133}$$

which is equivalent to considering that C_d is constant over an interval at least equal to the test filter cutoff length. The parameter C_d will thus be computed

[18] It is important to note that, for the present case, the tensor L_{ij} is replaced by its deviatoric part L_{ij}^d, because we are dealing with a zero-trace subgrid viscosity modeling.

in such a way as to minimize the error committed[19], which is evaluated using the residual E_{ij}:

$$E_{ij} = L_{ij} - \frac{1}{3}L_{kk}\delta_{ij} - C_\mathrm{d}\alpha_{ij} + C_\mathrm{d}\widetilde{\beta}_{ij} \quad . \tag{4.134}$$

This definition consists of six independent relations, which in theory makes it possible to determine six values of the constant[20]. In order to conserve a single relation and thereby determine a single value of the constant, Germano *et al.* propose contracting the relation (4.134) with the resolved strain rate tensor. The value sought for the constant is a solution of the problem:

$$\frac{\partial E_{ij}\overline{S}_{ij}}{\partial C_\mathrm{d}} = 0 \quad . \tag{4.135}$$

This method can be efficient, but does raise the problem of indetermination when the tensor $\overline{S}_{ij}$ cancels out. To remedy this problem, Lilly [195] proposes calculating the constant C_d by a least-squares method, by which the constant C_d now becomes a solution of the problem:

$$\frac{\partial E_{ij}E_{ij}}{\partial C_\mathrm{d}} = 0 \quad , \tag{4.136}$$

or

$$C_\mathrm{d} = \frac{m_{ij}L_{ij}^\mathrm{d}}{m_{kl}m_{kl}} \quad , \tag{4.137}$$

in which

$$m_{ij} = \alpha_{ij} - \widetilde{\beta}_{ij} \quad . \tag{4.138}$$

The constant C_d thus computed has the following properties:

- It can take negative values, so the model can have an anti-dissipative effect locally. This is a characteristic that is often interpreted as a modeling of the backward energy cascade mechanism. This point is detailed in Sect. 4.4.
- It is not bounded, since it appears in the form of a fraction whose denominator can cancel out[21].

[19] Meneveau and Katz [227] propose to use the dynamic procedure to rank the subgrid models, the best one being associated with the lowest value of the residual.

[20] Which would lead to the definition of a tensorial subgrid viscosity model.

[21] This problem is linked to the implementation of the model in the simulation. In the continuous case, if the denominator tends toward zero, then the numerator cancels out too. These are calculation errors that lead to a problem of division by zero.

These two properties have important practical consequences on the numerical solution because they are both potentially destructive of the stability of the simulation. Numerical tests have shown that the constant can remain negative over long time intervals, causing an exponential growth in the high frequency fluctuations of the resolved field. The constant therefore needs an ad hoc process to ensure the model's good numerical properties. There are a number of different ways of performing this process on the constant: statistical average in the directions of statistical homogeneity [118, 354], in time or local in space [366]; limitation using arbitrary bounds [366] (clipping); or by a combination of these methods [354, 366]. Let us note that the averaging procedures can be defined in two non-equivalent ways [367]: by averaging the denominator and numerator separately, which is denoted symbolically:

$$C_{\mathrm{d}} = \frac{\langle m_{ij} L_{ij}^{\mathrm{d}} \rangle}{\langle m_{kl} m_{kl} \rangle} \quad , \tag{4.139}$$

or by averaging the quotient, *i.e.* on the constant itself:

$$C_{\mathrm{d}} = \langle C_{\mathrm{d}} \rangle = \langle \frac{m_{ij} L_{ij}^{\mathrm{d}}}{m_{kl} m_{kl}} \rangle \quad . \tag{4.140}$$

The ensemble average can be performed over homogeneous directions of the simulation (if they exist) or over different realizations, *i.e.* over several statistically equivalent simulations carried out in parallel [48, 51].

The time average process is expressed:

$$C_{\mathrm{d}}(\mathbf{x}, (n+1)\Delta t) = a_1 C_{\mathrm{d}}(\mathbf{x}, (n+1)\Delta t) + (1 - a_1) C_{\mathrm{d}}(\mathbf{x}, n\Delta t) \quad , \tag{4.141}$$

in which Δt is the time step used for the simulation and $a_1 \leq 1$ a constant. Lastly, the constant clipping process is intended to ensure that the following two conditions are verified:

$$\nu + \nu_{\mathrm{sgs}} \geq 0 \quad , \tag{4.142}$$

$$C_{\mathrm{d}} \leq C_{\max} \quad . \tag{4.143}$$

The first condition ensures that the total resolved dissipation $\varepsilon = \nu \overline{S}_{ij} \overline{S}_{ij} - \tau_{ij} \overline{S}_{ij}$ remains positive or zero. The second establishes an upper bound. In practice, $C_{\max}$ is of the order of the theoretical value of the Smagorinsky constant, *i.e.* $C_{\max} \simeq (0.2)^2$.

The models in which the constant is computed by this procedure are called "dynamic"because they automatically adapt to the local state of the flow. When the Smagorinsky model is coupled with this procedure, it is habitually called the dynamic model, because this combination was the first to be put to the test and is still the one most extensively used among the dynamic models.

The use of the same value of the constant for the subgrid model at the two filtering levels appearing in equation (4.126) implicitely relies on the two following self-similarity assumptions:

- The two cutoff wave numbers are located in the inertial range of the kinetic energy spectrum;
- The filter kernels associated to the two filtering levels are themselves self-similar.

These two constraints are not automatically satisfied, and the validity of the dynamic procedure for computing the constant requires a careful analysis.

Meneveau and Lund [229] propose an extension of the dynamic procedure for a cutoff located in the viscous range of the spectrum. Writing the constant of the subgrid-scale model C as an explicit function of the filter characteristic length, the Germano–Lilly procedure leads to

$$C(\overline{\Delta}) = C(\widetilde{\overline{\Delta}}) = C_{\mathrm{d}} \quad . \tag{4.144}$$

Let η be the Kolmogorov lengthscale. It was said in the introduction that the flow is fully resolved if $\overline{\Delta} = \eta$. Therefore, the dynamic procedure is consistent if, and only if

$$\lim_{\overline{\Delta} \to \eta} C_{\mathrm{d}} = C(\eta) = 0 \quad . \tag{4.145}$$

Numerical experiments carried out by the two authors show that the Germano–Lilly procedure is not consistent, because it returns the value of the constant associated to the test filter level

$$C_{\mathrm{d}} = C(\widetilde{\overline{\Delta}}) \quad , \tag{4.146}$$

yielding

$$\lim_{\overline{\Delta} \to \eta} C_{\mathrm{d}} = C(r\eta) \neq 0, \quad r = \widetilde{\overline{\Delta}}/\overline{\Delta} \quad . \tag{4.147}$$

Numerical tests also showed that taking the limit $r \to 1$ or computing the two values $C(\overline{\Delta})$ and $C(r\overline{\Delta})$ using least-square-error minimization without assuming them to be equal yield inconsistent or ill-behaved solutions. A solution is to use prior knowledge to compute the dynamic constant. A robust algorithm is obtained by rewriting equation (4.134) as follows:

$$E_{ij} = L_{ij}^{\mathrm{d}} - C(\overline{\Delta}) \left(f(\overline{\Delta}, r) \alpha_{ij} - \widetilde{\beta}_{ij} \right) \quad , \tag{4.148}$$

where $f(\overline{\Delta}, r) = C(r\overline{\Delta})/C(\overline{\Delta})$ is evaluated by calculations similar to those of Voke (see page 89). A simple analytical fitting is obtained in the case $r = 2$:

$$f(\overline{\Delta}, 2) \approx \max(100, 10^{-x}), \; x = 3.23(Re_{2\overline{\Delta}}^{-0.92} - Re_{\overline{\Delta}}^{-0.92}) \quad , \tag{4.149}$$

where the mesh-Reynolds numbers are evaluated as (see equation (4.70)):

$$Re_{\overline{\Delta}} = \frac{\overline{\Delta}^2 |\overline{S}|}{\nu}, \quad Re_{2\overline{\Delta}} = \frac{4\overline{\Delta}^2 |\widetilde{\overline{S}}|}{\nu} \quad .$$

We now consider the problem of the filter self-similarity. Let G_1 and G_2 be the filter kernels associated to the first and second filtering level. For sake of simplicity, we use the notations $\overline{\Delta} = \Delta_1$ and $\widetilde{\overline{\Delta}} = \Delta_2$. We assume that the filter kernel are re-written in a form such that:

$$\overline{u}(x) = G_1 \star u(x) = \int G_1 \left(\frac{|x-\xi|}{\Delta_1} \right) u(\xi) d\xi \quad , \tag{4.150}$$

$$\widetilde{\overline{u}}(x) = G_2 \star u(x) = \int G_2 \left(\frac{|x-\xi|}{\Delta_2} \right) u(\xi) d\xi \quad . \tag{4.151}$$

We also introduce the test filter G_t, which is defined such that

$$\widetilde{\overline{u}} = G_2 \star u = G_t \star \overline{u} = G_t \star G_1 \star u \quad . \tag{4.152}$$

The filters G_1 and G_2 are self-similar if and only if

$$G_1(y) = \frac{1}{r^d} G_2 \left(\frac{y}{r} \right), \quad r = \Delta_2/\Delta_1 \quad . \tag{4.153}$$

Hence, the two filters must have identical shapes and may only differ by their associated characteristic length. The problem is that in practice only G_t is known, and the self-similarity property might not be *a priori* verified. Carati and Vanden Eijnden [49] show that the interpretation of the resolved field is fully determined by the choice of the test filter G_t, and that the use of the same model for the two levels of filtering is fully justified. This is demonstrated by re-interpreting previous filters in the following way. Let us consider an infinite set of self-similar filters $\{F_n \equiv F(l_n)\}$ defined as

$$F_n(x) = \frac{1}{r^n} \mathcal{F} \left(\frac{x}{l_n} \right), l_n = r^n l_0 \quad , \tag{4.154}$$

where $\mathcal{F}$, $r > 1$ and l_0 are the filter kernel, an arbitrary parameter and a reference length, respectively. Let us introduce a second set $\{F_n^* \equiv F^*(l_n^*)\}$ defined by

$$F_n^* \equiv F_n \star F_{n-1} \star ... \star F_{-\infty} \quad . \tag{4.155}$$

For positive kernel $\mathcal{F}$, we get the following properties:

- The length l_n^* obeys the same geometrical law as l_n :

$$l_n^* = r l_{n-1}^*, \quad \text{and} \quad l_n^* = \frac{r}{\sqrt{r^2-1}} l_n \quad . \tag{4.156}$$

- $\{F_n^*\}$ constitute a set of self-similar filters.

Using these two set of filters, the classical filters involved in the dynamic procedure can be defined as self-similar filters:

$$G_t(\Delta_t) = F_n(l_n) \quad , \tag{4.157}$$

$$G_1(\Delta_1) = F_{n-1}^*(l_{n-1}^*) \quad , \tag{4.158}$$

$$G_2(\Delta_2) = F_n^*(l_n^*) \quad . \tag{4.159}$$

For any test-filter G_t and any value of r, the first filter operator can be constructed explicitly :

$$G_1 = G_t(\Delta_t/r) \star G_t(\Delta_t/r^2) \star ... \star G_t(\Delta_t/r^\infty) \quad . \tag{4.160}$$

This relation shows that for any test filter of the form (4.157), the two filtering operators can be rewritten as self-similar ones, justifying the use of the same model at all the filtering levels.

Lagrangian Dynamic Procedure. The constant regularization procedures based on averages in the homogeneous directions have the drawback of not being usable in complex configurations, which are totally inhomogeneous. One technique for remedying this problem is to take this average along the fluid particle trajectories. This new procedure [230], called the dynamic Lagrangian procedure, has the advantage of being applicable in all configurations.

The trajectory of a fluid particle located at position $\mathbf{x}$ at time t is, for times t' previous to t, denoted as:

$$\mathbf{z}(t') = \mathbf{x} - \int_{t'}^{t} \overline{\mathbf{u}}[\mathbf{z}(t''), t''] dt'' \quad . \tag{4.161}$$

The residual (4.134) is written in the following Lagrangian form:

$$E_{ij}(\mathbf{z}, t') = L_{ij}(\mathbf{z}, t') - C_{\mathrm{d}}(\mathbf{x}, t) m_{ij}(\mathbf{z}, t') \quad . \tag{4.162}$$

We see that the value of the constant is fixed at point $\mathbf{x}$ at time t, which is equivalent to the same linearization operation as for the Germano–Lilly procedure. The value of the constant that should be used for computing the subgrid model at $\mathbf{x}$ at time t is determined by minimizing the error along the fluid particle trajectories. Here too, we reduce to a well-posed problem by defining a scalar residual E_{lag}, which is defined as the weighted integral along the trajectories of the residual proposed by Lilly:

$$E_{\mathrm{lag}} = \int_{-\infty}^{t} E_{ij}(\mathbf{z}(t'), t') E_{ij}(\mathbf{z}(t'), t') W(t-t') dt' \quad , \tag{4.163}$$

in which the weighting function $W(t-t')$ is introduced to control the memory effect. The constant is a solution of the problem:

$$\frac{\partial E_{\text{lag}}}{\partial C_{\text{d}}} = \int_{-\infty}^{t} 2E_{ij}(\mathbf{z}(t'),t') \frac{\partial E_{ij}(\mathbf{z}(t'),t')}{\partial C_{\text{d}}} W(t-t')dt' = 0 \quad , \tag{4.164}$$

or:

$$C_{\text{d}}(\mathbf{x},t) = \frac{\mathcal{J}_{\text{LM}}}{\mathcal{J}_{\text{MM}}} \quad , \tag{4.165}$$

in which

$$\mathcal{J}_{\text{LM}}(\mathbf{x},t) = \int_{-\infty}^{t} L_{ij} m_{ij}(\mathbf{z}(t'),t') W(t-t')dt' \quad , \tag{4.166}$$

$$\mathcal{J}_{\text{MM}}(\mathbf{x},t) = \int_{-\infty}^{t} m_{ij} m_{ij}(\mathbf{z}(t'),t') W(t-t')dt' \quad . \tag{4.167}$$

These expressions are non-local in time, which makes them unusable for the simulation, because they require that the entire history of the simulation be kept in memory, which exceeds the storage capacities of today's supercomputers. To remedy this, we choose a fast-decay memory function W:

$$W(t-t') = \frac{1}{T_{\text{lag}}} \exp\left(-\frac{t-t'}{T_{\text{lag}}}\right) \quad , \tag{4.168}$$

in which T_{lag} is the Lagrangian correlation time. With the memory function in this form, we can get the following equations:

$$\frac{D\mathcal{J}_{\text{LM}}}{Dt} \equiv \frac{\partial \mathcal{J}_{\text{LM}}}{\partial t} + \overline{u}_i \frac{\partial \mathcal{J}_{\text{LM}}}{\partial x_i} = \frac{1}{T_{\text{lag}}} \left(L_{ij} m_{ij} - \mathcal{J}_{\text{LM}}\right) \quad , \tag{4.169}$$

$$\frac{D\mathcal{J}_{\text{MM}}}{Dt} \equiv \frac{\partial \mathcal{J}_{\text{MM}}}{\partial t} + \overline{u}_i \frac{\partial \mathcal{J}_{\text{MM}}}{\partial x_i} = \frac{1}{T_{\text{lag}}} \left(m_{ij} m_{ij} - \mathcal{J}_{\text{MM}}\right) \quad , \tag{4.170}$$

the solution of which can be used to compute the subgrid model constant at each point and at each time step. The correlation time T_{lag} is estimated by tests in isotropic homogeneous turbulence at:

$$T_{\text{lag}}(\mathbf{x},t) = 1.5\,\overline{\Delta}\left(\mathcal{J}_{\text{MM}}\mathcal{J}_{\text{LM}}\right)^{-1/8} \quad , \tag{4.171}$$

which comes down to considering that the correlation time is reduced in the high-shear regions where $\mathcal{J}_{\text{MM}}$ is large, and in those regions where the non-linear transfers are high, *i.e.* where $\mathcal{J}_{\text{LM}}$ is large.

This procedure does not guarantee that the constant will be positive, and must therefore be coupled with a regularization procedure. Meneveau *et al.* [230] recommend a clipping procedure.

Solving equations (4.169) and (4.170) yields a large amount of additional numerical work, resulting in a very expensive subgrid model. To alleviate this problem, the solution to these two equations may be approximated using the following Lagrangian tracking technique [268]:

$$\begin{aligned}\mathcal{J}_{\text{LM}}(\mathbf{x},n\Delta t) &= aL_{ij}(\mathbf{x},n\Delta t)m_{ij}(\mathbf{x},n\Delta t) \\ &+ (1-a)\mathcal{J}_{\text{LM}}(\mathbf{x}-\Delta t\overline{\mathbf{u}}(\mathbf{x},n\Delta t),(n-1)\Delta t)\,, \quad (4.172)\\ \mathcal{J}_{\text{MM}}(\mathbf{x},n\Delta t) &= am_{ij}(\mathbf{x},n\Delta t)m_{ij}(\mathbf{x},n\Delta t) \\ &+ (1-a)\mathcal{J}_{\text{MM}}(\mathbf{x}-\Delta t\overline{\mathbf{u}}(\mathbf{x},n\Delta t),(n-1)\Delta t)\,, \quad (4.173)\end{aligned}$$

where

$$a = \frac{\Delta t/T_{\text{lag}}}{1+\Delta t/T_{\text{lag}}} \quad . \tag{4.174}$$

This new procedure requires only the storage of the two parameters $\mathcal{J}_{\text{LM}}$ and $\mathcal{J}_{\text{MM}}$ at the previous time step and the use of an interpolation procedure. The authors indicate that a linear interpolation is acceptable.

Constrained Localized Dynamic Procedure. Another generalization of the Germano–Lilly dynamic procedure was proposed for inhomogeneous cases by Ghosal *et al.* [122]. This new procedure is based on the idea of minimizing an integral problem rather than a local one in space, as is done in the Germano–Lilly procedure, which avoids the need to linearize the constant when applying the test filter. We now look for the constant C_{d} that will minimize the function $\mathcal{F}[C_{\text{d}}]$, with

$$\mathcal{F}[C_{\text{d}}] = \int E_{ij}(\mathbf{x})E_{ij}(\mathbf{x})d^3\mathbf{x} \quad , \tag{4.175}$$

in which E_{ij} is defined from relation (4.132) and not by (4.134) as was the case for the previously explained versions of the dynamic procedure. The constant sought is such that the variation of $\mathcal{F}[C_{\text{d}}]$ is zero:

$$\delta\mathcal{F}[C_{\text{d}}] = 2\int E_{ij}(\mathbf{x})\delta E_{ij}(\mathbf{x})d^3\mathbf{x} = 0 \quad , \tag{4.176}$$

or, by replacing E_{ij} with its value:

$$\int \left(-\alpha_{ij}E_{ij}\delta C_{\text{d}} + E_{ij}\widetilde{\beta_{ij}\delta C_{\text{d}}}\right) d^3\mathbf{x} = 0 \quad . \tag{4.177}$$

Expressing the convolution product associated with the test filter, we get:

$$\int \left(-\alpha_{ij}E_{ij} + \beta_{ij}\int E_{ij}(\mathbf{y})G(\mathbf{x}-\mathbf{y})d^3\mathbf{y}\right)\delta C_{\text{d}}(\mathbf{x})d^3\mathbf{x} = 0 \quad , \tag{4.178}$$

from which we deduce the following Euler-Lagrange equation:

$$-\alpha_{ij}E_{ij} + \beta_{ij}\int E_{ij}(\mathbf{y})G(\mathbf{x}-\mathbf{y})d^3\mathbf{y} = 0 \quad . \tag{4.179}$$

This equation can be re-written in the form of a Fredholm's integral equation of the second kind for the constant C_d:

$$f(\mathbf{x}) = C_\mathrm{d}(\mathbf{x}) - \int \mathcal{K}(\mathbf{x},\mathbf{y})C_\mathrm{d}(\mathbf{y})d^3\mathbf{y} \quad , \tag{4.180}$$

where

$$f(\mathbf{x}) = \frac{1}{\alpha_{kl}(\mathbf{x})\alpha_{kl}(\mathbf{x})}\left(\alpha_{ij}(\mathbf{x})L_{ij}(\mathbf{x}) - \beta_{ij}(\mathbf{x})\int L_{ij}(\mathbf{y})G(\mathbf{x}-\mathbf{y})d^3\mathbf{y}\right) \quad , \tag{4.181}$$

$$\mathcal{K}(\mathbf{x},\mathbf{y}) = \frac{\mathcal{K}_\mathcal{A}(\mathbf{x},\mathbf{y}) + \mathcal{K}_\mathcal{A}(\mathbf{y},\mathbf{x}) + \mathcal{K}_\mathcal{S}(\mathbf{x},\mathbf{y})}{\alpha_{kl}(\mathbf{x})\alpha_{kl}(\mathbf{x})} \quad , \tag{4.182}$$

and

$$\mathcal{K}_\mathcal{A}(\mathbf{x},\mathbf{y}) = \alpha_{ij}(\mathbf{x})\beta_{ij}(\mathbf{y})G(\mathbf{x}-\mathbf{y}) \quad , \tag{4.183}$$

$$\mathcal{K}_\mathcal{S}(\mathbf{x},\mathbf{y}) = \beta_{ij}(\mathbf{x})\beta_{ij}(\mathbf{y})\int G(\mathbf{z}-\mathbf{x})G(\mathbf{z}-\mathbf{y})d^3\mathbf{z} \quad . \tag{4.184}$$

This new formulation raises no problems concerning the linearization of the constant, but does not solve the instability problems stemming from the negative values it may take. This procedure is called the localized dynamic procedure.

To remedy the instability problem, the authors propose constraining the constant to remain positive. The constant $C_\mathrm{d}(\mathbf{x})$ is then expressed as the square of a new real variable $\xi(\mathbf{x})$. Replacing the constant with its decomposition as a function of ξ, the Euler-Lagrange equation (4.179) becomes:

$$\left(-\alpha_{ij}E_{ij} + \beta_{ij}\int E_{ij}(\mathbf{y})G(\mathbf{x}-\mathbf{y})d^3\mathbf{y}\right)\xi(\mathbf{x}) = 0 \quad . \tag{4.185}$$

This equality is true if either of the factors is zero, *i.e.* if $\xi(\mathbf{x}) = 0$ or if the relation (4.179) is verified, which is denoted symbolically $C_\mathrm{d}(\mathbf{x}) = \mathcal{G}[C_\mathrm{d}(\mathbf{x})]$. In the first case, the constant is also zero. To make sure it remains positive, the constant is computed by an iterative procedure:

$$C_\mathrm{d}^{(n+1)}(\mathbf{x}) = \begin{cases} \mathcal{G}[C_\mathrm{d}^{(n)}(\mathbf{x})] & \text{if } \mathcal{G}[C_\mathrm{d}^{(n)}(\mathbf{x})] \geq 0 \\ 0 & \text{otherwise} \end{cases} \quad , \tag{4.186}$$

in which

$$\mathcal{G}[C_\mathrm{d}(\mathbf{x})] = f(\mathbf{x}) - \int \mathcal{K}(\mathbf{x},\mathbf{y})C_\mathrm{d}(\mathbf{y})d^3\mathbf{y} \quad . \tag{4.187}$$

This completes the description of the constrained localized dynamic procedure. It is applicable to all configurations and ensures that the subgrid model constant remains positive. This solution is denoted symbolically:

$$C_\mathrm{d}(\mathbf{x}) = \left[f(\mathbf{x}) + \int \mathcal{K}(\mathbf{x},\mathbf{y})C_\mathrm{d}(\mathbf{y})d^3\mathbf{y}\right]_+ \quad , \tag{4.188}$$

in which + designates the positive part.

Approximate Localized Dynamic Procedure. The localized dynamic procedure decribed in the preceding paragraph makes it possible to regularize the dynamic procedure in fully non-homogeneous flows, and removes the mathematical inconsistency of the Germano–Lilly procedure. But it requires to solve an integral equation, and thus induces a significant overhead.

To alleviate this problem, Piomelli and Liu [268] propose an Approximate Localized Dynamic Procedure, which is not based on a variational approach but on a time extrapolation process. Equation (4.132) is recast in the form

$$L_{ij}^d = C_\mathrm{d}\alpha_{ij} - \widetilde{C_\mathrm{d}^*\beta_{ij}} \quad , \tag{4.189}$$

where C_d^* is an estimate of the dynamic constant C_d, which is assumed to be known. Writing the new formulation of the residual E_{ij}, the dynamic constant is now evaluated as

$$C_\mathrm{d} = \frac{\alpha_{ij}(L_{ij}^d + \widetilde{C_\mathrm{d}^*\beta_{ij}})}{\alpha_{ij}\alpha_{ij}} \quad . \tag{4.190}$$

The authors propose to evaluate the estimate C_d^* by a time extrapolation:

$$C_\mathrm{d}^* = C_\mathrm{d}^{(n-1)} + \Delta t\left.\frac{\partial C_\mathrm{d}}{\partial t}\right|^{(n-1)} + \ldots \quad , \tag{4.191}$$

where the superscript $(n-1)$ is related to the value of the variable at the $(n-1)$th time step, and Δ_t is the value of the time step. In practice, Piomelli and Liu consider first- and second-order extrapolation schemes. The resulting dynamic procedure is fully local, and does not induce large extra computational effort as the original localized procedure does. Numerical experiments carried out by these authors demonstrate that it still requires clipping to yield a well-behaved algorithm.

Generalized Dynamic Procedure. It is also possible to derive a dynamic procedure using the generalized Germano identity (3.84) [287]. We assume that the operator $\mathcal{L}$ appearing in equation (3.85) is linear, and that there exists a linear operator $\mathcal{L}'$ such that

$$\mathcal{L}(aN) = a\mathcal{L}(N) + \mathcal{L}'(a, N) \quad , \tag{4.192}$$

where a is a scalar real function and N an arbitrary second rank tensor. The computation of the dynamic constant C_d is now based on the minimization of the residual E_{ij}

$$E_{ij} = \mathcal{L}(L^\mathrm{d}_{ij}) - C_\mathrm{d}\mathcal{L}(m_{ij}) \quad , \tag{4.193}$$

where L^d_{ij} and m_{ij} are defined by equations (4.132) and (4.138). A least-square minimizations yields:

$$C'_\mathrm{d} = \frac{\mathcal{L}(L^\mathrm{d}_{ij})\mathcal{L}(m_{ij})}{\mathcal{L}(m_{ij})\mathcal{L}(m_{ij})} \quad . \tag{4.194}$$

The reduction of the residual obtained using this new relation with respect to the classical one is analyzed by evaluating the difference:

$$\delta E_{ij} = E'_{ij} - \mathcal{L}(E_{ij}) \quad , \tag{4.195}$$

where E'_{ij} is given by relation (4.193) and E_{ij} by (4.134). Inserting the two dynamic constants C'_d and C_d, defined respectively by relations (4.194) and (4.137), we get:

$$\delta E_{ij} = (C_\mathrm{d} - C'_\mathrm{d})\mathcal{L}(m_{ij}) + \mathcal{L}'(C_\mathrm{d}, m_{ij}) \quad . \tag{4.196}$$

An obvious example for the linear operator $\mathcal{L}$ is the divergence operator. The associated $\mathcal{L}'$ is the gradient operator.

An alternative consisting in minimizing a different form of the residual has been proposed by Morinishi and Vasilyev [248] and Mossi [249]:

$$\begin{aligned} E_{ij} &= \mathcal{L}(L^\mathrm{d}_{ij}) - \mathcal{L}(C_\mathrm{d} m_{ij}) && (4.197)\\ &= \mathcal{L}(L^\mathrm{d}_{ij}) - C_\mathrm{d}\mathcal{L}(m_{ij}) - \mathcal{L}'(C_\mathrm{d}, m_{ij}) \quad . && (4.198) \end{aligned}$$

The use of this new form of the residual generally requires solving a differential equation, and then yields a more complex procedure than the form (4.193).

These two procedures theoretically more accurate results than the classical one, because they provide reduce the error committed on the subgrid force term itself, rather than on the subgrid tensor. They also take into account for the numerical error associated to the discrete form of $\mathcal{L}$.

Dynamic Inverse Procedure. We have already seen that the use of the dynamic procedure may induce some problems if the cutoff is not located in the inertial range of the spectra, but in the viscous one. A similar problem arises if the cutoff wave number associated to the test filter occurs at the very beginning of the inertial range, or in the production range of the spectrum. It order to compensate inaccuracies arising from the use of a large filter length associated with the test filter, Kuerten *et al.* [174] developed a new approach, referred to as the Dynamic Inverse Procedure. It relies on the idea that if a dynamic procedure is developed involving only lengthscales comparable to the basic filter length, self-similarity properties will be preserved and consistent modeling may result. Such a procedure is obtained by defining the first filtering operator G and the second one F by

$$G = H^{-1} \circ L, \quad F = H \quad , \tag{4.199}$$

where L is the classical filter level and H an explicit test filter, whose inverse H^{-1} is assumed to be known explicitly. Inserting these definitions into the Germano identity (3.78), we get a direct evaluation of the subgrid tensor τ:

$$\begin{aligned} [F \star G\star, B](u_i, u_j) &= [L\star, B](u_i, u_j) && (4.200)\\ &= \overline{u_i u_j} - \overline{u}_i\overline{u}_j && (4.201)\\ &\equiv \tau_{ij} && (4.202)\\ &= [H\star, B] \circ (H^{-1} \star L\star)(u_i, u_j) \\ &\quad + (H\star) \circ [H^{-1} \star L\star, B](u_i, u_j) \quad . && (4.203) \end{aligned}$$

This new identity can be recast in a form similar to the original Germano identity

$$L^\diamond_{ij} = \tau_{ij} - H \star T^\diamond_{ij} \quad , \tag{4.204}$$

with

$$L^\diamond_{ij} = H \star ((H^{-1} \star \overline{u}_i)(H^{-1} \star \overline{u}_j)) - \overline{u}_i\overline{u}_j \quad ,$$

$$T^\diamond_{ij} = H^{-1} \star \overline{u_i u_j} - (H^{-1} \star \overline{u}_i)(H^{-1} \star \overline{u}_j) \quad .$$

The term $L^\diamond_{ij}$ is explicitly known in practice, and does not require any modeling. Using the same notation as in the section dedicated to the Germano–Lilly procedure, we get, for the Smagorinsky model:

$$\tau_{ij} = C_\mathrm{d}\beta_{ij}, \ \beta_{ij} = -2\overline{\Delta}^2|\overline{S}|\overline{S}_{ij} \quad , \tag{4.205}$$

$$T^\diamond_{ij} = C_\mathrm{d}\alpha_{ij}, \ \alpha_{ij} = -2\widehat{\overline{\Delta}}^2|\widehat{\overline{S}}|\widehat{\overline{S}}_{ij} \quad , \tag{4.206}$$

where $\widehat{\overline{\Delta}}$ and $\widehat{\overline{S}}$ are the characteristic length and the strain rate tensor associated to the $H^{-1} \circ L$ filtering level, respectively. Building the residual E_{ij} as

$$E_{ij} = L^{\diamond}_{ij} - C_{\mathrm{d}}(\beta_{ij} - H \star \alpha_{ij}) = L^{\diamond}_{ij} - C_{\mathrm{d}} m_{ij} \quad , \tag{4.207}$$

the least-square-error minimization procedure yields:

$$C_{\mathrm{d}} = \frac{L^{\diamond}_{ij} m_{ij}}{m_{ij} m_{ij}} \quad . \tag{4.208}$$

In this new procedure, the two lengths involved are $\overline{\Delta}$ and $\widehat{\overline{\Delta}}$. Since the latter is associated to an inverse filtering operator, we get $\widehat{\overline{\Delta}} \leq \overline{\Delta}$, ensuring that the dynamic procedure will not bring in lengths associated to the production range of the spectrum. In practice, this procedure is observed to suffer the same stability problems than the Germano–Lilly procedure, and needs to be used together with a stabilization procedure (averaging, clipping, etc.).

Structural Sensors. Selective Models. In order to improve the prediction of intermittent phenomena, we introduce a sensor based on structural information. This is done by incorporating a selection function in the model, based on the local angular fluctuations of the vorticity, developed by David [74, 190].

The idea here is to modulate the subgrid model in such a way as to apply it only when the assumptions underlying the modeling are verified, *i.e.* when all the scales of the exact solution are not resolved and the flow is of the fully developed turbulence type. The problem therefore consists in determining if these two hypotheses are verified at each point and each time step. David's structural sensor tests the second hypothesis. To do this, we assume that, if the flow is turbulent and developed, the highest resolved frequencies have certain characteristics specific to isotropic homogeneous turbulence, and particularly structural properties.

So the properties specific to isotropic homogeneous turbulence need to be identified. David, taking direct numerical simulations as a base, observed that the probability density function of the local angular fluctuation of the vorticity vector exhibit a peak around the value of 20^o. Consequently, he proposes identifying the flow as being locally under-resolved and turbulent at those points for which the local angular fluctuations of the vorticity vector corresponding to the highest resolved frequencies are greater than or equal to a threshold value θ_0.

The selection criterion will therefore be based on an estimation of the angle θ between the instantaneous vorticity vector $\boldsymbol{\omega}$ and the local average vortcity vector $\tilde{\boldsymbol{\omega}}$ (see Fig. 4.16), which is computed by applying a test filter to the vorticity vector.

The angle θ is given by the following relation:

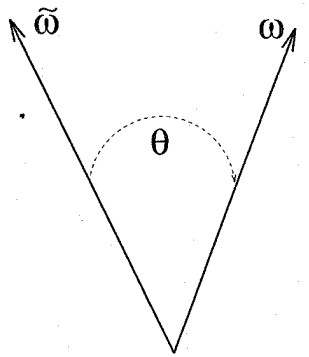

Fig. 4.16. Local angular fluctuation of the vorticity vector.

$$\theta(\mathbf{x}) = \arcsin\left(\frac{\|\tilde{\boldsymbol{\omega}}(\mathbf{x}) \times \boldsymbol{\omega}(\mathbf{x})\|}{\|\tilde{\boldsymbol{\omega}}(\mathbf{x})\| . \|\boldsymbol{\omega}(\mathbf{x})\|}\right) \quad . \tag{4.209}$$

We define a selection function to damp the subgrid model when the angle θ is less than a threshold angle θ_0.

In the original version developed by David, the selection function f_{θ_0} is a Boolean operator:

$$f_{\theta_0}(\theta) = \begin{cases} 1 \text{ if } \theta \geq \theta_0 \\ 0 \text{ otherwise} \end{cases} \quad . \tag{4.210}$$

This function is discontinuous, which may pose problems in the numerical solution. One variant of it that exhibits no discontinuity for the threshold value is defined as follows [293]:

$$f_{\theta_0}(\theta) = \begin{cases} 1 & \text{if } \theta \geq \theta_0 \\ r(\theta)^n & \text{otherwise} \end{cases} \quad , \tag{4.211}$$

in which θ_0 is the chosen threshold value and r the function:

$$r(\theta) = \frac{\tan^2(\theta/2)}{\tan^2(\theta_0/2)} \quad , \tag{4.212}$$

where the exponent n is positive. In practice, it is taken to be equal to 2. Considering the fact that we can express the angle θ as a function of the norms of the vorticity vector $\boldsymbol{\omega}$, the average vorticity vector $\tilde{\boldsymbol{\omega}}$, and the norm $\boldsymbol{\omega}'$ of the fluctuating vorticity vector defined as $\boldsymbol{\omega}' = \boldsymbol{\omega} - \tilde{\boldsymbol{\omega}}$, by the relation:

$$\omega'^2 = \tilde{\omega}^2 + \omega^2 - 2\tilde{\omega}\omega\cos\theta \quad ,$$

and the trigonometric [illegible]ation:

$$\tan^2(\theta/2) = \frac{1-\cos\theta}{1+\cos\theta} \quad ,$$

the quantity $\tan^2(\theta/2)$ is estimated using the relation:

$$\tan^2(\theta/2) = \frac{2\tilde{\omega}\omega - \tilde{\omega}^2 - \omega^2 + \omega'^2}{2\tilde{\omega}\omega + \tilde{\omega}^2 + \omega^2 - \omega'^2} \quad . \tag{4.213}$$

The selection function is used as a multiplicative factor of the subgrid viscosity, leading to the definition of selective models:

$$\nu_{\text{sgs}} = \nu_{\text{sgs}}(\mathbf{x},t) f_{\theta_0}(\theta(\mathbf{x})) \quad , \tag{4.214}$$

in which ν_{sgs} is calculated by an arbitrary subgrid viscosity model. It should be noted that, in order to keep the same average subgrid viscosity value over the entire fluid domain, the constant that appears in the subgrid model has to be multiplied by a factor of 1.65. This factor is evaluated on the basis of isotropic homogeneous turbulence simulations.

Accentuation Technique. Filtered Models

Accentuation Technique. Since large-eddy simulation is based on a frequency selection, improving the subgrid models in the physical space requires a better diagnostic concerning the spectral distribution of the energy in the calculated solution. More precisely, what we want to do here is to determine if the exact solution is entirely resolved, in which case the subgrid model should be reduced to zero, or if there exist subgrid scales that have to be taken into account by means of a model. When models expressed in the physical space do not use additional variables, they suffer from imprecision due to Gabor-Heisenberg's principle of uncertainty already mentioned above, because the contribution of the low frequencies precludes any precise determination of the energy at the cutoff. Let us recall that, if this energy is zero, the exact solution is completely represented and, if otherwise, then subgrid modes exist. In order to be able to detect the existence of the subgrid modes better, Ducros [91, 92] proposes an accentuation technique which consists in applying the subgrid models to a modified velocity field obtained by applying a frequency high-pass filter to the resolved velocity field. This filter, denoted HP^n, is defined recursively as:

$$\text{HP}^1(\overline{\mathbf{u}}) \simeq \overline{\Delta}^2 \nabla^2 \overline{\mathbf{u}} \quad , \tag{4.215}$$

$$\text{HP}^n(\overline{\mathbf{u}}) = \text{HP}(\text{HP}^{n-1}(\overline{\mathbf{u}})) \quad . \tag{4.216}$$

We note that the application of this filter in the discrete case results in a loss of localness in the physical space, which is in conformity with Gabor-Heisenberg's principle of uncertainty. We use $E_{\text{HP}^n}(k)$ to denote the energy spectrum of the field thus obtained. This spectrum is related to the initial spectrum $\overline{E}(k)$ of the resolved scales by:

$$\overline{E}_{\text{HP}^n}(k) = T_{\text{HP}^n}(k)\overline{E}(k) \quad , \tag{4.217}$$

in which $T_{\text{HP}^n}(k)$ is a transfer function which Ducros evaluates in the form:

$$T_{\text{HP}^n}(k) = b^n \left(\frac{k}{k_c}\right)^{\gamma n} \quad . \tag{4.218}$$

Here, b and γ are positive constants that depend on the discrete filter used in the numerical simulation[22]. The shape of the spectrum obtained by the transfer function to a Kolmogorov spectrum is graphed in Fig. 4.17 for several values of the parameter n. This type of filter modifies the spectrum of the initial solution by emphasizing the contribution of the highest frequencies.

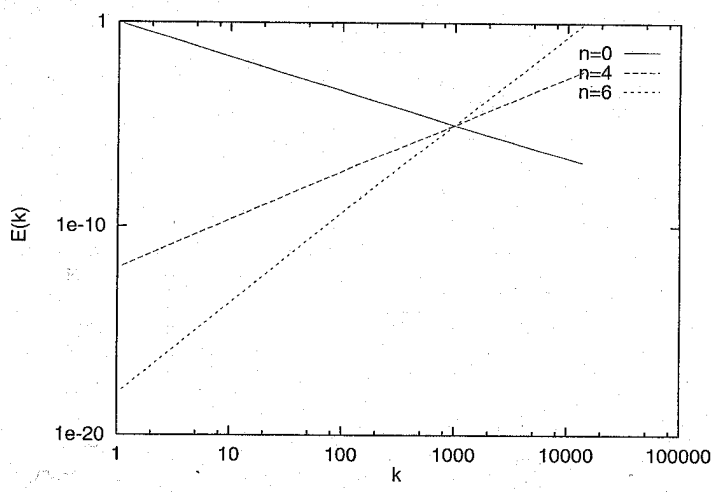

Fig. 4.17. Energy spectrum of the accentuation solution for different values of the parameter n ($b = \gamma = 1, k_c = 1000$).

The resulting field therefore represents mainly the high frequencies of the initial field and serves to compute the subgrid model. To remain consistent, the subgrid model has to be modified. Such models are called filtered models. The case of the Structure Function model is given as an example. Filtered versions of the Smagorinsky and Mixed Scale models have been developped by Sagaut, Comte and Ducros [286].

[22] For a Laplacian type filter discretized by second-order accurate finite difference scheme iterated three times ($n = 3$), Ducros finds $b^3 = 64,000$ and $3\gamma = 9.16$.

Filtered Structure Function Model. We define the second-order structure function of the filtered field:

$$\overline{F}_2^{\mathrm{HP}^n}(\mathbf{x},r,t)=\int_{|\mathbf{x}'|=r}\left[\mathrm{HP}^n(\overline{u})(\mathbf{x},t)-\mathrm{HP}^n(\overline{u})(\mathbf{x}+\mathbf{x}',t)\right]^2 d^3\mathbf{x}' \quad , \tag{4.219}$$

for which the statistical average over the entire fluid domain, denoted $\langle\overline{F}_2^{\mathrm{HP}^n}\rangle(r,t)$, is related to the kinetic energy spectrum by the relation:

$$\langle\overline{F}_2^{\mathrm{HP}^n}\rangle(r,t)=4\int_0^{k_\mathrm{c}}\overline{E}_{\mathrm{HP}^n}(k)\left(1-\frac{\sin(k\overline{\Delta})}{k\overline{\Delta}}\right)dk \quad . \tag{4.220}$$

According to the theorem of averages, there exists a wave number $k_*\in[0,k_\mathrm{c}]$ such that:

$$\overline{E}_{\mathrm{HP}^n}(k_*)=\frac{\langle\overline{F}_2^{\mathrm{HP}^n}\rangle(r,t)}{4(\pi/k_\mathrm{c})\displaystyle\int_0^\pi(1-\sin(\xi)/\xi)\,d\xi} \quad . \tag{4.221}$$

Using a Kolmogorov spectrum, we can state the equality:

$$\frac{\overline{E}(k_\mathrm{c})}{k_\mathrm{c}^{-5/3}}=\frac{\overline{E}_{\mathrm{HP}^n}(k_*)}{k_*} \quad . \tag{4.222}$$

Considering this last relation, along with (4.217) and (4.218), the subgrid viscosity models based on the energy at cutoff are expressed:

$$\langle\nu_\mathrm{sgs}\rangle=\frac{2}{3}\frac{K_0^{-3/2}}{k_\mathrm{c}^{1/2}}\sqrt{\left(\frac{k_*}{k_\mathrm{c}}\right)^{5/3-\gamma n}\frac{1}{b^n}\overline{E}_{\mathrm{HP}^n}(k_*)} \quad , \tag{4.223}$$

in which:

$$\left(\frac{k_*}{k_\mathrm{c}}\right)^{-5/3+\gamma n}=\frac{1}{\pi^{-5/3+\gamma n}}\frac{\displaystyle\int_0^\pi\xi^{-5/3+\gamma n}(1-\sin(\xi)/\xi)\,d\xi}{\displaystyle\int_0^\pi(1-\sin(\xi)/\xi)\,d\xi} \quad . \tag{4.224}$$

By localizing these relations in the physical space, we deduce the filtered structure function model:

$$\begin{aligned}\nu_\mathrm{sgs}(\mathbf{x},\overline{\Delta},t)&=\frac{2}{3}\frac{K_0^{-3/2}}{\pi^{4/3}}\frac{\overline{\Delta}}{2}\left(\frac{\pi^{\gamma n}}{b^n}\right)^{1/2}\frac{\left(\overline{F}_2^{\mathrm{HP}^n}(\mathbf{x},\overline{\Delta},t)\right)^{1/2}}{\left(\displaystyle\int_0^\pi\xi^{-5/3+\gamma n}(1-\sin(\xi)/\xi)\,d\xi\right)^{1/2}}\\&=C^{(n)}\overline{\Delta}\sqrt{\overline{F}_2^{\mathrm{HP}^n}(\mathbf{x},\overline{\Delta},t)} \quad .\end{aligned} \tag{4.225}$$

The values of the constant $C^{(n)}$ are given in the following Table:
In practice, Ducros recommends using $n=3$.

Table 4.2. Values of the Structure Function model constant for different iterations of the high-pass filter.

n	0	1	2	3	4
$C^{(n)}$	0.0637	0.020	0.0043	0.000841	$1.57\cdot10^{-4}$

Damping Functions for the Region Near a Wall. The presence of a solid wall modifies the turbulence dynamics in several ways, which are discussed in Chap. 9. The only fact concerning us here is that the presence of a wall inhibits the growth of the small scales. This phenomenon implies that the characteristic mixing length of the subgrid modes Δ_f has to be reduced in the near-surface region, which corresponds to a reduction in the intensity of the subgrid viscosity. To represent the dynamics in the near-wall region correctly, it is important to make sure that the subgrid models verify the good properties in this region. In the case of a canonical boundary layer (see Chap. 9), the statistical asymptotic behavior of the velocity components and subgrid tensions can be determined analytically. Let u be the main velocity component in the x direction, v the transverse component in the y direction, and w the velocity component normal to the wall, in the z direction. An asymptotic analysis yields the following decay laws:

$$\langle u\rangle\propto z,\ \langle v\rangle\propto z,\ \langle w\rangle\propto z^2, \tag{4.226}$$

$$\begin{aligned}&\langle\tau_{11}\rangle\propto z^2,\ \langle\tau_{22}\rangle\propto z^2,\ \langle\tau_{33}\rangle\propto z^4,\\&\langle\tau_{13}\rangle\propto z^3,\ \langle\tau_{12}\rangle\propto z^2,\ \langle\tau_{23}\rangle\propto z^3.\end{aligned} \tag{4.227}$$

Experience shows that it is important to reproduce the behavior of the component τ_{13} in order to ensure the quality of the simulation results. For a subgrid viscosity model, we deduce the following law from relations (4.226) and (4.227):

$$\langle\nu_\mathrm{sgs}\rangle\propto z^3 \quad . \tag{4.228}$$

We verify that the model is based on the large scales alone do not verify this behavior and therefore have to be modified. This is done by introducing damping functions. The usual relation:

$$\Delta_\mathrm{f}=C\overline{\Delta} \quad , \tag{4.229}$$

is replaced by:

$$\Delta_\mathrm{f}=C\overline{\Delta}f_w(z) \quad , \tag{4.230}$$

in which $f_w(z)$ is the damping function and z the distance to the wall. From Van Driest's results, we define:

$$f_w(z) = 1 - \exp\left(-zu_\tau/25\nu\right) \quad , \tag{4.231}$$

in which the friction velocity u_τ is defined in Sect. 9.2.1. Piomelli *et al.* [271] propose the alternate form:

$$f_w(z) = \left(1 - \exp\left(-(zu_\tau/25\nu)^3\right)\right)^{1/2} \quad . \tag{4.232}$$

From this last form we can get a correct asymptotic behavior of the subgrid viscosity, *i.e.* a decrease in z^{+3} in the near-wall region, contrary to the Van Driest function. Experience shows that we can avoid recourse to these functions by using a dynamic procedure, a filtered model, a selective model, or the Yoshizawa model.

4.3.4 Implicit Diffusion

Large-eddy simulation approaches using a numerical viscosity with no explicit modeling are all based implicitly on the hypothesis:

Hypothesis 4.6. *The action of subgrid scales on the resolved scales is equivalent to a strictly dissipative action.*

Simulations belonging to this category use dissipation terms introduced either in the framework of upwind schemes for the convection or explicit artificial dissipation term, or by the use of implicit [328] or explicit [93] frequency low-pass filters. The approach most used is doubtless the use of upwind schemes for the convective term. The diffusive term introduced then varies both in degree and order, depending on the scheme used (QUICK [187], PPM [66], TVD [68], FCT [27], among others) and the dissipation induced can in certain cases be very close[23] to that introduced by a physical model [126]. Let us note that most of the schemes introduce dissipations of the second and/or fourth order and, in so doing, are very close to subgrid models. This point is discussed more precisely in Chap. 7. This approach is widely used in cases where the other modeling approaches become difficult for one of the two following reasons:

- The dynamic mechanisms escape the physical modeling because they are unknown or too complex to be modeled exactly and explicitly, which is true when complex thermodynamic mechanisms, for example, interact strongly with the hydrodynamic mechanisms (e.g. in cases of combustion [60] or shock/turbulence interaction [185]).
- Explicit modeling offers *no a priori* guarantee of certain realizability constraints related to the quantities studied (such as the temperature or molar concentrations of pollutants [214]).

[23] In the sense where these dissipations are localized at the same points and are of the same order of magnitude.

In cases belonging to one of these two classes, the error committed by using an implicit viscosity may in theory have no more harmful consequence on the quality of the result obtained than that which would be introduced by using an explicit model based on inadequate physical considerations. This approach is used essentially for dealing with very complex configurations or those harboring numerical difficulties, because it allows the use of robust numerical methods. Nonetheless, high-resolution simulations of case-study flows are beginning to make their appearance [272, 344].

4.4 Modeling the Backward Energy Cascade Process

4.4.1 Preliminary Remarks

The above models reflect only the backward cascade process, *i.e.* the dominant average effect of the subgrid scales. The second energy transfer mechanism, the backward energy cascade, is much less often taken into account in simulations. We may mention two reasons for this. Firstly, the intensity of this return is very weak compared with that of the forward cascade toward the small scales (at least on the average in the isotropic homogeneous case) and its role in the flow dynamics is still very poorly understood. Secondly, modeling it requires the addition of an energy source term to the equations being computed, which is potentially a generator of numerical problems.

Two methods are used for modeling the backward energy cascade:

- Adding a stochastic forcing term constructed from random variables and the information contained in the resolved field. This approach makes it possible to include a random character of the subgrid scales, and each simulation can be considered a particular realization. The space-time correlations characteristic of the scales originating the backward cascade cannot be represented by this approach, though, which limits its physical representativeness.
- Modifying the viscosity associated with the backward cascade mechanism defined in the previous section, so as to take the energy injected at the large scales into account. The backward cascade is then represented by a negative viscosity, which is added to that of the cascade model. This approach is statistical and deterministic, and also subject to caution because it is not based on a physical description of the backward cascade phenomenon and, in particular, possesses no spectral distribution in k^4 predicted by the analytical theories like EDQNM. Its advantage resides mainly in the fact that it allows a reduction of the total dissipation of the simulation, which is generally too high. Certain dynamic procedures for automatically computing the constants can generate negative values of them, inducing an energy injection in the resolved field. This property is sometimes interpreted as the capacity of the dynamic procedure to reflect

the backward cascade process. This approach can therefore be classed in the category of statistical deterministic backward cascade models.

Representing the backward cascade by way of a negative viscosity is controversial because the theoretical analyses, such as by the EDQNM model, distinguish very clearly between the cascade and backward cascade terms, both in their intensity and in their mathematical form [192, 193]. This representation is therefore to be linked to other statistical deterministic descriptions of the backward cascade, which take into account only an average reduction of the effective viscosity, such as the Chollet–Lesieur effective viscosity spectral model.

The main backward cascade models belonging to these two categories are described in the following.

4.4.2 Deterministic Statistical Models

This section describes the deterministic models for the backward cascade. These models, which are based on a modification of the subgrid viscosity associated with the forward cascade process, are:

1. The spectral model based on the theories of turbulence proposed by Chasnov (p.126). A negative subgrid viscosity is computed directly from the EDQNM theory. No hypothesis is adopted concerning the spectrum shape of the resolved scales, so that the spectral disequilibrium mechanisms can be taken into account at the level of these scales, but the spectrum shape of the subgrid scales is set arbitrarily. Also, the filter is assumed to be of the sharp cutoff type.
2. The dynamic model with an equation for the subgrid kinetic energy (p.127), to make sure this energy remains positive. This ensures that the backward cascade process is represented physically, in the sense that a limited quantity of energy can be restored to the resolved scales by the subgrid modes. However, this approach does not allow a correct representation of the spectral distribution of the backward cascade. Only the quantity of restored energy is controlled.

Chasnov's Spectral Model. Chasnov [54] adds a model for the backward cascade, also based on an EDQNM analysis, to the cascade model already described (see Sect. 4.3.1). The backward cascade process is represented deterministically by a negative effective viscosity term $\nu_e^-(k|k_c)$, which is of the form:

$$\nu_e^-(k|k_c,t) = -\frac{F^-(k|k_c,t)}{2k^2E(k,t)} \quad . \tag{4.233}$$

The stochastic forcing term is computed as:

$$F^-(k|k_z,t) = \int_{k_c}^{\infty} dp \int_{p-k}^{p} dq \Theta_{kpq} \frac{k^3}{pq}(1-2x^2z^2-xyz)E(q,t)E(p,t), \tag{4.234}$$

in which x, y, and z are geometric factors associated with the triad $(\mathbf{k},\mathbf{p},\mathbf{q})$, and Θ_{kpq} is a relaxation time described in Appendix B. As is done when computing the draining term (see Chasnov's effective viscosity model in Sect. 4.3.1), we assume that the spectrum takes the Kolmogorov form beyond the cutoff k_c. To simplify the computations, formula (4.234) is not used for wave numbers $k_c \leq p \leq 3k_c$. For the other wave numbers, we use the asymptotic form

$$F^-(k|k_c,t) = \frac{14}{15}k^4 \int_{k_c}^{\infty} dp \Theta_{kpp}(t) \frac{E^2(p,t)}{p^2} \quad . \tag{4.235}$$

This expression complete Chasnov's spectral subgrid model which, though quite close to the Kraichnan type effective viscosity models, makes it possible to take into account the backward cascade effects that are dominant for very small wave numbers.

Localized Dynamic Model with Energy Equation. The Germano–Lilly dynamic procedure and the localized dynamic procedure lead to the definition of subgrid models that raise numerical stability problems because the model constant can take negative values over long time intervals, leading to exponential growth of the disturbances.

This excessive duration of the dynamic constant in the negative state corresponds to too large a return of kinetic energy toward the large scales [47]. This phenomenon can be interpreted as a violation of the spectrum realizability constraint: when the backward cascade is over-estimated, a negative kinetic energy is implicitly defined in the subgrid scales. A simple idea for limiting the backward cascade consists in guaranteeing spectrum realizability[24]. The subgrid scales cannot then restore more energy than they contain. To verify this constraint, local information is needed on the subgrid kinetic energy, which naturally means defining this as an additional variable in the simulation.

A localized dynamic model including an energy equation is proposed by Ghosal *et al.* [122]. Similar models have been proposed independently by Ronchi *et al.* [233, 281] and Wong [348]. The subgrid model used is based on the kinetic energy of the subgrid modes. Using the same notation as in Sect. (4.3.3), we get:

$$\alpha_{ij} = -2\widetilde{\Delta}\sqrt{Q^2_{sgs}}\widetilde{S}_{ij} \quad , \tag{4.236}$$

$$\beta_{ij} = -2\overline{\Delta}\sqrt{q^2_{sgs}}\overline{S}_{ij} \quad , \tag{4.237}$$

in which the energies Q^2_{sgs} and q^2_{sgs} are defined as:

[24] The spectrum $E(k)$ is said to be realizable if $E(k) \geq 0$, $\forall k$.

$$Q^2_{\rm sgs} = \frac{1}{2}\left(\widetilde{\overline{u_i}\overline{u_i}} - \widetilde{\overline{u}}_i\widetilde{\overline{u}}_i\right) = \frac{1}{2}T_{ii} \quad , \tag{4.238}$$

$$q^2_{\rm sgs} = \frac{1}{2}\left(\overline{u_i u_i} - \overline{u}_i\overline{u}_i\right) = \frac{1}{2}\tau_{ii} \quad . \tag{4.239}$$

Germano's identity (4.126) is written:

$$Q^2_{\rm sgs} = \widetilde{q^2_{\rm sgs}} + \frac{1}{2}L_{ii} \quad . \tag{4.240}$$

The model is completed by calculating $q^2_{\rm sgs}$ by means of an additional evolution equation. We use the equation already used by Schumann, Horiuti, and Yoshizawa, among others (see Sect. 4.3.2):

$$\frac{\partial q^2_{\rm sgs}}{\partial t} + \frac{\partial \overline{u}_j q^2_{\rm sgs}}{\partial x_j} = -\tau_{ij}\overline{S}_{ij} - C_1\frac{\left(q^2_{\rm sgs}\right)^{3/2}}{\overline{\Delta}} + C_2\frac{\partial}{\partial x_j}\left(\overline{\Delta}\sqrt{q^2_{\rm sgs}}\frac{\partial q^2_{\rm sgs}}{\partial x_j}\right) + \nu\frac{\partial^2 q^2_{\rm sgs}}{\partial x_j \partial x_j}, \tag{4.241}$$

in which the constants C_1 and C_2 are computed by a constrained localized dynamic procedure described above. The dynamic constant $C_{\rm d}$ is computed by a localized dynamic procedure.

This model ensures that the kinetic energy $q^2_{\rm sgs}$ will remain positive, *i.e.* that the subgrid scale spectrum will be realizable. This property ensures that the dynamic constant cannot remain negative too long and thereby destabilize the simulation. However, finer analysis shows that the realizability conditions concerning the subgrid tensor τ (see Sect. 3.3.5) are verified only on the condition:

$$-\frac{\sqrt{q^2_{\rm sgs}}}{3\overline{\Delta}|s_\gamma|} \leq C_{\rm d} \leq \frac{\sqrt{q^2_{\rm sgs}}}{3\overline{\Delta}s_\alpha} \quad , \tag{4.242}$$

where s_α and s_γ are, respectively, the largest and smallest eigenvalues of the strain rate tensor $\overline{S}$. The model proposed therefore does not ensure the realizability of the subgrid tensor.

The two constants C_1 and C_2 are computed using an extension of the constrained localized dynamic procedure. To do this, we express the kinetic energy $Q^2_{\rm sgs}$ evolution equation as:

$$\frac{\partial Q^2_{\rm sgs}}{\partial t} + \frac{\partial \widetilde{\overline{u}}_j Q^2_{\rm sgs}}{\partial x_j} = -T_{ij}\widetilde{\overline{S}}_{ij} - C_1\frac{\left(Q^2_{\rm sgs}\right)^{3/2}}{\widetilde{\overline{\Delta}}} + C_2\frac{\partial}{\partial x_j}\left(\sqrt{Q^2_{\rm sgs}}\frac{\partial Q^2_{\rm sgs}}{\partial x_j}\right) + \nu\frac{\partial^2 Q^2_{\rm sgs}}{\partial x_j \partial x_j}. \tag{4.243}$$

One variant of the Germano's relation relates the subgrid kinetic energy flux f_j to its analog at the level of the test filter F_j:

$$F_j - \widetilde{f}_j = Z_j \equiv \widetilde{\overline{u}}_j(\overline{p} + \widetilde{q^2_{\rm sgs}} + \widetilde{\overline{u}_i\overline{u}_i}/2) - \overline{u}_j(\overline{p} + \widetilde{q^2_{\rm sgs}} + \widetilde{\overline{u}_i\overline{u}_i}/2) \quad , \tag{4.244}$$

in which $\overline{p}$ is the resolved pressure.

To determine the constant C_2, we substitute in this relation the modeled fluxes:

$$f_j = C_2\overline{\Delta}\sqrt{q^2_{\rm sgs}}\frac{\partial q^2_{\rm sgs}}{\partial x_j} \quad , \tag{4.245}$$

$$F_j = C_2\widetilde{\overline{\Delta}}\sqrt{Q^2_{\rm sgs}}\frac{\partial Q^2_{\rm sgs}}{\partial x_j} \quad , \tag{4.246}$$

which leads to:

$$Z_j = X_j C_2 - \widetilde{Y_j C_2} \quad , \tag{4.247}$$

in which

$$X_j = \widetilde{\overline{\Delta}}\sqrt{Q^2_{\rm sgs}}\frac{\partial Q^2_{\rm sgs}}{\partial x_j} \quad , \tag{4.248}$$

$$Y_j = \overline{\Delta}\sqrt{q^2_{\rm sgs}}\frac{\partial q^2_{\rm sgs}}{\partial x_j} \quad . \tag{4.249}$$

Using the same method as was explained for the localized dynamic procedure, the constant C_2 is evaluated by minimizing the quantity:

$$\int \left(Z_j - X_j C_2 + \widetilde{Y_j C_2}\right)\left(Z_j - X_j C_2 + \widetilde{Y_j C_2}\right) \quad . \tag{4.250}$$

By analogy with the preceding developments, the solution is obtained in the form:

$$C_2(\mathbf{x}) = \left[f_{C_2}(\mathbf{x}) + \int \mathcal{K}_{C_2}(\mathbf{x},\mathbf{y})C_2(\mathbf{y})d^3\mathbf{y}\right]_+ \quad , \tag{4.251}$$

in which:

$$f_{C_2}(\mathbf{x}) = \frac{1}{X_j(\mathbf{x})X_j(\mathbf{x})}\left(X_j(\mathbf{x})Z_j(\mathbf{x}) - Y_j(\mathbf{x})\int Z_j(\mathbf{y})G(\mathbf{x}-\mathbf{y})d^3\mathbf{y}\right) \quad , \tag{4.252}$$

$$\mathcal{K}_{C_2}(\mathbf{x},\mathbf{y}) = \frac{\mathcal{K}^{C_2}_{\mathcal{A}}(\mathbf{x},\mathbf{y}) + \mathcal{K}^{C_2}_{\mathcal{A}}(\mathbf{y},\mathbf{x}) - \mathcal{K}^{C_2}_{\mathcal{S}}(\mathbf{x},\mathbf{y})}{X_j(\mathbf{x})X_j(\mathbf{x})} \quad , \tag{4.253}$$

in which

$$\mathcal{K}_{\mathcal{A}}^{C_2}(\mathbf{x},\mathbf{y}) = X_j(\mathbf{x})Y_j(\mathbf{y})G(\mathbf{x}-\mathbf{y}) \quad , \tag{4.254}$$

$$\mathcal{K}_{\mathcal{S}}^{C_2}(\mathbf{x},\mathbf{y}) = Y_j(\mathbf{x})Y_j(\mathbf{y}) \int G(\mathbf{z}-\mathbf{x})G(\mathbf{z}-\mathbf{y})d^3\mathbf{z} \quad . \tag{4.255}$$

This completes the computation of constant C_2. To determine the constant C_1, we substitute (4.240) in (4.243) and get:

$$\frac{\partial \widetilde{q_{\text{sgs}}^2}}{\partial t} + \frac{\partial \widetilde{\overline{u}_j q_{\text{sgs}}^2}}{\partial x_j} = -E\frac{\partial F_j}{\partial x_j} + \nu\frac{\partial^2 \widetilde{q_{\text{sgs}}^2}}{\partial x_j \partial x_j} \quad , \tag{4.256}$$

in which E is defined as:

$$E = T_{ij}\widetilde{\overline{S}}_{ij} + \frac{C_1(Q_{\text{sgs}}^2)^{3/2}}{\widetilde{\overline{\Delta}}} - \nu\frac{1}{2}\frac{\partial^2 L_{ii}}{\partial x_j \partial x_j} + \frac{1}{2}\left(\frac{\partial L_{ii}}{\partial t} + \frac{\partial \widetilde{\overline{u}}_j L_{ii}}{\partial x_j}\right) \quad . \tag{4.257}$$

Applying the test filter to relation (4.241), we get:

$$\frac{\partial \widetilde{q_{\text{sgs}}^2}}{\partial t} + \frac{\partial \widetilde{\overline{u}_j q_{\text{sgs}}^2}}{\partial x_j} = -\tau_{ij}\widetilde{\overline{S}}_{ij} - \left(C_1\frac{\widetilde{(q_{\text{sgs}}^2)^{3/2}}}{\overline{\Delta}}\right) + \frac{\partial \widetilde{f}_j}{\partial x_j} + \nu\frac{\partial^2 \widetilde{q_{\text{sgs}}^2}}{\partial x_j \partial x_j} \quad . \tag{4.258}$$

By eliminating the term $\partial \widetilde{q_{\text{sgs}}^2}/\partial t$ between relations (4.256) and (4.258), then replacing the quantity $F_j - \widetilde{f}_j$ by its expression (4.244) and the quantity T_{ij} by its value as provided by the Germano identity, we get:

$$\chi = \phi C_1 - \widetilde{\psi C_1} \quad , \tag{4.259}$$

in which

$$\chi = \widetilde{\tau_{ij}\overline{S}_{ij}} - \widetilde{\tau}_{ij}\widetilde{\overline{S}}_{ij} - L_{ij}\widetilde{\overline{S}}_{ij} + \frac{\partial \rho_j}{\partial x_j} - \frac{1}{2}D_t L_{ii} + \frac{1}{2}\nu\frac{\partial^2 L_{ii}}{\partial x_j \partial x_j} \quad , \tag{4.260}$$

$$\phi = (Q_{\text{sgs}}^2)^{3/2}/\widetilde{\overline{\Delta}} \quad , \tag{4.261}$$

$$\psi = (q_{\text{sgs}}^2)^{3/2}/\overline{\Delta} \quad , \tag{4.262}$$

and

$$\rho_j = \widetilde{\overline{u}}_j(\overline{p} + \widetilde{\overline{u}_i\overline{u}_i}/2) - \overline{u}_j(\overline{p} + \widetilde{\overline{u}_i\overline{u}_i}/2) \quad . \tag{4.263}$$

The symbol D_t designates the material derivative $\partial/\partial t + \widetilde{\overline{u}}_j\partial/\partial x_j$. The constant C_1 is computed by minimizing the quantity

$$\int \left(\chi - \phi C_1 + \widetilde{\psi C_1}\right)\left(\chi - \phi C_1 + \widetilde{\psi C_1}\right) \quad , \tag{4.264}$$

by a constrained localized dynamic procedure, which is written:

$$C_1(\mathbf{x}) = \left[f_{C_1}(\mathbf{x}) + \int \mathcal{K}_{C_1}(\mathbf{x},\mathbf{y})C_1(\mathbf{y})d^3\mathbf{y}\right]_+ \quad , \tag{4.265}$$

in which

$$f_{C_1}(\mathbf{x}) = \frac{1}{\phi(\mathbf{x})\phi(\mathbf{x})}\left(\phi(\mathbf{x})\chi(\mathbf{x}) - \psi(\mathbf{x})\int \chi(\mathbf{y})G(\mathbf{x}-\mathbf{y})d^3\mathbf{y}\right) \quad , \tag{4.266}$$

$$\mathcal{K}_{C_1}(\mathbf{x},\mathbf{y}) = \frac{\mathcal{K}_{\mathcal{A}}^{C_1}(\mathbf{x},\mathbf{y}) + \mathcal{K}_{\mathcal{A}}^{C_1}(\mathbf{y},\mathbf{x}) - \mathcal{K}_{\mathcal{S}}^{C_1}(\mathbf{x},\mathbf{y})}{\phi(\mathbf{x})\phi(\mathbf{x})} \quad , \tag{4.267}$$

in which

$$\mathcal{K}_{\mathcal{A}}^{C_1}(\mathbf{x},\mathbf{y}) = \phi(\mathbf{x})\psi(\mathbf{y})G(\mathbf{x}-\mathbf{y}) \quad , \tag{4.268}$$

$$\mathcal{K}_{\mathcal{S}}^{C_1}(\mathbf{x},\mathbf{y}) = \psi(\mathbf{x})\psi(\mathbf{y}) \int G(\mathbf{z}-\mathbf{x})G(\mathbf{z}-\mathbf{y})d^3\mathbf{z} \quad , \tag{4.269}$$

which completes the computation of the constant C_1.

4.4.3 Stochastic Models

Models belonging to this category are based on introducing a random forcing term into the momentum equations. It should be noted that this random character does not reflect the space-time correlation scales of the subgrid fluctuations, which limits the physical validity of this approach and can raise numerical stability problems. It does, however, obtain forcing term formulations at low algorithmic cost. The models described here are:

1. Bertoglio's model in the spectral space (p.132). The forcing term is constructued using a stochastic process, which is designed in order to induce the desired backward energy flux and to possess a finite correlation time scale. This is the only random model for the backward cascade deerived in the spectral space.
2. Leith's model (p.133). The forcing term is represented by an acceleration vector deriving from a vector potential, whose amplitude is evaluated by simple dimensional arguments. The backward cascade is completely decoupled from forward cascade here: there is no control on the realizability of the subgrid scales.

3. Mason–Thomson model (p.135), which can be considered as an improvement of the preceding model. The evaluations of the vector potential amplitude and subgrid viscosity modeling the forward cascade are coupled, so as to ensure that the local equilibrium hypothesis is verified. This ensures that the subgrid kinetic energy remains positive.
4. Schumann model (p.136), in which the backward cascade is represented not as a force deriving from a vector potential but rather as the divergence of a tensor constructed from a random solenoidal velocity field whose kinetic energy is equal to the subgrid kinetic energy.
5. Stochastic dynamic model (p.137), which makes it possible to calculate the subgrid viscosity and a random forcing term simultaneously and dynamically. This coupling guarantees that the subgrid scales are realizable, but at the cost of a considerable increase in the algorithmic complexity of the model.

Bertoglio Model. Bertoglio and Mathieu [22, 23] propose a spectral stochastic subgrid model based on the EDQNM analysis. This model appears as a new source term $f_i(\mathbf{k},t)$ in the filtered mometum equations, and is evaluated as a stochastic process. The following constraints are enforced:

- f must not modify the velocity field incompressibility, i.e. $k_i f_i(\mathbf{k},t)=0$;
- f will have a Gaussian probability density function;
- The correlation time of f, noted t_f, is finite;
- f must induce the desired effect on the statistical second-order moments of the resolved velocity field:

$$\langle f_i(\mathbf{k},t)\overline{\widehat{u}}_j^*(\mathbf{k},t)+f_j(\mathbf{k},t)\overline{\widehat{u}}_i(\mathbf{k},t)\rangle = T_{ij}^-(\mathbf{k},t)\left(\frac{2\pi}{L}\right)^3 \quad , \tag{4.270}$$

where $T_{ij}^-(\mathbf{k},t)$ is the exact backward transfer term appearing in the variation equation for $\langle\overline{\widehat{u}}_i(\mathbf{k},t)\overline{\widehat{u}}_j^*(\mathbf{k},t)\rangle$ and L the size of the computational domain in physical space.

Assuming that the response function of the simulated field is isotropic and independent of f, and that the time correlations exhibit an exponential decay, we get the following velocity-independent relation:

$$\langle f_i(\mathbf{k},t)f_j^*(\mathbf{k},t)+f_i^*(\mathbf{k},t)f_j(\mathbf{k},t)\rangle = T_{ij}^-(\mathbf{k},t)\left(\frac{2\pi}{L}\right)^3\left(\frac{1}{\theta(\mathbf{k},t)}+\frac{1}{t_f}\right) \quad , \tag{4.271}$$

where $\theta(\mathbf{k},t)$ is a relaxation time evaluated from the resolved scales. We now have to compute the stochastic variable f_i. The authors propose the following algorithm, which is based on three random variables a, b and c:

$$f_1^{(n+1)} = \left(1-\frac{\Delta t}{t_f}\right)f_1^{(n)} + \sqrt{h_{11}^{(n)}}\beta_{11}^{(n+1)}\sqrt{\frac{\Delta t}{t_f}}\exp(\mathrm{i}2\pi a^{(n+1)}) + \sqrt{h_{22}^{(n)}}\beta_{12}^{(n+1)}\sqrt{\frac{\Delta t}{t_f}}\exp(\mathrm{i}2\pi c^{(n+1)}) \quad , \tag{4.272}$$

$$f_2^{(n+1)} = \left(1-\frac{\Delta t}{t_f}\right)f_2^{(n)} + \sqrt{h_{22}^{(n)}}\beta_{22}^{(n+1)}\sqrt{\frac{\Delta t}{t_f}}\exp(\mathrm{i}2\pi b^{(n+1)}) + \sqrt{h_{11}^{(n)}}\beta_{21}^{(n+1)}\sqrt{\frac{\Delta t}{t_f}}\exp(\mathrm{i}2\pi c^{(n+1)}) \quad , \tag{4.273}$$

where the supserscipt (n) denotes the value at the nth time step, Δt is the value of the time step, and $h_{ij}(\mathbf{k},t)=\langle f_i(\mathbf{k},t)f_j^*(\mathbf{k},t)\rangle$. Moreover, we get the complementary set of equations, which close the system:

$$(\beta_{11}^{(n+1)})^2 = \frac{1}{h_{11}^{(n)}}\left((h_{11}^{(n+1)}-h_{11}^{(n)})\frac{t_f}{\Delta t}-h_{22}^{(n)}(\beta_{12}^{(n+1)})^2\right) + 2-\frac{\Delta t}{t_f} \quad , \tag{4.274}$$

$$(\beta_{22}^{(n+1)})^2 = \frac{1}{h_{22}^{(n)}}\left((h_{22}^{(n+1)}-h_{22}^{(n)})\frac{t_f}{\Delta t}-h_{11}^{(n)}(\beta_{21}^{(n+1)})^2\right) + 2-\frac{\Delta t}{t_f} \quad , \tag{4.275}$$

$$\beta_{12}^{(n+1)}\beta_{12}^{(n+1)} = \frac{1}{\sqrt{h_{11}^{(n)}h_{11}^{(n)}}}\left((h_{12}^{(n+1)}-h_{12}^{(n)})\frac{t_f}{\Delta t} + h_{12}^{(n)}\left(2-\frac{\Delta t}{t_f}\right)\right) \quad , \tag{4.276}$$

$$(\beta_{21}^{(n+1)})^2 = (\beta_{12}^{(n+1)})^2 \quad , \tag{4.277}$$

which completes the description of the model. The resulting random force satisfies all the cited constraints, but it requires the foreknowledge of the h_{ij} tensor. This tensor is evaluated using the EDQNM theory, which requires the spectrum of the subgrid scales to be known. To alleviate this problem, arbitrary form of the spectrum can be employed.

Leith Model. A stochastic backward cascade model expressed in the physical space was derived by Leith in 1990 [184]. This model takes the form of a random forcing term that is added to the momentum equations. This term is computed at each point in space and each time step with the introduction of a vector potential ϕ^{b} for the acceleration, in the form of a white isotropic noise in space and time. The random forcing term with null divergence $\mathbf{f}^{\mathrm{b}}$ is deduced from this vector potential.

We first assume that the space and time auto-correlation scales of the subgrid modes are small compared with the cutoff lengths in space $\overline{\Delta}$ and in time Δt associated with the filter[25]. This way, the subgrid modes appear to be de-correlated in space and time. The correlation at two points and two times of the vector potential ϕ^{b} is then expressed:

$$\langle \phi_i^{\mathrm{b}}(\mathbf{x},t)\phi_k^{\mathrm{b}}(\mathbf{x}',t')\rangle = \sigma(\mathbf{x},t)\delta(\mathbf{x}-\mathbf{x}')\delta(t-t')\delta_{ik} \quad , \tag{4.278}$$

in which σ is the variance. This is computed as:

$$\sigma(\mathbf{x},t) = \frac{1}{3}\int dt' \int d^3\mathbf{x}' \langle \phi_k^{\mathrm{b}}(\mathbf{x},t)\phi_k^{\mathrm{b}}(\mathbf{x}',t')\rangle \quad . \tag{4.279}$$

Simple dimensional reasoning shows that:

$$\sigma(\mathbf{x},t) \approx |\overline{S}|^3\overline{\Delta}^7 \quad . \tag{4.280}$$

Also, as the vector potential appears as a white noise in space and time at the fixed resolution level, the integral (4.279) is written:

$$\sigma(\mathbf{x},t) = \frac{1}{3}\langle \phi_k^{\mathrm{b}}(\mathbf{x},t)\phi_k^{\mathrm{b}}(\mathbf{x},t)\rangle \overline{\Delta}^3 \Delta t \quad . \tag{4.281}$$

Considering relations (4.280) and (4.281), we get:

$$\langle \phi_k^{\mathrm{b}}(\mathbf{x},t)\phi_k^{\mathrm{b}}(\mathbf{x},t)\rangle \approx |\overline{S}|^3\overline{\Delta}^4 \frac{1}{\Delta t} \quad . \tag{4.282}$$

The shape proposed for the kth component of the vector potential is:

$$\phi_k^{\mathrm{b}} = C_{\mathrm{b}}|\overline{S}|^{3/2}\overline{\Delta}^2 \Delta t^{-1/2} g \quad , \tag{4.283}$$

in which C_{b} is a constant of the order of unity, Δt the simulation time cutoff length (*i.e.* the time step), and g the random Gaussian variable of zero average and variance equal to unity. The vector $\mathbf{f}^{\mathrm{b}}$ is then computed by taking the rotational of the vector potential, which guarantees that it is solenoidal.

In practice, Leith sets the value of the constant C_{b} at 0.4 and applies a spatial filter with a cutoff length of $2\overline{\Delta}$, so as to ensure better algorithm stability.

[25] We again find here a total scale separation hypothesis that is not verified in reality.

Mason–Thomson Model. A similar model is proposed by Mason and Thomson [223]. The difference from the Leith model resides in the scaling of the vector potential. By calling Δ_{f} and $\overline{\Delta}$ the characteristic lengths of the subgrid scales and spatial filter, respectively, the variants of the resolved stresses due to the subgrid fluctuations is, if $\Delta_{\mathrm{f}} \ll \overline{\Delta}$, of the order of $(\Delta_{\mathrm{f}}/\overline{\Delta})^3 u_{\mathrm{e}}^4$, in which u_{e} is the characteristic subgrid velocity. The amplitude a of the fluctuations in the gradients of the stresses is:

$$a \approx \frac{\Delta_{\mathrm{f}}^{3/2}}{\overline{\Delta}^{5/2}} u_{\mathrm{e}}^2 \quad , \tag{4.284}$$

which is also the amplitude of the associated acceleration. The corresponding kinetic energy variation rate of the resolved scales, q_{r}^2, is estimated as:

$$\frac{\partial q_{\mathrm{r}}^2}{\partial t} \approx a^2 t_{\mathrm{e}} \approx \frac{\Delta_{\mathrm{f}}^3}{\overline{\Delta}^5} u_{\mathrm{e}}^4 t_{\mathrm{e}} \quad , \tag{4.285}$$

in which t_{e} is the characteristic time of the subgrid scales. As $t_{\mathrm{e}} \approx \Delta_{\mathrm{f}}/u_{\mathrm{e}}$ and the dissipation rate is evaluated by dimensional arguments as $\varepsilon \approx u_{\mathrm{e}}^3/\Delta_{\mathrm{f}}$, we can say:

$$\frac{\partial q_{\mathrm{r}}^2}{\partial t} = C_{\mathrm{b}} \frac{\Delta_{\mathrm{f}}^5}{\overline{\Delta}^5}\varepsilon \quad . \tag{4.286}$$

The ratio $\Delta_{\mathrm{f}}/\overline{\Delta}$ is evaluated as the ratio of the subgrid scale mixing length to the filter cutoff length, and is thus equal to the constant of the subgrid viscosity models discussed in Sect. 4.3.2. Previous developments have shown that this constant is not unequivocally determinate, but that it is close to 0.2. The constant C_{b} is evaluated at 1.4 by an EDQNM analysis.

The dissipation rate that appears in equation (4.286) is evaluated in light of the backward cascade. The local subgrid scale equilibrium hypothesis is expressed by:

$$-\tau_{ij}\overline{S}_{ij} = \varepsilon + C_{\mathrm{b}} \frac{\Delta_{\mathrm{f}}^5}{\overline{\Delta}^5}\varepsilon \quad , \tag{4.287}$$

in which τ_{ij} is the subgrid tensor. The term on the left represents the subgrid kinetic energy production, the first term in the right-hand side the dissipation, and the last term the energy loss to the resolved scales by the backward cascade. The dissipation rate is evaluated using this last relation:

$$\varepsilon = \frac{-\tau_{ij}\overline{S}_{ij}}{1+(\Delta_{\mathrm{f}}/\overline{\Delta})^5} \quad , \tag{4.288}$$

which completes the computation of the right-hand side of equation (4.286), with the tensor τ_{ij} being evaluated using a subgrid viscosity model. This equation can be re-written as:

$$\frac{\partial q_r^2}{\partial t} = \sigma_a^2 \Delta t \quad , \tag{4.289}$$

in which σ_a^2 is the sum of the variances of the acceleration component amplitudes. From the equality of the two relations (4.286) and (4.289), we can say:

$$\sigma_a^2 = C_b \frac{\Delta_f^5}{\overline{\Delta}^5} \frac{\varepsilon}{\Delta t} \quad . \tag{4.290}$$

The vector potential scaling factor a and σ_a^2 are related by:

$$a = \sqrt{\sigma_a^2 \frac{\Delta t}{t_e}} \quad . \tag{4.291}$$

To complete the model, we now have to evaluate the ratio of the subgrid scale characteristic time to the time resolution scale. This is done simply by evaluating the characteristic time t_e from the subgrid viscosity ν_{sgs} computed by the model used, to reflect the cascade:

$$t_e = \frac{\Delta_f^2}{\nu_{sgs}} \quad , \tag{4.292}$$

which completes the description of the model, since the rest of the procedure is the same as what Leith defined.

Schumann Model. Schumann proposed a stochastic model for subgrid tensor fluctuations that originate the backward cascade of kinetic energy [299]. The subgrid tensor τ is represented as the sum of a turbulent viscosity model and a stochastic part R^{st}:

$$\tau_{ij} = \nu_{sgs} \overline{S}_{ij} + \frac{2}{3} q_{sgs}^2 \delta_{ij} + R_{ij}^{st} \quad . \tag{4.293}$$

The average random stresses R_{ij}^{st} are zero:

$$\langle R_{ij}^{st} \rangle = 0 \quad . \tag{4.294}$$

They are defined as:

$$R_{ij}^{st} = \gamma_m \left(v_i v_j - \frac{2}{3} q_{sgs}^2 \delta_{ij} \right) \quad , \tag{4.295}$$

in which γ_m is a parameter and v_i a random velocity. From dimensional arguments, we can define this as:

$$v_i = \sqrt{\frac{2 q_{sgs}^2}{3}} g_i \quad , \tag{4.296}$$

in which g_i is a white random number in space and has a characteristic correlation time τ_v:

$$\langle g_i \rangle = 0 \quad , \tag{4.297}$$

$$\langle g_i(\mathbf{x},t) g_j(\mathbf{x}',t') \rangle = \delta_{ij} \delta(\mathbf{x}-\mathbf{x}') \exp(|t-t'|/\tau_v) \quad . \tag{4.298}$$

The v_i field is made solenoidal by applying a projection step. We note that the time scale τ_v is such that:

$$\tau_v \sqrt{q_{sgs}^2}/\overline{\Delta} \approx 1 \quad . \tag{4.299}$$

The parameter γ_m determines the portion of random stresses that generate the backward cascade. Assuming that only the scales belonging to the interval $[k_c, nk_c]$ are active, for a spectrum of slope of $-m$ we get:

$$\gamma_m^2 = \frac{\int_{k_c}^{nk_c} k^{-2m} dk}{\int_{k_c}^{\infty} k^{-2m} dk} = 1 - n^{1-2m} \quad . \tag{4.300}$$

For $n = 2$ and $m = 5/3$, we get $\gamma_m = 0.90$. The subgrid kinetic energy q_{sgs}^2 is evaluated from the subgrid viscosity model.

Stochastic Localized Dynamic Model. A localized dynamic procedure including a stochastic forcing term was proposed by Carati *et al.* [47]. The contribution of the subgrid terms in the momentum equation appears here as the sum of a subgrid viscosity model, denoted $C_d \beta_{ij}$ using the notation of Sect. 4.3.3, which models the energy cascade, and a forcing term denoted $\mathbf{f}$:

$$\frac{\partial \tau_{ij}}{\partial x_j} = \frac{\partial C_d \beta_{ij}}{\partial x_j} + f_i \quad . \tag{4.301}$$

The β_{ij} term can be computed using any subgrid viscosity model. The force $\mathbf{f}$ is chosen in the form of a white noise in time with null divergence in space. The correlation of this term at two points in space and two times is therefore expressed:

$$\langle f_i(\mathbf{x},t) f_j(\mathbf{x}',t') \rangle = A^2(\mathbf{x},t) H_{ij}(\mathbf{x}-\mathbf{x}') \delta(t-t') \quad . \tag{4.302}$$

The statistical average here is an average over all the realizations of f conditioned by a given velocity field $\mathbf{u}(\mathbf{x},t)$. The factor A^2 is such that $H_{ii}(0) = 1$. Since a stochastic term has been introduced into the subgrid model, the residual E_{ij} on which the dynamic procedure for computing the constant C_d is founded also possesses a stochastic nature. This property will therefore be shared by the dynamically computed constant, which is not acceptable. To find the original properties of the dynamic constant, we take a statistical average of the residual, denoted $\langle E_{ij} \rangle$, which gets rid of the random terms. The constant of the subgrid viscosity model is computed by a localized dynamic procedure based on the statistical average of the residual, which is written:

$$\langle E_{ij} \rangle = L_{ij} + \widetilde{C_{\rm d}\beta_{ij}} - C_{\rm d}\alpha_{ij} \quad . \tag{4.303}$$

The amplitude of the random forcing term can also be computed dynamically. To bring out the non-zero contribution of the stochastic term in the statistical average, we base this new procedure on the resolved kinetic energy balance at the level of the test filter $Q_{\rm r}^2 = \widetilde{\overline{u}_i}\widetilde{\overline{u}_i}/2$. The evolution equation of this quantity is obtained in two different forms (only the pertinent terms are detailed, the others are symbolized):

$$\frac{\partial Q_{\rm r}^2}{\partial t} = ... - \widetilde{\overline{u}_i}\frac{\partial}{\partial x_j}\left(C_{\rm d}\alpha_{ij} + P\delta_{ij}\right) + \mathcal{E}_F \quad , \tag{4.304}$$

$$\frac{\partial Q_{\rm r}^2}{\partial t} = ... - \widetilde{\overline{u}_i}\frac{\partial}{\partial x_j}\left(\widetilde{C_{\rm d}\beta_{ij}} + L_{ij} + \widetilde{p}\delta_{ij}\right) + \mathcal{E}_{\widetilde{f}} \quad . \tag{4.305}$$

The pressure terms P and p are in equilibrium with the velocity fields $\widetilde{\overline{\mathbf{u}}}$ and $\overline{\mathbf{u}}$, respectively. The quantities $\mathcal{E}_F$ and $\mathcal{E}_{\widetilde{f}}$ are the backward cascade energy injections associated, respectively, with the forcing term $\mathbf{F}$ computed directly at the level of the test filter, and with the forcing term $\widetilde{\mathbf{f}}$ computed at the first level and then filtered. The difference between equations (4.304) and (4.305) leads to:

$$Z \equiv \mathcal{E}_F - \mathcal{E}_{\widetilde{f}} - g \neq 0 \quad , \tag{4.306}$$

in which the fully known term g is of the form:

$$g = \widetilde{\overline{u}_i}\frac{\partial}{\partial x_j}\left(C_{\rm d}\alpha_{ij} + P\delta_{ij} - \widetilde{C_{\rm d}\beta_{ij}} - L_{ij} - \widetilde{p}\delta_{ij}\right) \quad . \tag{4.307}$$

The quantity Z plays a role for the kinetic energy that is analogous to the residual E_{ij} for the momentum. Minimizing the quantity

$$\mathcal{Z} = \int \langle Z \rangle^2 \tag{4.308}$$

can thus serve as a basis for defining a dynamic procedure for evaluating the stochastic forcing.

To go any further, the shape of the $\mathbf{f}$ term has to be specified. To simplify the use, we assume that the correlation length of $\mathbf{f}$ is small compared with the cutoff length $\overline{\Delta}$. The function $\mathbf{f}$ thus appears as de-correlated in space, which is reflected by:

$$\langle \mathcal{E}_{\rm f} \rangle = \frac{1}{2}A^2(\mathbf{x}, t) \quad . \tag{4.309}$$

In order to be able to calculate $\mathcal{E}_{\rm f}$ dynamically, we assume that the backward cascade is of equal intensity at the two filtering levels considered, *i.e.*

$$\langle \mathcal{E}_{\rm f} \rangle = \langle \mathcal{E}_F \rangle \quad . \tag{4.310}$$

Also, since $\mathbf{f}$ is de-correlated at the $\widetilde{\overline{\Delta}}$ scale, we assume:

$$\mathcal{E}_{\widetilde{f}} \ll \langle \mathcal{E}_{\rm f} \rangle = \langle \mathcal{E}_F \rangle \quad , \tag{4.311}$$

which makes it possible to change relation (4.306) to become

$$\langle Z \rangle = \langle \mathcal{E}_F \rangle - g \quad . \tag{4.312}$$

We now choose $\mathbf{f}$ in the form:

$$f_i = P_{ij}(\mathcal{A}e_j) \quad , \tag{4.313}$$

in which e_j is a random isotropic Gaussian function, $\mathcal{A}$ a dimensioned constant that will play the same role as the subgrid viscosity model constant, and P_{ij} the projection operator on a space of zero divergence. We have the relations:

$$\langle e_i(\mathbf{x}, t) \rangle = 0 \quad , \tag{4.314}$$

$$\langle e_i(\mathbf{x}, t) e_i(\mathbf{x}', t') \rangle = \frac{1}{3}\delta_{ij}\delta(t - t')\delta(\mathbf{x} - \mathbf{x}') \quad . \tag{4.315}$$

Considering (4.313), (4.315) and (4.309), we get:

$$\langle \mathcal{E}_{\rm f} \rangle = \frac{1}{2}A^2 = \frac{1}{3}\mathcal{A}^2 \quad . \tag{4.316}$$

The computation of the model is completed by evaluating the constant $\mathcal{A}$ by a constrained localized dynamic procedure based on minimizing the functional (4.308), which can be re-written in the form:

$$\mathcal{Z}[\mathcal{A}] = \int \left(\frac{\mathcal{A}^2}{3} - g\right)^2 \quad . \tag{4.317}$$

5. Functional Modeling: Extension to Anisotropic Cases

5.1 Statement of the Problem

The developments of the previous chapters are all conducted in the isotropic framework, which implies that both the filter used and the flow are isotropic. They can be extended to anisotropic or inhomogeneous cases only by localizing the statistical relations in space and time and introducing heuristic procedures for adjusting the models. But when large-eddy simulation is applied to inhomogeneous flows, we very often have to use anisotropic grids, which corresponds to using a anisotropic filter. So there are two factors contributing to the violation of the hypotheses underlying the models presented so far: filter anisotropy (respectively inhomogeneity) and flow anisotropy (respectively inhomogeneity).

This chapter is devoted to extensions of the modeling to anisotropic cases. Two situations are considered: application of a anisotropic homogeneous filter to an isotropic homogeneous turbulent flow, and application of an isotropic filter to an anisotropic flow.

5.2 Application of Anisotropic Filter to Isotropic Flow

The filters considered in the following are anisotropic in the sense that the filter cutoff length is different in each direction of space. The different types of anisotropy possible for Cartesian filtering cells are represented in Fig. 5.1.

In order to use an anisotropic filter to describe an isotropic flow, we are first required to modify the subgrid models, because theoretical work and numerical experiments have shown that the resolved fields and the subgrid thus defined are anisotropic [159]. For example, for a mesh cell with an aspect ratio $\overline{\Delta}_2/\overline{\Delta}_1 = 8, \overline{\Delta}_3/\overline{\Delta}_1 = 4$, the subgrid stresses will differ from their values obtained with an isotropic filter by about ten percent. It is very important to note, though, that this anisotropy is an artifact due to the filter but that the dynamic of the subgrid scales still corresponds that of isotropic homogeneous turbulence.

On the functional modeling level, the problem is in determining the characteristic length that has to be used to compute the model.

Two approaches are available:

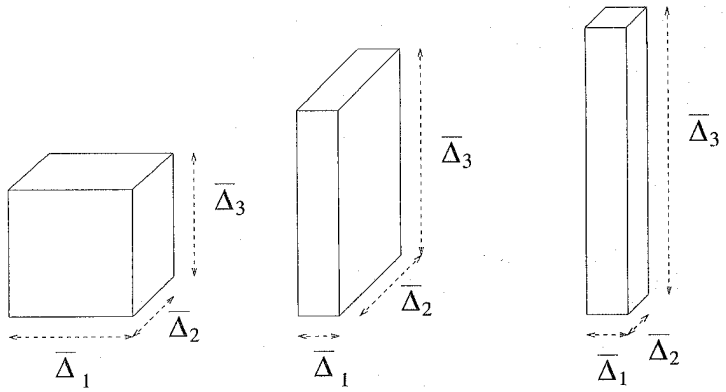

Fig. 5.1. Different types of filtering cells. Isotropic cell (on the left): $\overline{\Delta}_1 = \overline{\Delta}_2 = \overline{\Delta}_3$; pancake-type anisotropic cell (center): $\overline{\Delta}_1 \ll \overline{\Delta}_2 \approx \overline{\Delta}_3$; cigar-type anisotropic cell (right): $\overline{\Delta}_1 \approx \overline{\Delta}_2 \ll \overline{\Delta}_3$.

- The first consists in defining a single length scale for representing the filter. This lets us keep models analogous to those defined in the isotropic case, using for example scalar subgrid viscosities for representing the backward cascade process. This involves only a minor modification of the subgrid models since only the computation of the characteristic cutoff scale is modified. But it should be noted that such an approach can in theory be valid only for cases of low anisotropy, for which the different cutoff lengths are of the same order of magnitude.
- The second approach is based on the introduction of several characteristic length scales in the model. This sometimes entrains major modifications in the isotropic models, such as the definition of tensorial subgrid viscosities to represent the forward cascade process. In theory, this approach takes the filter anisotropy better into account, but complicates the modeling stage.

5.2.1 Scalar Models

These models are all of the generic form $\overline{\Delta} = \overline{\Delta}(\overline{\Delta}_1, \overline{\Delta}_2, \overline{\Delta}_3)$. We present here:

1. Deardorff's original model and its variants (p.142). These forms are empirical and have no theoretical basis. All we do is simply to show that they are consistent with the isotropic case, *i.e.* $\overline{\Delta} = \overline{\Delta}_1$ when $\overline{\Delta}_1 = \overline{\Delta}_2 = \overline{\Delta}_3$).
2. The model of Scotti *et al.* (p.143), which is based on a theoretical analysis considering a Kolmogorov spectrum with an anisotropic homogeneous filter. This model makes a complex evaluation possible of the filter cutoff length, but is limited to the case of Cartesian filtering cells.

Deardorff's Proposal. The method most widely used today is without doubt the one proposed by Deardorff [76], which consists in evaluating the filter cutoff length as the cube root of the volume V_Ω of the filtering cell Ω. Or, in the Cartesian case:

$$\overline{\Delta}(\mathbf{x}) = \left(\overline{\Delta}_1(\mathbf{x})\overline{\Delta}_2(\mathbf{x})\overline{\Delta}_3(\mathbf{x})\right)^{1/3} \quad , \tag{5.1}$$

in which $\overline{\Delta}_i(\mathbf{x})$ is the filter cutoff length in the ith direction of space at position $\mathbf{x}$.

Extensions of Deardorff's Proposal. Simple extensions of definition (5.1) are often used, but are limited to the case of Cartesian filtering cells:

$$\overline{\Delta}(\mathbf{x}) = \sqrt{(\overline{\Delta}_1^2(\mathbf{x}) + \overline{\Delta}_2^2(\mathbf{x}) + \overline{\Delta}_3^2(\mathbf{x}))/3} \quad , \tag{5.2}$$

$$\overline{\Delta}(\mathbf{x}) = \max\left(\overline{\Delta}_1(\mathbf{x}), \overline{\Delta}_2(\mathbf{x}), \overline{\Delta}_3(\mathbf{x})\right) \quad . \tag{5.3}$$

Proposal of Scotti et al. More recently, Scotti, Meneveau, and Lilly [305] proposed a new definition of $\overline{\Delta}$ based on an improved estimate of the dissipation rate ε in the anisotropic case. The filter is assumed to be anisotropic but homogeneous, *i.e.* the cutoff length is constant in each direction of space.

We define $\overline{\Delta}_{\max} = \max(\overline{\Delta}_1, \overline{\Delta}_2, \overline{\Delta}_3)$. Aspect ratios of less than unity, constructed from the other two cutoff lengths with respect to $\Delta_{\max}$, are denoted a_1 and a_2[1]. The form physically sought for the anisotropy correction is:

$$\overline{\Delta} = \overline{\Delta}_{\text{iso}} f(a_1, a_2) \quad , \tag{5.4}$$

in which $\overline{\Delta}_{\text{iso}}$ is Deardorff's isotropic evaluation computed by relation (5.1). Using the approximation:

$$\langle\varepsilon\rangle = \overline{\Delta}^2 \langle 2\overline{S}_{ij}\overline{S}_{ij}\rangle^{3/2} \quad , \tag{5.5}$$

and the following equality, which is valid for a Kolmogorov spectrum,

$$\langle\overline{S}_{ij}\overline{S}_{ij}\rangle = \langle\varepsilon\rangle^{2/3} \frac{K_0}{2\pi} \int |\widehat{G}(\mathbf{k})|^2 k^{-5/3} d^3\mathbf{k} \quad , \tag{5.6}$$

where $\widehat{G}(\mathbf{k})$ is the kernel of the anisotropic filter considered, after calculation we get:

$$\overline{\Delta} = \left(\frac{K_0}{2\pi} \int |\widehat{G}(\mathbf{k})|^2 k^{-5/3} d^3\mathbf{k}\right)^{-3/4} \quad . \tag{5.7}$$

Considering a sharp cutoff filter, we get the following approximate relation by integrating equation (5.7):

[1] For example, by taking $\Delta_{\max} = \overline{\Delta}_1$, we get $a_1 = \overline{\Delta}_2/\overline{\Delta}_1$ and $a_2 = \overline{\Delta}_3/\overline{\Delta}_1$.

$$f(a_1,a_2)=\cosh\sqrt{\frac{4}{27}\left[(\ln a_1)^2-\ln a_1\ln a_2+(\ln a_2)^2\right]}\quad . \tag{5.8}$$

It is interesting to note that the dynamic procedure (see Sect. 4.3.3) for the computation of the Smagorinsky constant can be interpreted as an implicit way to compute the $f(a_1,a_2)$ function [304]. Introducing the subgrid mixing length Δ_f, the Smagorinsky model reads

$$\begin{aligned}\nu_{\text{sgs}} &= \Delta_f^2|\overline{S}| &(5.9)\\ &= C_{\text{d}}\overline{\Delta}_{\text{iso}}^2|\overline{S}| &(5.10)\\ &= (C_{\text{S}}\overline{\Delta}_{\text{iso}}f(a_1,a_2))^2|\overline{S}| \quad , &(5.11)\end{aligned}$$

where C_{d} is the value of the constant computed using a dynamic procedure, and C_{S} the theoretical value of the Smagorinsky constant evaluated through the canonical analysis. A trivial identification leads to:

$$f(a_1,a_2)=\sqrt{C_{\text{d}}}/C_{\text{S}}\quad . \tag{5.12}$$

This interpretation is meaningful for positive values of the dynamic constant. A variant can be derived by using the anisotropy measure $f(a_1,a_2)$ instead of the isotropic one inside the dynamic procedure (see equation (5.10)), yielding new definitions of the tensors α_{ij} and β_{ij} appearing in the dynamic procedure (see Table 4.1). Taking the Smagorinsky model as an example, we get:

$$\beta_{ij}=-2(\overline{\Delta}_{\text{iso}}f(\overline{a}_1,\overline{a}_2))^2|\overline{S}|\overline{S}_{ij},\quad \alpha_{ij}=-2(\widetilde{\overline{\Delta}}_{\text{iso}}f(\widetilde{\overline{a}}_1,\widetilde{\overline{a}}_2))^2|\widetilde{\overline{S}}|\widetilde{\overline{S}}_{ij}\quad , \tag{5.13}$$

where $f(\overline{a}_1,\overline{a}_2)$ and $f(\widetilde{\overline{a}}_1,\widetilde{\overline{a}}_2)$ are the anisotropy measures associated to the first and second filtering levels, respectively. The corresponding formulation of the f function is now:

$$f(a_1,a_2)=\sqrt{C_{\text{d}}}/(C_{\text{S}}\overline{\Delta}_{\text{iso}})\quad . \tag{5.14}$$

5.2.2 Tensorial Models

The tensorial models presented in the following are constructed empirically, with no physical basis. They are justified only by intuition and only for highly anisotropic filtering cells of the cigar type, for example (see Fig. 5.1). Representing the filter by a single and unique characteristic length is no longer pertinent. The filter's characteristic scales and their inclusion in the subgrid viscosity model are determined intuitively. Two such models are described:

1. The model of Bardina *et al.* (p.145), which describes the geometry of the filtering cell by means of six characteristic lengths calculated from the inertia tensor of the filtering cell. This approach is completely general and is a applicable to all possible types of filtering cells (Cartesian, curvilinear, and other), but entrains a high complexification in the subgrid models.
2. The model of Zahrai *et al.* (p.146), which is applicable only to Cartesian cells and is simple to include in the subgrid viscosity models.

Proposal of Bardina et al.

Definition of a Characteristic Tensor. These authors [12] propose replacing the isotropic scalar evaluation of the cutoff length associated with the grid by an anisotropic tensorial evaluation linked directly to the filtering cell geometry: $V(\mathbf{x})=(\overline{\Delta}_1(\mathbf{x})\overline{\Delta}_2(\mathbf{x})\overline{\Delta}_3(\mathbf{x}))$. To do this, we introduce the moments of the inertia tensor $\mathcal{I}$ associated at each point $\mathbf{x}$:

$$\mathcal{I}_{ij}(\mathbf{x})=\frac{1}{V(\mathbf{x})}\int_V x_i x_j dV\quad . \tag{5.15}$$

Since the components of the inertia tensor are homogeneous at the square of a length, the tensor of characteristic lengths is obtained by taking the square root of them. In the case of a pancake filtering cell aligned with the axes of the Cartesian coordinate system, we get the diagonal matrix:

$$\mathcal{I}_{ij}=\frac{2}{3}\begin{pmatrix}\overline{\Delta}_1^2 & 0 & 0\\ 0 & \overline{\Delta}_2^2 & 0\\ 0 & 0 & \overline{\Delta}_3^2\end{pmatrix}\quad . \tag{5.16}$$

Application to the Smagorinsky Model. As we model only the anisotropic part of the subgrid tensor, the tensor $\mathcal{I}$ is decomposed into the sum of a spherical term $\mathcal{I}^{\text{i}}$ and an anisotropic term $\mathcal{I}^{\text{d}}$:

$$\mathcal{I}_{ij}=\mathcal{I}^{\text{i}}\delta_{ij}+(\mathcal{I}_{ij}-\mathcal{I}^{\text{i}}\delta_{ij})=\mathcal{I}^{\text{i}}\delta_{ij}+\mathcal{I}^{\text{d}}_{ij}\quad , \tag{5.17}$$

with

$$\mathcal{I}^{\text{i}}=\frac{1}{3}\mathcal{I}_{kk}=\frac{1}{3}(\overline{\Delta}_1^2+\overline{\Delta}_2^2+\overline{\Delta}_3^2)\quad . \tag{5.18}$$

Modifying the usual Smagorinsky model, the authors finally propose the following anisotropic tensorial model for deviator of the subgrid tensor τ:

$$\begin{aligned}\tau_{ij}-\frac{1}{3}\tau_{kk}\delta_{ij} &= C_1\mathcal{I}^{\text{i}}|\overline{S}|\overline{S}_{ij}\\ &+ C_2|\overline{S}|\left(\mathcal{I}_{ik}\overline{S}_{kj}+\mathcal{I}_{jk}\overline{S}_{ki}-\frac{1}{3}\mathcal{I}_{lk}\overline{S}_{kl}\delta_{ij}\right)\\ &+ C_3\frac{|\overline{S}|}{\mathcal{I}^{\text{i}}}\left(\mathcal{I}_{ik}\mathcal{I}_{jl}\overline{S}_{kl}-\frac{1}{3}\mathcal{I}_{mk}\mathcal{I}_{ml}\overline{S}_{kl}\delta_{ij}\right)\quad ,\end{aligned} \tag{5.19}$$

in which C_1, C_2 and C_3 are constants to be evaluated.

Proposal of Zahrai et al.

Principle. Zahrai *et al.* [364] proposed conserving the isotropic evaluation of the dissipation rate determined by Deardorff and further considering that this quantity is constant over each mesh cell:

$$\langle \varepsilon \rangle = \left(\overline{\Delta}_1(\mathbf{x}) \overline{\Delta}_2(\mathbf{x}) \overline{\Delta}_3(\mathbf{x}) \right)^{2/3} \langle 2 \overline{S}_{ij} \overline{S}_{ij} \rangle^{3/2} \quad . \tag{5.20}$$

On the other hand, when deriving the subgrid model, we consider that the filter's characteristic length in each direction is equal to the cutoff length in that direction. This procedure calls for the definition of a tensorial model for the subgrid viscosity.

Application to the Smagorinsky model. In the case of the Smagorinsky model, we get for component k:

$$\left(\nu_{\text{sgs}} \right)_k = C_1 (\overline{\Delta}_1 \overline{\Delta}_2 \overline{\Delta}_3)^{2/9} (\overline{\Delta}_k)^{4/3} \langle 2 \overline{S}_{ij} \overline{S}_{ij} \rangle^{3/2} \quad , \tag{5.21}$$

where C_1 is a constant.

5.3 Application of an Isotropic Filter to an Anisotropic Flow

We will now be examining the inclusion of subgrid scale anisotropy in the functional models.

The first part of this section presents theoretical results concerning subgrid scale anisotropy and the interaction mechanisms between the large and small scales in this case. These results are obtained either by the EDQNM theory or by asymptotic analysis of the triadic interactions.

The second part of the chapter describes the modifications that have been proposed for functional type subgrid models. Only models for the forward energy cascade will be presented, because no model for the backward cascade has yet been proposed in the anisotropic case.

5.3.1 Phenomenology of Inter-Scale Interactions

Anisotropic EDQNM Analysis. Aupoix [7] proposes a basic analysis of the effects of anisotropy in the homogeneous case using Cambon's anisotropic EDQNM model. The essential details of this model are given in Appendix B.

The velocity field $\mathbf{u}$ is decomposed as usual into average part $\langle \mathbf{u} \rangle$ and a fluctuating part $\mathbf{u}'$:

$$\mathbf{u} = \langle \mathbf{u} \rangle + \mathbf{u}' \quad . \tag{5.22}$$

To study anisotropic homogeneous flows, we define the spectral tensor

$$\Phi_{ij}(\mathbf{k}) = \langle \widehat{u}_i'^*(\mathbf{k}) \widehat{u}_j'(\mathbf{k}) \rangle \quad , \tag{5.23}$$

which is related to the double correlations in the physical space by the relation:

$$\langle u_i' u_j' \rangle(\mathbf{x}) = \int\int\int \Phi_{ij}(\mathbf{k}) d^3\mathbf{k} \quad . \tag{5.24}$$

Starting with the Navier–Stokes equations, we obtain the evolution equation (see Appendices A and B):

$$\begin{aligned} \left(\frac{\partial}{\partial t} + 2\nu k^2 \right) \Phi_{ij}(\mathbf{k}) \; + \; & \frac{\partial \langle u_i \rangle}{\partial x_l} \Phi_{jl}(\mathbf{k}) + \frac{\partial \langle u_j \rangle}{\partial x_l} \Phi_{il}(\mathbf{k}) \\ & - 2 \frac{\partial \langle u_l \rangle}{\partial x_m} \left(k_i \Phi_{jm}(\mathbf{k}) + k_j \Phi_{mi}(\mathbf{k}) \right) \\ & - \frac{\partial \langle u_l \rangle}{\partial x_m} \frac{\partial}{\partial k_m} \left(k_l \Phi_{ij}(\mathbf{k}) \right) \\ & = P_{il}(\mathbf{k}) T_{lj}(\mathbf{k}) + P_{jl}(\mathbf{k}) T_{li}^*(\mathbf{k}) \quad , \end{aligned} \tag{5.25}$$

where

$$T_{ij}(\mathbf{k}) = k_l \int\int\int \langle u_i(\mathbf{k}) u_l(\mathbf{p}) u_j(-\mathbf{k}-\mathbf{p}) \rangle d^3\mathbf{p} \quad , \tag{5.26}$$

and

$$P_{ij}(\mathbf{k}) = \left(\delta_{ij} - \frac{k_i k_j}{k^2} \right) \quad , \tag{5.27}$$

and where the * designates the complex conjugate number. We then simplify the equations by integrating the tensor Φ on spheres of radius k=cste:

$$\phi_{ij}(k) = \int \Phi_{ij}(\mathbf{k}) dA(\mathbf{k}) \quad , \tag{5.28}$$

and obtain the evolution equations:

$$\begin{aligned} \left(\frac{\partial}{\partial t} + 2\nu k^2 \right) \phi_{ij}(k) \; = \; & - \frac{\partial \langle u_i \rangle}{\partial x_k} \phi_{jl}(k) - \frac{\partial \langle u_j \rangle}{\partial x_l} \phi_{il}(k) \\ & + P_{ij}^{\text{l}}(k) + S_{ij}^{\text{l}}(k) + P_{ij}^{\text{nl}}(k) + S_{ij}^{\text{nl}}(k) \quad , \end{aligned} \tag{5.29}$$

where the terms $P^{\text{l}}, S^{\text{l}}, P^{\text{nl}}$ and S^{nl} are the linear pressure, linear transfer, non-linear pressure, and non-linear transfer contributions, respectively. The linear terms are associated with the action of the average velocity gradient, and the non-linear terms with the action of the turbulence on itself.

The expression of these terms and their closure by the anisotropic EDQNM approximation are given in Appendix B. Using these relations, Aupoix derives

an expression for the interaction between the modes corresponding to wave numbers greater than a given cutoff wave number k_c (*i.e.* the small or subgrid scales) and those associated with small wave numbers such that $k \leq k_c$ (*i.e.* the large or resolved scales). To obtain a simple expression for the coupling among the different scales by the non-linear terms P^{nl} and S^{nl}, we adopt the hypothesis that there exists a total separation of scales (in the sense defined in Sect. 4.3.2) between the subgrid and resolved modes, so that we can obtain the following two asymptotic forms:

$$\begin{aligned} P_{ij}^{nl}(k) &= -\frac{32}{175}k^4 \int_{k_c}^{\infty} \Theta_{0pp}\left[10 + a(p)\right] \frac{E^2(p)H_{ij}(p)}{p^2} dp \\ &+ \frac{16}{105}k^2 E(k) \int_{k_c}^{\infty} \Theta_{0pp} \left[(a(p)+3) p \frac{\partial}{\partial p}\left(E(p)H_{ij}(p)\right) \right. \\ &\left. + E(p)H_{ij}(p)\left(5\left\{a(p)+3\right\} + p\frac{\partial a(p)}{\partial p}\right)\right] dp \quad , \end{aligned} \tag{5.30}$$

$$\begin{aligned} S_{ij}^{nl}(k) &= 2k^4 \int_{k_c}^{\infty} \Theta_{0pp} \frac{E^2(p)}{p^2} \left[\frac{14}{15}\left(\frac{1}{3}\delta_{ij} + 2H_{ij}(p)\right) + \frac{8}{25}a(p)H_{ij}(p)\right] dp \\ &- 2k^2\phi_{ij}(k)\frac{1}{15}\int_{k_c}^{\infty} \Theta_{0pp}\left[5E(p) + p\frac{\partial E(p)}{\partial p}\right] dp \\ &- 2k^2 E(k) \int_{k_c}^{\infty} \Theta_{0pp}\left[\frac{2}{15}\left\{5E(p)H_{ij}(p) + p\frac{\partial}{\partial p}(E(p)H_{ij}(p))\right\}\right. \\ &\left. + E(p)H_{ij}(p)\left\{\frac{8}{15}(a(p)+3) + \frac{8}{25}a(p)\right\}\right] dp \quad , \end{aligned} \tag{5.31}$$

where $E(k)$ is the energy spectrum, defined as:

$$E(k) = \frac{1}{2}\phi_{ll}(k) \quad , \tag{5.32}$$

and $H_{ij}(k)$ the anisotropy spectrum:

$$H_{ij}(k) = \frac{\phi_{ij}(k)}{2E(k)} - \frac{1}{3}\delta_{ij} \quad . \tag{5.33}$$

It is easily verified that, in the isotropic case, H_{ij} cancels out by construction. The function $a(k)$ is a structural parameter that represents the anisotropic distribution on the sphere of radius k, and Θ_{kpq} the characteristic relaxation time evaluated by the EDQNM hypotheses. The expression of this term is given in Appendix B.

These equations can be simplified by using the asymptotic value of the structural parameter $a(k)$. By taking $a(k) = -4.5$, we get:

$$\begin{aligned} P_{ij}^{nl}(k) + S_{ij}^{nl}(k) &= k^4 \int_{k_c}^{\infty} \Theta_{0pp}\frac{E^2(p)}{p^2}\left[\frac{28}{45}\delta_{ij} - \frac{368}{175}H_{ij}(p)\right] dp \\ &- 2k^2\phi_{ij}(k)\frac{1}{15}\int_{k_c}^{\infty}\Theta_{0pp}\left[5E(p) + p\frac{\partial E(p)}{\partial p}\right] dp \\ &+ k^2 E(k)\int_{k_c}^{\infty}\Theta_{0pp}\left[\frac{1052}{525}E(p)H_{ij}(p)\right. \\ &\left. - \frac{52}{105}\frac{\partial}{\partial p}\left(E(p)H_{ij}(p)\right)\right] dp \quad . \end{aligned} \tag{5.34}$$

From this equation, it can be seen that the anisotropy of the small scales takes on a certain importance. In a case where the anisotropic spectrum has the same (resp. opposite) sign for the small scales as it does for the large, the term in k^4 constitutes a return of energy that has the effect of a return toward isotropy (resp. departure from isotropy), and the term in $k^2E(k)$ represents an backward energy cascade associated with an increasing anisotropy (resp. a return to isotropy). Lastly, the term in $k^2\phi_{ij}(k)$ is a term of isotropic drainage of energy to the large scales by the small, and represents here the energy cascade phenomenon modeled by the isotropic subgrid models.

Asymptotic Analysis of Triadic Interactions. Another analysis of inter-scale interactions in the isotropic case is the asymptotic analysis of triadic interactions [35, 356].

The evolution equation of the Fourier mode $\widehat{\mathbf{u}}(\mathbf{k})$ is written in the symbolic form:

$$\frac{\partial \widehat{\mathbf{u}}(\mathbf{k})}{\partial t} = \dot{\mathbf{u}}(\mathbf{k}) = \left[\dot{\mathbf{u}}(\mathbf{k})\right]_{nl} + \left[\dot{\mathbf{u}}(\mathbf{k})\right]_{vis} \quad , \tag{5.35}$$

where $\left[\dot{\mathbf{u}}(\mathbf{k})\right]_{nl}$ and $\left[\dot{\mathbf{u}}(\mathbf{k})\right]_{vis}$ represent, respectively, the non-linear terms associated with the convection and pressure, and the linear term associated with the viscous effects, defined as:

$$\left[\dot{\mathbf{u}}(\mathbf{k})\right]_{nl} = -\mathrm{i}\sum_{p} \widehat{\mathbf{u}}(\mathbf{p})_{\perp k}\left(\mathbf{k}\cdot\widehat{\mathbf{u}}(\mathbf{k}-\mathbf{p})\right) \quad , \tag{5.36}$$

with

$$\widehat{u}_i(\mathbf{p})_{\perp k} = \left(\delta_{ij} - \frac{k_i k_j}{k^2}\right)\widehat{u}_j(\mathbf{p}) \quad , \tag{5.37}$$

$$\left[\dot{\mathbf{u}}(\mathbf{k})\right]_{vis} = -\nu k^2 \widehat{\mathbf{u}}(\mathbf{k}) \quad . \tag{5.38}$$

The evolution equation of the modal energy, $e(\mathbf{k}) = \widehat{\mathbf{u}}(\mathbf{k})\cdot\widehat{\mathbf{u}}^*(\mathbf{k})$, is of the form:

$$\frac{\partial e(\mathbf{k})}{\partial t} = \widehat{\mathbf{u}}(\mathbf{k})\cdot\dot{\mathbf{u}}^*(\mathbf{k}) + cc = \left[\dot{e}(\mathbf{k})\right]_{nl} + \left[\dot{e}(\mathbf{k})\right]_{vis} \quad , \tag{5.39}$$

with

$$[\dot{e}(\mathbf{k})]_{\text{nl}} = -\mathrm{i}\sum_{p}[\widehat{\mathbf{u}}^*(\mathbf{k})\cdot\widehat{\mathbf{u}}(\mathbf{p})]\,[\mathbf{k}\cdot\widehat{\mathbf{u}}(\mathbf{k}-\mathbf{p})] + cc \quad , \tag{5.40}$$

$$[\dot{e}(\mathbf{k})]_{\text{vis}} = -2\nu k^2 e(\mathbf{k}) \quad , \tag{5.41}$$

where the symbol cc designates the complex conjugate number of the term that precedes it. The non-linear energy transfer term brings in three wave vectors ($\mathbf{k}, \mathbf{p}, \mathbf{q} = \mathbf{k}-\mathbf{p}$) and is consequently a linear sum of non-linear triadic interactions. We recall (see Sect. 4.1.2) that the interactions can be classified into various categories ranging from local interactions, for which the norms of the three wave vectors are similar (*i.e.* $k \sim p \sim q$), to distant interactions for which the norm of one of the wave vectors is very small compared with the other two (for example $k \ll p \sim q$). The local interactions therefore correspond to the inter-scale interactions of the same size and the distant interactions to the interactions between a large scale and two small scales. Also, any interaction that introduces a $(\mathbf{k}, \mathbf{p}, \mathbf{q})$ triad that does not verify the relation $k \sim p \sim q$ is called a non-local interaction.

In the following, we will be analyzing an isolated distant triadic interaction associated with three modes: $\mathbf{k}, \mathbf{p}$ and $\mathbf{q}$. We adopt the configuration $k \ll p \sim q$ and assume that $\mathbf{k}$ is large scale located in the energetic portion of the spectrum. An asymptotic analysis shows that:

$$[\dot{\mathbf{u}}(\mathbf{k})]_{\text{nl}} = O(\delta) \quad , \tag{5.42}$$

$$[\dot{\mathbf{u}}(\mathbf{p})]_{\text{nl}} = -\mathrm{i}\,(\widehat{\mathbf{u}}^*(\mathbf{q})\,[\mathbf{p}\cdot\widehat{\mathbf{u}}^*(\mathbf{k})]) + O(\delta) \quad , \tag{5.43}$$

$$[\dot{\mathbf{u}}(\mathbf{q})]_{\text{nl}} = -\mathrm{i}\,(\widehat{\mathbf{u}}^*(\mathbf{p})\,[\mathbf{p}\cdot\widehat{\mathbf{u}}^*(\mathbf{k})]) + O(\delta) \quad , \tag{5.44}$$

where δ is the small parameter defined as

$$\delta = \frac{k}{p} \ll 1 \quad .$$

The corresponding energy transfer analysis leads to the following relations:

$$[\dot{e}(\mathbf{k})]_{\text{nl}} = O(\delta) \quad , \tag{5.45}$$

$$[\dot{e}(\mathbf{p})]_{\text{nl}} = -\,[\dot{e}(\mathbf{q})]_{\text{nl}} = \mathrm{i}\,\{\widehat{\mathbf{u}}(\mathbf{p})\cdot\widehat{\mathbf{u}}(\mathbf{q})\,[\mathbf{p}\cdot\widehat{\mathbf{u}}(\mathbf{k})] + cc\} + O(\delta) \quad . \tag{5.46}$$

Several remarks can be made:

- The interaction between large and small scales persists in the limit of the infinite Reynolds numbers. Consistently with the Kolmogorov hypotheses, these interactions occur with no energy transfer between the large and small scales. Numerical simulations have shown that the energy transfers are negligible between two modes separated by more than two decades.
- The variation rate of the high frequencies $\widehat{\mathbf{u}}(\mathbf{p})$ and $\widehat{\mathbf{u}}(\mathbf{q})$ is directly proportional to the amplitude of the low-frequency mode $\widehat{\mathbf{u}}(\mathbf{k})$. This implies that the strength of the coupling with the low-frequency modes increases with the energy of the modes.

Moreover, complementary analysis shows that, for modes whose wavelength is of the order of the Taylor micro-scale λ defined as (see Appendix A):

$$\lambda = \sqrt{\frac{\overline{u'^2}}{\overline{\left(\frac{\partial u'}{\partial x}\right)^2}}} \quad , \tag{5.47}$$

the ratio between the energy transfers due to the distant interactions and those due to the local interactions vary as:

$$\frac{[\dot{e}(k_\lambda)]_{\text{distant}}}{[\dot{e}(k_\lambda)]_{\text{local}}} \sim Re_\lambda^{11/6} \quad , \tag{5.48}$$

where Re_λ is the Reynolds number referenced to the Taylor micro-scale and the velocity fluctuation u'. This relation shows that the coupling increases with the Reynolds number, with the result that an anisotropic distribution of the energy at the low frequencies creates an anisotropic forcing of the high frequencies, leading to a deviation from isotropy of these high frequencies.

A competitive mechanism exists that has an isotropy reduction effect at the small scales. This is the energy cascade associated with non-local triadic interactions that do not enter into the asymptotic limit of the distant interactions.

For a wave vector of norm k, the ratio of the characteristic times $\tau(k)_{\text{cascade}}$ and $\tau(k)_{\text{distant}}$, associated respectively with the energy transfer of the cascade mechanism and that due to the distant interactions, is evaluated as:

$$\frac{\tau(k)_{\text{cascade}}}{\tau(k)_{\text{distant}}} \sim \text{constant} \times (k/k_{\text{injection}})^{11/6} \quad , \tag{5.49}$$

where $k_{\text{injection}}$ is the mode in which the energy injection occurs in the spectrum. So we see that the distant interactions are much faster than the energy cascade. Also, the first effect of a sudden imposition of large scale anisotropy will be to anisotropize the small scales, followed by competition between the two mechanisms. The dominance of one of the two depends on a number of factors, such as the separation between the k and $k_{\text{injection}}$ scales, or the intensity and co tency of the anisotropy at the large scale.

Numerical simulations [356] performed in the framework of homogeneous turbulence have shown a persistence of anisotropy at the small scales. However, it should be noted that this anisotropy is detected only on statistical moments of the velocity field of order three or more, with first- and second-order moments being isotropic.

5.3.2 Anisotropic Models

Here we describe the main models proposed in the anisotropic framework. Except for Aupoix's spectral model, none of these take explicit account of the backward cascade mechanism. They are:

1. Aupoix's spectral model (p.153), which is based on the anisotropic EDQNM analysis. The interaction terms are evaluated by adopting a preset shape of the energy spectra and subgrid mode anisotropy. This model, which requires a great deal of computation, has the advantage of including all the coupling mechanisms between large and small scales.
2. Horiuti's model (p.154), which is based on an evaluation of the anisotropy tensor of the subgrid modes from the equivalent tensor constructed from the highest frequencies in the resolved field. This tensor is then used to modulate the subgrid viscosity empirically in each direction of space. This is equivalent to considering several characteristic velocity scales for representing the subgrid modes. This model can only modulate the subgrid dissipation differently for each velocity component and each direction of space, but does not include the more complex anisotropic transfer mechanisms through the cutoff.
3. The model of Carati and Cabot (p.155), who propose a general form of the subgrid viscosity in the form of a fourth-rank tensor. The components of this tensor are determined on the basis of symmetry relations. However, this model is a applicable only when the flow statistically exhibits an axial symmetry, which restricts its field of validity.
4. The model of Abba *et al.* (p.156) which, as in the previous example, considers the subgrid viscosity in the form of a fourth-rank tensor. The model is based on the choice of a local adapted reference system for representing the subgrid modes, and which is chosen empirically when the flow possesses no obvious symmetries.
5. Models based on the idea of separating the field into an isotropic part and inhomogeneous part (p.157), in order to be able to isolate the contribution of the mean field in the computation of the subgrid viscosity, for models based on the large scales, and thereby better localize the information contained in these models by frequency. This technique, however, is applicable only to flows exhibiting at least one direction of homogeneity.

Aupoix Spectral Model. In order to take the anisotropy of the subgrid scales into account, Aupoix [7] proposes adopting preset shapes of the energy spectra and anisotropy so that the relations stemming from the previously described EDQNM analysis of anisotropy can be used. Aupoix proposes the following model for the energy spectrum:

$$E(k) = K_0 \varepsilon^{2/3} k^{-5/3} \exp\{f(k/k_\mathrm{d})\} \quad , \tag{5.50}$$

where

$$f(x) = \exp\left[-3.5x^2\left(1 - \exp\left\{6x + 1,2 - \sqrt{196x^2 - 33.6x + 1.4532}\right\}\right)\right] \quad . \tag{5.51}$$

This spectrum is illustrated in Fig. 5.2. The anisotropy spectrum is modeled by:

$$\begin{aligned} H_{ij}(k) = {} & b_{ij}\left[5 + \frac{k}{E(k)}\frac{\partial E(k)}{\partial k}\right] \\ & \times \left[1 + \mathcal{H}\left(\frac{k}{k_\mathrm{max}} - 1\right)\mathcal{H}\left(|\mathcal{F}(\overline{\mathbf{u}})|\right)\left\{\left(\frac{k}{k_\mathrm{max}}\right)^{-2/3} - 1\right\}\right] , \end{aligned} \tag{5.52}$$

where $\mathcal{F}(\overline{\mathbf{u}}) = \nabla \times \overline{\mathbf{u}}$, k_max is the wave number corresponding to the energy spectrum maximum, and $\mathcal{H}$ the Heaviside function defined by:

$$\mathcal{H}(x) = \begin{cases} 0 & \text{if } x \leq 0 \\ 1 & \text{otherwise} \end{cases} \quad ,$$

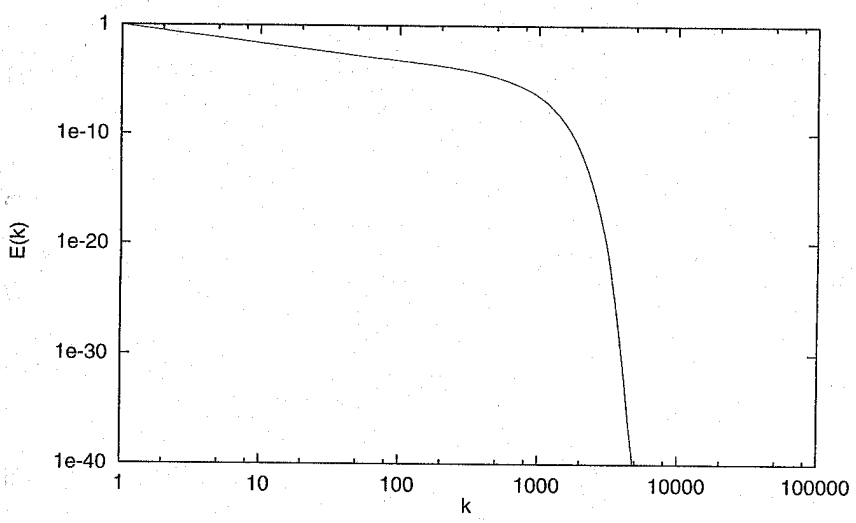

Fig. 5.2. Aupoix spectrum ($k_d = 1000$).

and where b_{ij} is the anisotropy tensor defined as:

$$b_{ij} = \frac{\overline{u_i' u_j'}}{q_{\text{sgs}}^2} - \frac{1}{3}\delta_{ij} \quad . \tag{5.53}$$

Horiuti's Model. Horiuti [141] proposes extending the Smagorinsky model to the isotropic case by choosing a different velocity scale for characterizing each component of the subgrid tensor.

Starting with an ordinary dimensional analysis, the subgrid viscosity ν_{sgs} is expressed as a function of the subgrid kinetic energy q_{sgs}^2 and the dissipation rate ε:

$$\nu_{\text{sgs}} = C_1 \frac{(q_{\text{sgs}}^2)^2}{\varepsilon} \quad . \tag{5.54}$$

To make a better adjustment of the dissipation induced by the subgrid model to the local state of the flow, Horiuti proposes replacing equation (5.54) by:

$$\nu_{\text{sgs}} = C_1 \frac{(q_{\text{sgs}}^2)^2}{\varepsilon} \Upsilon \quad , \tag{5.55}$$

in which Υ is a dimensionless parameter whose function is to regulate the dissipation rate as a function of the anisotropy of the resolved field. The proposed form for Υ is:

$$\Upsilon = \frac{3E^{\text{s}}}{2q_{\text{sgs}}^2} \quad , \tag{5.56}$$

where E^{s} is the square of a characteristic velocity scale of the subgrid modes. For example, near solid walls, Horiuti proposes using the fluctuation of the velocity component normal to the wall, which makes it possible for the model to cancel out automatically. To generalize this approach, we associate a characteristic velocity E_{ij}^{s} with each subgrid stress τ_{ij}.

In practice, the author proposes evaluating these characteristic velocities by the scale similarity hypothesis by means of a test filter indicated by a *tilde*:

$$E_{ij}^{\text{s}} = (\overline{u}_i - \tilde{\overline{u}}_i)(\overline{u}_j - \tilde{\overline{u}}_j) \quad , \tag{5.57}$$

which makes it possible to define a tensorial parameter Υ_{ij} as:

$$\Upsilon_{ij} = \frac{3(\overline{u}_i - \tilde{\overline{u}}_i)(\overline{u}_j - \tilde{\overline{u}}_j)}{\sum_{l=1,3}(\overline{u}_l - \tilde{\overline{u}}_l)^2} \quad . \tag{5.58}$$

This tensorial parameter characterizes the anisotropy of the test field $(\overline{\mathbf{u}} - \tilde{\overline{\mathbf{u}}})$ and can be considered as an approximation of the anisotropy tensor associated with this velocity field (to within a coefficient of $-3\,\delta_{ij}$). Using a

model based on the large scales, Horiuti derives the tensorial subgrid viscosity $\nu_{e_{ij}}$:

$$\nu_{e_{ij}} = \left(C_1 \overline{\Delta}\right)^2 |\mathcal{F}(\overline{\mathbf{u}})|\, \Upsilon_{ij} \quad , \tag{5.59}$$

with

$$\mathcal{F}(\overline{\mathbf{u}}) = \nabla \times \overline{\mathbf{u}}, \quad \text{or} \quad \left(\nabla\overline{\mathbf{u}} + \nabla^T\overline{\mathbf{u}}\right) \quad ,$$

where the constant C_1 is evaluated as it is for the scalar models. He proposes a model of the general form for the subgrid tensor τ:

$$\tau_{ij} = \delta_{ij}\left(\frac{2}{3}K + \frac{2}{3}P\right) - \nu_{e_{il}}\frac{\partial \overline{u}_j}{\partial x_l} - \nu_{e_{jl}}\frac{\partial \overline{u}_i}{\partial x_l} \quad , \tag{5.60}$$

where

$$K = \frac{1}{2}\sum_{l=1,3}(\overline{u}_l - \tilde{\overline{u}}_l)^2, \qquad P = \nu_{e_{lm}}\frac{\partial \overline{u}_m}{\partial x_l} \quad .$$

It is important to note that this is a model for the entire subgrid tensor and not for its deviator part alone, as is the case for the isotropic models.

Carati and Cabot Model. Carati and Cabot [46] propose a tensorial anisotropic extension of the subgrid viscosity models. Generally, the deviator τ^{d} of the subgrid tensor τ is modeled as:

$$\tau_{ij}^{\text{d}} = \nu_{ijkl}^{(1)}\overline{S}_{kl} + \nu_{ijkl}^{(2)}\overline{\Omega}_{kl} \quad , \tag{5.61}$$

where the tensors $\overline{S}$ and $\overline{\Omega}$ are defined as:

$$\overline{S} = \frac{1}{2}\left(\nabla\overline{\mathbf{u}} + \nabla^T\overline{\mathbf{u}}\right), \qquad \overline{\Omega} = \frac{1}{2}\left(\nabla\overline{\mathbf{u}} - \nabla^T\overline{\mathbf{u}}\right) \quad .$$

The two viscosities $\nu^{(1)}$ and $\nu^{(2)}$ are fourth-rank tensors theoretically defined by 81 independent coefficients. However, the properties of the tensors τ^{d}, $\overline{S}$ and $\overline{\Omega}$ make it possible to reduce the number of these parameters.

The tensors τ^{d} and $\overline{S}$ are symmetrical and have zero trace, which entails:

$$\begin{aligned}
\nu_{ijkl}^{(1)} &= \nu_{jikl}^{(1)} \quad , \\
\nu_{ijkl}^{(1)} &= \nu_{jilk}^{(1)} \quad , \\
\nu_{iikl}^{(1)} &= 0 \quad , \\
\nu_{ijkk}^{(1)} &= 0 \quad .
\end{aligned}$$

The tensor $\nu^{(1)}$ therefore contains 25 independent coefficients. By a similar analysis, we can say:

$$\begin{aligned}\nu^{(2)}_{ijkl} &= \nu^{(2)}_{jikl} \quad ,\\ \nu^{(2)}_{ijkl} &= -\nu^{(2)}_{jilk} \quad ,\\ \nu^{(2)}_{iikl} &= 0 \quad .\end{aligned} \tag{5.62}$$

The tensor $\nu^{(2)}$ therefore contains 15 independent coefficients, which raises the number of coefficients to be determined to 40.

Further reductions can be made using the symmetry properties of the flow. For the case of symmetry about the axis defined by the vector $\mathbf{n} = (n_1, n_2, n_3)$, the authors show that the model takes a reduced form that now uses only four coefficients, $C_1, ..., C_4$:

$$\begin{aligned}\tau^{\mathrm{d}}_{ij} &= -2C_1\overline{S}_{ij} - 2C_2\left(n_i\overline{s}_j + \overline{s}_i n_j - \frac{2}{3}\overline{s}_k n_k \delta_{ij}\right)\\ &\quad - C_3\left(n_i n_j - \frac{1}{3}n^2\delta_{ij}\right)\overline{s}_k n_k - 2C_4\left(\overline{r}_i n_j + n_i \overline{r}_j\right) \quad ,\end{aligned} \tag{5.63}$$

where $\overline{s}_i = \overline{S}_{ik}n_k$ and $\overline{r}_i = \overline{\Omega}_{ik}n_k$.

Adopting the additional hypothesis that the tensors $\nu^{(1)}$ and $\nu^{(2)}$ verify the Onsager symmetry relations for the covariant vector $\mathbf{n}$ and the contravariant vector $\mathbf{p}$:

$$\begin{aligned}\nu^{(1)}_{ijkl}(\mathbf{n}) &= \nu^{(1)}_{klij}(\mathbf{n}) \quad ,\\ \nu^{(2)}_{ijkl}(\mathbf{n}) &= \nu^{(2)}_{klij}(\mathbf{n}) \quad ,\\ \nu^{(1)}_{ijkl}(\mathbf{p}) &= \nu^{(1)}_{klij}(-\mathbf{p}) \quad ,\\ \nu^{(2)}_{ijkl}(\mathbf{p}) &= \nu^{(2)}_{klij}(-\mathbf{p}) \quad ,\end{aligned} \tag{5.64}$$

we get the following reduced form:

$$\tau^{\mathrm{d}}_{ij} = -2\nu_1\overline{S}^{\parallel}_{ij} - 2\nu_2 n^2 \overline{S}^{\perp}_{ij} \quad , \tag{5.65}$$

where ν_1 and ν_2 are two scalar viscosities and

$$\overline{S}^{\parallel}_{ij} = \frac{1}{n^2}\left(n_i\overline{s}_j + \overline{s}_i n_j\right) - \frac{1}{3n^2}\overline{s}_k n_k \delta_{ij}, \quad \overline{S}^{\perp}_{ij} = \overline{S}_{ij} - \overline{S}^{\parallel}_{ij} \quad .$$

Carati then proposes determining the two parameters ν_1 and ν_2 by an ordinary dynamic procedure.

Model of Abba et al. Another tensor formulation was proposed by Abba *et al.* [1]. These authors propose defining the subgrid viscosity in the form of the fourth-rank tensor denoted ν_{ijkl}. This tensor is defined as the product of a scalar isotropic subgrid viscosity ν_{iso} and an fourth-rank tensor denoted $\mathcal{C}$,

whose components are dimensionless constants which will play the role of the scalar constants ordinarily used. The tensor subgrid viscosity ν_{ijkl} thus defined is expressed:

$$\nu_{ijkl} = \mathcal{C}_{ijkl}\nu_{\mathrm{iso}} = \left(\sum_{\alpha,\beta} C_{\alpha\beta}a_{i\alpha}a_{j\beta}a_{k\alpha}a_{l\beta}\right)\nu_{\mathrm{iso}} \quad , \tag{5.66}$$

where $a_{i\alpha}$ designates the ith component of the unit vector $\mathbf{a}_\alpha$ ($\alpha = 1, 2, 3$), $C_{\alpha\beta}$ is a symmetrical 3×3 matrix that replaces the scalar Smagorinsky constant. The three vectors $\mathbf{a}_\alpha$ are arbitrary and have to be defined as a function of some foreknowledge of the flow topology and its symmetries. When this information is not known, the authors propose using the local framework defined by the following three vectors:

$$\mathbf{a}_1 = \frac{\mathbf{u}}{u}, \quad \mathbf{a}_3 = \frac{\nabla(|u|^2)\times\mathbf{u}}{|\nabla(|u|^2)\times\mathbf{u}|}, \quad \mathbf{a}_2 = \mathbf{a}_3 \times \mathbf{a}_1 \quad . \tag{5.67}$$

The authors apply this modification to the Smagorinsky model. The scalar viscosity is thus evaluated by the formula:

$$\nu_{\mathrm{iso}} = \overline{\Delta}^2|\overline{S}| \quad . \tag{5.68}$$

The subgrid tensor deviator is then modeled as:

$$\tau^{\mathrm{d}}_{ij} = -2\sum_{k,l}\mathcal{C}_{ijkl}\overline{\Delta}^2|\overline{S}|\overline{S}_{kl} + \frac{2}{3}\delta_{ij}\overline{\Delta}^2\mathcal{C}_{mmkl}|\overline{S}|\overline{S}_{kl} \quad . \tag{5.69}$$

The model constants are then evaluated by means of a dynamic procedure.

Models Based on a Splitting Technique. Subgrid viscosity models are mostly developed in the framework of the hypotheses of the canonical analysis, *i.e.* for homogeneous turbulent flows. Experience shows that the performance of these models declines when they are used in an inhomogeneous framework, which corresponds to a non-uniform average flow. One simple idea initially proposed by Schumann [298] is to separate the velocity field into inhomogeneous and isotropic parts and to compute a specific subgrid term for each of these parts.

In practice, Schumann proposes an anisotropic subgrid viscosity model for dealing with flows whose average gradient is non-zero, and in particular any flow regions close to solid walls. The model is obtained by splitting the deviator part of the subgrid tensor τ^{d} into one locally isotropic part and one inhomogeneous:

$$\tau^{\mathrm{d}}_{ij} = -2\nu_{\mathrm{sgs}}\left(\overline{S}_{ij} - \langle\overline{S}_{ij}\rangle\right) - 2\nu^{\mathrm{a}}_{\mathrm{sgs}}\langle\overline{S}_{ij}\rangle \quad , \tag{5.70}$$

where the angle brackets $\langle . \rangle$ designate an statistical average, which in practice is a spatial average in the directions of homogeneity in the solution.

The coefficients ν_{sgs} and ν^a_{sgs} are the scalar subgrid viscosities representing a locally isotropic turbulence and an inhomogeneous turbulence, respectively. Moin and Kim [245] and Horiuti [138] give the following definitions:

$$\nu_{sgs} = \left(C_1\overline{\Delta}\right)^2 \sqrt{2\left(\overline{S}_{ij} - \langle\overline{S}_{ij}\rangle\right)\left(\overline{S}_{ij} - \langle\overline{S}_{ij}\rangle\right)} \quad , \tag{5.71}$$

$$\nu^a_{sgs} = \left(C_2\overline{\Delta}_z\right)^2 \sqrt{2\langle\overline{S}_{ij}\rangle\langle\overline{S}_{ij}\rangle} \quad , \tag{5.72}$$

where C_1 and C_2 are two constants. Horiuti recommends $C_1 = 0.1$ and $C_2 = 0.254$, while Moin and Kim use $C_1 = C_2 = 0.254$. The isotropic part is a function of the fluctuation of the viscosity gradients, so as to make sure that the extra-diagonal components thus predicted for the subgrid tensor cancel out on the average over time. This is consistent with the isotropic hypothesis.

The two characteristic lengths $\overline{\Delta}$ and $\overline{\Delta}_z$ represent the cutoff lengths for the two types of structures, and are evaluated as:

$$\overline{\Delta}(z) = (\overline{\Delta}_1\overline{\Delta}_2\overline{\Delta}_3)^{1/3}(1 - \exp(zu_\tau/A\nu)) \quad , \tag{5.73}$$

$$\overline{\Delta}_z(z) = \overline{\Delta}_3(1 - \exp([zu_\tau/A\nu]^2)) \quad , \tag{5.74}$$

where z is the distance to the solid wall, $\overline{\Delta}_3$ the cutoff length in the direction normal to the surface, and u_τ the friction velocity at the surface (see Sect. 9.2.1). The constant A is taken to be equal to 25.

This model was initially designed for the case of a plane channel flow. It requires being able to compute the statistical average of the velocity field, and thus can be extended only to sheared flows exhibiting at least one direction of homogeneity, or requires the use of several statistically equivalent simulations to perform the ensemble average [48, 51].

Sullivan *et al.* [321] propose a variant of it that incorporates an anisotropy factor (so that the model constant can be varied to represent the field anisotropy better):

$$\tau^d_{ij} = -2\nu_{sgs}\gamma\overline{S}_{ij} - 2\nu^a_{sgs}\langle\overline{S}_{ij}\rangle \quad . \tag{5.75}$$

The authors propose computing the viscosity ν^a_{sgs} as before. The ν_{sgs} term, on the other hand, is now calculated by a model with one evolution equation for the subgrid kinetic energy (see equation (4.108) in Chap. 4). Only the subgrid kinetic energy production by the isotropic is included, which is equivalent to replacing the II term in equation (4.108) with

$$2\nu_{sgs}\gamma\left(\overline{S}_{ij} - \langle\overline{S}_{ij}\rangle\right)\left(\overline{S}_{ij} - \langle\overline{S}_{ij}\rangle\right) \quad . \tag{5.76}$$

The authors evaluate the anisotropy factor from the shearing rates of the large and small scales. The average per plane of fluctuation homogeneity of the resolved strain rate tensor, calculated by

$$S' = \sqrt{2\langle\left(\overline{S}_{ij} - \langle\overline{S}_{ij}\rangle\right)\left(\overline{S}_{ij} - \langle\overline{S}_{ij}\rangle\right)\rangle} \quad , \tag{5.77}$$

is used for evaluating the shear of the small scales. The shear of the large scales is estimated as

$$S^\diamond = \sqrt{2\langle\overline{S}_{ij}\rangle\langle\overline{S}_{ij}\rangle} \quad . \tag{5.78}$$

The isotropy factor is evaluated as:

$$\gamma = \frac{S'}{S' + S^\diamond} \quad . \tag{5.79}$$

6. Structural Modeling

This chapter describes some of the family of structural models. As has already been said, these are established with no prior knowledge of the nature of the interactions between the subgrid scales and those that make up the resolved field.

These models can be grouped into several categories:

- Those derived by formal series expansions (Sect. 6.1). These models make no use of any foreknowledge of the physics of the flows, and are based only on series expansions of the various terms that appear in the filtered Navier–Stokes equations.
- Those based on transport equations for the subgrid tensor components (Sect. 6.2). These models, though they require no information concerning the way the subgrid modes act on the resolved scales, require a very complex level of modeling since all the unknown terms in the transport equations for the subgrid tensor components have to be evaluated.
- Those constructed from deterministic models for the subgrid structures (Sect. 6.3). They assume that preferential directions of alignments are known for the subgrid structures.
- Those that use the physical hypothesis of scale similarity (Sect. 6.4). The models of the last category are based on the scale similarity hypothesis, which establishes a correspondence between the statistical structure of the flow at different filtering levels. The mixed models, which are based on linear combinations of the functional and structural types (presented in Sect. 6.5).
- Those based on an explicit reconstruction of the subgrid velocity fluctuations on an auxiliary grid (Sect. 6.6). These models are the only ones which aim at reconstructing the subgrid motion directly.
- Those based on specific numerical algorithms, whose errors are designed to mimic the subgrid forces (Sect. 6.7).

6.1 Formal Series Expansions

6.1.1 Models Based on Approximate Deconvolution

Differential Interpretation of the Filters. We recall the definition of filtering by a convolution product:

$$\overline{\phi}(x) = \int_{-\infty}^{+\infty} \phi(y) G(x-y) dy \quad . \tag{6.1}$$

To obtain a differential interpretation of the filtering, we perform a Taylor expansion of the $\phi(y)$ term about x:

$$\phi(y) = \phi(x) + (y-x)\frac{\partial \phi(x)}{\partial x} + \frac{1}{2}(y-x)^2 \frac{\partial^2 \phi(x)}{\partial x^2} + \ldots \tag{6.2}$$

Introducing this expansion into (6.1), and considering the symmetry and conservation properties of the constants of the kernel G, we get:

$$\begin{aligned} \overline{\phi}(x) &= \phi(x) + \frac{1}{2}\frac{\partial^2 \phi(x)}{\partial x^2} \int_{-\infty}^{+\infty} z^2 G(z) dz + \ldots \\ &\quad + \frac{1}{n!}\frac{\partial^n \phi(x)}{\partial x^n} \int z^n G(z) dz + \ldots \\ &= \phi(x) + \sum_{l=1,\infty} \frac{\alpha^{(l)}}{l!} \frac{\partial^l \phi(x)}{\partial x^l} \quad , \end{aligned} \tag{6.3}$$

where $\alpha^{(l)}$ designates the lth-order moment of the convolution kernel:

$$\alpha^{(l)} = \int_{-\infty}^{+\infty} z^l G(z) dz \quad . \tag{6.4}$$

The values of the first moments of the box and Gaussian filters are given in Table 6.1.

Table 6.1. Values of the first five non-zero moments for the box and Gaussian filters.

$\alpha^{(n)}$	$n=0$	$n=2$	$n=4$	$n=6$	$n=8$
box	1	$\overline{\Delta}^2/12$	$\overline{\Delta}^4/80$	$\overline{\Delta}^6/448$	$\overline{\Delta}^8/2304$
Gaussian	1	$\overline{\Delta}^2/12$	$\overline{\Delta}^4/48$	$5\overline{\Delta}^6/576$	$35\overline{\Delta}^8/6912$

For these two filters, we have the estimate:

$$\alpha^{(n)} = O(\overline{\Delta}^n) \quad . \tag{6.5}$$

With this relation, we can interpret the filtering as the application of a differential operator to the primitive variable ϕ. The various terms that appear in the filtered equations can be re-written using the relation

$$\phi'(x) = \phi(x) - \overline{\phi}(x) = -\sum_{l=1,\infty} \frac{\alpha^{(l)}}{l!} \frac{\partial^l \phi(x)}{\partial x^l} \quad . \tag{6.6}$$

The subgrid model can only reveal the contribution of the resolved field $\overline{\phi}$, so it is necessary to evaluate the fluctuation ϕ' as a function of this field. This is done by a reconstruction operation, sometimes called de-filtering or deconvolution. This operation is performed by inverting relation (6.3) and writing it in symbolic form:

$$\overline{\phi} = \left(Id + \sum_{l=1,\infty} C_l \overline{\Delta}^{2l} \frac{\partial^{2l}}{\partial x^{2l}} \right) \phi \quad . \tag{6.7}$$

The inverse relation is[1]:

$$\phi = \left(Id + \sum_{l=1,\infty} C_l \overline{\Delta}^{2l} \frac{\partial^{2l}}{\partial x^{2l}} \right)^{-1} \overline{\phi} \quad . \tag{6.8}$$

By truncating the expansion (6.3) at order p, this becomes[2]:

$$\phi = \left(Id + \sum_{l=1,p} C'_l \overline{\Delta}^{2l} \frac{\partial^{2l}}{\partial x^{2l}} \right) \overline{\phi} \quad . \tag{6.9}$$

This last form can be computed immediately from the resolved field. Limiting the expansion to the second order, the subgrid part is expressed as:

$$\begin{aligned} \phi'(x) &= \frac{1}{2}\alpha^{(2)} \frac{\partial^2 \phi(x)}{\partial x^2} + O(\overline{\Delta}^4) \\ &= \frac{1}{2}\alpha^{(2)} \frac{\partial^2}{\partial x^2} \left(\overline{\phi} + O(\overline{\Delta}^2) \right) \\ &= \overline{\phi}'(x) + O(\overline{\Delta}^2) \quad . \end{aligned} \tag{6.10}$$

This can be used to express all the contributions as a function of the resolved field, with second-order accuracy. The various terms of the Leonard decomposition are approximated to the second order as:

[1] Note that Galdi and Layton [108] use an implicit inversion.

[2] This result is obtained using the Taylor expansion

$$(1+\epsilon)^{-1} = 1 - \epsilon + O(\epsilon^2) \quad .$$

$$L_{ij} \equiv \overline{\overline{u}_i \overline{u}_j} - \overline{u}_i \overline{u}_j = \frac{1}{2}\alpha^{(2)} \frac{\partial^2}{\partial x^2}(\overline{u}_i \overline{u}_j) + O(\overline{\Delta}^4) \quad , \tag{6.11}$$

$$C_{ij} \equiv \overline{\overline{u}_i u'_j} + \overline{\overline{u}_j u'_i} = -\frac{1}{2}\alpha^{(2)} \left(\overline{u}_i \frac{\partial^2}{\partial x^2}\overline{u}_j + \overline{u}_j \frac{\partial^2}{\partial x^2}\overline{u}_i \right) + O(\overline{\Delta}^4) \quad . \tag{6.12}$$

The combination of these two terms leads to:

$$L_{ij} + C_{ij} = \alpha^{(2)} \frac{\partial \overline{u}_i}{\partial x} \frac{\partial \overline{u}_j}{\partial x} + O(\overline{\Delta}^4) \quad . \tag{6.13}$$

As for the subgrid Reynolds tensor, it appears only as a fourth-order term:

$$R_{ij} \equiv \overline{u'_i u'_j} = \frac{1}{4}\left(\alpha^{(2)}\right)^2 \frac{\partial^2 \overline{u}_i}{\partial x^2} \frac{\partial^2 \overline{u}_j}{\partial x^2} + O(\overline{\Delta}^6) \quad , \tag{6.14}$$

so that it disappears in a second-order expansion of the full subgrid tensor. In practice, this approach is used only to derive models for the tensors L and C, which escape functional modeling [43, 65, 71, 72, 202]. Certain authors also use these evaluations to neglect these tensors when the numerical scheme produces errors of the same order, which is the case for second-order accurate schemes.

Finer analysis allows a better evaluation of the order of magnitude of the subgrid tensor. By using a subgrid viscosity model, *i.e.*

$$\tau_{ij} = -2\nu_{\text{sgs}} \overline{S}_{ij} \quad , \tag{6.15}$$

and using the local equilibrium hypothesis:

$$\varepsilon = -\tau_{ij} \overline{S}_{ij} = \nu_{\text{sgs}} |\overline{S}|^2 \quad , \tag{6.16}$$

the amplitude of the subgrid tensor can be evaluated as:

$$|\tau_{ij}| \approx \nu_{\text{sgs}} |\overline{S}| \approx \sqrt{\varepsilon \nu_{\text{sgs}}} \quad . \tag{6.17}$$

By basing the computation of the subgrid viscosity on the subgrid kinetic energy:

$$\nu_{\text{sgs}} \approx \overline{\Delta} \sqrt{q^2_{\text{sgs}}} \quad , \tag{6.18}$$

and computing this energy from a Kolmogorov spectrum:

$$\begin{aligned} \sqrt{q^2_{\text{sgs}}} &= \left(\int_{k_c}^{\infty} E(k) dk \right)^{1/2} \\ &\propto \left(\int_{k_c}^{\infty} k^{-5/3} dk \right)^{1/2} \\ &\propto (k_c)^{-1/3} \\ &\propto \overline{\Delta}^{1/3} \quad , \end{aligned}$$

we get for the subgrid viscosity:

$$\nu_{\text{sgs}} \propto \overline{\Delta}\, \overline{\Delta}^{1/3} = \overline{\Delta}^{4/3} \quad . \tag{6.19}$$

The order of magnitude of the corresponding subgrid tensor is:

$$|\tau_{ij}| \propto \sqrt{\varepsilon \nu_{\text{sgs}}} \propto \overline{\Delta}^{2/3} \quad . \tag{6.20}$$

This estimation is clearly different from those given previously, and shows that the subgrid tensor is theoretically dominant compared with the terms in $\overline{\Delta}^2$. This last evaluation is usually interpreted as being of the subgrid Reynolds tensor R_{ij}, while the estimations of the tensors C_{ij} and L_{ij} given above are generally considered to be correct.

A generalized expansion for the whole subgrid tensor is proposed by Carati *et al.* [50]. These authors have proved that the differential expansion:

$$\overline{\phi\psi} = \sum_{l,m=0}^{\infty} C_{lm}(G) \frac{\partial^l \overline{\phi}}{\partial x^l} \frac{\partial^m \overline{\psi}}{\partial x^m} \quad , \tag{6.21}$$

where $\phi(x)$ and $\psi(x)$ are two C^∞ real functions, $C_{lm}(G)$ some real coefficients which depend explicitly on the filter, is valid for all the filter kernels G such that:

$$\frac{G(-\mathrm{i}(\phi+\psi))}{G(-\mathrm{i}\phi)G(-\mathrm{i}\psi)} \in \mathbb{R}, \quad \mathrm{i}^2 = -1 \quad . \tag{6.22}$$

This is in particular true of all symmetric kernels. The resulting general form of the gradient model deduced from (6.21) is:

$$\tau_{ij} = \overline{u_i u_j} - \overline{u}_i \overline{u}_j = \sum_{l,m=0,\infty;(l,m)\neq(0,0)} C_{lm}(G) \frac{\partial^l \overline{u}_i}{\partial x^l} \frac{\partial^m \overline{u}_j}{\partial x^m} \quad . \tag{6.23}$$

Derivation in Spectral Space. The same results can be derived in the spectral space, but by Taylor expansion of the transfer function $\widehat{G}$ about zero:

$$\widehat{G}(k) = \widehat{G}(0) + k \frac{\partial \widehat{G}(0)}{\partial k} + \frac{k^2}{2} \frac{\partial^2 \widehat{G}(0)}{\partial k^2} + \ldots \tag{6.24}$$

The preservation of the constants by the filtering process implies that $\widehat{G}(0) = 1$. The filtered component is therefore written:

$$\overline{\widehat{\phi}}(k) = \left(1 + k \frac{\partial \widehat{G}(0)}{\partial k} + \frac{k^2}{2} \frac{\partial^2 \widehat{G}(0)}{\partial k^2} + \ldots \right) \widehat{\phi}(k) \quad , \tag{6.25}$$

and the fluctuation:

$$\widehat{\phi}'(k) = -\left(k\frac{\partial \widehat{G}(0)}{\partial k} + \frac{k^2}{2}\frac{\partial^2 \widehat{G}(0)}{\partial k^2} + ...\right)\widehat{\phi}(k) \quad . \tag{6.26}$$

Simple algebraic manipulations, which consist in substituting these relations into those of Sect. 3.3.1, lead to the same results as those that have just been explained for the physical space. To do this, we need simply identify groups of the form $k^n\widehat{\phi}(k)$ with the term $\partial^n\phi(x)/\partial x^n$.

Iterative Deconvolution. If the filter kernel G has an inverse G^{-1}, the latter can also be obtained using the following expansion [319, 320]:

$$G^{-1} \star \phi = \sum_{p=0,\infty} (I - G)^p \star \phi \quad , \tag{6.27}$$

yielding the following reconstruction for the defiltered variable ϕ:

$$\phi = \overline{\phi} + (\overline{\phi} - \overline{\overline{\phi}}) + (\overline{\phi} - 2\overline{\overline{\phi}} + \overline{\overline{\overline{\phi}}}) + ... \quad , \tag{6.28}$$

or equivalently

$$\phi' = (\overline{\phi} - \overline{\overline{\phi}}) + (\overline{\phi} - 2\overline{\overline{\phi}} + \overline{\overline{\overline{\phi}}}) + ... \tag{6.29}$$

The series are known to be convergent if $|I - G| < 1$. A practical model is obtained by truncating the expansion at a given power. Stolz and Adams [319] recommend using a fifth-order expansion.

6.1.2 Non-linear Models

There are a number of ways of deriving non-linear models: Horiuti [140], Speziale [315], Yoshizawa [359], and Wong [348] start with an expansion in a small parameter, while Lund and Novikov [205] use the mathematical properties of the tensors considered. It is this last approach that will be described first, because it is the one that best reveals the difference with the functional models. Kosovic's simplified model [167] and Wong's dynamic model [348] are then described.

Generic Model of Lund and Novikov. We assume that the deviator of the subgrid tensor can be expressed as a function of the resolved velocity field gradients (and not the velocity field itself, to ensure the Galilean invariance property), the unit tensor, and the square of the cutoff length $\overline{\Delta}$:

$$\tau_{ij} - \frac{1}{3}\tau_{kk}\delta_{ij} \equiv \tau_{ij}^{\mathrm{d}} = \mathcal{F}(\overline{S}_{ij}, \overline{\Omega}_{ij}, \delta_{ij}, \overline{\Delta}^2) \quad . \tag{6.30}$$

The isotropic part of τ is not taken into account, and is integrated in the pressure term because $\overline{S}$ and $\overline{\Omega}$ have zero traces. To simplify the expansions in the following, we use the reduced notation:

$$\overline{S}\,\overline{\Omega} = \overline{S}_{ik}\overline{\Omega}_{kj}, \quad \mathrm{tr}(\overline{S}\,\overline{\Omega}^2) = \overline{S}_{ij}\overline{\Omega}_{jk}\overline{\Omega}_{ki}$$

The most general form for relation (6.30) is a polynomial of infinite degree of tensors whose terms are of the form $\overline{S}^{a_1}\overline{\Omega}^{a_2}\overline{S}^{a_3}\overline{\Omega}^{a_4}...$, where the a_i are positive integers. Each terms in the series is multiplied by a coefficient, which is itself a function of the invariants of $\overline{S}$ and $\overline{\Omega}$. This series can be reduced to a finite number of linearly independent terms by the Cayley- Hamilton theorem. Since the tensor τ^{d} is symmetrical, we retain only the symmetrical terms here. The computations lead to the definition of eleven tensors, $m_1, ..., m_{11}$, with which $I_1, ..., I_6$ are associated:

$$\begin{aligned}
m_1 &= \overline{S}, & m_2 &= \overline{S}^2,\\
m_3 &= \overline{\Omega}^2, & m_4 &= \overline{S}\,\overline{\Omega} - \overline{\Omega}\,\overline{S},\\
m_5 &= \overline{S}^2\overline{\Omega} - \overline{\Omega}\overline{S}^2, & m_6 &= Id,\\
m_7 &= \overline{S}\,\overline{\Omega}^2 + \overline{\Omega}^2\overline{S}, & m_8 &= \overline{\Omega}\,\overline{S}\,\overline{\Omega}^2 - \overline{\Omega}^2\overline{S}\,\overline{\Omega},\\
m_9 &= \overline{S}\,\overline{\Omega}\,\overline{S}^2 - \overline{S}^2\overline{\Omega}\,\overline{S}, & m_{10} &= \overline{S}^2\overline{\Omega}^2 + \overline{\Omega}^2\overline{S}^2,\\
m_{11} &= \overline{\Omega}\,\overline{S}^2\overline{\Omega}^2 - \overline{\Omega}^2\overline{S}^2\overline{\Omega},
\end{aligned} \tag{6.31}$$

$$\begin{aligned}
I_1 &= \mathrm{tr}(\overline{S}^2), & I_2 &= \mathrm{tr}(\overline{\Omega}^2),\\
I_3 &= \mathrm{tr}(\overline{S}^3), & I_4 &= \mathrm{tr}(\overline{S}\,\overline{\Omega}^2),\\
I_5 &= \mathrm{tr}(\overline{S}^2\overline{\Omega}^2), & I_6 &= \mathrm{tr}(\overline{S}^2\overline{\Omega}^2\overline{S}\,\overline{\Omega}),
\end{aligned} \tag{6.32}$$

where Id designates the identity tensor.

These tensors are independent in the sense that none can be decomposed into a linear sum of the ten others, if the coefficients are constrained to appear as polynomials of the six invariants defined above. If we relax this last constraint by considering the polynomial quotients of the invariants too, then only six of the eleven tensors are linearly independent. The tensors defined above are no longer linearly independent in two cases: when the tensor $\overline{S}$ has a double eigenvalue and when two components of the vorticity disappear when expressed in the specific reference of $\overline{S}$. The first case corresponds to an axisymmetrical shear and the second to a situation where the rotation is about a single axis aligned with one of the eigenvectors of $\overline{S}$. Assuming that neither of these conditions is verified, six of the terms of (6.31) are sufficient for representing the tensor τ, and five for representing its deviator part, which is consistent with the fact that a second-order symmetrical tensor with zero trace has only five degrees of freedom in the third dimension. We then obtain the generic polynomial form:

$$\begin{aligned}
\tau^{\mathrm{d}} &= C_1\overline{\Delta}^2|\overline{S}|\overline{S} + C_2\overline{\Delta}^2(\overline{S}^2)^{\mathrm{d}} + C_3\overline{\Delta}^2(\overline{\Omega}^2)^{\mathrm{d}}\\
&+ C_4\overline{\Delta}^2(\overline{S}\,\overline{\Omega} - \overline{\Omega}\,\overline{S}) + C_5\overline{\Delta}^2\frac{1}{|\overline{S}|}(\overline{S}^2\overline{\Omega} - \overline{S}\,\overline{\Omega}^2) \quad ,
\end{aligned} \tag{6.33}$$

where the C_i, $i = 1, 5$ are constants to be determined. This type of model is analogous in form to the non-linear statistical turbulence models [314, 315]. Numerical experiments performed by the authors on cases of isotropic

homogeneous turbulence have shown that this modeling, while yielding good results, is very costly. Also, computing the different constants raises problems because their dependence as a function of the tensor invariants involved is complex. Meneveau *et al.* [231] attempted to compute these components by statistical techniques, but achieved no significant improvement over the linear model in the prediction of the subgrid tensor eigenvectors.

We note that the first term of the expansion corresponds to subgrid viscosity models for the forward energy cascade based on large scales, which makes it possible to interpret this type of expansion as a sequence of departures from symmetry: the isotropic part of the tensor is represented by a spherical tensor, and the first term represents a first departure from symmetry but prevents the inclusion of the inequality of the normal subgrid stresses[3]. The anisotropy of the normal stresses is included by the following terms, which therefore represent a new departure from symmetry.

Kosovic's Simplified Non-Linear Model. In order to reduce the algorithmic cost of the subgrid model, Kosovic [167] proposes neglecting certain terms in the generic model presented above. After neglecting the high-order terms on the basis of an analysis of their orders of magnitude, the author proposes the following model:

$$\begin{aligned}\tau_{ij} &= -(C_s\overline{\Delta})^2\left[2(2|\overline{S}|^2)^{1/2}\overline{S}_{ij} + C_1\left(\overline{S}_{ik}\overline{S}_{kj} - \frac{1}{3}\overline{S}_{mn}\overline{S}_{mn}\delta_{ij}\right)\right.\\ &\quad \left. + C_2\left(\overline{S}_{ik}\overline{\Omega}_{kj} - \overline{\Omega}_{ik}\overline{S}_{kj}\right)\right] \quad , \end{aligned} \tag{6.34}$$

where C_s is the constant of the subgrid viscosity model based on the large scales (see Sect. 4.3.2) and C_1 and C_2 two constants to be determined. After computation, the local equilibrium hypothesis is expressed:

$$\begin{aligned}\langle\varepsilon\rangle &= -\langle\tau_{ij}\overline{S}_{ij}\rangle\\ &= (C_s\overline{\Delta})^2\langle 2\left[(2|\overline{S}|^2)^{1/2}\overline{S}_{ij}\overline{S}_{ij} + C_1\overline{S}_{ik}\overline{S}_{kj}\overline{S}_{ji}\right]\rangle \quad . \end{aligned} \tag{6.35}$$

In the framework of the canonical case (isotropic turbulence, infinite inertial range, sharp cutoff filter), we get (see [17]):

$$\begin{aligned}\langle\overline{S}_{ij}\overline{S}_{ij}\rangle &= \frac{30}{4}\langle\left(\frac{\partial\overline{u}_1}{\partial x_1}\right)^2\rangle\\ &= \frac{3}{4}K_0\langle\varepsilon\rangle^{2/3}k_c^{4/3} \quad , \end{aligned} \tag{6.36}$$

[3] This is true for all modeling of the form $\tau = (\mathbf{V}\otimes\mathbf{V})$ in which $\mathbf{V}$ is an arbitrary vector. It is trivially verified that the tensor $(\mathbf{V}\otimes\mathbf{V})$ admits only a single non-zero eigenvalue $\lambda = (V_1^2+V_2^2+V_3^2)$, while the subgrid tensor in the most general case has three distinct eigenvalues.

$$\begin{aligned}\langle\overline{S}_{ik}\overline{S}_{kj}\overline{S}_{ji}\rangle &= \frac{105}{8}\langle\left(\frac{\partial\overline{u}_1}{\partial x_1}\right)^3\rangle\\ &= -\frac{105}{8}\mathcal{S}(k_c)\left(\frac{1}{10}K_0\right)^{3/2}\langle\varepsilon\rangle k_c^2 \quad , \end{aligned} \tag{6.37}$$

where coefficient $\mathcal{S}(k_c)$ is defined as:

$$\mathcal{S}(k_c) = -\langle\left(\frac{\partial\overline{u}_1}{\partial x_1}\right)^3\rangle/\langle\left(\frac{\partial\overline{u}_1}{\partial x_1}\right)^2\rangle^{3/2} \quad . \tag{6.38}$$

Substituting these expressions in relation (6.35) yields:

$$\langle\varepsilon\rangle = (C_s\overline{\Delta})^2\left[1 - \frac{7}{\sqrt{960}}C_1\mathcal{S}(k_c)\right]\left(\frac{3}{2}K_0\right)^{3/2}k_c^2\langle\varepsilon\rangle \quad . \tag{6.39}$$

This relation provides a way of relating the constants C_s and C_1 and thereby computing C_1 once C_s is determined by reasoning similar to that explained in the chapter on functional models. The asymptotic value of $\mathcal{S}(k_c)$ is evaluated by theory and experimental observation at between 0.4 and 0.8, as $k_c \to \infty$. The constant C_2 cannot be determined this way, since the contribution of the anti-symmetrical of the velocity gradient to the energy transfer is null[4].

On the basis of simple examples of anisotropic homogeneous turbulence, Kosovic proposes:

$$C_2 \approx C_1 \quad , \tag{6.40}$$

which completes the description of the model.

Dynamic Non-Linear Model. Kosovic's approach uses some hypotheses intrinsic to the subgrid modes, for example the existence of a theoretical the spectrum shape and the local equilibrium hypothesis. To relax these constraints, Wong [348] proposes computing the constants of the non-linear models by means of a dynamic procedure.

To do this, the author proposes a model of the form (we use the same notation here as in the description of the dynamic model with one equation for the kinetic energy, in Sect. 4.4.2):

$$\tau_{ij} = \frac{2}{3}q_{sgs}^2\delta_{ij} - 2C_1\overline{\Delta}\sqrt{q_{sgs}^2}\,\overline{S}_{ij} - C_2\overline{N}_{ij} \quad , \tag{6.41}$$

where C_1 and C_2 are constants and q_{sgs}^2 the subgrid kinetic energy, and

[4] This is because we have the relation

$$\overline{\Omega}_{ij}\overline{S}_{ij} \equiv 0 \quad ,$$

since the tensors $\overline{\Omega}$ and $\overline{S}$ are anti-symmetrical and symmetrical, respectively.

$$\overline{N}_{ij} = \overline{S}_{ik}\overline{S}_{kj} - \frac{1}{3}\overline{S}_{mn}\overline{S}_{mn}\delta_{ij} + \dot{\overline{S}}_{ij} - \frac{1}{3}\dot{\overline{S}}_{mm}\delta_{ij} \quad , \tag{6.42}$$

where $\dot{\overline{S}}_{ij}$ is the Oldroyd[5] derivative of $\overline{S}_{ij}$:

$$\dot{\overline{S}}_{ij} = \frac{D\overline{S}_{ij}}{Dt} - \frac{\partial \overline{u}_i}{\partial x_k}\overline{S}_{kj} - \frac{\partial \overline{u}_j}{\partial x_k}\overline{S}_{ki} \quad , \tag{6.43}$$

where D/Dt is the material derivative associated with the velocity field $\overline{\mathbf{u}}$. The isotropic part of this model is based on the kinetic energy of the subgrid modes (see Sect. 4.3.2). Usually, we introduce a test filter symbolized by a *tilde*, the cutoff length of which is denoted $\widetilde{\overline{\Delta}}$. Using the same model, the subgrid tensor corresponding to the test filter is expressed:

$$T_{ij} = \frac{2}{3}Q^2_{\text{sgs}}\delta_{ij} - 2C_1\widetilde{\overline{\Delta}}\sqrt{Q^2_{\text{sgs}}}\,\widetilde{\overline{S}}_{ij} - C_2\widetilde{\overline{H}}_{ij} \quad , \tag{6.44}$$

where Q^2_{sgs} is the subgrid kinetic energy corresponding to the test filter, and $\widetilde{\overline{H}}_{ij}$ the tensor analogous to $\overline{N}_{ij}$, constructed from the velocity field $\widetilde{\overline{\mathbf{u}}}$. Using the two expressions (6.41) and (6.44), the Germano identity (4.126) is expressed:

$$\begin{aligned} L_{ij} &= T_{ij} - \widetilde{\tau}_{ij} \\ &\simeq \frac{2}{3}(Q^2_{\text{sgs}} - \widetilde{q^2_{\text{sgs}}})\delta_{ij} + 2C_1\overline{\Delta}A_{ij} + C_2\overline{\Delta}^2 B_{ij} \quad , \end{aligned} \tag{6.45}$$

in which

$$A_{ij} = \overline{S}_{ij}\sqrt{q^2_{\text{sgs}}} - \frac{\widetilde{\overline{\Delta}}}{\overline{\overline{\Delta}}}\widetilde{\overline{S}}_{ij}\sqrt{Q^2_{\text{sgs}}} \quad , \tag{6.46}$$

$$B_{ij} = \widetilde{\overline{N}}_{ij} - \left(\frac{\widetilde{\overline{\Delta}}}{\overline{\overline{\Delta}}}\right)^2 \widetilde{\overline{H}}_{ij} \quad . \tag{6.47}$$

We then define the residual E_{ij}:

$$E_{ij} = L_{ij} - \frac{2}{3}(Q^2_{\text{sgs}} - \widetilde{q^2_{\text{sgs}}})\delta_{ij} + 2C_1\overline{\Delta}A_{ij} + C_2\overline{\Delta}^2 B_{ij} \quad . \tag{6.48}$$

The two constants C_1 and C_2 are then computed in such a way as to minimize the scalar residual $E_{ij}E_{ij}$, *i.e.*

$$\frac{\partial E_{ij}E_{ij}}{\partial C_1} = \frac{\partial E_{ij}E_{ij}}{\partial C_2} = 0 \quad . \tag{6.49}$$

[5] This derivative responds to the principle of objectivity, *i.e.* it is invariant if the reference system in which the motion is observed is changed

A simultaneous evaluation of these two parameters leads to:

$$2\overline{\Delta}C_1 \approx \frac{L_{mn}(A_{mn}B_{pq}B_{pq} - B_{mn}A_{pq}B_{pq})}{A_{kl}A_{kl}B_{ij}B_{ij} - (A_{ij}B_{ij})^2} \quad , \tag{6.50}$$

$$\overline{\Delta}^2 C_2 \approx \frac{L_{mn}(B_{mn}A_{pq}A_{pq} - A_{mn}A_{pq}B_{pq})}{A_{kl}A_{kl}B_{ij}B_{ij} - (A_{ij}B_{ij})^2} \quad . \tag{6.51}$$

The quantities q^2_{sgs} and Q^2_{sgs} are obtained by solving the corresponding evolution equations, which are described in the chapter on functional models. This completes computation of the subgrid model.

One variant that does not require the use of additional evolution equations is derived using a model based on the gradient of the resolved scales instead of one based on the subgrid kinetic energy, to describe the isotropic term. The subgrid tensor deviator is now modeled as:

$$\tau_{ij} - \frac{1}{3}\tau_{kk}\delta_{ij} = -2C_1\overline{\Delta}^2|\overline{S}|\overline{S}_{ij} - C_2\overline{N}_{ij} \quad . \tag{6.52}$$

The two parameters computed by the dynamic procedure are now $\overline{\Delta}^2 C_1$ and $\overline{\Delta}^2 C_2$. The expressions obtained are identical in form to relations (6.50) and (6.51), where the tensor A_{ij} is defined as:

$$A_{ij} = |\overline{S}|\overline{S}_{ij} - |\widetilde{\overline{S}}|\widetilde{\overline{S}}_{ij}\left(\frac{\widetilde{\overline{\Delta}}}{\overline{\overline{\Delta}}}\right)^2 \quad . \tag{6.53}$$

6.1.3 Homogenization Technique: Perrier and Pironneau Models

General Description. Another category of models derived from an expansion in a small parameter is that of the models obtained by Perrier and Pironneau [263] by means of the homogenization theory. This approach, which consists in solving the evolution equations of the filtered field separately from those of the subgrid modes, is based on the assumption that the cutoff is located within the inertial range at each point. The resolved field $\overline{\mathbf{u}}$ and the subgrid field $\mathbf{u}'$ are computed on two different grids by a coupling algorithm. In all of the following, we adopt the hypothesis that $\overline{\mathbf{u}'} = 0$. The subgrid modes $\mathbf{u}'$ are then represented by a random process $\mathbf{v}^\delta$, which depends on the dissipation ε, and the viscosity ν, and which is transported by the resolved field $\overline{\mathbf{u}}$. This modeling is denoted symbolically:

$$\mathbf{u}' = \mathbf{v}^\delta\left(\varepsilon, \frac{\mathbf{x} - \overline{\mathbf{u}}t}{\delta}, \frac{t}{\delta^2}\right) \quad , \tag{6.54}$$

in which δ^{-1} is the largest wave number in the inertial range and δ^{-2} the highest frequency cons[illegible]red. As the inertial range is assumed to extend to

the high wave numbers, δ is taken as small parameter. Let $\mathbf{u}^\delta$ be the solution to the problem:

$$\frac{\partial u_i^\delta}{\partial t} + \frac{\partial (u_i^\delta + v_i^\delta)(u_j^\delta + v_j^\delta)}{\partial x_j} - \nu \frac{\partial^2 u_i^\delta}{\partial x_k \partial x_k} = -\frac{\partial p^\delta}{\partial x_i} - \frac{\partial v_i^\delta}{\partial t} + \nu \frac{\partial^2 v_i^\delta}{\partial x_k \partial x_k} \quad . \tag{6.55}$$

If $\mathbf{v}^\delta$ is close to $\mathbf{u}'$, then $\overline{\mathbf{u}^\delta}$ is close to $\overline{\mathbf{u}}$. More precisely, we have:

$$\mathbf{u}^\delta = \overline{\mathbf{u}} + \delta \mathbf{u}^1 + \delta^2 \mathbf{u}^2 + ... \tag{6.56}$$

A modeling of this kind, while satisfactory on the theoretical level, is not so in practice because the function $\mathbf{v}^\delta$ oscillates very quickly in space and time, and the number of degrees of freedom needed in the discrete system to describe its variations remains very high. To reduce the size of the discrete system significantly, other hypotheses are needed, leading to the definition of simplified models which are described in the following.

First Model. The first simplification consists in choosing the random process in the form:

$$\mathbf{v}^\delta(\mathbf{x}, t) = \frac{1}{\delta} \mathbf{v}(\mathbf{x}, t, \mathbf{x}', t') \quad , \tag{6.57}$$

in the space and time scales $\mathbf{x}'$ and t', respectively, of the subgrid modes are defined as:

$$\mathbf{x}' = \frac{\mathbf{x} - \overline{\mathbf{u}} t}{\delta}, \; t' = \frac{t}{\delta^2} \quad . \tag{6.58}$$

The new variable $\mathbf{v}(\mathbf{x}, t, \mathbf{x}', t')$ oscillates slowly and can thus be represented with fewer degrees of freedom. Assuming that $\mathbf{v}$ is periodical depending on the variables $\mathbf{x}'$ and t' on a domain $\Omega_v = Z \times]0, T'[$, and that the average of $\mathbf{v}$ is null over this domain[6], it is demonstrated that the subgrid tensor is expressed in the form:

$$\tau = B \nabla \overline{\mathbf{u}} \quad , \tag{6.59}$$

where the term $B \nabla \overline{\mathbf{u}}$ is computed by taking the average on the cell of periodicity Ω_v of the term $(\mathbf{v} \cdot \nabla \mathbf{u}^1 + \mathbf{u}^1 \cdot \nabla \mathbf{v})$, where $\mathbf{u}^1$ is the a solution on this cell of the problem:

$$\frac{\partial \mathbf{u}^1}{\partial t'} - \nu \nabla^2_{\mathbf{x}'} \mathbf{u}^1 + \mathbf{v} \cdot \nabla_{\mathbf{x}'} \mathbf{u}^1 + \mathbf{u}^1 \cdot \nabla_{\mathbf{x}'} \mathbf{v} = \nabla q - \mathbf{v} \cdot \nabla \overline{\mathbf{u}} - \overline{\mathbf{u}} \cdot \nabla \mathbf{v} \quad , \tag{6.60}$$

[6] This is equivalent to considering that $\mathbf{v}(\mathbf{x}, t, \mathbf{x}', t')$ is statistically homogeneous and isotropic, which is theoretically justifiable by the physical hypothesis of local isotropy.

$$\nabla_{\mathbf{x}'} \cdot \mathbf{u}^1 = 0 \quad , \tag{6.61}$$

where $\nabla_{\mathbf{x}'}$ designates the gradient with respect to the $\mathbf{x}'$ variables and q the Lagrange multiplier that enforces the constraint (6.61). This model, though simpler, is still difficult to use because the variable $(\mathbf{x} - \overline{\mathbf{u}} t)$ is difficult to manipulate. So other simplifications are needed.

Second Model. To arrive at a usable model, the authors propose neglecting the transport of the random variable by the filtered field in the field's evolution equation. This way, the random variable can be chosen in the form:

$$\mathbf{v}^\delta(\mathbf{x}, t) = \frac{1}{\delta} \mathbf{v}(\mathbf{x}, t, \mathbf{x}'', t') \quad , \tag{6.62}$$

with

$$\mathbf{x}'' = \frac{\mathbf{x}}{\delta} \quad , \tag{6.63}$$

and where the time t' is defined as before. Assuming that $\mathbf{v}$ is periodic along $\mathbf{x}''$ and t' on the domain Ω_v and has an average of zero over this interval, the subgrid term takes the form:

$$\tau = A \nabla \overline{\mathbf{u}} \quad , \tag{6.64}$$

where A is a definite positive tensor such that the term $A \nabla \overline{\mathbf{u}}$ is equal to the average of the term $(\mathbf{v} \otimes \mathbf{u}^1)$ over Ω_v, in which $\mathbf{u}^1$ is a solution on Ω_v of the problem:

$$\frac{\partial \mathbf{u}^1}{\partial t'} - \nu \nabla^2_{\mathbf{x}''} \mathbf{u}^1 + \mathbf{v} \cdot \nabla_{\mathbf{x}''} \mathbf{u}^1 = \nabla q + \mathbf{v} \cdot \nabla \overline{\mathbf{u}} \quad , \tag{6.65}$$

$$\nabla_{\mathbf{x}''} \cdot \mathbf{u}^1 = 0 \quad . \tag{6.66}$$

6.2 Differential Subgrid Stress Models

6.2.1 Deardorff Model

Another approach for obtaining a model for the subgrid tensor consists in solving an evolution equation for each of its components. This approach, proposed by Deardorff [77] and recently re-investigated by Fureby *et al.* [107], is analogous in form to two-point statistical modeling. Here, we adopt the case where the filter is a Reynolds operator. The subgrid tensor τ_{ij} is thus reduced to the subgrid Reynolds tensor R_{ij}. We deduce the evolution equation of the subgrid tensor components from that of the subgrid modes (3.29)[7]:

[7] This is done by applying the filter to the relation obtained by multiplying (3.29) by u'_j and taking the half-sum with the relation obtained by inverting the subscripts i and j.

$$\frac{\partial \tau_{ij}}{\partial t} = -\frac{\partial}{\partial x_k}(\overline{u}_k \tau_{ij}) - \tau_{ik}\frac{\partial \overline{u}_j}{\partial x_k} - \tau_{jk}\frac{\partial \overline{u}_i}{\partial x_k} - \frac{\partial}{\partial x_k}\overline{u'_i u'_j u'_k} + \overline{p'\left(\frac{\partial u'_i}{\partial x_j} + \frac{\partial u'_j}{\partial x_i}\right)} - \frac{\partial}{\partial x_j}\overline{u'_i p'} - \frac{\partial}{\partial x_i}\overline{u'_j p'} - 2\nu\overline{\frac{\partial u'_i}{\partial x_k}\frac{\partial u'_j}{\partial x_k}} \quad . \tag{6.67}$$

The various terms in this equation have to be modeled. The models Deardorff proposes are:

– For the pressure–strain correlation term:

$$\overline{p'\left(\frac{\partial u'_i}{\partial x_j} + \frac{\partial u'_j}{\partial x_i}\right)} = -C_{\mathrm{m}}\frac{\sqrt{q^2_{\mathrm{sgs}}}}{\overline{\Delta}}\left(\tau_{ij} - \frac{2}{3}q^2_{\mathrm{sgs}}\delta_{ij}\right) + \frac{2}{5}q^2_{\mathrm{sgs}}\overline{S}_{ij} \quad , \tag{6.68}$$

where C_{m} is a constant, q^2_{sgs} the subgrid kinetic energy, and $\overline{S}_{ij}$ the strain rate tensor of the resolved field.

– For the dissipation term:

$$\nu\overline{\frac{\partial u'_i}{\partial x_k}\frac{\partial u'_j}{\partial x_k}} = \delta_{ij}C_{\mathrm{e}}\frac{(q^2_{\mathrm{sgs}})^{3/2}}{\overline{\Delta}} \quad , \tag{6.69}$$

where C_{e} is a constant.

– For the triple correlations:

$$\overline{u'_i u'_j u'_k} = -C_{3\mathrm{m}}\overline{\Delta}\left(\frac{\partial}{\partial x_i}\tau_{jk} + \frac{\partial}{\partial x_j}\tau_{ik} + \frac{\partial}{\partial x_k}\tau_{ij}\right) \quad . \tag{6.70}$$

The pressure–velocity correlation terms $\overline{p'u'_i}$ are neglected. The values of the constants are determined in the case of isotropic homogeneous turbulence:

$$C_{\mathrm{m}} = 4.13,\ C_{\mathrm{e}} = 0.70,\ C_{3\mathrm{m}} = 0.2 \quad . \tag{6.71}$$

Lastly, the subgrid kinetic energy is determined using evolution equation (4.108).

6.2.2 Link with the Subgrid Viscosity Models

We reach the functional subgrid viscosity models again starting with a model with transport equations for the subgrid stresses, at the cost of additional assumptions. For example, Yoshizawa *et al.* [363] proposed neglecting all the terms of equation (6.67), except those of production. The evolution equation thus reduced comes to:

$$\frac{\partial \tau_{ij}}{\partial t} = -\tau_{ik}\frac{\partial \overline{u}_j}{\partial x_k} - \tau_{jk}\frac{\partial \overline{u}_i}{\partial x_k} \quad . \tag{6.72}$$

Assuming that the subgrid modes are isotropic or quasi-isotropic, *i.e.* that the extra-diagonal elements of the subgrid tensor are very small compared with the diagonal elements, and that the latter are almost mutually equal, the right-hand side of the reduced equation (6.72) comes down to the simplified form:

$$-q^2_{\mathrm{sgs}}\overline{S}_{ij} \quad , \tag{6.73}$$

in which $q^2_{\mathrm{sgs}} = \overline{u'_k u'_k}/2$ is the subgrid kinetic energy. Let t_0 be the characteristic time of the subgrid modes. Considering the relations (6.72) and (6.73), and assuming that the relaxation time of the subgrid modes is much shorter than that of the resolved scales[8], we get

$$\tau_{ij} - \frac{1}{3}\tau_{kk}\delta_{ij} \approx -t_0 q^2_{\mathrm{sgs}}\overline{S}_{ij} \quad . \tag{6.74}$$

The time t_0 can be evaluated by dimensional argument using the cutoff length $\overline{\Delta}$ and the subgrid kinetic energy:

$$t_0 \approx \frac{\overline{\Delta}}{\sqrt{q^2_{\mathrm{sgs}}}} \quad . \tag{6.75}$$

By entering this estimate into equation (6.74), we get an expression analogous to the one used in the functional modeling framework:

$$\tau_{ij} - \frac{1}{3}\tau_{kk}\delta_{ij} \approx -\overline{\Delta}\sqrt{q^2_{\mathrm{sgs}}}\,\overline{S}_{ij} \quad . \tag{6.76}$$

6.3 Deterministic Models of the Subgrid Structures

6.3.1 General

Misra and Pulin [236], following on the works of Pullin and Saffman [273], proposed subgrid models using the assumption that the subgrid modes can be represented by stretched vortices whose orientation is governed by the resolved scales.

Supposing that the subgrid modes can be linked to a random superimposition of fields generated by axisymmetrical vortices, the subgrid tensor can be written in the form:

$$\tau_{ij} = 2\int_{k_{\mathrm{c}}}^{\infty} E(k)dk\langle E_{pi}Z_{pq}E_{qj}\rangle \quad , \tag{6.77}$$

[8] We again find here the ...al scale-separation hypothesis 4.4.

in which $E(k)$ is the energy spectrum, E_{lm} the rotation matrix used to switch from the vortex coordinate system to the reference system, Z_{ij} the diagonal tensor whose main elements are $(1/2, 1/2, 0)$ and $\langle E_{pi} Z_{pq} E_{qj} \rangle$, the moment of the probability density function $P(\alpha, \beta)$ of the Euler angles α and β giving the orientation of the vortex axis with respect to the frame of reference. The statistical average performed on the Euler angles of a function f is defined as:

$$\langle f(E_{ij}) \rangle = \frac{1}{4\pi} \int_0^{\pi} \int_0^{2\pi} f(E_{ij}) P(\alpha, \beta) \sin(\alpha) d\alpha d\beta \quad . \tag{6.78}$$

Two pieces of information are therefore needed to compute the subgrid term: the shape of the energy spectrum for the subgrid modes and the subgrid structure orientation distribution function. As the use of an evolution equation for the probability density function yielded no satisfactory results, Misra and Pullin propose modeling this function as a product of Dirac functions or a linear combination of such products. These are of the general form:

$$P(\alpha, \beta) = \frac{4\pi}{\sin(\alpha)} \delta(\alpha - \theta) \delta(\beta - \phi) \quad , \tag{6.79}$$

where $\theta(\mathbf{x}, t)$ and $\phi(\mathbf{x}, t)$ determine the specific orientation considered. Defining the two unit vectors $\mathbf{e}$ and $\mathbf{e}^v$:

$$e_1 = \sin(\alpha)\cos(\beta), \; e_2 = \sin(\alpha)\sin(\beta), \; e_3 = \cos(\alpha), \tag{6.80}$$

$$e_1^v = \sin(\theta)\cos(\phi), \; e_2^v = \sin(\theta)\sin(\phi), \; e_3^v = \cos(\theta), \tag{6.81}$$

the subgrid tensor can be re-written in the form:

$$\tau_{ij} = \left(\delta_{ij} - e_i^v e_j^v\right) \int_{k_c}^{\infty} E(k) dk = \left(\delta_{ij} - e_i^v e_j^v\right) q_{sgs}^2 \quad . \tag{6.82}$$

The various models must thus specify the specific orientation directions of the subgrid structures. Three models are presented in the following. The subgrid kinetic energy q_{sgs}^2 can be computed in different ways (see the sections on the functional models), for example by solving an additional evolution equation, or by using a double filtering technique.

6.3.2 S3/S2 Alignment Model

A first hypothesis is to assume that the subgrid structures are oriented along the eigenvectors of the resolved strain rate tensor $\overline{S}_{ij}$ that corresponds to its two largest eigenvalues. This is equivalent to assuming that they respond instantaneously to the forcing of the large scales. Using $\mathbf{e}^{s2}$ and $\mathbf{e}^{s3}$ to denote these two vectors, and λ_2 and $\lambda_3 \geq \lambda_2$ the associated eigenvalues, we get

$$\tau_{ij} = q_{sgs}^2 \left[\lambda \left(\delta_{ij} - e_i^{s3} e_j^{s3}\right) + (1 - \lambda)\left(\delta_{ij} - e_i^{s2} e_j^{s2}\right)\right] \quad , \tag{6.83}$$

where the weighting coefficient is taken proportional to the norms of the eigenvalues:

$$\lambda = \frac{\lambda_3}{\lambda_3 + |\lambda_2|} \quad . \tag{6.84}$$

6.3.3 S3/ω Alignment Model

The second model is derived on the assumption that the subgrid structures are oriented along the third eigenvector of the tensor $\overline{S}_{ij}$, denoted $\mathbf{e}^{s3}$ as before, and the vorticity vector of the resolved field. The unit vector it carries is denoted $\mathbf{e}^{\omega}$ and is computed as:

$$\mathbf{e}^{\omega} = \frac{\nabla \times \overline{\mathbf{u}}}{|\nabla \times \overline{\mathbf{u}}|} \quad . \tag{6.85}$$

The subgrid tensor is evaluated as:

$$\tau_{ij} = q_{sgs}^2 \left[\lambda \left(\delta_{ij} - e_i^{s3} e_j^{s3}\right) + (1 - \lambda)\left(\delta_{ij} - e_i^{\omega} e_j^{\omega}\right)\right] \quad . \tag{6.86}$$

The weighting parameter λ is chosen arbitrarily. The authors performed tests considering the three values 0, 0.5, and 1.

6.3.4 Kinematic Model

Starting with the kinematics of a vortex filament entrained by a fixed velocity field, Misra and Pullin propose a third model, for which the vector $\mathbf{e}^v$ is obtained by solving an evolution equation. The equation for the ith component of this vector is:

$$\frac{\partial e_i^v}{\partial t} = e_j^v \frac{\partial \overline{u}_i}{\partial x_j} - e_i^v e_k^v e_j^v \frac{\partial \overline{u}_k}{\partial x_j} \quad . \tag{6.87}$$

The subgrid tensor is then evaluated by inserting the vector $\mathbf{e}^v$ thus computed into the expression (6.82).

6.4 Scale Similarity Hypotheses and Models Using Them

6.4.1 Scale Similarity Hypotheses

Basic Hypothesis. The scale similarity hypothesis such as proposed by Bardina *et al.* [12, 13] consists in assuming that the statistical structure of the tensors constructed on the basis of the subgrid scales is similar to that of

their equivalents evaluated on the basis of the smallest resolved scales. The spectrum of the solution based on this hypothesis is therefore broken down into three bands: the largest resolved scales, the smallest resolved scales (*i.e.* the test field), and the unresolved scales (see Fig. 4.14).

This statistical consistency can be interpreted in two complementary ways. The first uses the energy cascade idea. That is, the unresolved scales and the smallest resolved scales have a common history due to their interactions with the largest resolved scales. The classical representation of the cascade has it that the effect of the largest resolved scales is exerted on the smallest resolved scales, which in turn influences the subgrid scales, which are therefore indirectly forced by the largest resolved scales, but similarly to the smallest. The second interpretation is based on the idea of coherent structures. These structures have a non-local frequency signature[9], *i.e.* they have a contribution on the three spectral bands considered. Scale similarity is therefore associated with the fact that certain structures appear in each of the three bands, inducing a strong correlation of the field among the various levels of decomposition.

Extended Hypothesis. This hypothesis was generalized by Liu *et al.* [200] (see [228] for a more complete discussion) to a spectrum split into an arbitrary number of bands, as illustrated in Fig. 6.1. The scale similarity hypothesis is then re-formulated for two consecutive spectrum bands, with the consistent forcing being associated with the low frequency band closest to those considered. Thus the specific elements of the tensors constructed from the velocity field u^n and their analogous elements constructed from u^{n+1} are assumed to be the same. This hypothesis has been successfully verified in experiments in the case of a jet turbulence [200] and plane wake turbulence [258]. Liu *et al.* have also demonstrated that scale similarity persists during rapid straining [199].

6.4.2 Scale Similarity Models

This section presents the structural models constructed on the basis of the scale similarity hypothesis. All of them make use of a frequency extrapolation technique: the subgrid tensor is a approximated by an analogous tensor computed from the highest resolved frequencies. The following are described:

1. Bardina's model (p.179) in which the subgrid tensor is computed by applying the analytical filter a second time and thereby evaluating the fluctuation of the resolved scales. This model is therefore inoperative when the filter is idempotent, because this fluctuation is then null.
2. Filtered Bardina model (p.180), which is an improvement on the previous one. By construction, the subgrid tensor is a filtered quantity, which results in the application of a convolution product and is therefore non-local in the sense that it incorporates all the information contained in the support of the filter convolution kernel. It is proposed in this model to cover this non-local character by applying the filter to the modeled subgrid tensor.
3. Liu–Meneveau–Katz model (p.181), which generalizes the Bardina model to the use of two consecutive filters of different shapes and cutoff frequencies, for computing the small scale fluctuations. This model can therefore be used for any type of filter.
4. The dynamic similarity model (p.182), which can be used to compute the intensity of the modeled subgrid stresses by a dynamic procedure, whereas in the previous cases this intensity is prescribed by hypotheses on the form of the energy spectrum.

[9] This is due to the fact that the variations of the velocity components associated with a vortex cannot be represented by a monochromatic wave. For example, the Lamb-Oseen vortex tangential velocity radial distribution is:

$$U_\theta = \frac{q}{r}\left(1 - e^{-r^2}\right) \quad ,$$

where r is the distance to the center and q the maximum v ity.

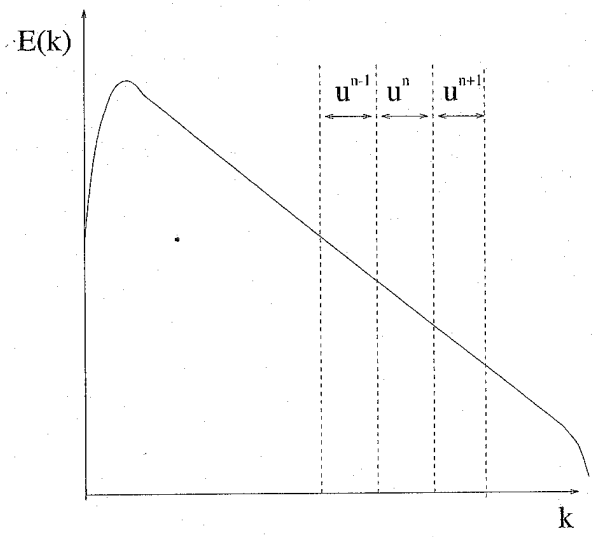

Fig. 6.1. Spectral decomposition based on the extended scale similarity hypothesis.

Bardina Model. Starting with the hypothesis, Bardina, Ferziger, and Reynolds [13] proposed modeling the C and R terms of the Leonard decomposition by a second application of the filter that was used to separate the scales. We furthermore have the approximation:

$$\overline{\phi\psi} \simeq \overline{\phi}\,\overline{\psi} \quad , \tag{6.88}$$

which allows us to say:

$$R_{ij} = (\overline{u}_i - \overline{\overline{u}}_i)(\overline{u}_j - \overline{\overline{u}}_j) \quad , \tag{6.89}$$

$$C_{ij} = (\overline{u}_i - \overline{\overline{u}}_i)\overline{\overline{u}}_j + (\overline{u}_j - \overline{\overline{u}}_j)\overline{\overline{u}}_i \quad , \tag{6.90}$$

or

$$R_{ij} + C_{ij} = (\overline{u}_i\overline{u}_j - \overline{\overline{u}}_i\overline{\overline{u}}_j) \quad . \tag{6.91}$$

Adding Leonard's term, which is computed directly from the resolved scales, we get:

$$\tau_{ij} = L_{ij} + R_{ij} + C_{ij} = (\overline{\overline{u}_i\overline{u}_j} - \overline{\overline{u}}_i\overline{\overline{u}}_j) \quad . \tag{6.92}$$

This can be re-written in another using the generalized central moments proposed by Germano [113]:

$$\tau_{ij} = \tau_G([u_i]_G, [u_j]_G) \equiv \mathcal{L}_{ij} \quad . \tag{6.93}$$

The subgrid tensor is therefore approximated by the generalized central moment of the filtered field defined like the tensor $\mathcal{L}_{ij}$ in the Germano decomposition (see Sect. 3.3.2). Experience shows that this model is not effective when the filter is a Reynolds operator, because the contribution thus computed then cancels out. Contrary to the subgrid viscosity models, this one does not induce an alignment of the proper axis system of the subgrid tensor on those of the strain rate tensor. Tests performed on databases generated by direct numerical simulation have shown that this model leads to a very good level of correlation with the true subgrid tensor, including when the flow is anisotropic [139].

Despite its very good level of correlation[10], experience shows that this model is only slightly dissipative and that it underestimates the energy cascade. It does, on the other hand, include the backward cascade mechanism.

Filtered Bardina Model. The Bardina model (6.92) is local in space in the sense that it appears as a product of local values. This local character is in contradiction with the non-local nature of the subgrid tensor, so that each component appears in the form of a convolution product. To remedy this problem, Horiuti [142] proposes the filtered Bardina model:

$$\tau_{ij} = \overline{(\overline{u}_i\overline{u}_j - \overline{\overline{u}}_i\overline{\overline{u}}_j)} = \overline{\mathcal{L}}_{ij} \quad . \tag{6.94}$$

With this additional filtering operation, we recover the non-local character of the subgrid tensor.

[10] The correlation coefficient at the scalar level is generally higher than 0.8.

Liu–Meneveau–Katz Model. The Bardina model uses a second application of the same filter, and therefore a single cutoff scale. This model is generalized to the case of two cutoff levels as [200]:

$$\tau_{ij} = C_l(\widetilde{\overline{u}_i\overline{u}_j} - \widetilde{\overline{u}}_i\widetilde{\overline{u}}_j) = C_l\mathcal{L}^m_{ij} \quad , \tag{6.95}$$

where the tensor $\mathcal{L}^m_{ij}$ is now defined by two different levels of filtering. The test filter cutoff length designated by the *tilde* is larger than that of the first level. The constant C_l can be evaluated theoretically to ensure that the average value of the modeled generalized subgrid kinetic energy is equal to its exact counterpart [67]. This leads to the relation:

$$C_l = \frac{\langle\overline{u_k u_k} - \overline{u}_k\overline{u}_k\rangle}{\langle\widetilde{\overline{u}_k\overline{u}_k} - \widetilde{\overline{u}}_k\widetilde{\overline{u}}_k\rangle} \quad . \tag{6.96}$$

Let $\widehat{F}(k)$ and $\widehat{G}(k)$ be transfer functions associated with the grid filter and test filter, respectively, and let $E(k)$ be the energy spectrum of the exact solution. Relation (6.96) can then be re-written as:

$$C_l = \frac{\int_0^\infty (1 - \widehat{F}^2(k))E(k)dk}{\int_0^\infty (1 - \widehat{G}^2(k))\widehat{F}^2(k)E(k)dk} \quad . \tag{6.97}$$

Evaluations made using experimental data come to $C_l \simeq 1$ [200, 258][11]. Shah and Ferziger [307] propose extending this model to the case of non-symmetric filters.

To control the amplitude of the backward cascade induced by the model, especially near solid walls, Liu *et al.* [200] propose the modified form:

$$\tau_{ij} = C_l f(I_{LS})\mathcal{L}^m_{ij} \quad , \tag{6.98}$$

where the dimensionless invariant I_{LS}, defined as

$$I_{LS} = \frac{\mathcal{L}^m_{lk}\overline{S}_{lk}}{\sqrt{\mathcal{L}^m_{lk}\mathcal{L}^m_{lk}}\sqrt{\overline{S}_{lk}\overline{S}_{lk}}} \tag{6.99}$$

measures the alignment of the proper axes of the tensors $\mathcal{L}^m$ and $\overline{S}$. As the kinetic energy dissipated by the subgrid model is expressed

$$\varepsilon = -\tau_{ij}\overline{S}_{ij} \quad , \tag{6.100}$$

we get, using model (6.98):

$$\varepsilon = -C_l f(I_{LS})I_{LS} \quad . \tag{6.101}$$

[11] The initial value of 0.45 ± 0.15 given in [200] does not take the backward cascade into account.

The backward energy cascade is modulated by controlling the sign and amplitude of the product $f(I_{\rm LS})I_{\rm LS}$. The authors considered a number of choices. The first is:

$$f(I_{\rm LS}) = \begin{cases} 1 & \text{if} \quad I_{\rm LS} \geq 0 \\ 0 & \text{otherwise} \end{cases} \quad . \tag{6.102}$$

This solution makes it possible to cancel out the representation of the backward cascade completely by forcing the model to be strictly dissipative. One drawback to this is that the function f is discontinuous, which can generate numerical problems. A second solution that is continuous consists in taking:

$$f(I_{\rm LS}) = \begin{cases} I_{\rm LS} & \text{if} \quad I_{\rm LS} \geq 0 \\ 0 & \text{otherwise} \end{cases} \quad . \tag{6.103}$$

One last positive, continuous, upper-bounded solution is of the form:

$$f(I_{\rm LS}) = \begin{cases} (1 - \exp(-\gamma I_{\rm LS}^2)) & \text{if} \quad I_{\rm LS} \geq 0 \\ 0 & \text{otherwise} \end{cases} \quad , \tag{6.104}$$

in which $\gamma = 10$.

Dynamic Similarity Model. A dynamic version of the Liu–Meneveau–Katz model (6.95) was also proposed [200] for which the constant $C_{\rm l}$ will no longer be set arbitrarily. To compute this model, we introduce a third level of filtering identified by $\widehat{\cdot}$. The Q analogous to tensor $\mathcal{L}^{\rm m}$ for this new level of filtering is expressed:

$$Q_{ij} = (\widehat{\widetilde{\overline{u}}_i \widetilde{\overline{u}}_j} - \widehat{\widetilde{\overline{u}}}_i \widehat{\widetilde{\overline{u}}}_j) \quad . \tag{6.105}$$

The Germano–Lilly dynamic procedure, based here on the difference:

$$M_{ij} = f(I_{\rm QS}) Q_{ij} - \widehat{f(I_{\rm LS})\mathcal{L}_{ij}^{\rm m}} \quad , \tag{6.106}$$

where

$$I_{\rm QS} = \frac{Q_{mn}\widetilde{\overline{S}}_{mn}}{|Q|\,|\widetilde{\overline{S}}|} \quad , \tag{6.107}$$

yields:

$$C_{\rm l} = \frac{\mathcal{L}_{lk}^{\rm m} M_{lk}}{M_{pq} M_{pq}} \quad . \tag{6.108}$$

6.4.3 A Bridge Between Scale Similarity and Approximate Deconvolution Models. Generalized Similarity Models

The Bardina model can be interpreted as a particular case of the approximate deconvolution based models described in Sect. 6.1.

Using the second order differential approximation

$$\overline{\phi} = \phi + \frac{\alpha^{(2)}}{2} \frac{\partial^2 \phi}{\partial x^2} \quad , \tag{6.109}$$

the Bardina model (6.92) is strictly equivalent to the second order gradient model given by relations (6.13) and (6.14).

It can also be derived using the iterative deconvolution procedure: a zeroth-order truncation in (6.27) is used to recover relation (6.88), while a first-order expansion is employed to derive (6.89).

The Bardina model then appears as a low-order formal expansion model for the subgrid tensor. Generalized scale similarity models can then be defined using higher-order truncations for the formal expansion [119]. They are formulated as

$$\tau_{ij} = \overline{(G_d^{-1} \star \overline{u}_i)(G_d^{-1} \star \overline{u}_j)} - \overline{(G_d^{-1} \star \overline{u})}_i - \overline{(G_d^{-1} \star \overline{u})}_j \quad , \tag{6.110}$$

where $G_d^{-1}\star$ designates the approximate deconvolution operator, defined using equation (6.9) or equation (6.27).

6.5 Mixed Modeling

6.5.1 Motivations

The structural models based on the scale similarity idea, and the functional models, each have their advantages and disadvantages that make the seem complementary:

- The functional models, generally, correctly take into account the level of the energy transfers between the resolved scales and the subgrid modes. However, their prediction of the subgrid tensor structure, *i.e.* its eigenvectors, is very poor.
- The models based on the scale-similarity hypothesis or an approximate deconvolution procedure generally predict well the structure of the subgrid tensor better (and then are able to capture anisotropic effects and disequilibrium), but are less efficient for dealing with the level of the energy transfers.

Tests have shown that they are able to capture disequilibrium and anisotropy effects.

Shao *et al.* [308] propose a splitting of the kinetic energy transfer across the cut-off that enlights the role of each one of these two model classes. These authors combine the classical large-eddy simulation convolution filter to the ensemble average, yielding the following decompositions:

$$\mathbf{u} = \langle \mathbf{u} \rangle + \mathbf{u}'^e \tag{6.111}$$
$$= \overline{\mathbf{u}} + \mathbf{u}' \tag{6.112}$$
$$= \langle \overline{\mathbf{u}} \rangle + \langle \mathbf{u}' \rangle + \overline{\mathbf{u}'^e} + \mathbf{u}'' \quad . \tag{6.113}$$

Using this hybrid decomposition, the subgrid tensor splits into

$$\tau_{ij} = \tau_{ij}^{\text{rapid}} + \tau_{ij}^{\text{slow}} \quad , \tag{6.114}$$

with

$$\tau_{ij}^{\text{slow}} = \overline{u_i'^e u_j'^e} - \overline{u'^e}_i \overline{u'^e}_j \quad , \tag{6.115}$$

$$\tau_{ij}^{\text{rapid}} = \overline{\langle u_i \rangle \langle u_j \rangle} - \langle \overline{u}_i \rangle \langle \overline{u}_j \rangle + \overline{u_i'^e \langle u_j \rangle} - \overline{u'^e}_i \langle \overline{u}_j \rangle + \overline{u_j'^e \langle u_i \rangle} - \overline{u'^e}_j \langle \overline{u}_i \rangle \quad . \tag{6.116}$$

These two parts can be analysed as follows:

- The rapid part explicitly depends on the mean flow. This contribution arises only if the convolution filter is applied in directions where the mean flow gradients are non-zero. It is referred to as rapid because the time scale of its response to variations of the mean flow is small. Numerical experiments show that this part plays an important role when the turbulence is in a desiquilibrium state when: (i) production of kinetic energy is much larger than dissipation or (ii) the filter length is of the same order as the integral scale of turbulence. Subgrid stresses anisotropy is observed to be due to the interaction of this rapid part and the mean shear. Numerical simulations have shown that the rapid part escapes the functional modeling, but scale-similarity models succeed in representing anisotropic energy transfer (both forward and backward cascades) associated to the rapid part.
- The slow part is always present in large-eddy simulation, because it does not depend on the mean flow gradients. It corresponds to the subgrid tensor analyzed through the previously described canonical analysis. It is referred to as slow because its relaxation time is long with respect to rapid part. Numerical tests show that subgrid viscosity model correctly capture the associated kinetic energy transfer.

One simple idea for generating subgrid models possessing good qualities on both the structural and energy levels is to combine a functional with a structural model, making what is called mixed models. This is generally done by combining a subgrid viscosity model for representing the energy cascade mechanism with a scale similarity. The stochastic backward cascade models are usually not included because the structural models are capable of including this phenomenon. The resulting form is

$$\tau_{ij} - \frac{1}{3}\tau_{kk}\delta_{ij} = -2\nu_{\text{sgs}}\overline{S}_{ij} + (L_{ij} - \frac{1}{3}L_{kk}\delta_{ij}) \quad , \tag{6.117}$$

where ν_{sgs} is the subgrid viscosity (evaluated using one of the previously described model), and L_{ij} the evaluation obtained using one of the structural model[12].

Examples of such models are described in the following.

6.5.2 Examples of Mixed Models

We present several examples of mixed models here:

1. The Smagorinsky–Bardina model (p.185), for which the respective weights of each of the contributions are preset. This model is limited by the hypotheses underlying each of the two parts constituting it: the subgrid viscosity is still based on arguments of the infinite inertial range type. Experience shows, though, that combining the two models reduces the importance of the constraints associated with these underlying hypotheses, which improves the results.
2. A one-parameter mixed model whose subgrid viscosity is computed by a dynamic procedure of the Germano–Lilly type (p.186). With this procedure, the respective weights of the structural and functional parts of the model can be modified, so that the subgrid viscosity model is now computed as a complement to the scale similarity model, which allows a better control of the dissipation induced. It can be said, though, that this procedure innately prefers the structural part.
3. The general form of N-parameter dynamic mixed model, as derived by Sagaut *et al.* (p.187). This procedure is an extension of the previous one: the weights of the different parts of the model are dynamically computed, resulting in a possibly better approximation of the true subgrid stresses. The case of two-parameter dynamic mixed model is emphasized.

Mixed Smagorinsky–Bardina Model. The first example is proposed by Bardina *et al.* [13] in the form of a linear combination of the Smagorinsky model (4.90) and the scale similarity model (6.92). The subgrid tensor deviator is then written:

[12] Only scale-similarity models or approximate deconvolution models are used in practice to derive mixed models, because they are very easy to implement.

$$\tau_{ij} - \frac{1}{3}\tau_{kk}\delta_{ij} = \frac{1}{2}\left(-2\nu_{\text{sgs}}\overline{S}_{ij} + \mathcal{L}_{ij} - \frac{1}{3}\mathcal{L}_{kk}\delta_{ij}\right) \quad , \tag{6.118}$$

in which

$$\mathcal{L}_{ij} = \left(\overline{\overline{u}_i\overline{u}_j} - \overline{\overline{u}}_i\overline{\overline{u}}_j\right) \quad , \tag{6.119}$$

and

$$\nu_{\text{sgs}} = C_s\overline{\Delta}^2|\overline{S}| \quad . \tag{6.120}$$

Variants are obtained either by changing the subgrid viscosity model used or by replacing the tensor $\mathcal{L}$ with the tensor $\mathcal{L}^{\text{m}}$ (6.98) or the tensor $\overline{\mathcal{L}}$ (6.94).

One-Parameter Mixed Dynamic Model. A mixed dynamic modeling was proposed by Zang, Street, and Koseff [366]. This is based initially on the Bardina model coupled with the Smagorinsky model, but the latter can be replaced by any other subgrid viscosity model. The subgrid viscosity model constant is computed by a dynamic procedure. The subgrid tensors corresponding to the two filtering levels are modeled by a mixed model:

$$\tau_{ij} - \frac{1}{3}\tau_{kk}\delta_{ij} = -2\nu_{\text{sgs}}\overline{S}_{ij} + \mathcal{L}^{\text{m}}_{ij} - \frac{1}{3}\mathcal{L}^{\text{m}}_{kk}\delta_{ij} \quad , \tag{6.121}$$

$$T_{ij} - \frac{1}{3}T_{kk}\delta_{ij} = -2\nu_{\text{sgs}}\widetilde{\overline{S}}_{ij} + \mathcal{Q}_{ij} - \frac{1}{3}\mathcal{Q}_{kk}\delta_{ij} \quad , \tag{6.122}$$

in which

$$\mathcal{Q}_{ij} = \widetilde{\overline{\overline{u}_i\overline{u}_j}} - \widetilde{\overline{\overline{u}}}_i\widetilde{\overline{\overline{u}}}_j \quad , \tag{6.123}$$

and

$$\nu_{\text{sgs}} = C_{\text{d}}\overline{\Delta}|\overline{S}| \quad . \tag{6.124}$$

The residual E_{ij} is now of the form:

$$E_{ij} = \mathcal{L}^{\text{m}}_{ij} - \mathcal{H}_{ij} - \left(-2C_{\text{d}}\overline{\Delta}^2 m_{ij} + \delta_{ij}P_{kk}\right) \quad , \tag{6.125}$$

in which

$$\mathcal{H}_{ij} = \widetilde{\overline{\overline{u}_i\overline{u}_j}} - \widetilde{\overline{\overline{u}}}_i\widetilde{\overline{\overline{u}}}_j \quad , \tag{6.126}$$

$$\mathcal{L}^{\text{m}}_{ij} = \widetilde{\overline{u}_i\overline{u}_j} - \widetilde{\overline{u}}_i\widetilde{\overline{u}}_j \quad , \tag{6.127}$$

$$m_{ij} = \left(\frac{\widetilde{\overline{\Delta}}}{\overline{\overline{\Delta}}}\right)^2 |\widetilde{\overline{S}}|\widetilde{\overline{S}}_{ij} - \widetilde{|\overline{S}|\overline{S}_{ij}} \quad , \tag{6.128}$$

and where P_{kk} represents the trace of the subgrid tensor. The Germano–Lilly dynamic procedure leads to:

$$C_{\text{d}} = \frac{(\mathcal{L}^{\text{m}}_{ij} - \mathcal{H}_{ij})m_{ij}}{m_{ij}m_{ij}} \quad . \tag{6.129}$$

In simulations performed with this model, the authors observed a reduction in the value of the dynamic constant with respect to that predicted by the usual dynamic model (*i.e.* based on the Smagorinsky model alone). This can be explained by the fact that the difference between the $\mathcal{L}^{\text{m}}$ and $\mathcal{H}$ terms appears in the numerator of the fraction (6.129) and that this difference is small because these terms are very similar. This shows that the subgrid viscosity model serves only to model a residual part of the full subgrid tensor and not its entirety, as in the usual dynamic model.

Vreman *et al.* [341] propose a variant of this model. For the sake of mathematical consistency, by making the model for the tensor T_{ij} dependent only on the velocity field that corresponds to the same level of filtering, *i.e.* $\widetilde{\overline{\mathbf{u}}}$, these authors propose the following alternate form for the tensor $\mathcal{Q}_{ij}$:

$$\mathcal{Q}_{ij} = \widetilde{\widetilde{\overline{u}_i}\widetilde{\overline{u}_j}} - \widetilde{\overline{\overline{u}}}_i\widetilde{\overline{\overline{u}}}_j \quad . \tag{6.130}$$

N-Parameter Dynamic Mixed Model

General Formulation and Formal Resolution. A general form of multiparameter dynamic model was derived by Sagaut *et al.* [288]. Considering a formal N-part parametrization of the subgrid tensor, each term being associated to a real constant $C_l, k = 1, .., N$

$$\tau_{ij} = \sum_{l=1,N} C_l f^l_{ij}(\overline{\mathbf{u}}, \overline{\Delta}) \quad , \tag{6.131}$$

where the functions f^l_{ij} are the kernels of the different parts of the complete model. The equivalent formulation obtained at the test filter level is

$$T_{ij} = \sum_{l=1,N} C_l f^l_{ij}(\widetilde{\overline{\mathbf{u}}}, \widetilde{\overline{\Delta}}) \quad . \tag{6.132}$$

Inserting (6.131) and (6.132) into the Germano identity (4.126), we get the following definition of the residual E_{ij}:

$$E_{ij} = L_{ij} - \sum_{l=1,N} C_l m^l_{ij}, \quad m^l_{ij} = f^l_{ij}(\widetilde{\overline{\mathbf{u}}}, \widetilde{\overline{\Delta}}) - \widetilde{f^l_{ij}}(\overline{\mathbf{u}}, \overline{\Delta}) \quad . \tag{6.133}$$

In order to obtain N linearly independent relations to compute the constants C_l, a first solution is to operate the contraction of the residual (6.133) with N independent tensors A^l_{ij}. The constants will then appear as the solutions of the follow linear algebraic problem of rank N:

$$\sum_{l=1,N} C_l m_{ij}^l A_{ji}^k = L_{ij} A_{ji}^k, \quad k = 1, N \quad . \tag{6.134}$$

It is worth noting that the N constants are coupled, resulting in a global self-adaption of each constant. The particular case of the least-square minimization is recovered by taking $A_{ij}^k = m_{ij}^k, k = 1, N$.

In the case where some constants are not computed dynamically but are arbitrarily set, the linear system (6.134) corresponds to a ill-posed problem containing more constraints than degrees of freedom. Assuming that the N' first constants are arbitrarily chosen, we recover a well-posed problem of rank $N - N'$ by replacing L_{ij} with L'_{ij}, where

$$L'_{ij} = L_{ij} - \sum_{l=1,N'} C_l m_{ij}^l \quad . \tag{6.135}$$

Two-Parameter Dynamic Models. Mixed models have also been proposed by Salvetti [296, 297] and Horiuti [143] with two dynamic constants (one for the subgrid-viscosity part and one for the scale-similarity), corresponding to the $N = 2$ case in the previous section. These models have the advantage of avoiding any a priori preference for the contribution of one or the other model component. An extensive study of dynamic mixed model has been carried out by Sarghini *et al.* [295] for the plane channel case.

Numerical simulations show that two-paramater mixed models may yield disappointing results, because of a too low dissipation level. This is due to the fact that the coupled dynamic procedure described in the previous section gives a heavy weigth to the scale-similarity part of the model, because its correlation coefficient with the exact subgrid tensor is much higher than the one of the subgrid-viscosity model. To relieve this problem, Morinishi [248] proposes to uncouple the computation of the dynamic constants. The modified algorithm for the dynamic procedure is:

1. Compute the constant associated to the subgrid-viscosity part of the model using a classical dynamic procedure, without taking the scale similarity part into account. This corresponds to the $N = 1$ case in the previous section. The resulting constant will ensure a correct level of dissipation.
2. Compute the constant associated to the scale-similarity part using a two-parameter dynamic procedure, but considering that the constant of the subgrid-viscosity part is fixed. This corresponds to $N = 2$ and $N' = 1$ in the previous section.

6.6 Explicit Evaluation of Subgrid Scales

The models described in the present section are all based on an explicit evaluation of the subgrid scales $\mathbf{u}' \equiv (Id - G) \star \mathbf{u}$. Because the subgrid

modes correspond to scales of motion that can not be represented at the considered filtering level (*i.e.* in practice on the computational grid), a new higher-resolution filtering level is introduced. Numerically, this is done by introducing an auxiliary computational grid (or a set of embedded auxiliary grids), whose mesh size is smaller than the original one. The subgrid field $\mathbf{u}'$ is evaluated on that grid using one of the model presented below, and then the non-linear $G\star((\overline{\mathbf{u}}+\mathbf{u}')\otimes(\overline{\mathbf{u}}+\mathbf{u}'))$ is computed. The corresponding general algorithmic frame is

1. $\overline{\mathbf{u}}$ is known from a previous calculation, on the computational grid, *i.e.* at the G filtering level, whose characteristic length is $\overline{\Delta}$.
2. Define an auxiliary grid, associated to a new filtering level F with characteristic length $\Delta < \overline{\Delta}$.
3. Compute the approximate subgrid field $\mathbf{u}'_a = (F - G) \star \mathbf{u}$ using a model on the auxiliary grid.
4. Compute the approximate non-filtered non-linear term at the F level on the auxiliary grid:
$$(\overline{\mathbf{u}} + \mathbf{u}'_a) \otimes (\overline{\mathbf{u}} + \mathbf{u}'_a) \quad .$$
5. Compute the approximate filtered non-linear term at the G level on the computational grid:
$$G \star ((\overline{\mathbf{u}} + \mathbf{u}'_a) \otimes (\overline{\mathbf{u}} + \mathbf{u}'_a)) \quad ,$$
and use it to compute the evolution of $\overline{\mathbf{u}}$.

Several ways to compute the subgrid motion on the auxiliary grid have been proposed by different authors. They are classified by increasing order of complexity (computational cost):

1. Fractal Interpolation Procedure of the fluctuations, as proposed by Scotti and Meneveau (p. 190). The subgrid fluctuations are reconstructed in a deterministic way on the fine grid using an iterative fractal interpolation technique (several similar fractal reconstruction techniques can be found in [157]). This model is based on geometrical considerations only, and does not take into account any information dealing with the flow dynamics such as disequilibrium, anisotropy, ... But it provides an estimate of the subgrid motion at a very low cost.
2. Chaotic Map Model of McDonough *et al.* (p. 191). The subgrid fluctuations are approximated in a deterministic way using a very simple chaotic dynamical system, which is chosen in order to mimic some properties of the real turbulent fluctuations (amplitude, autocorrelation, distribution of velocity fluctuations, ...). This model is the easiest to implement, and induces a very small overhead. A problem is that it requires the definition of a realistic dynamical system, and then a complete knowledge of the turbulent motion characteristics at each point of the numerical simulation.

3. Subgrid Scale Estimation Procedure proposed by Domaradzki and his coworkers (p. 194). The subgrid fluctuation are now deduced from a simplified advection equation, deduced from the filtered Navier–Stokes operator. An evaluation of the subgrid motion production term is derived, and integrated over a time interval associated to characteristic relaxation time of the subgrid scale. This model makes it possible to evaluate the subgrid motion at a very low computational cost, but requires the computation of an approximate inverse filter.
4. Multilevel Simulations (p. 196), which are based on the use of the exact Navier–Stokes equations on a set of embedded computational grids. The reduction of the computational effort with respect to the Direct Numerical Simulation is obtained by freezing (quasi-static approximation) the high-frequencies represented on fine grids for some time interval, leading to the definition of a cyclic strategy. These methods can be interpreted as a time-consistent extension of the classical multigrid procedures for steady computations. They correspond to the maximal computational effort, but also to the most realistic approach.

6.6.1 Fractal Interpolation Procedure

Scotti and Meneveau [302, 303] propose to reconstruct the subgrid velocity field using two informations: (i) the resolved velocity field, which is known on the coarsest grid, and (ii) the fractality of the velocity field. The fluctuations are evaluated by interpolating the resolved coarse-grid velocity field on the fine grid using a fractal interpolation technique.

We first describe this interpolation technique in the monodimensional case. It is based on an iterative mapping procedure. The fluctuating field $\mathbf{u}'_a$ is reconstructed within each interval of the coarse grid by introducing a local coordinate $\xi \in [0,1]$. Let us consider the interval $[x_{i-1}, x_{i+1}]$, where $i-1$ and $i+1$ are related to the grid index on the coarse grid. We have $\xi = (x - x_{i-1})/2\overline{\Delta}$. The proposed map kernel W for a function ϕ to interpolated on the considered interval is:

$$W[\phi](\xi) = \begin{cases} d_{i,1}\phi(2\xi) + q_{i,1}(2\xi) & \text{if } \xi \in [0,1/2] \\ d_{i,2}\phi(2\xi) + q_{i,2}(2\xi) & \text{if } \xi \in]1/2,1] \end{cases} , \tag{6.136}$$

where $q_{i,j}$ are polynomials and $d_{i,j}$ are stretching parameters. The authors propose to use the following linear polynomials:

$$\begin{aligned} q_{i,1}(\xi) &= (\phi(x_i) - \phi(x_{i-1}) - d_{i,1}(\phi(x_{i+1}) - \phi(x_{i-1}))\xi \\ &\quad + \phi(x_{i-1})(1 - d_{i,1} \quad , \end{aligned} \tag{6.137}$$

$$\begin{aligned} q_{i,2}(\xi) &= (\phi(x_{i+1}) - \phi(x_i) - d_{i,2}(\phi(x_{i+1}) - \phi(x_{i-1}))\xi \\ &\quad - \phi(x_{i-1})d_{i,2} \quad . \end{aligned} \tag{6.138}$$

The fluctuation is defined as

$$\mathbf{u}'_a = \lim_{n\to\infty} W^n[\overline{\mathbf{u}}] = \underbrace{W \circ W \circ \ldots \circ W[u]}_{n \text{ times}} \quad . \tag{6.139}$$

The stretching parameters are such that the Hausdorff dimension D of the synthetic signal is equal to

$$D = \begin{cases} 1 + \frac{\log(|d_{i,1}|+|d_{i,2}|)}{\log(2)} & \text{if } 1 < |d_{i,1}| + |d_{i,2}| < 2 \\ 1 & \text{if } |d_{i,1}| + |d_{i,2}| \leq 1 \end{cases} . \tag{6.140}$$

In order to conserve then mean value of the signal over the considered interval, we have $d_{i,1} = -d_{i,2} = d$. For three-dimensional isotropic turbulence, we have $D = 5/3$, yielding $d = \mp 2^{1/3}$.

This procedure theoretically require an infinite number of iterations to build the fluctuating field. In practice, a finite number of iterations is used. The statistical convergence rate of process being exponential, it still remains a good approximation. A limited number of iterations can also be seen as a way to account for viscous effects.

The extension to the multidimensional case is straightforward, each direction of space being treated sequentially.

This procedure also makes it possible to compute analytically the subgrid tensor. The resulting model will not be presented here (see [303] for a complete description).

6.6.2 Chaotic Map Model

McDonough and his coworkers [148, 211, 251] propose an estimation procedure based on the definition of a choatic dynamical system. The resulting model generates a contravariant subgrid-scale velocity field, represented at discrete time intervals on the computational grid:

$$\mathbf{u}'_a = A_u \boldsymbol{\zeta} \odot \mathbf{V} \quad , \tag{6.141}$$

where A is an amplitude coefficient evaluated from canonical analysis, $\boldsymbol{\zeta}$ an anisotropy correction vector consisting mainly of first-order structure function of high-pass filtered resolved scales, and $\mathbf{V}$ is a vector of chaotic algebraic maps. It is important noting that the two vectors are multiplied using a vector Hadamard product, defined for two vectors and a unit vector $\mathbf{i}$ according to:

$$(\boldsymbol{\zeta} \odot \mathbf{V}) \cdot \mathbf{i} \equiv (\boldsymbol{\zeta} \cdot \mathbf{i})(\mathbf{V} \cdot \mathbf{i}) \quad . \tag{6.142}$$

The amplitude factor is chosen such that the kinetic energy of the synthetic subgrid motion is equal to the energy contained in all the scales not resolved by the simulation. It is given by the expression:

$$A_u = C_u u_* Re_{\overline{\Delta}}^{1/6} \quad , \tag{6.143}$$

with

$$u_* = (\nu|\nabla \mathbf{u}|)^{1/2}, \quad Re_{\overline{\Delta}} = \frac{\overline{\Delta}^2 |\nabla \mathbf{u}|}{\nu} \quad ,$$

where ν is the molecular viscosity. The scalar coefficient C_u is evaluated from classical inertial range arguments. The suggested value is $C_u = 0.62$.

The anisotropy vector $\boldsymbol{\zeta}$ is computed making the assumption that the flow anisotropy is smoothly varying in wave-number. In a way similar to the one proposed by Horiuti (see Sect. 5.3.2), the first step consists in evaluating the anisotropy vector from the highest resolved frequency. In order to account for the anisotropy of the filter, the resolved contravariant velocity field $\mathbf{u}_c$ is considered. The resulting expression for $\boldsymbol{\zeta}$ is:

$$\boldsymbol{\zeta} = \sqrt{3} \frac{\mathbf{s}}{|J^{-1} \cdot \mathbf{s}|} \quad , \tag{6.144}$$

where J^{-1} is the inverse of the coordinate transformation matrix associated to the computational grid (and to the filter). The vector $\mathbf{s}$ is defined according to

$$\mathbf{s} \cdot \mathbf{i} = \sqrt{3} \frac{|\nabla(\widetilde{\mathbf{u}_c}' \cdot \mathbf{i})|}{|\nabla \widetilde{\mathbf{u}_c}'|} \quad , \tag{6.145}$$

where the $\widetilde{\mathbf{u}_c}'$ is related to the test field computed thanks to the use of the test filter of characteristic length $\widetilde{\overline{\Delta}} > \overline{\Delta}$.

We now describe the estimation procedure for the stochastic vector $\mathbf{V}$. In order to recover the desired cross-correlation between the subgrid velocity component, the vector $\mathbf{V}$ is defined as:

$$\mathbf{V} = A\mathbf{M} \quad , \tag{6.146}$$

where A is a tensor such that $R = A \cdot A^T$, where R is the correlation tensor of the subgrid scale velocity. In practice, McDonough proposes to use the evaluation:

$$A_{ij} = \frac{(\nabla \widetilde{u}_i')_j}{|\nabla \widetilde{u}_i'|} \quad . \tag{6.147}$$

Each component $M_i, i = 1, 2, 3$ of the vector $\mathbf{M}$ is of the form:

$$M_i = \sigma \sum_{l=0,N} a_l \sum_{m=1,N_l} M'_{lm} \quad , \tag{6.148}$$

where N_l is the binomial coefficient

$$N_l \equiv \binom{N}{l} \quad ,$$

and $\sigma = 1.67$ is the standard deviation for the variable, and the weights a_l are given by

$$a_l = \sqrt{3} \left(p^l (1-p)^{(N-l)} \right)^{1/2}, \quad p = 0.7 \quad . \tag{6.149}$$

The maps M'_{lm} are all independent instances of one of the three following normalized maps:

– The *tent map*:

$$m^{(n+1)} = \begin{cases} R(-2 - 3m^{(n)}) & \text{if } m^{(n)} < -1/3 \\ R(3m^{(n)}) & \text{if } -1/3 \leq m^{(n)} \leq 1/3 \\ R(-2 - 3m^{(n)}) & \text{if } m^{(n)} > 1/3 \end{cases} \quad , \tag{6.150}$$

where $m^{(n)}$ is the nth instance of the discrete dynamical system, and $R \in [-1, 1]$.

– The *logistic map*:

$$m^{(n+1)} = R A_R m^{(n)} (1 - |m^{(n)}| A_m) \quad , \tag{6.151}$$

with

$$A_R = 2 + 2\sqrt{2}, \quad A_m = \left(1 + \frac{1}{A_R}\right) \sqrt{\frac{3}{2}} \quad .$$

– The *sawtooth map*:

$$m^{(n+1)} = \begin{cases} R(2 + 3m^{(n)}) & \text{if } m^{(n)} < -1/3 \\ R(3m^{(n)}) & \text{if } -1/3 \leq m^{(n)} \leq 1/3 \\ R(-2 + 3m^{(n)}) & \text{if } m^{(n)} > 1/3 \end{cases} \quad . \tag{6.152}$$

The map parameter R is related to some physical flow parameter, since the bifurcation and autocorrelation behaviors of the map are governed by R. An *ad hoc* choice for R will make it possible to model some of the local history effects in a turbulent flow in a way that is quantitatively and qualitatively correct. It is chosen here to set the bifurcation parameter R on the basis of local flow values, rather than on global values such as the Reynolds number. That choice allows us to account for large-scale intermittency effects. Selecting the ratio of the Taylor λ and Kolmogorov η scales, a possible choice is:

$$R = \tanh \left\{ \left[\frac{(\lambda/\eta)}{(\lambda/\eta)_c} \right]^r \tanh^{-1}(R_c) \right\} \quad , \tag{6.153}$$

Table 6.2. Parameters of the Chaotic Map Model.

Map	R_c	$(\lambda/\eta)_c$	r
Logistic	$-(2+2\sqrt{2})^{1/2}$	26	5
Tent	-1/3	28.6	5
Sawtooth	-1/3	28.6	5

where r is a scaling exponent empirically assumed to lie in the range $[4,6]$, and $(\lambda/\eta)_c$ is a critical value of the microscale ratio that is mapped onto R_c, the critical value of R. Suggested values are given in Table 6.2.

The last point is related to the time scale of the subgrid scales. Let t_e be the characteristic relaxation time of the subgrid scales, to be evaluated using inertial range considerations. If this time scale is smaller than the time step Δt of the simulation (*the characteristic filter time*), then the stochastic variables M_i' must be updated n_u times per time step, with

$$n_u \approx \frac{\Delta t}{t_e} = \left(\frac{\Delta t|\nabla \overline{\mathbf{u}}|}{f_M}\right) Re_{\overline{\Delta}}^{-1/3} \quad , \tag{6.154}$$

where f_M is a fundamental frequency associated with the chaotic maps used to generate the variables. It is defined as:

$$f_M = \frac{C}{\theta} \quad , \tag{6.155}$$

where C is some positive constant and θ the *integral iteration scale*

$$\theta = \frac{1}{2}\rho(0) + \sum_{l=1,\infty} \rho(l), \quad \rho(l) = \frac{\langle m^{(n)} m^{(n+l)} \rangle}{\langle m^{(n)} m^{(n)} \rangle} \quad , \tag{6.156}$$

which completes the description of the model. This model is Galilean- and coordinate-invariant, and automatically generates realizable Reynolds stresses. It reproduces the desired root-mean-square amplitude of subgrid fluctuations, along with the probability density function for this amplitude. Finally, the proper temporal auto-correlation function can be enforced.

6.6.3 Subgrid Scale Estimation Procedure

A two-step subgrid scale estimation procedure in the physical space[13] is proposed by Domaradzki and his coworkers [83, 201]. In the first (kinematic) step, an approximate inversion of the filtering operator is performed, providing the

[13] A corresponding procedure in the spectral space is described Ref.[85].

value of the defiltered velocity field on the auxiliary grid. In the second (non-linear dynamic) step, scales smaller than the filter length associated to the primary grid are generated, resulting in an approximation of the full solution.

Let $\overline{\mathbf{u}}$ be the filtered field obtained on the primary computational grid, and $\mathbf{u}^\bullet$ the defiltered field on the secondary grid. That secondary grid is chosen such that the associated mesh size is twice as fine as the mesh size of the primary grid. We introduce the discrete filtering operator G_d, defined such that

$$G_\mathrm{d}\mathbf{u}^\bullet = \overline{\mathbf{u}} \quad . \tag{6.157}$$

It is important to note that in this two-grid implementation, the right hand side of equation (6.157) must first be interpolated on the auxiliary grid to recover a well-posed linear algebra problem. To avoid this interpolation step, Domaradzki proposes to solve directly the filtered Navier–Stokes equations on the finest grid, and to define formally the G filtering level by taking $\widetilde{\overline{\Delta}} = 2\widetilde{\Delta}$. The defiltered field $\mathbf{u}^\bullet$ is obtained by solving the inverse problem

$$\mathbf{u}^\bullet = (G_\mathrm{d})^{-1}\overline{\mathbf{u}} \quad . \tag{6.158}$$

This is done in practice by solving the corresponding linear system. In practice, the authors use an three-point discrete approximation of the box filter for G_d (see Sect. 10.2 for a description of discrete test filters). This step corresponds to an implicit deconvolution procedure (the previous ones were explicit procedures, based on the construction of the inverse operator *via* Taylor expansions or iterative procedures), and can be interpreted as an interpolation step of the filtered field on the auxiliary grid.

The $\mathbf{u}_a'$ subgrid velocity field is then evaluated using an approximation of its associated non-linear production term:

$$\mathbf{u}_a' = \theta_a N' \quad , \tag{6.159}$$

where θ_a and N' are a characteristic time scale and N' the production rate. These terms are evaluated as follows. The full convection term on the auxiliary grid is

$$-u_j^\bullet \frac{\partial u_i^\bullet}{\partial x_j}, j = 1,2,3 \quad . \tag{6.160}$$

This term accounts for the production of all the frequencies resolved on the auxiliary grid. Since we are interested in the production of the small scales only, we must remove the advection by the large scales, and restrict the resulting term tho the desired frequency range. The resulting term N_i' is

$$N_i' = (Id - G) \star \left(-(u_j^\bullet - \overline{u}_j)\frac{\partial u_i^\bullet}{\partial x_j}\right) \quad . \tag{6.161}$$

In practice, the convolution filter G is replaced by the discrete operator G_{d}. The production time θ_a is evaluated making the assumption that the subgrid kinetic energy is equal to the kinetic energy contained in the smallest resolved scales:

$$|\mathbf{u}'_a|^2 = \theta_a^2 |N'|^2 = \alpha^2 |\mathbf{u}^\bullet - \overline{\mathbf{u}}|^2 \implies \theta_a = \alpha \frac{2|\mathbf{u}^\bullet - \overline{\mathbf{u}}|}{|N'|} \quad , \tag{6.162}$$

where α is a proportionality constant, nearly equal to 0.5 for the box filter. This completes the description of the model.

6.6.4 Multilevel Simulations

This class of simulation relies on the resolution of an evolution equation for $\mathbf{u}'_a$ on the auxiliary grid. These simulations can be analyzed within the framework of the multiresolution representation of the data [5, 132–134], or similar theories such as the Additive Turbulent Decomposition [148, 213].

Let us consider N filters $G_1, ..., G_N$, with associated cutoff lenghtes $\overline{\Delta}_1 \leq ... \leq \overline{\Delta}_N$. We define the two following set of velocity fields:

$$\overline{\mathbf{u}}^n = G_n \star ... \star G_1 \star u = \mathcal{G}_1^n \star \mathbf{u} \quad , \tag{6.163}$$

$$\mathbf{v}^n = \overline{\mathbf{u}}^n - \overline{\mathbf{u}}^{n+1} = (\mathcal{G}_1^n - \mathcal{G}_1^{n+1}) \star \mathbf{u} = \mathcal{F}_n \star \mathbf{u} \quad . \tag{6.164}$$

The fields $\overline{\mathbf{u}}^n$ and $\mathbf{v}^n$ are respectively the resolved field at the nth level of filtering and the nth level details. We have the decomposition

$$\overline{\mathbf{u}}^n = \overline{\mathbf{u}}^{n-k} + \sum_{l=1,k} \mathbf{v}^{n-l} \quad , \tag{6.165}$$

yielding the following multiresolution representation of the data:

$$\mathbf{u} \equiv \{\mathbf{u}', \mathbf{v}^1, ..., \mathbf{v}^{N-1}\}, \quad \text{with } \mathbf{u}' \equiv \mathbf{u} - \overline{\mathbf{u}}^1 \quad . \tag{6.166}$$

The multilevel simulations are based on the use of embedded computational grids or hierarchical polynomial basis to solve the evolution equations associated to each filtering level/details level. The evolution equations are expressed

$$\frac{\partial \overline{\mathbf{u}}^n}{\partial t} + \mathcal{NS}(\overline{\mathbf{u}}^n) = \tau^n = [\mathcal{G}_1^n \star, \mathcal{NS}](\mathbf{u}), \quad n \in [1, N] \quad , \tag{6.167}$$

where $\mathcal{NS}$ is the symbolic Navier–Stokes operator and $[.,.]$ the commutator operator. The equation for the details are

$$\frac{\partial \mathbf{v}^n}{\partial t} + \mathcal{NS}(\overline{\mathbf{v}}^n) = \tau^n = [\mathcal{F}_n \star, \mathcal{NS}](\mathbf{u}), \quad n \in [1, N-1] \quad , \tag{6.168}$$

or equivalently

$$\frac{\partial \mathbf{v}^n}{\partial t} + \mathcal{NS}(\overline{\mathbf{u}}^n) - \mathcal{NS}(\overline{\mathbf{u}}^{n+1}) = \tau^n - \tau^{n+1}, \quad n \in [1, N-1] \quad . \tag{6.169}$$

There are three possibilities to reduce the complexity of the simulation with respect to Direct Numerical Simulation:

- The use of a cycling strategy between the different grid levels. Freezing the high-frequency details over some times while integrating the equations for the low-frequency part of the solution results in a reduction of the simulation complexity. This is referred to as the quasi-static approximation for the high frequencies. The main problem associated to the cycling strategy is the determination of the time over which the high frequencies can be frozen without destroying the quality of the solution. Some examples of such cycling strategy can be found in the Multimesh method of Voke [336], the Non-Linear Galerkin Method [41, 78, 100–102, 262, 325], the Incremental Unknowns technique [34, 55, 89, 90], Tziperman's MTS algorithm [329], Liu's multigrid method [197, 198] and the Multilevel algorithm proposed by Terracol *et al.* [290, 327].
- The use of simplified evolution equations for the details instead of (6.168). A linear model equation is often used, which can be solved more easily than the full non-linear mathematical model. Some examples among others are the Non-Linear Galerkin method, the Variational Multiscale approach proposed by Hughes and his co-workers [145–147]. Another possibility is to assume that the nth level details are periodic within the filtering cell associated to the $(n-1)$th filtering level. Each cell can then be treated separately from the others. An example is the Local Galerkin method of Mc Donough [208–210]. It is interesting to note that this last assumption is shared by the Homogenization approach developped by Perrier and Pironneau (see Sect. 6.1.3).
- The use of a limited number of filtering levels. In this case, even at the finest description level, subgrid scales exist and have to be parametrized. The gain is effective because it is assumed that simple subgrid models can be used at the finest filtering level, the associated subgrid motion motion being closer to isotropy and containing much less energy than at the coarser filtering levels. An example among others are the Multilevel algorithm of Terracol [290, 327] and the Modified Estimation Procedure of Domarradzki [87].

Some strategies combining these three possibilities can of course be defined. The efficiency of the method can be further improved by using a local grid refinement [25, 164, 322]. Non-overlapping multidomain techniques can also be used to get a local enrichment of the solution [274, 290].

6.7 Implicit Structural Models

The last class of structural subgrid models discussed in this chapter is the implicit structural model family. These models are structural ones, *i.e.* they do not rely on any foreknowledge about the nature of the interactions between the resolved scales and the subgrid scales. They can be classified as implicit, because they can be interpreted as improvements of basic numerical methods for solving the filtered Navier–Stokes equations, leading to the definition of higher-order accurate numerical fluxes. We note that, because the modification of the numerical method can be isolated as a new source term in the momentum equation, these models could also be classified as exotic formal expansion models. A major specificity of these models is that they all aim at reproducing directly the subgrid force appearing in the momentum equation, and not the subgrid tensor τ.

The three models presented in the following are:

1. The Local Average Method of Denaro (p.199), which consists in a particular reconstruction of the discretized non-linear fluxes associated to the convection term. This approach incorporates a strategy to filter the subgrid-scale by means of an integration over a control volume and to recover the contribution of the subgrid scales with an integral formulation. It can be interpreted as a high-order space-time reconstruction procedure for the convective numerical fluxes based on a defiltering process.
2. The Approximate Deconvolution Procedure proposed by Stolz and Adams (p.201). The exact non-filtered field is here approximated by truncated series expansion of the inverse filter operator, as previously done in Sect. 6.1. The main difference with respect to the usual defiltering aproach is that the full subgrid term, defined as the commutation error between the filter operator and the Navier–Stokes operator (see Sect. 3.3.1), is now approximated, rather than the subgrid tensor. This procedure is thus the most general form of a subgrid model relying on the defiltering approach, and can be interpreted as the definition of a specific numerical method for the computation of the defiltered velocity field.
3. The Scale Residual Model of Maurer and Fey (p.202). As for the Approximate Deconvolution Procedure, the purpose is to evaluate the commutation error which defines the subgrid term. This evaluation is carried out using the residual between the time evolution of the solutions of the Navier–Stokes equations on two different grids (*i.e.* at two different filtering levels) and assuming some self-similarity properties of this residual. This model can be considered as: (i) a generalization of the previous one, which does not involve the deconvolution process anymore, but requires the use of the second computational grid and (ii) a generalization of the scale-similarity models, the use of a test filter for defining the test field being replaced by the explicit computation (by solving the Navier–Stokes equations) of the field at the test filter level.

Other implicit approaches for large-eddy simulation exist, which make it possible to obtain reliable results without subgrid scale model (in the common sense given to that term), and without explicit addition of numerical diffusion[14]. An example is the Spectro-Consistent Discretization proposed by Verstappen and Veldman [333, 334]. Because these approaches rely on numerical considerations only, they escape the modeling concept and will not be presented here.

6.7.1 Local Average Method

An other approach to the traditional large-eddy simulation technique was proposed by Denaro and his co-workers in a serie of papers [75, 79]. It is based on a space-time high-order accurate reconstruction of the convective fluxes, which account for the subgrid-scale contribution. As a consequence, it can be seen as a particular numerical scheme based on a differential approximation of the filtering process. For sake of simplicity, we will present the method in the case of a dummy variable ϕ advected by a velocity field $\mathbf{u}$, whose evolution equation is (only convective terms are retained):

$$\frac{\partial \phi}{\partial t} = -\nabla \cdot (\mathbf{u}\phi) = A(\mathbf{u}, \phi) \quad . \tag{6.170}$$

The local average of ϕ in a filtering cell Ω is defined as the mean value of ϕ in this cell[15]:

$$\overline{\phi}(\mathbf{x}, t) \equiv \frac{1}{V} \int_{\Omega} \phi(\boldsymbol{\xi}, t) d\boldsymbol{\xi} = \overline{\phi}(t), \quad \forall x \in \Omega \quad , \tag{6.171}$$

where V is the measure of Ω. We now consider an arbitrary filtering cell. Applying this operator to equation (6.170), and integrating the resulting evolution equation over the time interval $[t, t + \Delta t]$, we get:

$$(\overline{\phi}(t + \Delta t) - \overline{\phi}(t))V = \int_{t}^{t+\Delta t} \int_{\partial\Omega} \mathbf{n} \cdot \mathbf{u}\phi(\boldsymbol{\xi}, t') d\boldsymbol{\xi} dt' \quad , \tag{6.172}$$

where $\partial\Omega$ is the boundary of Ω, and $\mathbf{n}$ the vector normal to it. The right hand side of this equation, which appears as the application of a time-box filter to the boundary fluxes, can be approximated by means of a differential operator, exactly in the same way as for the space-box filter (see Sect. 6.1.1), yielding:

[14] Dissipative numerical methods should be classified as Implicit Functional Modeling.

[15] This filtering operator corresponds to a modification of the box filter defined in Sect. 2.1.5: the original box filter is defined as a $\mathbb{R} \to \mathbb{R}$ operator, while the local average is a $\mathbb{R} \to \mathbb{N}$ operator. It is worth noting that the local average operator is a projector.

$$\int_t^{t+\Delta t}\int_{\partial\Omega} \mathbf{n}\cdot\mathbf{u}\phi(\boldsymbol{\xi},t')d\boldsymbol{\xi}dt' \simeq \Delta t\int_{\partial\Omega}\mathbf{n}\cdot\mathbf{u}\left(Id+\sum_{l=1,\infty}\frac{\Delta t^{l-1}}{l!}\frac{\partial^l}{\partial t^l}\right)\phi(\boldsymbol{\xi},t)d\boldsymbol{\xi} \quad (6.173)$$

The time expansion is then writen as a space differential operator using the balance equation (6.170):

$$\left(Id+\sum_{l=1,\infty}\frac{\Delta t^{l-1}}{l!}\frac{\partial^l}{\partial t^l}\right)\phi(\boldsymbol{\xi},t) = \left(Id+\sum_{l=1,\infty}\frac{\Delta t^{l-1}}{l!}A^{l-1}(\mathbf{u},\cdot)\right)\phi(\boldsymbol{\xi},t) \quad , \quad (6.174)$$

with

$$A^l(\mathbf{u},\phi) \equiv \underbrace{A(\mathbf{u},\cdot)\circ A(\mathbf{u},\cdot)\circ ...\circ A(\mathbf{u},\phi)}_{l \text{ times}} \quad .$$

The second step of this method consists in the reconstruction step. At each point x located inside the filtering cell Ω, we have

$$\begin{aligned}
\phi(\mathbf{x},t) &= \overline{\phi}(t)+\phi'(\mathbf{x},t) \quad , & (6.175)\\
\phi(\mathbf{x},t+\Delta t) &= \overline{\phi}(t+\Delta t)+\phi'(\mathbf{x},t+\Delta t)\\
&= \overline{\phi}(t)+(\overline{\phi}(t+\Delta t)-\overline{\phi}(t))+\phi'(x,t+\Delta t)\\
&\quad +(\phi'(\mathbf{x},t+\Delta t)-\phi'(\mathbf{x},t))\\
&= \phi(\mathbf{x},t)+(\overline{\phi}(t+\Delta t)-\overline{\phi}(t))\\
&\quad +(\phi'(\mathbf{x},t+\Delta t)-\phi'(\mathbf{x},t)) \quad . & (6.176)
\end{aligned}$$

The first term in the left hand side of relation (6.176) is known. The second one, which corresponds to the contribution of the low frequency part of the solution (*i.e. the local averaged part*), is computed using equation (6.172). The third term remains to be evaluated. This is done using the differential operator (6.6), leading to the final expression:

$$\phi(\mathbf{x},t+\Delta t) = \phi(\mathbf{x},t)+(Id-P_d)\left(\overline{\phi}(t+\Delta t)-\overline{\phi}(t)\right) \quad , \quad (6.177)$$

with

$$P_d = \sum_{l=1,\infty}\frac{1}{l!}\left(\frac{1}{V}\int_\Omega\left(\sum_{i=1,d}(\xi_i-x_i^c)\frac{\partial}{\partial x_i}\right)^l\right)d\xi \quad , \quad (6.178)$$

where d is the dimension of space and x_i^c the ith coordinate of the center of the filtering cell. In practice, the serie expansions are truncated to a finite order. The repeated use of equation (6.177) makes it possible to compute the value of the new pointwise value at each time step.

6.7.2 Approximate Deconvolution Procedure

This approach, as proposed by Stolz and Adams [319,320], is based on an approximate evaluation of the full subgrid force term in the momentum equation, thanks to the use of an approximate inverse of the filter. We recall that, writing symbolically the Navier–Stokes equations as

$$\frac{\partial\mathbf{u}}{\partial t}+\mathcal{NS}(\mathbf{u}) = 0 \quad , \quad (6.179)$$

we get the following for the filtered field evolution equation (see Chap. 3)

$$\frac{\partial\overline{\mathbf{u}}}{\partial t}+\mathcal{NS}(\overline{\mathbf{u}}) = -[\mathcal{NS},G\star](\mathbf{u}) \quad , \quad (6.180)$$

where G is the filter kernel, and $[\cdot,\cdot]$ is the commutator operator. The exact subgrid term, which corresponds to the right hand side of relation (6.180), appears as a function of the exact non-filtered field $\mathbf{u}$. This field being unknown during the computation, the idea is here to approximate it by a deconvolution procedure:

$$\mathbf{u}\approx\mathbf{u}^\bullet \equiv G_l^{-1}\star\overline{\mathbf{u}} = G_l^{-1}\star G\star\mathbf{u} \quad , \quad (6.181)$$

where G_l^{-1} is the lth order approximate inverse of the filter G

$$G_l^{-1}\star G = Id+O(\overline{\Delta}^l) \quad .$$

The subgrid term is then approximated as

$$[\mathcal{NS},G\star](\mathbf{u})\simeq[\mathcal{NS},G\star](\mathbf{u}^\bullet) = [\mathcal{NS},G\star](G_l^{-1}\star\overline{\mathbf{u}}) \quad , \quad (6.182)$$

achieving the description of the procedure. Combining the right-hand side and the left-hand side of the resulting equation, we get:

$$\frac{\partial\overline{\mathbf{u}}}{\partial t}+G\star\mathcal{NS}(G_l^{-1}\star\overline{\mathbf{u}}) = 0 \quad . \quad (6.183)$$

It is worth noting that, like all other approaches based on a deconvolution procedure, the efficiency of the present strategy will be conditionned by our capability to find the approximate inverse operator. In practice, some computations have been carried out using a fifth-order ($l=5$) approximation of the inverse filter kernel.

In order to account for kinetic energy transfer with scales which are not recovered by the deconvolution procedure, a relaxation term is introduced, yielding

$$\frac{\partial\overline{\mathbf{u}}}{\partial t}+G\star\mathcal{NS}(G_l^{-1}\star\overline{\mathbf{u}}) = -\frac{1}{T}(Id-G_l^{-1}\star G)\star\overline{\mathbf{u}} \quad , \quad (6.184)$$

where T is an empirical relaxation time.

A link of this model to artificial diffusion can be made by interpreting it as the following evolution equation for the approximate defiltered field $\mathbf{u}^\bullet$:

$$\frac{\partial \mathbf{u}^\bullet}{\partial t} + G_l^{-1} \star G \star \mathcal{NS}(\mathbf{u}^\bullet) = 0 \quad . \tag{6.185}$$

As the operator G is associated to a low-pass filter, its application to the Navier–Stokes operator has a regularizing effect, similar to the one of an artificial dissipation procedure. The application of the approximate deconvolution operator can then be interpreted as the reconstruction of higher-order numerical fluxes.

6.7.3 Scale Residual Model

Maurer and Fey [224] propose to evaluate the full subgrid term, still defined as the commutation error between the Navier–Stokes operator and the filter (see Chap. 3 or equation (6.180)), by means of a two-grid level procedure. A deconvolution procedure is no longer needed, but some self-invariance properties of the subgrid term have to be assumed. First we note that a subgrid model, referred to as $m(\overline{\mathbf{u}})$, is defined in order to minimize the residual E, with

$$E = [\mathcal{NS}, G\star](\mathbf{u}) - m(G \star \mathbf{u}) \quad . \tag{6.186}$$

Assuming that the filter G has the two following properties:

- G is a projector,
- G commutes with the Navier–Stokes operator in the sense that

$$\mathcal{NS} \circ (G\star)\mathbf{u} = \mathcal{NS} \circ (G\star) \circ (G\star)\mathbf{u} = (G\star) \circ \mathcal{NS} \circ (G\star)\mathbf{u} \quad ,$$

the residual can be rewritten as

$$E = (G\star) \circ (\mathcal{NS} \circ Id - \mathcal{NS} \circ (G\star))\mathbf{u} - m \circ (G\star)\mathbf{u} \quad . \tag{6.187}$$

We now introduce a set of filter $G_k, k = 0, N$, whose characteristic lengths $\overline{\Delta}_k$ are such that $0 = \overline{\Delta}_N < \overline{\Delta}_{N-1} < .... < \overline{\Delta}_0$. The residual E_k obtained for the kth level of filtering is easily deduced from relation (6.187):

$$\begin{aligned} E_k &= (G_k\star) \circ (\mathcal{NS} \circ (G_N\star) - \mathcal{NS} \circ (G_k\star))\mathbf{u} \\ &\quad - m \circ (G_k\star)\mathbf{u} \qquad (6.188) \\ &= (G_k\star) \circ \sum_{j=0,k-1} (\mathcal{NS} \circ (G_j\star) - \mathcal{NS} \circ (G_{j+1}\star))\mathbf{u} \\ &\quad - m \circ (G_k\star)\mathbf{u} \quad . \qquad (6.189) \end{aligned}$$

To construct the model m, we now make the two followin sumptions:

- The interactions between spectral bands are local, in that sense that the influence of each spectral band gets smaller with decreasing values of $j < k$.
- The residuals between two filtering levels have the following self-invariance property:

$$(\mathcal{NS} \circ (G_{j+1}\star) - \mathcal{NS} \circ (G_j\star))\mathbf{u} = \alpha(\mathcal{NS} \circ (G_j\star) - \mathcal{NS} \circ (G_{j-1}\star))\mathbf{u} \,, \tag{6.190}$$

where $\alpha < 1$ is a constant parameter. It is important noting that this can only be true if the cut-offs occur in the inertial range of the spectrum (see the discussion about the validity of the dynamic procedure in Sect. 4.3.3). Using these hypotheses, the following model is derived:

$$m \circ (G_k\star)\mathbf{u} = G_k \star (\sum_{j=1,k} \alpha^j)(\mathcal{NS} \circ (G_k\star) - \mathcal{NS} \circ (G_{k+1}\star))\mathbf{u} \,, \tag{6.191}$$

where the operator $(G_k\star) \circ \mathcal{NS} \circ (G_{k+1}\star)$ corresponds to a local reconstruction of the evolution of the coarse solution $G_{k+1} \star \mathbf{u}$ according to the fluctuations of the fine solution $G_k \star \mathbf{u}$. The implementation of the model is carried out as follows: a short history of both the coarse and the fine solutions are computed on two different compuational grids, and the model (6.191) is computed and added as a source term into the momentum equations solved on the fine grid. This algorithm can be written in the following symbolic form:

$$\mathbf{u}_k^{n+1} = \left(\mathcal{NS}^2_{k,\Delta t} + \omega(\mathcal{NS}^2_{k,\Delta t} - \mathcal{NS}^1_{k+1,2\Delta t})\right) \mathbf{u}_k^{n+1} \,, \tag{6.192}$$

where $\mathbf{u}_k^{n+1}$ designates the solution on the fine grid (kth filtering level) at the $(n+1)$th time step, $(\mathcal{NS}^n_{k,\Delta t}$ refers to n applications of the discretized Navier–Stokes operator on the grid associated to the filtering level k with a time step Δt (*i.e.* the computation of n time steps on that grid without any subgrid model), and ω is a parameter deduced from relation (6.191). The weight α is evaluated analytically through some inertial range consideration, and is assumed to be equal to the ratio of the kinetic energy contained in the two spectral bands (see equation (4.121). An additional correction factor (lower than 1) can also be introduced to account for the numerical errors.

7. Numerical Solution: Interpretation and Problems

This chapter is devoted to analyzing certain practical aspects of large-eddy simulation.

The first point concerns the differences between the filtering such as it is defined by a convolution product and such as it is imposed on the solution during the computation by the subgrid model. We distinguish here between statistical and dynamic interpretations of the filtering process. The analysis is developed only for subgrid viscosity models because their mathematical form makes this possible. However, the general ideas resulting from this analysis can in theory be extended to other types of models. The second point has to do with the link between the filter cutoff length and the mesh cell size used in the numerical solution. It is important to note that all of the previous developments proceed in a continuous, non-discrete framework and make no mention of the spatial discretization used for solving the equations of the problem numerically. The third point addressed is the comparative analysis of the numerical error and the subgrid terms. We propose here to compare the amplitude of the two sources of error scale separation and numerical discretization to try to establish criteria for the required numerical scheme accuracy so that the errors committed will not overly mar the computed solution.

7.1 Dynamic Interpretation of the Large-Eddy Simulation

7.1.1 Static and Dynamic Interpretations: Effective Filter

The approach that has been followed so far in explaining large-eddy simulation consists in filtering the momentum equations explicitly, decomposing the non-linear terms that appear, and then modeling the unknown terms. If the subgrid model is well designed (in a sense defined in the following chapter), then the energy spectrum of the computed solution, for an exact solution verifying the Kolmogorov spectrum, is of the form

$$E(k) = K_0 \varepsilon^{2/3} k^{-5/3} \widehat{G}^2(k) \quad , \tag{7.1}$$

where $\widehat{G}(k)$ is the transfer function associated with the filter. This is the classical approach corresponding to a static and explicit view of the filtering process.

An alternate approach is proposed by Mason *et al.* [220–222], who first point out that the subgrid viscosity models use an intrinsic length scale denoted Δ_f, which can be interpreted as the mixing length associated with the subgrid scales. A subgrid viscosity model based on the large scales is written thus (see Sect. 4.3.2):

$$\nu_{\mathrm{sgs}} = \Delta_\mathrm{f}^2 |\overline{S}| \quad . \tag{7.2}$$

The ratio between this mixing length and the filter cutoff length $\overline{\Delta}$ is:

$$\frac{\Delta_\mathrm{f}}{\overline{\Delta}} = C_\mathrm{s} \quad . \tag{7.3}$$

Referring to the results explained in the section on subgrid viscosity models, C_s can be recognized as the subgrid model constant. Varying this constant is therefore equivalent to modifying the ratio between the filter cutoff length and the length scale included in the model. These two scales can consequently be considered as independent. Also, during the simulation, the subgrid scales are represented only by the subgrid models which, by their effects, impose the filter on the computed solution[1]. But since the subgrid models are not perfect, going from the computed solution to the exact one does not correspond to the application of the desired theoretical filter. This switch is ensured by applying an implicit filter, which is intrinsically contained in each subgrid model. Here we have a dynamic, implicit concept of the filtering process that takes the modeling errors into account. The question then arises of the qualification of the filters associated with the different subgrid models, both for their form and for their cutoff length.

The discrete dynamical system represented by the numerical simulation is therefore subjected to two filtering operations:

- The first is imposed by the choice of a level of representation of the physical system and is represented by application of a filter using the Navier–Stokes equations in the form of a convolution product.
- The second is induced by the existence of an intrinsic cutoff length in the subgrid model to be used.

In order to represent the sum of these two filtering processes, we define the effective filter, which is the filter actually seen by the dynamical system. To qualify this filter, we therefore raise the problem of knowing what is the share of each of the two filtering operations mentioned above.

[1] They do so by a dissipation of the resolved kinetic energy $-\tau_{ij}\overline{S}_{ij}$ equal to the flux $\widetilde{\varepsilon}$ through the cutoff located at the desired wave numbe

7.1.2 Theoretical Analysis of the Turbulence Generated by Large-Eddy Simulation

We first go into the analysis of the filter associated with a subgrid viscosity model.

This section resumes Muschinsky's [250] analysis of the properties of a homogeneous turbulence simulated by a Smagorinsky model. The analysis proceeds by establishing an analogy between the large-eddy simulation equations incorporating a subgrid viscosity model and those that describe the motions of a non-Newtonian fluid. The properties of the latter are studied in the framework of isotropic homogeneous turbulence, so as to bring out the role of the different subgrid model parameters.

Analogy with Generalized Newtonian Fluids. Smagorinsky Fluid. The constitutive equations of large-eddy simulation for a Newtonian fluid, at least in the case where a subgrid viscosity model is used, can be interpreted differently as being those that describe the dynamics of a non-Newtonian fluid of the generalized Newtonian type, in the framework of direct numerical simulation, for which the constitutive equation is expressed

$$\sigma_{ij} = -p\delta_{ij} + \nu_{\mathrm{sgs}} S_{ij} \quad , \tag{7.4}$$

where σ_{ij} is the stress tensor, S the strain rate tensor defined as above, and ν_{sgs} will be an invariant function of S. Effects stemming from the molecular viscosity are ignored because this is a canonical analysis using the idea of an inertial range. It should be noted that the filtering bar symbol no longer appears because we now interpret the simulation as a direct one of a fluid having a non-linear constitutive equation. If the Smagorinsky model is used, *i.e.*

$$\nu_{\mathrm{sgs}} = \Delta_\mathrm{f}^2 |S| = \left(C_\mathrm{s}\overline{\Delta}\right)^2 |S| \quad , \tag{7.5}$$

such a fluid will be called a Smagorinsky fluid.

Laws of Similarity of the Smagorinsky Fluid. The first step consists in extending the Kolmogorov similarity hypotheses (recalled in Appendix A):

1. First similarity hypothesis. $E(k)$ depends only on ε, Δ_f and $\overline{\Delta}$.
2. Second similarity hypothesis. $E(k)$ depends only on ε and $\overline{\Delta}$ for wave numbers k much greater than $1/\Delta_\mathrm{f}$.
3. Third similarity hypothesis. $E(k)$ depends only on ε et Δ_f if $\overline{\Delta} \ll \Delta_\mathrm{f}$.

The spectrum can then be put in the form:

$$E(k) = \varepsilon^{2/3} k^{-5/3} G_\mathrm{s}(\Pi_1, \Pi_2) \quad , \tag{7.6}$$

where G_s is a dimensionless function whose two arguments are defined as:

$$\Pi_1 = k\Delta_f, \quad \Pi_2 = \frac{\overline{\Delta}}{\Delta_f} = \frac{1}{C_s} \quad . \tag{7.7}$$

By analogy, the limit in the inertial range of G_s is a quantity equivalent to the Kolmogorov constant for large-eddy simulation, denoted $K_{les}(C_s)$:

$$K_{les}(C_s) = G_s(0, \Pi_2) \quad . \tag{7.8}$$

By introducing the shape function

$$f_{les}(k\Delta_f, C_s) = \frac{G_s(\Pi_1, \Pi_2)}{G_s(0, \Pi_2)} \quad , \tag{7.9}$$

the spectrum is expressed:

$$E(k) = K_{les}(C_s)\varepsilon^{2/3}k^{-5/3}f_{les}(k\Delta_f, C_s) \quad . \tag{7.10}$$

By analogy with Kolmogorov's work, we define the dissipation scale of the non-Newtonian fluid η_{les} as:

$$\eta_{les} = \left(\frac{\nu_{sgs}^3}{\varepsilon}\right)^{1/4} \quad . \tag{7.11}$$

For the Smagorinsky model, by replacing ε with its value, we get:

$$\eta_{les} = \Delta_f = C_s\overline{\Delta} \quad . \tag{7.12}$$

Using this definition and postulating that Kolmogorov's similarity theory for the usual turbulence remains valid, the third similarity hypothesis stated implies, for large values of the constant C_s:

$$E(k) = \left(\lim_{C_s\to\infty} K_{les}(C_s)\right)\varepsilon^{2/3}k^{-5/3}\left(\lim_{C_s\to\infty} f_{les}(k\eta_{les}, C_s)\right) \quad , \tag{7.13}$$

which allows us to presume that the two following relations are valid:

$$\lim_{C_s\to\infty} K_{les}(C_s) = K_0 \quad , \tag{7.14}$$

$$\lim_{C_s\to\infty} f_{les}(x, C_s) = f(x) \quad , \tag{7.15}$$

where $f(x)$ is the damping function including the small scale viscous effects, for which the Heisenber-Chandresekhar, Kovazsnay, and Pao models have already been discussed in Sect. 4.3.2.

The corresponding normalized spectrum of the dissipation[2] is of the form:

[2] The dissipation spectrum, denoted $D(k)$, associated with the energy spectrum $E(k)$ is defined by the relation:

$$D(k) = k^2E(k) \quad .$$

$$g_{les}(x, C_s) = x^{1/3}f_{les}(x, C_s) \quad , \tag{7.16}$$

where x is the reduced variable $x = k\eta_{les}$.

By comparing the dissipation computed by integrating this spectrum with the one evaluated from the energy spectrum (7.10), the dependency of the Kolmogorov constant as a function of the Smagorinsky constant is formulated as:

$$K_{les}(C_s) = \frac{1}{2\int_0^\infty g_{les}(x, C_s)} \approx \frac{1}{2\int_0^{C_s\pi} g_{les}(x, C_s)} \quad . \tag{7.17}$$

When this expression is computed using the formulas of Heisenberg–Chandrasekhar and Pao, it shows that the function K_{les} does tend asymptotically to the value $K_0 = 1.5$ for large values values of C_s, as the error is negligible beyond $C_s = 0.5$. The variation of the parameter K_{les} as a function of C_s for the spectra of Heisenberg–Chandrasekhar and Pao is presented in Fig. 7.1. When C_s is less than 0.5, the Kolmogorov constant is over-evaluated, as has actually been observed in the course of numerical experiments [215]. These numerical simulations have also demonstrated that the damping function is subgrid-model dependent.

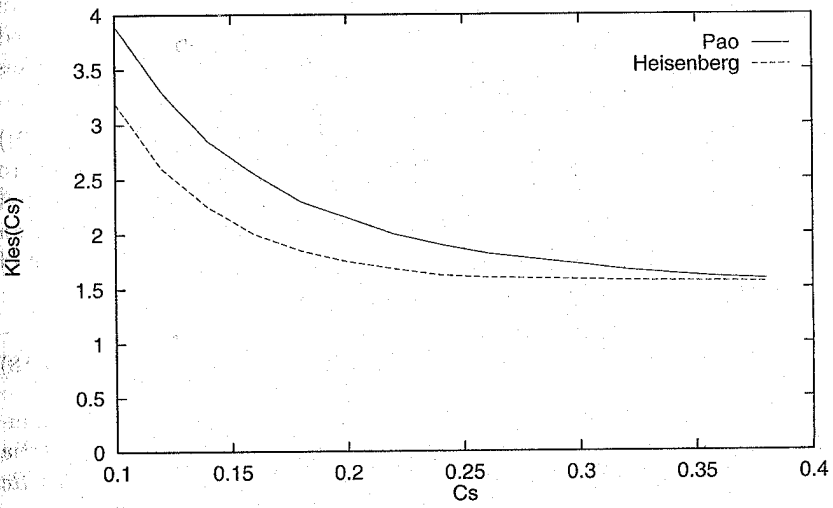

Fig. 7.1. Variation of the Kolmogorov constant as a function of the Smagorinsky constant for the Heisenberg–Chandrasekhar spectrum and the Pao spectrum.

Interpretation of Simulation Parameters

Effective Filter. The above results allow us to refine the analysis concerning the effective filter. For large values of the Smagorinsky constant ($C_s \geq 0.5$), the characteristic cutoff length is the mixing length produced by the model. The model then dissipates more energy than if it were actually located at the scale $\overline{\Delta}$ because it ensures the energy flux balance through the cutoff associated with a longer characteristic length. The effective filter is therefore fully determined by the subgrid model. This solution criterion should be compared with the one defined for hot-wire measurements, which recommends that the wire length be less than twice the Kolmogorov scale in developed turbulent flows.

For small values of the constant, it is the cutoff length $\overline{\Delta}$ that plays the role of characteristic length and the effective filter corresponds to the usual analytical filter. It should be noted in this case that the energy drainage induced by the model is less than the transfer of kinetic energy through the cutoff, so the energy balance is no longer maintained. This is reflected in an accumulation of energy in the resolved scales, and the pertinence of the simulation results should be taken with caution.

For intermediate values of the constant, *i.e.* values close to the theoretical one predicted in Sect. 4.3.2 (*i.e.* $C_s \approx 0.2$), the effective filter is a combination of the analytical filter and model's implicit filter, which makes it difficult to interpret the dynamics of the smallest resolved scales. The dissipation induced by the model in this case correctly insures the equilibrium of the energy fluxes through the cutoff.

Microstructure Knudsen Number. It has already been seen (relation (7.12)) that the mixing length can be interpreted as playing a role analogous to that of the Kolmogorov scale for the direct numerical simulation. The cutoff length $\overline{\Delta}$, for its part, can be linked to the mean free path for Newtonian fluids. We can use the ratio of these two quantities to define an equivalent of the microstucture Knudsen number K_{nm} for the large-eddy simulation:

$$K_{\mathrm{nm}} = \frac{\overline{\Delta}}{\Delta_{\mathrm{f}}} = \frac{1}{C_s} \quad . \tag{7.18}$$

Effective Reynolds Number. Let us also note that the effective Reynolds number of the simulation, denoted Re_{les}, which measures the ratio of the inertia effects to the dissipation effects, is taken in ratio to the Reynolds number Re corresponding to the exact solution by the relation:

$$Re_{\mathrm{les}} = \left(\frac{\eta}{\eta_{\mathrm{les}}}\right)^{4/3} Re \quad , \tag{7.19}$$

where η is the dissipative scale of the full solution. This decrease in the effective Reynolds number in the simulation may pose some problems, if the physical mechanism determining the dynamics of the resol scales depends

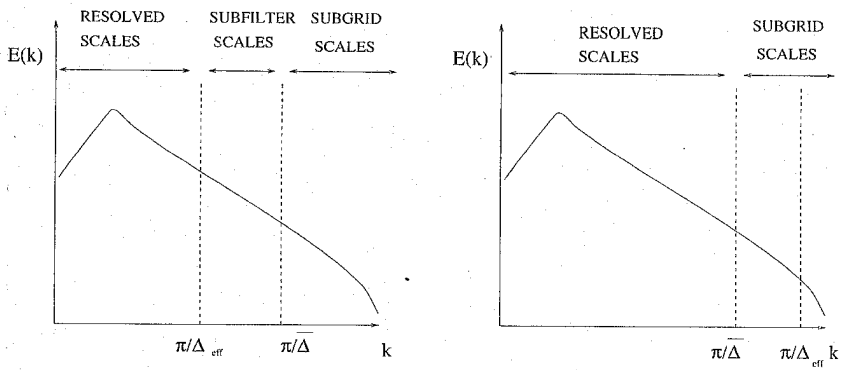

Fig. 7.2. Representation of different scale families in the cases of $\Delta_{eff} < \overline{\Delta}$ (*right*) and $\Delta_{eff} > \overline{\Delta}$ (*left*).

explicitly on it. This will, for example, be the case for all flows where critical Reynolds numbers can be defined for which bifurcations in the solution are associated[3].

Subfilter Scale Concept. By analysis of the decoupling between the cutoff length of the analytical filter $\overline{\Delta}$ and the mixing length Δ_{f}, we can define three families of scales [220, 250] instead of the usual two families of resolved and subgrid scales. These three categories, illustrated in Fig. 7.2, are the:

1. Subgrid scales, which are those that are excluded from the solution by the analytical filter.
2. Subfilter scales, which are those of a size less than the effective filter cutoff length, denoted Δ_{eff}, which are scales resolved in the usual sense but whose dynamics is strongly affected by the subgrid model. Such scales exist only if the effective filter is determined by the subgrid viscosity model. There is still the problem of evaluating Δ_{eff}, and depends both on the presumed shape of the spectrum and on the point beyond which we consider to be "strongly affected". For example, by using Pao's spectrum and defining the non-physically resolved modes as those for which the energy level is reduced by a factor $e = 2.7181...$, we get:

$$\Delta_{\mathrm{eff}} = \frac{C_s}{C_{\mathrm{theo}}} \overline{\Delta} \quad , \tag{7.20}$$

where C_{theo} is the theoretical value of the constant that corresponds to the cutoff length $\overline{\Delta}$.

[3] Numerical experiments show that too strong a dissipation induced by the subgrid model in such flows may inhibit the flow driving mechanisms and consequently lead to unusable simulations. One known example is the use of a Smagorinsky model to simulate a plane channel flow: the dissipation is strong enough to prevent the transitio o turbulence.

3. Physically resolved scales, which are those of a size greater than the effective filter cutoff length, whose dynamics is perfectly captured by the simulation, as in the case of direct numerical simulations.

Characterization of the Filter Associated with the Subgrid Model. The above discussion is based on a similarity hypothesis between the properties of isotropic homogeneous turbulence and those of the flow simulated using a subgrid viscosity model. This is mainly true of the dissipative effects, which are described using the Pao spectrum or that of Heisenberg-Kovazsnay. So here, we adopt the hypothesis that the subgrid dissipation acts like an ordinary dissipation (which was already partly assumed by using a subgrid viscosity model). The spectrum $E(k)$ of the solution from the simulation can therefore be interpreted as the product of the spectrum of the exact solution $E_{\text{tot}}(k)$ by the square of the transfer function associated with the effective filter $\widehat{G}_{\text{eff}}(k)$:

$$E(k) = E_{\text{tot}}(k)\widehat{G}^2_{\text{eff}}(k) \quad . \tag{7.21}$$

Considering that the exact solution corresponds to the Kolmogorov spectrum, and using the form (7.10), we get:

$$\widehat{G}_{\text{eff}}(k) = \sqrt{\frac{K_{\text{les}}(C_s)}{K_0} f_{\text{les}}(k\Delta_f, C_s)} \quad . \tag{7.22}$$

The filter associated with the Smagorinsky model is therefore a "smooth" filter in the spectral space, which corresponds to a gradual damping, very different from the sharp cutoff filter.

7.2 Ties Between the Filter and Computational Grid. Pre-filtering

The above developments completely ignore the computational grid used for solving the constitutive equations of the large-eddy simulation numerically. If we consider this new element, it introduces another space scale: the spatial discretization step Δx for simulations in the physical space, and the maximum wave number $k_{\max}$ for simulations based on spectral methods.

The discretization step has to be small enough to be able to correctly integrate the convolution product that defines the analytical filtering. For filters with fastly-decaying kernel, we have the relation:

$$\Delta x \leq \overline{\Delta} \quad . \tag{7.23}$$

The case where $\Delta x = \overline{\Delta}$ is the optimum case as concerns the number of degrees of freedom needed in the discrete system for performing the simulation. This case is illustrated in Fig. 7.3.

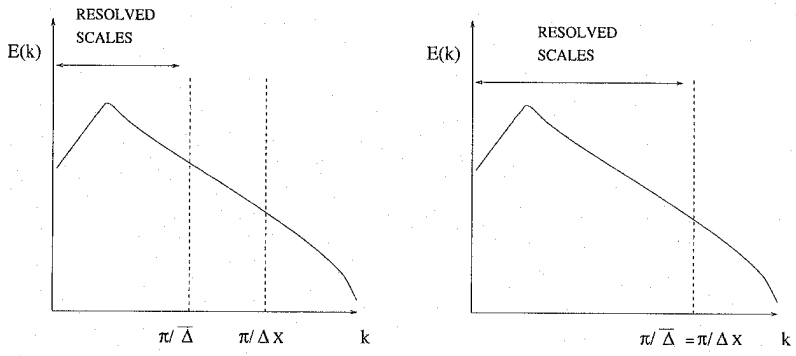

Fig. 7.3. Representation of spectral decompositions associated with pre-filtering (*left*) and in the optimum case (*right*).

The numerical errors stemming from the resolution of the discretized system still have to be evaluated. To ensure the quality of the results, the numerical error committed on the physically resolved modes has to be negligible, and therefore committed only on the subfilter scales. The theoretical analysis of this error by Ghosal in the simple case of isotropic homogeneous turbulence is presented in the following.

As the numerical schemes used are consistent, the discretization error cancels out as the space and time steps tend toward zero. One way of minimizing the effect of numerical error is to reduce the discretization step while maintaining the filter cutoff length, which comes down to increasing the ratio $\overline{\Delta}/\Delta x$ (see Fig. 7.3). This technique, based on the decoupling of the two space scales, is called pre-filtering [4], and aims to ensure the convergence of the solution regardless of the grid[4]. It minimizes the numerical error but induces more computations because it increases the number of degree of freedoms in the numerical solution without increasing the number of degrees of freedom in the physically resolved solution, and requires that the analytical filtering be performed explicitly [4] [24]. Because of its cost[5], this solution is rarely used in practice.

Another approach is to link the analytical filter to the computed grid. The analytical cutoff length is associated with the space step using the optimum ratio of these quantities and the form of the convolution kernel is associated

[4] A simplified analysis shows that, for an nth-order accurate numerical method, the weight of the numerical error theoretically decreases as $(\overline{\Delta}/\Delta x)^{-n}$. A finer estimate is given in the remainder of this chapter.

[5] For a fixed value of $\overline{\Delta}$, increasing the ratio $\overline{\Delta}/\Delta x$ by a factor n leads to an increase in the number of points of the simulation by a factor of n^3 and increases the number of time steps by a factor n in order to maintain the same ratio between the time and space steps. In all, this makes an overall increase in the cost of the simulation by a factor n^4.

with the numerical method. Let us point out a problem here that is analogous to that of the effective filter already mentioned: the effective numerical filter and therefore the effective numerical cutoff length, are generally unknown. This method has the advantage of reducing the size of the system as best possible and not requiring the use of an analytical filter, but it allows no explicit control of the effective numerical filter, which makes it difficult to calibrate the subgrid models. This method, because of its simplicity, is used by nearly all the authors.

7.3 Numerical Errors and Subgrid Terms

7.3.1 Ghosal's General Analysis

Ghosal [120] proposes a non-linear analysis of the numerical error in the solution of the Navier–Stokes equations for an isotropic homogeneous turbulent flow whose energy spectrum is approximated by the Von Karman model.

Classification of Different Sources of Error. In order to analyze and estimate the discretization error, we first need a precise definition of it. In all of the following, we consider a uniform Cartesian grid of N^3 points, which are the degrees of freedom of the numerical solution. Periodicity conditions are used on the domain boundaries.

A first source of error stems from the approximation we make of a continuous solution $\overline{\mathbf{u}}$ by a making a discrete solution $\mathbf{u}_\mathrm{d}$ with a set of N^3 values. This is evaluated as:

$$|\mathbf{u}_\mathrm{d} - \mathcal{P}(\overline{\mathbf{u}})| \quad , \tag{7.24}$$

where $\mathcal{P}$ is a definite projection operator of the space of continuous solutions to that of the discrete solutions. This error is minimum (in the L^2 sense) if $\mathcal{P}$ is associated with the decomposition of the continuous solution on a finite base of trigonometric polynomials, with the components of $\mathbf{u}_\mathrm{d}$ being the associated Fourier coefficients. This error is intrinsic and cannot be canceled. Consequently, it will not enter into the definition of the numerical error discussed in this present section. The best possible discrete solution is $\mathbf{u}_\mathrm{opt} \equiv \mathcal{P}(\overline{\mathbf{u}})$.

The equations of the continuous problem are written in the symbolic form:

$$\frac{\partial \overline{\mathbf{u}}}{\partial t} = \mathcal{NS}(\overline{\mathbf{u}}) \quad , \tag{7.25}$$

where $\mathcal{NS}$ is the Navier–Stokes operator. The optimum discrete solution $\mathbf{u}_\mathrm{opt}$ is a solution of the problem:

$$\frac{\partial \mathcal{P}\overline{\mathbf{u}}}{\partial t} = \mathcal{P} \circ \mathcal{NS}(\overline{\mathbf{u}}) \quad , \tag{7.26}$$

where $\mathcal{P} \circ \mathcal{NS}$ is the optimal discrete Navier–Stokes operator which, in the fixed framework, corresponds to the discrete operators obtained by a spectral method.

Also, we note the discrete problem associated with a fixed discrete scheme as:

$$\frac{\partial \mathbf{u}_\mathrm{d}}{\partial t} = \mathcal{NS}_\mathrm{d}(\mathbf{u}_\mathrm{d}) \quad . \tag{7.27}$$

By taking the difference between (7.26) and (7.27), it appears that the best possible numerical method, denoted $\mathcal{NS}_\mathrm{opt}$, is the one that verifies the relation:

$$\mathcal{NS}_\mathrm{opt} \circ \mathcal{P} = \mathcal{P} \circ \mathcal{NS} \quad . \tag{7.28}$$

The numerical error E_num associated with the $\mathcal{NS}_\mathrm{d}$ scheme, and which is analyzed in the following, is defined as:

$$E_\mathrm{num} \equiv (\mathcal{P} \circ \mathcal{NS} - \mathcal{NS}_\mathrm{d} \circ \mathcal{P})(\overline{\mathbf{u}}) \quad . \tag{7.29}$$

This represents the discrepancy between the numerical solution and the optimum discrete one. To simplify the analysis, we consider in the following that the subgrid models are perfect, *i.e.* that they induce no error with respect to the exact solution of the filtered problem. By assuming this, we can clearly separate the numerical errors from the modeling errors.

The numerical error $E_\mathrm{num}(k)$ associated with the wave number k is decomposed as the sum of two terms of distinct origins:

- The differentiation error $E_\mathrm{df}(k)$, which measures the error the discrete operators make in evaluating the derivatives of the wave associated with k. Let us note that this error is null for a spectral method if the cutoff frequency of the numerical approximation is high enough.
- The spectrum aliasing error $E_\mathrm{rs}(k)$, which is due to the fact that we are computing non-linear terms in the physical space in a discrete space of finite dimension. For example, a quadratic term will bring in higher frequencies than those of each of the arguments in the product. While some of these frequencies are too high to be represented directly on the discrete base, they do combine with the low frequencies and introduce an error in the representation of them[6].

[6] Let us take the Fourier expansions of two discrete functions u and v represented by N degrees of freedom. At the point of subscript j, the expansions are expressed:

$$u_j = \sum_{n=-N/2}^{N/2-1} \widehat{u}_n e^{(\mathrm{i}(2\pi/N)jn)}, \quad v_j = \sum_{m=-N/2}^{N/2-1} \widehat{v}_m e^{(\mathrm{i}(2\pi/N)jm)} \quad j = 1, N \quad .$$

The Fourier coefficient of the product $w_j = u_j v_j$ (without summing on j) splits into the form:

$$w_k = \sum_{n+m=k} \widehat{u}_n \widehat{v}_m + \sum_{n+m=k\pm N} \widehat{u}_n \widehat{v}_m \quad .$$

Estimations of the Error Terms. For a solution whose spectrum is of the form proposed by Von Karman:

$$E(k) = \frac{ak^4}{(b+k^2)^{17/6}} \quad , \tag{7.30}$$

with $a = 2.682$ and $b = 0.417$, and using a quasi-normality hypothesis for evaluating certain non-linear terms, Ghosal proposes a quantitative evaluation of the different error terms, the subgrid terms, and the convection term, for various Finite Difference schemes as well as for a spectral scheme. The convection term is written in conservative form and all the schemes in space are centered. The time integration is assumed to be exact.

The exact forms of these terms, available in the original reference work, are not reproduced here. For a cutoff wave number k_c and a sharp cutoff filter, simplified approximate estimates of the average amplitude can be derived for some of these terms.

The amplitude of the subgrid term $\sigma_{sgs}(k_c)$, defined as

$$\sigma_{sgs}(k_c) = \left[\int_0^{k_c} |\tau(k)|dk\right]^{1/2} \quad , \tag{7.31}$$

where $\tau(k)$ is the subgrid term for the wave number k, is bounded by:

$$\sigma_{sgs}(k_c) = \begin{cases} 0.36\ k_c^{0.39} & \text{upper limit} \\ 0.62\ k_c^{0.48} & \text{lower limit} \end{cases} \quad , \tag{7.32}$$

that of the sum of the convection term and subgrid term by:

$$\sigma_{tot}(k_c) = 1.04\ k_c^{0.97} \quad , \tag{7.33}$$

in which

$$\frac{\sigma_{sgs}(k_c)}{\sigma_{tot}(k_c)} \approx k_c^{-0.5} \quad . \tag{7.34}$$

The amplitude of the differentiation error $\sigma_{df}(k_c)$, defined by:

$$\sigma_{df}(k_c) = \left[\int_0^{k_c} E_{df}(k)dk\right]^{1/2} \quad , \tag{7.35}$$

is evaluated as:

The last term in the right-hand side represents the spectrum aliasing error. These are terms of frequencies higher than the Nyquist frequency, associated the sampling, which will generate spurious resolved frequencies.

$$\sigma_{df}(k_c) = k_c^{0.75} \times \begin{cases} 1.03 & \text{(second order)} \\ 0.82 & \text{(fourth order)} \\ 0.70 & \text{(sixth order)} \\ 0.5 & \text{(heigth order)} \\ 0 & \text{(spectral)} \end{cases} \quad , \tag{7.36}$$

and the spectrum aliasing error $\sigma_{rs}(k_c)$, which is equal to:

$$\sigma_{rs}(k_c) = \left[\int_0^{k_c} E_{rs}(k)dk\right]^{1/2} \tag{7.37}$$

is estimated as:

$$\sigma_{rs} = \begin{cases} 0.90\ k_c^{0.46} & \text{(minimum estimation, spectral, no de-aliasing)} \\ 2.20\ k_c^{0.66} & \text{(maximum estimation, spectral, no de-aliasing)} \\ 0.46\ k_c^{0.41} & \text{(minimum estimation, second order)} \\ 1.29\ k_c^{0.65} & \text{(maximum estimation, second order)} \end{cases} \quad . \tag{7.38}$$

The spectrum aliasing error for the spectral method can be reduced to zero by using the 2/3 rule, which consists of not considering the last third of the wave numbers represented by the discrete solution. It should be noted that, in this case, only the first two-thirds of the modes of the solution are correctly represented numerically. The error of the finite difference schemes of higher order is intermediate between that of the second-order accurate scheme and that of the spectral scheme.

From these estimations, we can see that the discretization error dominates the subgrid terms for all the finite difference schemes considered. The same is true for the spectrum aliasing error, including for the finite difference schemes. Finer analysis on the basis of the spectra of the various terms shows that the discretization error dominant for all wave numbers for the second-order accurate scheme, whereas the subgrid terms are dominant at the low frequencies for the heigth-order accurate scheme. In the former case, the effective numerical filter is dominant and governs the solution dynamics. Its cutoff length can be considered as being of the order of the size of the computational domain. In the latter, its cutoff length, defined as the wavelength of the mode beyond which it becomes dominant with respect to the subgrid terms, is smaller and there exist numerically well-resolved scales.

Pre-filtering Effect. The pre-filtering effect is clearly visible from relations (7.32) to (7.38). By decoupling the analytical from the numerical filter, two different cutoff scales are introduced and thereby two different wave numbers for evaluating the numerical error terms and the subgrid terms: while the cutoff scale $\overline{\Delta}$ associated with the filter remains constant, the scale associated with the numerical error (*i.e.* Δx) is now variable.

By designating the ratio of the two cutoff lengths by $C_{rap} = \Delta x/\overline{\Delta} < 1$, we see that the differentiation error $\sigma_{df}(k_c)$ of the finite difference scheme is

reduced by a factor $C_{\text{rap}}^{-3/4}$ with respect to the previous case, since it varies as $k_c^{3/4}$. This reduction is much greater than the one obtained by increasing the order of accuracy of the the schemes.

Thus, more detailed analysis shows that, for the second-order accurate scheme, the dominance of the subgrid term on the whole of the solution spectrum is ensured for $C_{\text{rap}} = 1/8$. For a ratio of $1/2$, this dominance is once again found for schemes of order of accuracy of 4 or more.

Conclusions. This analysis can be used only for reference, because it is based on very restrictive hypotheses. It nonetheless indicates that the numerical error is not negligible and that it can even be dominant in certain cases over the subgrid terms. The effective numerical filter is then dominant over the scale separation filter.

This error can be reduced either by increasing the order of accuracy of the numerical scheme or by using a pre-filtering technique that decouples the cutoff length of the analytical filter of the discretization step. Ghosal's findings seem to indicate that a combination of these two techniques would be the most effective solution.

These theoretical findings are confirmed by the numerical experiments of Najjar and Tafti [257] and Kravenchko and Moin [172], who observed that the effect of the subgrid models is completely or partially masked by the numerical error when second-order accurate methods are employed. It should be noted here that practical experience leads us to less pessimistic conclusions than the theoretical analyses: large-eddy simulations performed with a scheme accurate to the second order show a dependency with respect to the subgrid model used. The effects of these models are not entirely masked, which justifies using them. However, no precise qualification exists today of the information loss due to the use of a given scheme. These observations are made empirically, case by case.

7.3.2 Remarks on the Use of Artificial Dissipations

Many comments have been made over recent decades on the sensitivity of large-eddy simulation results, for example concerning the formulation of the convection term [138, 172], the discrete form of the test filter [257], and the formulation of the subgrid term [291], but there are far too many, too dispersed, and too far from general to be detailed here. Moreover, countless analyses have been made of the numerical error associated with various schemes, especially as concerns the treatment of the non-linear terms, which will not be resumed here, but we will still take more special note of the findings of Fabignon *et al.* [94] concerning the characterization of the effective numerical filter of several schemes.

Special attention should still be paid to the discretization of the convective terms. To capture strong gradients without having the numerical solution polluted with spurious high-frequency wiggles, the scheme is ve often stabilized

by introducing artificial dissipation. This dissipation is added explicitly or implicitly using an upwind scheme for the convection term. Introducing an additional dissipation term for the large-eddy simulation is still controversial [104, 110, 239, 257, 306] because the effective filter is then very similar in form to that which would be imposed by subgrid viscosity model, making for two competing resolved kinetic energy spectrum mechanisms. The similarity between the numerical dissipation and that associated with the energy cascade model is still being investigated, but a few conclusions have already been drawn.

It seems that the total numerical dissipation is still greater than that of the subgrid viscosity models, if no pre-filtering method is used. This is true even for seventh-order accurate upwind schemes [18]. These two dissipations are correlated in space (especially in the case of the Smagorinsky model), but have different spectral distributions: a subgrid viscosity model corresponds to a second-order dissipation associated with a spectrum of the form $(k/k_c)^2 E(k)$, while an nth-order numerical dissipation is associated with a spectrum of the form $(k/k_c)^n E(k)$. For $n > 2$ (resp. $n < 2$), the numerical (resp. subgrid) dissipation will be dominant for the highest resolved frequencies and the subgrid (resp. numerical) dissipation will govern the dynamics of the low frequencies.

The studies that have been made show a sensitivity of the results to the subgrid model used, which proves that the effects of the model are not entirely masked by the numerical dissipation. The theoretical analysis presented above should therefore be taken relative to this. But consistently with it, Beaudan *et al.* [18] have brought out a reduction in the numerical cutoff length as the order of accuracy of the scheme increases. This type of finding should nonetheless be treated with caution, because the conclusions may be reversed if we bring in an additional parameter, which is the grid refinement. Certain studies have shown that, for coarse grids, *i.e.* high values of the numerical cutoff length, increasing the order of accuracy of the upwind scheme can lead to a degradation of the results [323].

This relative similarity between artificial dissipation and direct energy cascade model has induced certain authors to perform "no-model"large-eddy simulations, with the filtering based entirely on the numerical method. Thus many flow simulations have been seen in complex geometries, based on the use of an third-order accurate upwind scheme proposed by Kawamura and Kuwahara [165], yielding interesting results. In the compressible case, this approach has been called the Monotone Integrated Large-Eddy Simulation (MILES) method [28, 104, 110].

The use of artificial dissipation therefore raises many questions, but is very common in simulations that are physically very strongly under-resolved in complex configurations, because experience shows that adding subgrid models does not ensure a monotonic solution. To ensure that certain variables remain positive, such as concentrations of pollutants or the temperature, it

seems to be necessary to resort to such numerical methods. Alternatives based on local refinement of the solution, *i.e.* decreasing the effective cutoff length by enriching or adapting the grid, have been studied by certain authors but no final conclusion has been drawn.

While the Navier–Stokes equations contain energy information, they also contain information concerning the signal phase. Using centered schemes for the convection term therefore raises problems too, because of the dispersive errors they induce in the high resolved frequencies.

Generally, estimates of the wave number beyond which the modes are considered to be well resolved numerically vary from $2\Delta x$ to $12\Delta x$, depending on the schemes and authors.

7.3.3 Remarks Concerning the Time Integration Method

Large-eddy simulation is ordinarily addressed using a spatial filtering, but without explicitly stating the associated time filtering. This is due to the fact that most computations are made for moderate time steps (CFL $\equiv u\Delta t/\Delta x < 1$) and it is felt that the time filtering effects are masked by those of the space filtering. Choi and Moin [56], however, have shown by direct simulations of a plane channel flow that the time filtering effects can be very large, even for CFLs of the order of 0.5, since the turbulence cannot be maintained numerically if the time step is greater than the characteristic time associated with the Kolmogorov scale. Most authors use second-order accurate integration methods, but no complete study has been published to date to determine what time scales are well resolved numerically and physically. We should also note the results of Beaudan and Moin [18] and Mittal and Moin [239], who showed that the use of artificial viscosity affects the solution of a very large share of the simulated time frequencies (about 75 % for the particular case studied).

8. Analysis and Validation of Large-Eddy Simulation Data

8.1 Statement of the Problem

8.1.1 Type of Information Contained in a Large-Eddy Simulation

The solution to the equations that define the large-eddy simulation furnishes explicit information only on the scales that are resolved, *i.e.* those that are left after reduction of the number of degrees of freedom in the exact solution. We are therefore dealing with information that is truncated in space and time. The time filtering is induced implicitly by the spatial filtering because, as the filtering eliminates certain space scales, it eliminates the corresponding time scales with them (see footnote p. 13).

The information of use for analysis or validation is what is contained in those scales that are both physically and numerically well-resolved. It should be remembered that, since the effective numerical and physical filters are unknown, the usable scales are most often identified empirically.

Adopting the assumption that all the scales represented by the simulation are physically and numerically well-resolved, the statistical average of the usable resolved field is expressed $\langle\overline{\mathbf{u}}\rangle$. The statistical fluctuation of the resolved field, denoted $\overline{\mathbf{u}}''$, is defined by:

$$\overline{u}_i'' = \overline{u}_i - \langle\overline{u}_i\rangle \quad . \tag{8.1}$$

The difference between the statistical average of the resolved scales and that of the exact solution is defined as:

$$\langle u_i\rangle - \langle\overline{u}_i\rangle = \langle u'_i\rangle \quad , \tag{8.2}$$

which corresponds to the statistical average of the unresolved scales. The Reynolds stresses computed from the resolved scales are equal to $\langle\overline{u}_i''\overline{u}_j''\rangle$. The difference from the exact stresses $\langle u_i'^e u_j'^e\rangle$, where the exact fluctuation is defined as $\mathbf{u}'^e = \mathbf{u} - \langle\mathbf{u}\rangle$, is:

$$\begin{aligned}
\langle u_i'^e u_j'^e\rangle &= \langle(u_i - \langle u_i\rangle)(u_j - \langle u_j\rangle)\rangle \\
&= \langle u_i u_j\rangle - \langle u_i\rangle\langle u_j\rangle \\
&= \langle\overline{u}_i\overline{u}_j + \tau_{ij}\rangle - \langle\overline{u}_i + u_i'\rangle\langle\overline{u}_j + u_j'\rangle \\
&= \langle\overline{u}_i\overline{u}_j\rangle + \langle\tau_{ij}\rangle - \langle\overline{u}_i\rangle\langle\overline{u}_j\rangle - \langle u_i'\rangle\langle\overline{u}_j\rangle - \langle\overline{u}_i\rangle\langle u_j'\rangle - \langle u_i'\rangle\langle u_j'\rangle \\
&= \langle\overline{u}_i''\overline{u}_j''\rangle + \langle\tau_{ij}\rangle - \langle u_i'\rangle\langle\overline{u}_j\rangle - \langle\overline{u}_i\rangle\langle u_j'\rangle - \langle u_i'\rangle\langle u_j'\rangle \quad .
\end{aligned}$$

Since the subgrid scales are not known, the terms containing the contribution $\langle \mathbf{u}' \rangle$, cannot be computed from the simulation. When the statistical average of the subgrid modes is very small compared with the other terms, we get:

$$\langle u_i'^e u_j'^e \rangle \simeq \langle \overline{u}_i'' \overline{u}_j'' \rangle + \langle \tau_{ij} \rangle \quad . \tag{8.3}$$

The two terms in the right-hand side can be evaluated from the numerical simulation, but the quality of the model's representation of the subgrid tensor partly conditions that of the result.

8.1.2 Validation Methods

The subgrid models and their various underlying hypotheses can be validated in two ways [99]:

- A priori validation. The exact solution, which is known in this case, is filtered analytically, leading to the definition of a fully determined resolved field and subgrid field. The various hypotheses or models can then be tested. The exact solutions are usually generated by direct numerical simulations at moderate or low Reynolds numbers, which limits the field of investigation. A priori tests like this have also been performed using experimental data, making it possible to reach higher Reynolds numbers. This type of validation raises a fundamental problem, though. By comparing the exact subgrid stresses with those predicted by a subgrid model evaluated on the basis of the filtered exact solution, the effects of the modeling errors are neglected and the implicit filter associated with the model is not considered[1]. This means that the results of a priori validations are only relative in value.
- A posteriori validation. Here, we perform a large-eddy simulation computation and validate by comparing its results with a reference solution. This is a dynamic validation that takes all the simulation factors into consideration, while the previous method is static. Experience shows that models yielding poor a priori results can be satisfactory *a posteriori*, and vice versa [269]. It is more advantageous to validate models *a posteriori* because it corresponds to their use in the simulation; but it is sometimes difficult to draw any conclusions on a precise point because of the multitude of often imperfectly controlled factors at play in a numerical simulation.

[1] This field could not have been obtained by a large-eddy simulation since it is a solution of the filtered momentum equations in which the exact subgrid tensor appears. In the course of a simulation, the subgrid model is applied to a velocity field that is a solution of the momentum equation where the modeled subgrid tensor appears. These two fields are therefore different in theory. Consequently, in order to be fully representative, an a priori test has to be performed on the basis of a velocity field that can be obtained from the subgr odel studied.

8.1.3 Statistical Equivalency Classes of Realizations

The subgrid models are statistical models and it seems pointless to expect them to produce deterministic simulations in which the resolved scales coincide exactly with those of other realizations, for example of the experimental sort. On the other hand, large-eddy simulation should correctly reproduce the statistical behavior of the scales making up the resolved field. Equivalency classes can thus be defined among the realizations [225] by considering that one of the classes consists of realizations that lead to the same values of certain statistical quantities computed from the resolved scales.

Belonging to the same class of equivalency as a reference solution is a validation criterion for the other realizations. If we set aside the numerical errors, we can define the necessary conditions on the subgrid models such that two realizations will be equivalent, by verifying these validity criteria. These conditions will be discussed in the following sections. A subgrid model can thus be considered validated if it can generate realizations that are equivalent to a reference solution, in a sense defined below.

Theoretically, while we overlook the effect of the discretization on the modeling, it can be justifiably thought that a model reproducing the interscale interactions exactly will produce good results, whereas the opposite proposition is not true. That is, the idea of sufficient complexity of a model has to be introduced in order to obtain a type of result on a given configuration with a tolerated margin of error in order to say what a good model is. The idea of a universal or best model might not be rejected outright, but should be taken relatively. The question is thus raised of knowing what statistical properties two subgrid models should share in order for the two resulting solutions to have common properties.

Let $\overline{\mathbf{u}}$ and $\overline{\mathbf{u}}^*$ be the filtered exact solution and the solution computed with a subgrid model, respectively, for the same filter. The exact (unmodeled) subgrid tensor corresponding to $\overline{\mathbf{u}}$ is denoted τ_{ij}, and the modeled subgrid tensor computed from the $\overline{\mathbf{u}}^*$ field is denoted $\tau_{ij}^*(\overline{\mathbf{u}}^*)$. The two velocity fields are solutions of the following momentum equations:

$$\frac{\partial \overline{\mathbf{u}}}{\partial t} + \nabla \cdot (\overline{\mathbf{u}} \otimes \overline{\mathbf{u}}) = -\nabla \cdot \overline{p} + \nu \nabla^2 \overline{\mathbf{u}} - \nabla \cdot \tau \quad , \tag{8.4}$$

$$\frac{\partial \overline{\mathbf{u}}^*}{\partial t} + \nabla \cdot (\overline{\mathbf{u}}^* \otimes \overline{\mathbf{u}}^*) = -\nabla \cdot \overline{p}^* + \nu \nabla^2 \overline{\mathbf{u}}^* - \nabla \cdot \tau^*(\overline{\mathbf{u}}^*) \quad . \tag{8.5}$$

A simple analysis shows that, if all the statistical moments (at all points of space and time) of τ_{ij} conditioned by the $\overline{\mathbf{u}}$ field are equal to those of $\tau_{ij}^*(\overline{\mathbf{u}}^*)$ conditioned by $\overline{\mathbf{u}}^*$, then all the statistical moments of $\overline{\mathbf{u}}$ and $\overline{\mathbf{u}}^*$ will be equal. This is a full statistical equivalency, which implies that the subgrid models fulfill an infinity of conditions. To relax this constraint, we define less restrictive equivalency classes of solutions which are described in the following secti . They are defined in such a way as to bring out

the necessary conditions applying to the subgrid models, in order to qualify them [225]. We try to define conditions such that the statistical moments of moderate order[2] (1 and 2) of the field resulting from the large-eddy simulation $\overline{\mathbf{u}}^*$ are equal to those of a reference solution $\overline{\mathbf{u}}$.

Equivalency of First-Order Moments. The equivalency relation is built on the equality of the first-order statistical moments of the realizations. A velocity and a pressure field are associated with each realization. Let $(\overline{\mathbf{u}}, \overline{p})$ and $(\overline{\mathbf{u}}^*, \overline{p}^*)$ be the doublets associated with the first and second realizations, respectively. The evolution equations of the first-order statistical moments of the velocity field of these two realizations are expressed:

$$\frac{\partial \langle \overline{\mathbf{u}} \rangle}{\partial t} + \nabla \cdot (\langle \overline{\mathbf{u}} \rangle \otimes \langle \overline{\mathbf{u}} \rangle) \tag{8.6}$$
$$= -\nabla \cdot \langle \overline{p} \rangle + \nu \nabla^2 \langle \overline{\mathbf{u}} \rangle - \nabla \cdot \langle \tau \rangle - \nabla \cdot (\langle \overline{\mathbf{u}} \otimes \overline{\mathbf{u}} \rangle - \langle \overline{\mathbf{u}} \rangle \otimes \langle \overline{\mathbf{u}} \rangle) \ ,$$

$$\frac{\partial \langle \overline{\mathbf{u}}^* \rangle}{\partial t} + \nabla \cdot (\langle \overline{\mathbf{u}}^* \rangle \otimes \langle \overline{\mathbf{u}}^* \rangle) \tag{8.7}$$
$$= -\nabla \cdot \langle \overline{p}^* \rangle + \nu \nabla^2 \langle \overline{\mathbf{u}}^* \rangle - \nabla \cdot \langle \tau^* (\overline{\mathbf{u}}^*) \rangle - \nabla \cdot (\langle \overline{\mathbf{u}}^* \otimes \overline{\mathbf{u}}^* \rangle - \langle \overline{\mathbf{u}}^* \rangle \otimes \langle \overline{\mathbf{u}}^* \rangle) \ ,$$

where $\langle \ \rangle$ designates an ensemble average performed using independent realizations. The two realizations will be called equivalent if their first- and second-order moments are equivalent, *i.e.*

$$\langle \overline{u}_i \rangle = \langle \overline{u}_i^* \rangle \quad , \tag{8.8}$$
$$\langle \overline{p} \rangle = \langle \overline{p}^* \rangle \quad , \tag{8.9}$$
$$\langle \overline{u}_i \overline{u}_j \rangle = \langle \overline{u}_i^* \overline{u}_j^* \rangle \quad . \tag{8.10}$$

Analysis of evolution equations (8.6) and (8.7) shows that one necessary condition is that the resolved and subgrid stresses be statistically equivalent. The last condition is expressed:

$$\langle \tau_{ij} \rangle = \langle \tau_{ij}^* \rangle + C_{ij} \quad , \tag{8.11}$$

where C_{ij} is a null-divergence tensor. This condition is not sufficient because a model that leads to a good prediction of the mean stresses can generate an error on the mean field if the mean resolved stresses are not correct. To obtain a sufficient condition, the equivalency of the stresses $\langle \overline{u}_i \overline{u}_j \rangle$ and $\langle \overline{u}_i^* \overline{u}_j^* \rangle$ must be ensured by another relation.

[2] Because these are the quantities sought in practice.

Equivalency of Second-Order Moments. We now base the equivalency relation on the equality of the second-order moments of the resolved scales. Two realizations will be called equivalent if the following conditions are satisfied:

$$\langle \overline{u}_i \rangle = \langle \overline{u}_i^* \rangle \quad , \tag{8.12}$$
$$\langle \overline{u}_i \overline{u}_j \rangle = \langle \overline{u}_i^* \overline{u}_j^* \rangle \quad , \tag{8.13}$$
$$\langle \overline{u}_i \overline{u}_j \overline{u}_k \rangle = \langle \overline{u}_i^* \overline{u}_j^* \overline{u}_k^* \rangle \quad , \tag{8.14}$$
$$\langle \overline{p} \overline{u}_i \rangle = \langle \overline{p}^* \overline{u}_i^* \rangle \quad , \tag{8.15}$$
$$\langle \overline{p} \overline{S}_{ij} \rangle = \langle \overline{p}^* \overline{S}_{ij}^* \rangle \quad , \tag{8.16}$$
$$\langle \frac{\partial \overline{u}_i}{\partial x_k} \frac{\partial \overline{u}_i}{\partial x_k} \rangle = \langle \frac{\partial \overline{u}_i^*}{\partial x_k} \frac{\partial \overline{u}_i^*}{\partial x_k} \rangle \quad . \tag{8.17}$$

Analysis of the equation for the second-order moments $\langle \overline{u}_i \overline{u}_j \rangle$ shows that, in order for two realizations to be equivalent, the following necessary condition must be satisfied:

$$\langle \tau_{ik} \overline{S}_{kj} \rangle + \langle \tau_{jk} \overline{S}_{ki} \rangle - \frac{\partial}{\partial x_k} \left(\langle \overline{u}_i \tau_{jk} \rangle + \langle \overline{u}_j \tau_{ik} \rangle \right)$$
$$= \langle \tau_{ik}^* \overline{S}_{kj}^* \rangle + \langle \tau_{jk}^* \overline{S}_{ki}^* \rangle - \frac{\partial}{\partial x_k} \left(\langle \overline{u}_i^* \tau_{jk}^* \rangle + \langle \overline{u}_j^* \tau_{ik}^* \rangle \right) \quad .$$

This condition is not sufficient. To obtain such an realization, the equality of the third-order moments also has to be ensured. It is noted that the nonlinear coupling prohibits the definition of sufficient conditions on the subgrid model to ensure the equality of the nth-order moments of the resolved field without adding necessary conditions on the equality of the $(n+1)$th-order moments.

Equivalency of the Probability Density Functions. We now base the definition of the equivalency classes on the probability density function $f_{\text{prob}}(\mathbf{V}, \mathbf{x}, t)$ of the resolved scales. The field $\mathbf{V}$ is the test velocity field from which the conditional average is taken. The function f_{prob} is defined as the statistical average of the one-point probabilities:

$$f_{\text{prob}}(\mathbf{V}, \mathbf{x}, t) \equiv \langle \delta(\overline{\mathbf{u}}(\mathbf{x}, t) - \mathbf{V}) \rangle \quad , \tag{8.18}$$

and is a solution of the following transport equation:

$$\frac{\partial f_{\text{prob}}}{\partial t} + V_j \frac{\partial f_{\text{prob}}}{\partial x_j} = \frac{\partial}{\partial V_j} \left\{ f_{\text{prob}} \langle \frac{\partial p}{\partial x_j} + \frac{\partial \tau_{ij}}{\partial x_j} - \nu \nabla^2 \overline{u}_j | \overline{\mathbf{u}} = \mathbf{V} \rangle \right\} \quad . \tag{8.19}$$

Two realizations can be called equivalent if:

$$f_{\text{prob}}(\mathbf{V},\mathbf{x},t) = f^*_{\text{prob}}(\mathbf{V},\mathbf{x},t) \quad , \tag{8.20}$$

$$\langle \overline{u}_i(\mathbf{y})|\overline{\mathbf{u}}=\mathbf{V}\rangle = \langle \overline{\mathbf{u}}^*_i(\mathbf{y})|\overline{\mathbf{u}}=\mathbf{V}\rangle \quad , \tag{8.21}$$

$$\langle \overline{u}_i(\mathbf{y})\overline{u}_j(\mathbf{y})|\overline{\mathbf{u}}=\mathbf{V}\rangle = \langle \overline{\mathbf{u}}^*_i\overline{\mathbf{u}}^*_j(\mathbf{y})|\overline{\mathbf{u}}=\mathbf{V}\rangle \quad . \tag{8.22}$$

Once the pressure gradient is expressed as a function of the velocity (by an integral formulation using a Green function) and the conditional average of the strain rate tensor is expressed using gradients of the two-point conditional averages, equation (8.19) can be used to obtain the following necessary condition:

$$\begin{aligned} -\frac{1}{4\pi}\int \frac{\partial^2}{\partial y_i \partial y_k}\langle \tau_{ik}|\overline{\mathbf{u}}(\mathbf{x})=\mathbf{V}\rangle \frac{x_j-y_j}{|\mathbf{x}-\mathbf{y}|}d^3\mathbf{y} + \lim_{\mathbf{y}\to\mathbf{x}}\frac{\partial}{\partial y_i}\langle \tau_{ij}|\overline{\mathbf{u}}(\mathbf{x})=\mathbf{V}\rangle \\ = -\frac{1}{4\pi}\int \frac{\partial^2}{\partial y_i \partial y_k}\langle \tau^*_{ik}|\overline{\mathbf{u}}^*(\mathbf{x})=\mathbf{V}\rangle \frac{x_j-y_j}{|\mathbf{x}-\mathbf{y}|}d^3\mathbf{y} \\ + \lim_{\mathbf{y}\to\mathbf{x}}\frac{\partial}{\partial y_i}\langle \tau^*_{ij}|\overline{\mathbf{u}}^*(\mathbf{x})=\mathbf{V}\rangle + C_j \quad , \end{aligned}$$

in which the divergence of vector C_j is null. It is noted that the condition defined from the one-point probability density uses two-point probabilities. We again find here the problem of non-localness already encountered when the equivalency class is based on statistical moments. A more restrictive condition is:

$$\langle \tau_{ik}|\overline{\mathbf{u}}(\mathbf{x})=\mathbf{V}\rangle = \langle \tau^*_{ik}|\overline{\mathbf{u}}^*(\mathbf{x})=\mathbf{V}\rangle \quad . \tag{8.23}$$

8.1.4 Ideal LES and Optimal LES

An abstract subgrid model can be defined, which is in all senses ideal [175]. An LES using this model will exactly reproduce all single-time, multipoint statistics, and at the same time will exhibit minimum possible error in instantaneous dynamics. Such a LES will be referred to as *ideal LES*. Using the same notations as in Sect. 8.1.3, ideal LES is governed by the conditional average

$$\frac{d\overline{\mathbf{u}}^*}{dt} = \left\langle \overline{\frac{d\mathbf{u}}{dt}}\middle| \overline{\mathbf{u}}=\overline{\mathbf{u}}^* \right\rangle \quad , \tag{8.24}$$

where $\overline{\mathbf{u}}$ and $\overline{\mathbf{u}}^*$ are the solution of the exact LES equation and the LES equation with a subgrid model, respectively. It can be shown that such ideal LES is associated to the minimum mean-square error between the evolution of the LES field $\overline{\mathbf{u}}^*(t)$ and the exact solution $\overline{\mathbf{u}}(t)$, defined as an instantaneous pointwise measurement on $\partial\overline{\mathbf{u}}/\partial t$:

$$e_i(\mathbf{x}) = \frac{\partial \overline{u}^*_i}{\partial t} - \frac{\partial \overline{u}_i}{\partial t} \quad . \tag{8.25}$$

Equivalently, this error can be evaluated using the exact and the modeled subgrid forces, referred to as $\mathbf{M} = \nabla\cdot\tau$ and $\mathbf{m} = \nabla\cdot\tau^*$:

$$\mathbf{e}(\mathbf{x}) = \mathbf{M}(\mathbf{x}) - \mathbf{m}(\mathbf{x}) \quad . \tag{8.26}$$

The ideal subgrid model τ^* is then such that

$$\nabla\cdot\tau^* = \mathbf{m} = \langle \mathbf{M}|\overline{\mathbf{u}}=\overline{\mathbf{u}}^*\rangle \quad . \tag{8.27}$$

This model is written as an average over the real turbulent fields whose resolved scales match the current LES field, making it impossible to compute in practical applications. In order to approximate in an optimal sense this ideal model, several authors [2, 19, 62, 175] propose to formally approximate the conditional average by a stochastic estimation. These new models can be referred to as *optimal* or *nearly-optimal models*, leading to *optimal LES*. The estimation of the subgrid force is based on the convolution of an estimation kernel K_{ij} with velocity event data at N points $(\xi_1,...,\xi_N)$:

$$m_i(\mathbf{x}) = \int K_{ij}(\mathbf{x},\xi_1,...,\xi_N)E_j(\overline{\mathbf{u}}^*;\xi_1,...,\xi_N)d\xi_1...d\xi_N \quad , \tag{8.28}$$

where E_j is an event vector. Chosing

$$\mathbf{E}(\xi_1,...\xi_N) = (1, \overline{u}^*_i(\xi_1), \overline{u}^*_j(\xi_1)\overline{u}^*_k(\xi_2), ...) \quad , \tag{8.29}$$

we recover the expansion

$$\begin{aligned} m_i(\mathbf{x}) &= A_i(\mathbf{x}) + \int B_{ij}(\mathbf{x},\xi_1)\overline{u}^*_j(\xi_1)d\xi_1 \\ &+ \int C_{ijk}(\mathbf{x},\xi_1,\xi_2)\overline{u}^*_j(\xi_1)\overline{u}^*_k(\xi_2)d\xi_1 d\xi_2 \quad . \end{aligned} \tag{8.30}$$

The random mean square error between M_i and m_i is minimal when

$$\langle e_i(\mathbf{x})E_k(\eta_1,...,\eta_N)\rangle = 0 \quad , \tag{8.31}$$

yielding the following definition of the optimal kernel K_{ij}

$$\begin{aligned} \langle M_i(\mathbf{x})E_k(\eta_1,...,\eta_N)\rangle &= \int K_{ij}(\mathbf{x},\xi_1,...,\xi_N) \\ &\times \langle E_j(\xi_1,...,\xi_N)E_k(\eta_1,...,\eta_N)\rangle\, d\xi_1...d\xi_N \end{aligned} \tag{8.32}$$

The resulting optimal subgrid models have the property that the correlation of the parametrized subgrid force with any event data is the same as the correlation of the exact subgrid force with the same event data:

$$\langle m_i(\mathbf{x})E_j(\xi_1,...,\xi_N)\rangle = \langle M_i(\mathbf{x})E_j(\xi_1,...,\xi_N)\rangle \quad . \tag{8.33}$$

8.2 Correction Techniques

As relations (8.2) and (8.3) show, the statistical moments computed from the resolved field cannot be equal to those computed from the exact solution. In order to be able to compare these moments for validation purposes, or analyze the large-eddy simulation data, the error term has to be evaluated or eliminated. Several possible techniques are described in the following for doing this.

8.2.1 Filtering the Reference Data

The first solution is to apply the same filtering as was used for the scale separation to the reference solution [243]. Strict comparisons can be made with this technique, but it does not provide access to theoretically usable values, which makes it difficult to use the data generated by large-eddy simulation for predicting physical phenomena, because only filtered data are available. In order for physical analyses to be fully satisfactory, they should be made on complete data. However, analysis is possible when the quantities considered are independent or weakly dependent on the subgrid scales[3].

Moreover, this approach is difficult to apply when the effective filter is not known analytically, because the reference data cannot be filtered consistently. It may also be difficult to apply an analytical to experimental data, because in order to do so, access is needed to the data spectra that are to serve for validation or analysis. We see another source of problems cropping up here [256]: experimentally measured spectra are time spectra in the vast majority of cases, while the large-eddy simulation is based on space filtering. This may introduce essential differences, especially when the flow is highly anisotropic in space, as it is in the regions near a solid wall. Similar remarks can be made concerning the spatial filtering of data from a direct numerical simulation for a priori test purposes: applying a one- or two-dimensional filter can produce observations that are different from those that would be obtained with a three-dimensional filter.

8.2.2 Evaluation of Subgrid Scale Contribution

A second solution is to evaluate the error term and reconstruct from the filtered solution moments that are equal to those obtained from the full field.

Use of a De-filtering Technique. One way is to try to reconstruct the full field from the resolved one, and compute the statistical moments from the reconstructed field. In theory, this makes it possible to obtain exact results if the reconstruction itself is exact. This reconstruction operation can be interpreted as de-filtering, *i.e.* as an inversion of the scale separation operation. As

[3] As is generally the case for the mean velocity field. See the examples given in Chap. 11.

was seen in Chap. 2, this operation is possible if the filter is an analytical one not belonging to the class of Reynolds operators. In other cases, *i.e.* when the effective filter is unknown or possesses projector properties, this technique is not strictly applicable and we have to do with an approximate recontruction. We then use a technique based on the differential interpretation of the filter analogous to the one described in Sect. 6.1.1. With this interpretation, we can express the filtered field $\overline{\mathbf{u}}$ as:

$$\overline{\mathbf{u}} = \left(Id + \sum_{n=1}^{\infty} C_n \overline{\Delta}^{2n} \frac{\partial^{2n}}{\partial x^{2n}} \right) \mathbf{u} \quad . \tag{8.34}$$

This relation can be formally inverted writing:

$$\mathbf{u} = \left(Id + \sum_{n=1}^{\infty} C_n \overline{\Delta}^{2n} \frac{\partial^{2n}}{\partial x^{2n}} \right)^{-1} \overline{\mathbf{u}} \quad , \tag{8.35}$$

and, by interpreting the differential operator as an expansion function of the small parameter $\overline{\Delta}$, we get:

$$\mathbf{u} = \left(Id + \sum_{n=1}^{\infty} C'_n \overline{\Delta}^{2n} \frac{\partial^{2n}}{\partial x^{2n}} \right) \overline{\mathbf{u}} \quad . \tag{8.36}$$

By truncating the series at some arbitrary order, we thus get a recontruction method that is local in space and easy to use. The difficulty resides in the choice of the coefficients C_n, which describe the effective filter and can only be determined empirically.

Use of a Subgrid Model. Another means that is easier to use is to compute the contribution of the subgrid terms by means of the subgrid stresses representation generated by the model used in the simulation. This technique cannot evaluate all the error terms present in equations (8.2) and (8.3) and can only reduce the error committed in computing the second-order moments.

It does, however, offer the advantage of not requiring additional computations as in the recontruction technique.

It should be noted here that this technique seems to be appropriate when the models used are structural, representing the subgrid tensor, but that it is no longer justified when functional models are used because these ensure only an energy balance.

8.3 Practical Experience

Practice shows that nearly all authors make comparisons with reference data or analyze large-eddy simulation data with no processing of the data. The agreements observed with the reference data can then be explained by

the fact that the quantities being compared are essentially related to scale ranges contained in the resolved field. This is generally true of the first-order moments (*i.e.* the mean velocity field) and, in certain cases, of the second-order moments (the Reynolds stresses). This lack of processing prior to data analysis seems to be due mainly to the uncertainties in the techniques for evaluating the contributions of the subgrid scales and to the difficulty of ad hoc filtering of the reference data. Large-eddy simulation also allows a satisfactory prediction of the time frequency associated with large-scale repetitive phenomena (such as vortex shedding) and the first harmonics of this frequency for fine mesh.

9. Boundary Conditions

Like all the other approaches mentioned in the introduction, large-eddy simulation requires the setting of boundary conditions in order to fully determine the system and obtain a mathematically well-posed problem. This chapter is devoted to questions of determining suitable boundary conditions for large-eddy simulation computations. The first section is a discussion of general order, the second is devoted to the representation of solid walls, and the third discusses methods used for representing an unsteady upstream flow.

9.1 General Problem

9.1.1 Mathematical Aspects

The discussions so far clearly show that the constitutive equations of large-eddy simulation can be of a degree different from that of the original Navier–Stokes equations. This is trivially verified by considering the differential interpretation of the filters: the resolved equations are obtained by applying a differential operator of arbitrarily high order to the basic equations. Moreover, it has been seen that certain subgrid models generate high-order derivatives of the velocity field.

This change of degree in the resolved equations raises the problem of determining the associated boundary conditions, because those associated with the equations governing the evolution of the exact solution can no longer be used in theory for obtaining a mathematically well-posed problem [108, 332]. This problem is generally not considered, arguing the fact that the higher-order terms appear only in the form of $O(\overline{\Delta}^p), p \geq 1$ perturbations of the Navier–Stokes equations and the same boundary conditions are used both for the large-eddy simulation and for direct numerical simulation of the Navier–Stokes equations. Moreover, when the effective filter is unknown, it is no longer possible to derive suitable boundary conditions strictly, which also leads to the use of the boundary conditions of the basic problem.

9.1.2 Physical Aspects

The boundary conditions, along with the similarity parameters of the equations, specify the flow to determine the solution. These conditions represent

the whole fluid domain beyond the computational domain. To specify the solution completely, these conditions must apply to all of its scales, *i.e.* to all the space-time modes it comprises.

So in order to characterize a particular flow, the amount of information in the boundary conditions is a function of the number of degrees of freedom of the boundary condition system. This poses the problem of representing a particular solution, in order to be able to reproduce it numerically. We have a new modeling problem here, which is that of modeling the physical test configuration.

This difficulty is increased for the large-eddy simulation and direct numerical simulation, because these simulations contain a large number of degrees of freedom and require a precise space-time deterministic representation of the solution at the computational domain boundaries.

Two special cases will be discussed in the following sections: that of representing solid walls and that of representing a turbulent inflow. The problem of the outflow conditions, which is not specific to the large-eddy simulation technique, will not be addressed[1].

9.2 Solid Walls

9.2.1 Statement of the Problem

Specific Features of the Near-Wall Region. The structure of the boundary layer flow has certain characteristics that call for special treatment in the framework of large-eddy simulation. In this section, we describe the elements characteristic of the boundary layer dynamics and kinematics, which shows up the difference with an isotropic homogeneous turbulence. For a detailed description, the reader may refer to the work of Cousteix [68].

Definitions. Here we adopt the ideal framework of a flat-plate, turbulent boundary layer, without pressure gradient. The external flow is in the (Ox) direction and the (Oz) direction is normal to the wall. The external velocity is denoted U_e. In the following, the Cartesian coordinate system will be denoted either (x, y, z) or (x_1, x_2, x_3), for convenience. Similarly, the velocity vector is denoted (u, v, w) or (u_1, u_2, u_3).

We first recall a few definitions. The boundary layer thickness δ is defined as the distance from the plate beyond which the fluid becomes irrotational, and thus where the fluid velocity is equal to the external velocity.

The wall shear stress τ_p is defined as:

$$\tau_p = \sqrt{\tau_{p,13}^2 + \tau_{p,23}^2} \quad , \tag{9.1}$$

[1] See [69] for a specific study of exit boundary conditions for the plane channel flow case.

in which $\tau_{p,ij} = \nu \overline{S}_{ij}(x, y, 0)$. The friction velocity u_τ is defined as:

$$u_\tau = \sqrt{\tau_p} \quad . \tag{9.2}$$

In the case of the canonical boundary layer, we get:

$$u_\tau = \sqrt{\nu \frac{\partial u_1}{\partial z}(x, y, 0)} \quad . \tag{9.3}$$

We define the Reynolds number Re_τ by:

$$Re_\tau = \frac{\delta u_\tau}{\nu} \quad . \tag{9.4}$$

The reduced velocity $\mathbf{u}^+$, expressed in wall units, is defined as:

$$\mathbf{u}^+ = \mathbf{u}/u_\tau \quad . \tag{9.5}$$

The wall coordinates (x^+, y^+, z^+) are obtained by the transformation:

$$(x^+, y^+, z^+) = (x/l_\tau, y/l_\tau, z/l_\tau) \quad , \tag{9.6}$$

where the viscous length l_τ is defined as $l_\tau = \nu/u_\tau$.

Statistical Description of the Canonical Boundary Layer. The boundary layer is divided into two parts: the inner region $(0 \leq z < 0.2\delta)$ and the outer region $(0.2\delta \leq z)$. This decomposition is illustrated in Fig. 9.1. In the inner region, the dynamics is dominated by the viscous effects. In the outer region, it is controlled by the turbulence. Each of these regions is split into several layers, corresponding to different types of dynamics.

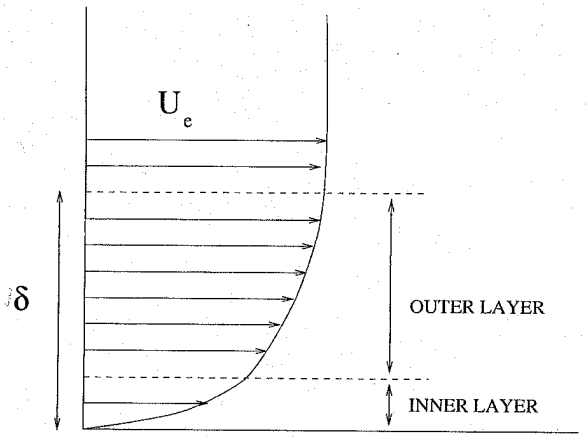

Fig. 9.1. Mean longitudinal velocity profile for the canonical turbulent boundary layer, and its decompostion into inner and outer regions.

In the case of the canonical boundary layer, we have three layers in the inner region in which the mean longitudinal velocity profile follows special laws. The positions of these layers are referenced in the reduced coordinate system, because the dynamics of the inner region is dominated by the wall effects and l_τ is the pertinent length scale for describing the dynamics. The characteristic velocity scale is the friction velocity. These three layers are the:

– Viscous sublayer: $z^+ \leq 5$, in which

$$\langle u_1^+(z^+)\rangle = z^+ \quad . \tag{9.7}$$

– Buffer layer: $5 < z^+ \leq 30$, where

$$\langle u_1^+(z^+)\rangle \simeq 5 \ln z^+ - 3.05 \quad . \tag{9.8}$$

– Prandtl or logarithmic inertial layer: $30 < z^+; z/\delta \ll 1$, for which

$$\langle u_1^+(z^+)\rangle \simeq \frac{1}{\kappa} \ln z^+ + 5,5 \pm 0,1, \quad \kappa = 0,4 \quad . \tag{9.9}$$

The outer region includes the end of the logarithmic inertial region and the wake region. In this zone, the characteristic length is no longer l_τ but rather the thickness δ. The characteristic velocity scale remains unchanged, though. The average velocity profiles are described by:

– For the logarithmic inertial region:

$$\frac{\langle u_1(z)\rangle}{u_\tau} = A \ln \frac{z u_\tau}{\nu} + B \quad , \tag{9.10}$$

where A and B are constants;

– For the wake region:

$$\frac{\langle u_1(z)\rangle}{u_\tau} = A \ln \frac{z u_\tau}{\nu} + B + \frac{\Pi}{\kappa} W\left(\frac{z}{\delta}\right) \quad , \tag{9.11}$$

where A, B and Π are constants and W the wake function defined by Clauser as:

$$W(x) = 2 \sin^2(\pi x/2) \quad . \tag{9.12}$$

Concerning the Dynamics of the Canonical Boundary Layer. Experimental and numerical studies have identified dynamic processes within the boundary layer. We will summarize here the main elements of the boundary layer dynamics that originate the turbulence in the near-wall region.

Observations show that the flow is highly agitated very close to the wall, consisting of pockets of fast and slow fluid that organize in ribbons parallel to the outer velocity (streaks). The low-velocity pockets migrate slowly outward in the boundary layer (ejection) and are subject to an inst[illegible]ity that makes

them explode near the outer edge of the inner region. This burst is followed by an arrival of fast fluid toward the wall, sweeping the near-wall region almost parallel to it. These highly intermittent events in time and space induce strong variation in the unsteady Reynolds stresses and originate a very large part of the production and dissipation of the turbulent kinetic energy. These variations produce fluctuations in the subgrid dissipation that can reach 300 % of the average value and can make it change sign. Analyses of direct numerical simulations [130, 156, 196, 270] indicate that a very intense small scale dissipation in the buffer region is correlated with the presence of sheared layers that form the interfaces between the fluid pockets of different velocities. These mechanisms are highly anisotropic. Their characteristic scales in the longitudinal and transverse directions λ_x and λ_y, respectively, are such that $\lambda_x^+ \approx 200 - 1000$ and $\lambda_y^+ \approx 100$. The maximum turbulent energy production is observed at $z^+ \approx 15$. This energy production at small scales gives rise to a high backward energy cascade and associated with the sweeping type events. The forward cascade, for its part, is associated with the ejections.

In the outer regions of the boundary layer where the viscous effects no longer dominate the dynamics, the energy cascade mechanism is predominant. Both cascade mechanisms are associated preferentially with the ejections.

Härtel and his coworkers [128–130] give a more precise analysis of the subgrid transfer in the boundary layer by introducing a new splitting[2] of the subgrid dissipation ε

$$\varepsilon = -\tau_{ij}\overline{S}_{ij} = \varepsilon^{\mathrm{MS}} + \varepsilon^{\mathrm{FS}} \quad , \tag{9.13}$$

with

$$\varepsilon^{\mathrm{MS}} = -\langle\tau_{ij}\rangle\langle\overline{S}_{ij}\rangle \quad , \tag{9.14}$$

$$\varepsilon^{\mathrm{FS}} = -\langle(\tau_{ij} - \langle\tau_{ij}\rangle)(\overline{S}_{ij} - \langle\overline{S}_{ij}\rangle)\rangle \quad . \tag{9.15}$$

The $\varepsilon^{\mathrm{MS}}$ is related to the mean strain, and accounts for an enhancement of subgrid kinetic energy in the presence of mean-flow gradients. The second term, which is linked to the strain fluctuations, represents the redistribution of energy without affecting the mean flow directly.

A priori tests [128–130] perfomed using plane channel flow and circular pipe data reveal that the net effect of the coupling is a forward energy transfer, and;

– The mean strain part is always associated to a net forward kinetic energy cascade.

[2] It differs from the splitt[illegible] proposed by Shao (see Sect. 6.5.1).

– The fluctuating strain part results in a net backward kinetic cascade in a zone located in the buffer layer, with a maximun near $z^+ = 15$. This net backward cascade is correlated to the presence of coherent events associated to turbulence production.

Kinematics of the Turbulent Boundary Layer. The processes described above are associated with existence of coherent structures [278].

The buffer layer is dominated by isolated quasi-longitudinal structures that form an average angle with the wall of 5^0 at $z^+ = 15$ and 15^0 at $z^+ = 30$. Their mean diameter increases with their distance from the wall[3].

The logarithmic inertial region belongs both to the inner and outer regions, and thus contains characteristic space scales, which is compatible with the existence of two different types of structures. The dynamics is governed by quasi-longitudinal and arch structures. The quasi-longitudinal structures can be connected to transverse structures and form an angle with the surface that varies from 15^0 to 30^0. The span of the arch structures is of the order of the width of the slow-fluid pockets at the bottom of the layer, and increases linearly with the distance from the wall. The relative number of quasi-longitudinal structures decreases with the distance from the wall, until it cancels out at the beginning of the wake region.

The wake region is populated with arch structures forming an angle of 45^0 with the wall. Their x and y spacing is of the order of δ.

Resolving or Modeling. The description we have just made of the boundary layer flow structure clearly shows the problem of applying the large-eddy simulation technique in this case. Firstly, the mechanisms originating the turbulence, *i.e.* the flow driving mechanisms, are associated with fixed characteristic length scales on the average. Also, this turbulence production is associated with an backward energy cascade, which is largely dominant over the cascade mechanism in certain regions of the boundary layer. These two factors make it so that the subgrid models presented in the previous chapters become inoperative because they no longer permit a reduction of the number of degrees of freedom while ensuring at the same time a fine representation of the flow driving mechanisms. There are then two possible approaches [244]:

– Resolving the near-wall dynamics directly. Since the production mechanisms escape the usual subgrid modeling, if we want to take them into account, we have to use a sufficiently fine resolution to capture them. This is illustrated in Fig. 9.2. The solid wall is then represented by a no-slip condition: the fluid velocity is set equal to that of the solid wall. This equality implicitly relies on the hypothesis that the mean free path of the molecules is small compared with the characteristic scales of the

[3] It should be noted that contradictory observations can be found. Lamballais [176] observes that the most probable angle of the vorticity (projected on a plane perpendicular to the wall) is close to 90^0 for $5 < z^+ < 25$, which goes against the model of longitudinal vortices at the wall.

motion, and that these scales are large compared with the distance of the first grid point from the wall. In practice, this is done by placing the first point in the zone ($0 \leq z^+ \leq 1$). To represent the turbulence production mechanisms completely, Schumann [300] recommends a spatial resolution such that $\overline{\Delta}_1^+ < 10, \overline{\Delta}_2^+ < 5$ and $\overline{\Delta}_3^+ < 2$. Also, Zang [365] indicates that the minimum resolution for capturing the existence of these mechanisms is $\overline{\Delta}_1^+ < 80, \overline{\Delta}_2^+ < 30$ and that three grid points should be located in the $z^+ \leq 10$ zone. Zahrai *et al.* [364] indicate that $\overline{\Delta}_1^+ \simeq 100, \overline{\Delta}_2^+ = 12$ should be used as an upper limit if a second-order accurate numerical method is used. These values are given here only for reference, since larger values can also be found in the literature. For example, Piomelli [264] uses $\overline{\Delta}_1^+ = 244$ for a plane channel flow. This implies using a large number of degrees of freedom. Chapman [53] estimates that representing the dynamics of the inner region, which contributes about one percent to the thickness of the full boundary layer, requires $O(Re^{1.8})$ degrees of freedom, while only $O(Re^{0.4})$ are needed to represent the outer zone. This corresponds to $\overline{\Delta}_1^+ \simeq 100, \overline{\Delta}_2^+ \simeq 20$ and $\overline{\Delta}_3^+ < 2$. Considering that non-isotropic modes must be directly resolved, Bagget *et al.* [10] show that the number of degrees of freedom of the solution (in space) scales as Re_τ^2.

– Modeling the near-wall dynamics. To reduce the number degrees of freedom and especially avoid having to represent the inner region, we use a model for representing the dynamics of the zone included between the first point of the grid and the solid wall (see Fig. 9.2). This is a special subgrid model called the wall model. Since the distance from the first grid point to the wall is greater than the characteristic scales of the modes existing in the modeled region, the no-slip condition can no longer be used. The boundary condition will apply to the values of the velocity components and/or their gradients, which will be provided by the wall model. This approach makes

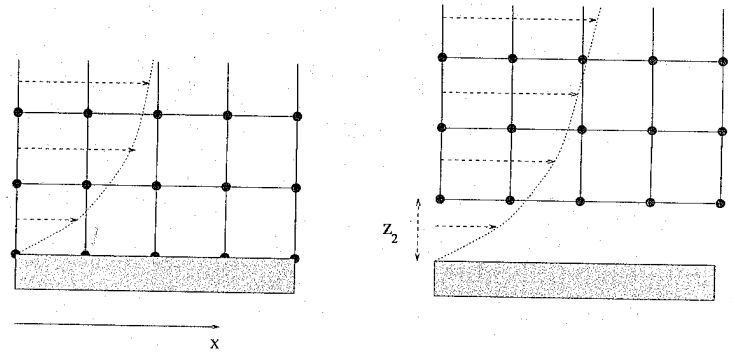

Fig. 9.2. Treatment of the near-wall region. No-slip condition type grid (*left*) and wall model type grid (*right*).

it possible to place the first point in the logarithmic layer (in practice, $20 \leq z^+ \leq 200$). The main advantage of this approach is that the number of degrees of freedom in the simulation can be reduced greatly; but since a part of the dynamics is modeled, it constitutes an additional source of error.

9.2.2 A Few Wall Models

In the following, we present the main wall models used for large-eddy simulation. These models all represent an impermeable wall.

Deardorff Model. In the framework of a plane channel simulation with infinite Reynolds number, Deardorff [76] proposes using the following conditions for representing the solid walls:

$$\frac{\partial^2 \overline{u}_1}{\partial z^2} = -\frac{1}{\kappa (z_2/2)^2} + \frac{\partial^2 \overline{u}_1}{\partial y^2} \quad , \tag{9.16}$$

$$\overline{u}_3 = 0 \quad , \tag{9.17}$$

$$\frac{\partial^2 \overline{u}_2}{\partial z^2} = \frac{\partial^2 \overline{u}_2}{\partial x^2} \quad , \tag{9.18}$$

where z_2 is the distance from the first point to the wall and $\kappa = 0.4$ the Von Karman constant. The first condition assumes that the average velocity profile verifies the logarithmic law and that the second derivatives of the fluctuation $\mathbf{u}'' = \overline{\mathbf{u}} - \langle \mathbf{u} \rangle$ in the y and z directions are equal. The impermeability condition (9.17) implies that the resolved stresses $\overline{u}_1\overline{u}_3$, $\overline{u}_3\overline{u}_3$ and $\overline{u}_2\overline{u}_3$ are zero at the wall. This model suffers from a number of defects. Namely, it shows no dependency as a function of the Reynolds number, and assumes that the shear-stress near the wall is entirely due to the subgrid scales.

Schumann Model. Schumann [298] has developed a wall model for performing a plane channel flow simulation at a finite Reynolds number. As he uses a staggered grid, only the values of the velocity component normal to the wall and of two stress tensor components have to be specified. The boundary conditions proposed are:

$$\tau_{\mathrm{p},13}(x,y) = \left(\frac{\overline{u}_1(x,y,z_2)}{\langle \overline{u}_1(x,y,z_2) \rangle} \right) \langle \tau_\mathrm{p} \rangle \quad , \tag{9.19}$$

$$\overline{u}_3 = 0 \quad , \tag{9.20}$$

$$\tau_{\mathrm{p},23}(x,y) = \frac{2}{Re_\tau} \left(\frac{\overline{u}_3(x,y,z_2)}{z_2} \right) \quad , \tag{9.21}$$

where $\langle\rangle$ designates a statistical average (associated here with a time average), and z_2 the distance of the first point to the wall. The condition (9.19) is equivalent to adopting the hypothesis that the longitudinal velocity component at position z_2 is in phase with the instantaneous wall shear stress. The mean velocity profile can be obtained by the logarithmic law, and the mean wall shear stress $\langle \tau_\mathrm{p} \rangle$, is, for a plane channel flow, equal to the driving pressure gradient. This wall model therefore implies that the mean velocity field verifies the logarithmic law and can be applied only to plane channel flows for which the value of the driving pressure gradient is known *a priori*. The second condition is the impermeability condition, and the third corresponds to a no-slip condition for the transverse velocity component $\overline{u}_2$.

Grötzbach Model. Grötzbach [127] proposes extending the Schumann model to avoid having to know the mean wall shear stress *a priori*. To do this, the statistical average $\langle\rangle$ is now associated with a mean on the plane parallel to the solid wall located at $z = z_2$. Knowing $\langle \overline{u}_1(z_2) \rangle$, the mean wall shear stress $\langle \tau_\mathrm{p} \rangle$ is computed from the logarithmic law. The friction velocity is computed from equation (9.9), *i.e.*:

$$u_1^+(z_2) = \langle \overline{u}_1(z_2) \rangle / u_\tau = \frac{1}{\kappa} \log(z_2 u_\tau / \nu) + 5.5 \pm 0.1 \quad , \tag{9.22}$$

then $\langle \tau_\mathrm{p} \rangle$, by relation (9.2). This model is more general than Schumann's, but it still requires that the mean velocity profile verify the logarithmic law. Another advantage of Grötzbach's modification is that it allows variations of the total mass flux through the channel.

Shifted Correlations Model. Another modification of Schumann's model can be made on the basis of the experimental works of Rajagopalan and Antonia [276]. These two authors observed that the correlation between the wall shear stress and the velocity increases when we consider a relaxation time between these two evaluations. This phenomenon can be explained by the existence of coherent inclined structures that are responsible for the velocity fluctuations and the wall shear stress. The modified model is expressed:

$$\tau_{\mathrm{p},13}(x,y) = \left(\frac{\overline{u}_1(x+\Delta_\mathrm{s},y,z_2)}{\langle \overline{u}_1(x,y,z_2) \rangle} \right) \langle \tau_\mathrm{p} \rangle \quad , \tag{9.23}$$

$$\overline{u}_3 = 0 \quad , \tag{9.24}$$

$$\tau_{\mathrm{p},23}(x,y) = \left(\frac{\overline{u}_2(x+\Delta_\mathrm{s},y,z_2)}{\langle \overline{u}_1(x,y,z_2) \rangle} \right) \langle \tau_\mathrm{p} \rangle \quad , \tag{9.25}$$

where the value of the length Δ_s is given by the approximate relation:

$$\Delta_\mathrm{s} = \begin{cases} (1-z_2)\cot(8^0) & \text{for } 30 \leq z_2^+ \leq 50-60 \\ (1-z_2)\cot(13^0) & \text{for } z_2^+ \geq 60 \end{cases} . \tag{9.26}$$

Rough Wall Model. Mason and Callen [222] propose a wall model including the roughness effects. The three velocity components are specified at the first computation point by the relations:

$$\overline{u}_1(x,y,z_2) = \cos\theta \left(\frac{u_\tau(x,y)}{\kappa}\right) \ln(1+z_2/z_0) \quad , \tag{9.27}$$

$$\overline{u}_2(x,y,z_2) = \sin\theta \left(\frac{u_\tau(x,y)}{\kappa}\right) \ln(1+z_2/z_0) \quad , \tag{9.28}$$

$$\overline{u}_3(x,y,z_2) = 0 \quad , \tag{9.29}$$

where z_0 is the roughness thickness of the wall and angle θ is given by the relation $\theta = \arctan(\overline{u}_2(z_2)/\overline{u}_1(z_2))$. These equations can be used to compute the friction velocity u_τ as a function of the instantaneous velocity components $\overline{u}_1$ and $\overline{u}_2$. The instantaneous surface friction vector $\mathbf{u}_\tau^2$ is then evaluated as:

$$\mathbf{u}_\tau^2 = \frac{1}{M}|\mathbf{u}_\parallel|\mathbf{u}_\parallel \quad , \tag{9.30}$$

where $\mathbf{u}_\parallel$ is the vector $(\overline{u}_1(x,y,z_2), \overline{u}_2(x,y,z_2), 0)$ and

$$\frac{1}{M} = \frac{1}{\kappa^2}\ln^2(1+z_2/z_0) \quad .$$

The instantaneous wall shear stresses in the x and y directions are then evaluated respectively as $|u_\tau^2|\cos\theta$ and $|u_\tau^2|\sin\theta$. This model is based on the hypothesis that the logarithmic distribution is verified locally and instantaneously by the velocity field. This becomes even truer as the grid is coarsened, and the large scale velocity approaches the mean velocity.

Ejection Model. Another wall model is proposed by Piomelli, Ferziger, Moin, and Kim [267] in consideration of the fact that the fast fluid motions toward or away from the wall greatly modify the wall shear stress. The impact of fast fluid pockets on the wall causes the longitudinal and lateral vortex lines to stretch out, increasing the velocity fluctuations near the wall. The ejection of fast fluid masses induces the inverse effect, *i.e.* reduces the wall shear stress. To represent the correlation between the wall shear stress and the velocity fluctuations, the authors propose the following conditions:

$$\tau_{p,13}(x,y) = \langle\tau_p\rangle - Cu_\tau\overline{u}_3(x+\Delta_s,y,z_2) \quad , \tag{9.31}$$

$$\tau_{p,23}(x,y) = \left(\frac{\langle\tau_p\rangle}{\langle\overline{u}_1(z_2)\rangle}\right)\overline{u}_2(x+\Delta_s,y,z_2) \quad , \tag{9.32}$$

$$\overline{u}_3(x,y) = 0 \quad , \tag{9.33}$$

where C is a constant of the order of unity, $\langle\tau_p\rangle$ is computed from the logarithmic law as it is for the Grötzbach model, and Δ_s is computed by the relation (9.26).

Simplified Boundary Layer Model. Balaras *et al.* [11] and Cabot [38, 39] propose more sophisticated models based on a system of simplified equations derived from the boundary layer equations. Between the first grid point and the solid wall, a secondary grid is included on which the following system is resolved:

$$\frac{\partial\overline{u}_i}{\partial t} + \frac{\partial}{\partial x_1}(\overline{u}_1\overline{u}_i) + \frac{\partial}{\partial x_n}(\overline{u}_n\overline{u}_i) = -\frac{\partial\overline{p}}{\partial x_i} + \frac{\partial}{\partial x_n}\left((\nu+\nu_{sgs})\frac{\partial\overline{u}_i}{\partial x_n}\right), \quad i \neq n, \tag{9.34}$$

where n is the index corresponding to the direction normal to the wall.

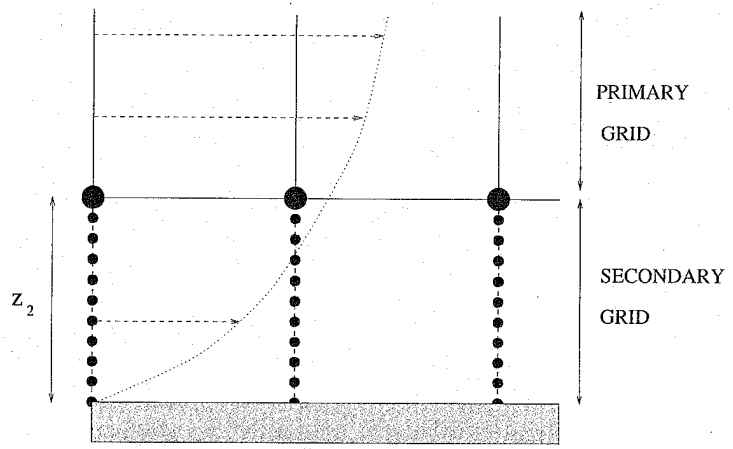

Fig. 9.3. Representation of the primary and secondary grids.

This approach is equivalent to assuming that the inner zone of the boundary layer behaves like a Stokes layer forced by the outer flow. Balaras *et al.* propose computing the viscosity ν_{sgs} by the simplified mixing length model:

$$\nu_{sgs} = (\kappa z)^2 D_b(z)|\overline{S}| \quad , \tag{9.35}$$

where z is the distance to the wall, κ the Von Karman constant, and $D_b(z)$ the damping function:

$$D_b(z) = \left(1 - \exp(-(z^+/A^+)^3)\right) \quad , \tag{9.36}$$

with $A^+ = 25$. Cabot proposes the alternate definition:

$$\nu_{sgs} = \kappa u_s z D_C^2(z) \quad , \tag{9.37}$$

in which

$$D_C(z) = (1 - \exp(-z u_d / A\nu)) \quad , \tag{9.38}$$

where u_s and u_d are velocity scales to be determined, and $A = 19$. The simplest choice is $u_s = u_d = u_\tau$.

When this system is solved, it generates longitudinal and transverse velocity component distributions at each time step, so that the value of the wall shear stress can be calculated for solving the Navier–Stokes equations on the main grid. The pressure gradient appears as a source term, because this is obtained using the relation $\partial \overline{p}/\partial x_n = 0$.

The vertical velocity component is obtained from the continuity equation:

$$\overline{u}_3(x,y,z_2) = -\int_0^{z_2} \left(\frac{\partial \overline{u}_1}{\partial x}(x,y,\xi) + \frac{\partial \overline{u}_2}{\partial y}(x,y,\xi) \right) d\xi \quad . \tag{9.39}$$

The boundary conditions applied to the secondary system are:

- On the solid wall: no-slip condition;
- On the upper boundary: Dirichlet condition obtained from the value of the velocity field computed on the first cell of the main grid.

Model of Murakami *et al.* Murakami, Mochida, and Hibi [255] developed a wall model for dealing with the case of the separated flow around a cube mounted on a flat plate. This model is based on power-law solutions for the mean longitudinal velocity profile of the form:

$$\frac{\langle \overline{u}_1(z) \rangle}{U_e} \simeq \left(\frac{z}{\delta} \right)^n \quad . \tag{9.40}$$

The authors recommend using $n = 1/4$ on the flat plate and $n = 1/2$ on the cube surface. When the first grid point is located close enough to the wall, the following boundary conditions are used:

$$\overline{u}_i(x,y) = \left(\frac{z_2}{z_2 + \Delta z} \right)^n \overline{u}_i(x,y,z_2 + \Delta z), \quad i = 1,2 \quad , \tag{9.41}$$

$$\overline{u}_3(x,y) = 0 \quad , \tag{9.42}$$

where Δz is the size of the first cell. The first equation is obtained by assuming that the instantaneous profile also verifies the law (9.40). When the distance of the first point from the wall is too large for the convection effects to be neglected, the relation (9.42) is replaced by:

$$\frac{\partial \overline{u}_3}{\partial z} = 0 \quad . \tag{9.43}$$

Werner and Wengle Model. In order to be able to process the same flow as Murakami et al., Werner and Wengle [345] propose a wall model based on the following hypotheses:

- The instantaneous tangential velocity components at the wall $u_2(x,y,z_2)$ and $u_3(x,y,z_2)$ are in phase with the associated instantaneous wall shear stresses.
- The instantaneous velocity profile follows the law:

$$u^+(z) = \begin{cases} z^+ & \text{if } z^+ \leq 11.81 \\ A(z^+)^B & \text{otherwise} \end{cases} \quad , \tag{9.44}$$

in which $A = 8.3$ and $B = 1/7$.

The values of the tangential velocity components can be related to the corresponding values of the wall shear stress components by integrating the velocity profile (9.44) over the distance separating the first cell from the wall. This allows a direct analytical evaluation of the wall shear stress components from the velocity field:

- If $|\overline{u}_i(x,y,z_2)| \leq \frac{\nu}{2z_m} A^{2/(1-B)}$, then:

$$|\tau_{p,i3}(x,y)| = \frac{2\nu |\overline{u}_i(x,y,z_2)|}{z_2} \quad , \tag{9.45}$$

- and otherwise:

$$|\tau_{p,i3}(x,y)| = \left[\frac{1-B}{2} A^{\frac{1+B}{1-B}} \left(\frac{\nu}{z_2} \right)^{1+B} + \frac{1+B}{A} \left(\frac{\nu}{z_2} \right)^B |\overline{u}_i(x,y,z_2)| \right]^{\frac{2}{1+B}} , \tag{9.46}$$

where z_m is the distance to the wall that corresponds to $z^+ = 11.81$. This model has the advantage of not using average statistical values of the velocity and/or wall shear stresses, which makes it easier to use for inhomogeneous configurations. An impermeability condition is used to specify the value of the velocity component normal to the wall:

$$\overline{u}_3 = 0 \quad . \tag{9.47}$$

9.3 Case of the Inflow Conditions

9.3.1 Required Conditions

Representing the flow upstream of the computational domain also raises difficulties when this flow is not fully known deterministically, because the lack of information introduces sources of error. This situation is encountered for transitional or turbulent unsteady flows that generally contain a very large number of space-time modes. Several boundary condition generation techniques are used for furnishing information about all the modes it contains to the large-eddy simul n computation.

9.3.2 Inflow Condition Generation Techniques

Stochastic Recontruction from a Statistical One-Point Description. When the freestream flow is described statistically (usually the mean velocity field and the one-point second-order moments), the deterministic information is irremediably lost. The solution is then to generate instantaneous realizations that are statistically equivalent to the freestream flow, *i.e.* that have the same statistical moments.

In practice, this is done by superimposing random noises having the same statistical moments as the velocity fluctuations, on the mean statistical profile. This is expressed:

$$\mathbf{u}(x_0,t) = U(x_0) + \mathbf{u}'(x_0,t) \quad , \tag{9.48}$$

where the mean field U is given by experiment, theory, or steady computations, and where the fluctuation $\mathbf{u}'$ is generated from random numbers. This technique makes it possible to remain in keeping with the energy level of the fluctuations as well as the one-point correlations (Reynolds stresses) in the directions of statistical homogeneity of the solution, but does not reproduce the two-point (and two-time) space-time correlations [183, 219, 246]. The information concerning the phase is lost, which can have very harmful consequences when the consistency of the fluctuations is important, as is the case for shear flows (mixing layer, jet, boundary layer, and so forth). That is, the computations performed show the existence of a region in the computational domain in which the solution regenerates the space-time consistency specific to the Navier–Stokes equations [63]. The solution is not usable in this region, which can cover a large part[4] of the computational domain, and this entails an excess cost for the simulation. Also, it appears that this technique prevents controlling precisely the dynamics of the solution, in the sense that it is very difficult to reproduce a particular solution for a given geometry.

Deterministic Computation. One way of minimizing the errors is to perform a simulation of the freestream flow [103, 339], called a precursor simulation, with a degree of resolution equivalent to that desired for the final simulation. This technique almost completely eliminates the errors encountered before, and offers very good results. On the other hand, it is hardly practical in the general case because it requires reproducing the entire history of the flow which, for complex configurations, implies very high computation costs. Another problem stemming from this approach is that of causality: since the precursor is computed separately, no feedback of information from the second simulation is possible. This is a one-way coupling between two simulations that can become problematic when a signal (acoustic wave, for example) is emitted by the second.

[4] Numerical experiments show that this region can cover more than 50 % of the total number of simulation points.

Lund *et al.* [206] developed a variant of this approach for boundary layers, in which the information at the entrance plane is produced from that contained in the computation. There is no longer any need to use a precursor.

Semi-deterministic Recontruction. Bonnet *et al.* [26] propose an intermediate approach between the two previous ones, to recover the two-point correlations of the inflow with no preliminary computations. The signal at the inflow plane is decomposed in the form:

$$\mathbf{u}(x_0,t) = U(x_0) + U_c(x_0,t) + \mathbf{u}'(x_0,t) \quad , \tag{9.49}$$

where $U(x_0)$ is the mean field, $U_c(x_0,t)$ the coherent part of turbulent fluctuations, and $\mathbf{u}'(x_0,t)$ the random part of these fluctuations. In practice, this last part is generated by means of random variables and the coherent part is provided by a dynamical system with a low number of degrees of freedom (like the POD, as seen in the Introduction), or by linear stochastic estimation, which gives access to the two-point correlations.

10. Implementation

This chapter is devoted to the practical details of implementing the large-eddy simulation technique. The following are described:

- Cutoff length computation procedures for an arbitrary grid;
- Discrete test filters used for computing the subgrid models or in a pre-filtering technique;
- Computing the Structure Function model on an arbitrary grid.

10.1 Filter Identification. Computing the Cutoff Length

The theoretical developments of the previous chapters have identified several filters of different origins:

1. Analytical filter, represented by a convolution product. This is the filter used for expressing the filtered Navier–Stokes equations.
2. Filter associated with a given computational grid. No frequency higher than the Nyquist frequency associated with this grid can be represented in the simulation.
3. Filter induced by the numerical scheme. The error committed by approximating the partial derivative operators by discrete operators modifies the computed solution mainly the high-frequency modes.
4. Filter associated with the subgrid model, which acts like a control process on the computed solution.

The computed solution is the result of these four filtering processes constituting the simulation effective filter. When performing a computation, then, the question arises as to what the effective filter is, that governs the dynamics of the numerical solution, in order to determine the characteristic cutoff length. This length is needed for several reasons.

- In order to be able to determine the physically and numerically well-resolved scale beyond which we will be able to start using the results for analysis.
- In order to be able to use the subgrid models like the subgrid viscosity models that use this c f length explicitly.

While the filters mentioned above are definable theoretically, they are almost never quantifiable in practice. This is particularly true of the filter associated with the numerical schemes used. In face of this uncertainty, practitioners have one of two positions they can adopt:

1. Arrange it so that one of the four filters becomes predominant over the others and is controllable. The effective filter is then known. This is done in practice by using a pre-filtering technique.
   Normally, this is done by ensuring the dominance of the analytical filter, which allows us strict control of the form of the filter and of its cutoff length, so that we can get the most out of the theoretical analyses and thereby minimize the relative uncertainty concerning the nature of the computed solution. In the numerical solution, an analytical filter is then applied here to each computed term. In order for this filter to be dominant, its cutoff length must be large compared with the other three. Theoretically, this analytical filter should be a convolution filter which, to keep the computation cost within acceptable limits, can only be applied for simulations performed in the spectral space[1]. For the simulations performed in the physical space, discrete filters are used, based on weighted averages with compact support. These operators enter into the category of explicit discrete filters, which are discussed in the following section.
   We may point out here that the methods based on implicit diffusion with no physical subgrid model can be re-interpreted as a pre-filtering method, in which case it is the numerical filter that is dominant. We can see the major problem of this approach looming here: the filter associated with a numerical method is often unknown and is highly dependent on the simulation parameters (grid, boundary conditions, regularity of the solution, and so forth). This approach is therefore an empirical one that offers little in the way of an a priori guarantee of the quality of the results. It does, however, have the advantage of minimizing the computation costs because we are then limited to solving the Navier–Stokes equations without implanting any subgrid model or explicit discrete filter.
2. Considering that the effective filter is associated with the computational grid. This position, which can be qualified as minimalist on the theoretical level, is based on the intuitive idea that the frequency cutoff associated with a fixed computational grid is unavoidable and that this filter is therefore still present. The problem then consists in determining the cutoff length associated with the grid at each point, in order to be able to use the subgrid models.
   In the case of a Cartesian grid, we take the filtering cell itself as Cartesian. The cutoff length $\overline{\Delta}$ is evaluated locally as follows:
   - For uniform grid, the characteristic filtering length in each direction is taken equal to the mesh size in this same direction:

[1] The convolution product is then reduced to a simple product of two arrays.

$$\overline{\Delta}_i = \Delta x_i \quad . \tag{10.1}$$

   The cutoff length is then evaluated by means of one of the formulas presented in Chap. 5.
   - For a variable mesh size grid, the cutoff length in the ith direction of the grid point of index l is computed as:

$$\overline{\Delta}_i|_l = (x_i|_{l+1} - x_i|_{l-1})/2 \quad . \tag{10.2}$$

   The cutoff length is then computed locally according to the results of Chap. 5.

In the case of a curvilinear structured grid, two options are possible depending on the way the partial derivative operators are constructed:

- If the method is of the finite volume type in the sense of Vinokur [335], *i.e.* if the control volumes are defined directly on the grid in the physical space and their topologies are described by the volume of the control cells, of the surface area, and of the normal to each of their facets, the filter cutoff length can be computed at each point either by taking it equal to the cube root of the control volume to which the point considered belongs, or by using what Bardina *et al.* propose (see Sect. 5.2.2).
- If the method is of the finite differences type in the Vinokur sense [335], *i.e.* if the partial derivative operators are computed on a uniform Cartesian grid after a change of variables whose Jacobian is denoted J, then the cutoff length can be evaluated at the point of index (l, m, n) either by Bardina's method or by the relation:

$$\overline{\Delta}_{l,m,n} = (J_{l,m,n}\Delta\xi\Delta\eta\Delta\zeta)^{1/3} \quad , \tag{10.3}$$

  where $\Delta\xi$, $\Delta\eta$ and $\Delta\zeta$ are the grid steps in the reference space.

In the case of an unstructured grid, we use the same evaluations as for a structured curvilinear grid with a finite volume type method, in the sense given above.

10.2 Explicit Discrete Filters

Several techniques and subgrid models described in the previous chapters use a test filter. For reference, these are the:

- Pre-filtering technique;
- Scale similarity models;
- Mixed Scale Model;
- Dynamic constant adjustment procedures;
- Models incorporating a structural sensor;
- Accentuation procedure.

The corresponding theoretical developments all assume that we are able to apply an analytical filter in the simulation. This operation comes down to a product of two arrays in the spectral space, which is a simple operation of little cost, and all the analytical filters whose transfer function is known explicitly can be used. The problem is very different, though, when we consider the simulations performed in the physical space on bounded domains: applying a convolution filter becomes very costly and non-local filters cannot be employed. In order to be able to use the models and techniques mentioned above, we have to use discrete filters with compact support in the physical space. These are described in the rest of this section. These discrete filters are defined as linear combinations of the values at points neighboring the one where the filtered quantity is computed [204, 257, 289, 332].

The weighting coefficients of these linear combinations can be computed in several ways, which are described in the following. We first present the one-dimensional case and then that of the Cartesian grids of more than one dimension, and lastly extend this to arbitrary grids.

The discrete approximation of the convolution filters is then discussed.

10.2.1 Uniform One-Dimensional Grid Case

We restrict ourselves here to the case of a uniform one-dimensional grid of mesh size Δx. The abscissa of the grid point of index i is denoted x_i, such that we can say $x_{i+1} - x_i = \Delta x$. The filtered value of the variable ϕ at the grid point of index i is defined by the relation:

$$\overline{\phi}_i \equiv \sum_{l=-N}^{N} a_l \phi_{i+l} \quad , \tag{10.4}$$

where N is the radius of the discrete filter stencil. The filter is said to be symmetrical if $a_l = a_{-l} \, \forall l$ and anti-symmetrical if $a_0 = 0$ and $a_l = -a_{-l} \, \forall l \neq 0$. The constant preservation property is represented by the following relation:

$$\sum_{l=-N}^{N} a_l = 1 \quad . \tag{10.5}$$

A discrete filter defined by the relation (10.4) is associated with the continuous convolution kernel:

$$G(x-y) = \sum_{l=-N}^{N} a_l \delta(x - y + l\Delta x) \quad , \tag{10.6}$$

where δ is a Dirac function. Simple computations show that the associated transfer function $\widehat{G}(k)$ is of the form:

$$\widehat{G}(k) = \sum_{l=-N}^{N} a_l^{\mathrm{i}kl\Delta x} \quad . \tag{10.7}$$

The real and imaginary parts of this transfer function are:

$$\Re(\widehat{G}(k)) = a_0 + \sum_{l=1}^{N} (a_l + a_{-l}) \cos(kl\Delta x) \quad ,$$

$$\Im(\widehat{G}(k)) = \sum_{l=1}^{N} (a_l - a_{-l}) \sin(kl\Delta x) \quad .$$

The continuous differential operator can be associated with the discrete filter (10.4). To do this, we introduce the Taylor expansion of the variable ϕ about the point i:

$$\phi_{i\pm n} = \sum_{l=0}^{\infty} \frac{(\pm n\Delta x)^l}{l!} \left(\frac{\partial^l \phi}{\partial x^l} \right)_i \quad . \tag{10.8}$$

By substituting in relation (10.4), we get:

$$\overline{\phi}_i = \left(1 + \sum_{l=1}^{\infty} a_l^* \Delta x^l \frac{\partial^l}{\partial x^l} \right) \phi_i \quad , \tag{10.9}$$

in which

$$a_l^* = \frac{1}{l!} \sum_{n=-N}^{N} a_n n^l \quad .$$

We note that these filters belong to the class of elliptic filters as defined in Sect. 2.1.3. In practice, the filters most used are the two following three-point symmetrical filters:

$$a_0 = \frac{1}{2}, a_{-1} = a_1 = \frac{1}{4} \quad ,$$

$$a_0 = \frac{2}{3}, a_{-1} = a_1 = \frac{1}{6} \quad .$$

Vasilyev *et al.* [332] have defined nonsymmetric filters, which have a large number of vanishing moments[2]. These filters are presented in Table 10.1.

Linearly constrained filters can also be defined, which satisfy additional constraints.

[2] These filters are necessary to obtain high-order commuting discrete filters (see Sect. 2.2.2).

Table 10.1. Coefficients of discrete nonsymmetrical filters. N is the number of vanishing moments

N	a_{-2}	a_{-1}	a_0	a_1	a_2	a_3	a_4
1		1/4	1/2	1/4			
2			7/8	3/8	-3/8	1/8	
2		1/8	5/8	3/8	-1/8		
3			15/16	1/4	-3/8	1/4	-1/16
3		1/16	3/4	3/8	-1/4	1/16	
3	-1/16	1/4	5/8	1/4	-1/16		

Optimized filters, whose coefficients are computed to minimize the functional

$$\int_0^{\pi/\Delta x} (\Re\{\widehat{G}(k) - \widehat{G}_t(k)\})^2 dk + \int_0^{\pi/\Delta x} (\Im\{\widehat{G}(k) - \widehat{G}_t(k)\})^2 dk \quad , \tag{10.10}$$

where $\widehat{G}_t(k)$ is the targeted transfer function, have been proposed [289, 332]. These filters ensure a better spectral response of the filter, resulting in a better localization of the information in spectral space.

For certain uses, such as in the Germano-Lilly dynamic procedure, the characteristic length of the discrete filter, denoted Δ_{d}, has to be known. For a definite positive filter, one measure of this length is obtained by computing the standard deviation of the associated convolution filter [204, 257]:

$$\Delta_{\mathrm{d}} = \sqrt{12 \int_{-\infty}^{+\infty} \xi^2 G(\xi) d\xi} \quad . \tag{10.11}$$

The characteristic lengths of the two three-point filters mentioned above are $2\Delta x$ for the $(1/6, 2/3, 1/6)$ filter and $\sqrt{6}\Delta x$ for the $(1/4, 1/2, 1/4)$ filter. This method of evaluating the characteristic lengths of the discrete filters is inefficient for filters whose second-order moment is zero. One alternative is work directly with the associated transfer function and define the wave number associated with the discrete filter, as for the one for which the transfer function takes the value 1/2. Let k_{d} be this wave number. The discrete filter cutoff length is now evaluated as:

$$\Delta_{\mathrm{d}} = \frac{\pi}{k_{\mathrm{d}}} \quad . \tag{10.12}$$

10.2.2 Extension to the Multidimensional Case

For Cartesian grids, we extend to the multidimensional case by applying a one-dimensional filter in each direction of space. This application can be performed simultaneously or sequentially. When simultaneously, the multidimensional filter is written symbolically as a summation:

$$G^n = \frac{1}{n} \sum_{i=1}^{n} G_i \quad , \tag{10.13}$$

where n is the dimension of the space and G_i the one-dimensional filter in the ith direction of space. If applied sequentially, the resulting filter takes the form of a product:

$$G^n = \prod_{i=1}^{n} G_i \quad . \tag{10.14}$$

The multidimensional filters constructed by these two techniques from the same one-dimensional filter are not the same in the sense that their transfer functions and equivalent differential operators are not the same. In practice, it is the product construction that is most often used, for two reasons:

- This approach makes it possible to call the easily implemented one-dimensional filtering routines sequentially.
- Such filters are more sensitive to the cross modes than are the filters constructed by summation, and allow a better analysis of the three-dimensional aspect of the field.

10.2.3 Extension to the General Case. Convolution Filters

For structured curvilinear grids (or Cartesian grids with variable mesh size), one method is to employ the filters defined in the uniform Cartesian grid and take no account of the variations of the metric coefficients. This method, which is equivalent to applying the filter in a reference space, is very easy to implement but allows no control of the discrete filter transfer function or its equivalent differential operator. So it should be used only for grids whose metric coefficients vary slowly.

Another method that is completely general and applicable to unstructured grids consists in defining the discrete filter by discretizing a chosen differential operator. The weighting coefficients of the neighboring nodes are then the coefficients of the discrete scheme associated with this differential operator. In practice, this method is most often used by discretizing second-order elliptic operators:

$$\overline{\phi} = (Id + \alpha \overline{\Delta}^2 \nabla^2)\phi \quad , \tag{10.15}$$

where α is a positive constant and $\overline{\Delta}$ the desired cutoff length. Limiting the operator to the second order yields filters with compact support using only the immediate neighbors of each node. This has the advantages of:

- Making it possible to define operators that cost little to implement;

– Making a multiblock and/or multidomain technique easier to use, and the boundary conditions easier to process.

The fast-decay convolution filters (box or Gaussian) can thus be approximated by discretizing the differential operators associated with them. These operators are described in Sect. 6.1.1. The sharp cutoff filter, which is not of compact support, is used only when fast Fourier transforms are usable, which implies that the grid step is constant and the data periodic.

10.2.4 High-Order Elliptic Filters

Convolution filters are non-local, and may sometimes be difficult to use together with complex numerical algorithms (multidomain topology, unstructured grid, ...). An alternative, that can be implemented with all numerical methods, consists in high-order elliptic filters [252].

The filtered variable is computed as being the solution of the general elliptic equation:

$$[-(\nabla^2)^m + \alpha Id]\overline{\phi} = \alpha\phi, \quad m \geq 1 \quad . \tag{10.16}$$

High values of m make it possible to obtain very sharp filters in the spectral space. Mullen and Fischer show that the solution of equation (10.16) can be approximated through numerical solution of a much simpler problem, namely the Poisson equation

$$-\nabla^2\psi = \phi \quad . \tag{10.17}$$

10.3 Implementation of the Structure Function Model

In order to use the subgrid viscosity model based on the second-order structure function of the velocity (see p. 95), we have to establish a discrete approximation of the operator:

$$F_2(\mathbf{x}, r, t) = \int_{|\mathbf{x}'|=r} [\mathbf{u}(\mathbf{x}, t) - \mathbf{u}(\mathbf{x} + \mathbf{x}', t)]^2 \, d^3\mathbf{x}' \quad . \tag{10.18}$$

In practice, this integration is approximated as a sum of the contributions of the neighboring points. In the case of uniform Cartesian grid with $\Delta x = r$, the structure function is evaluated at the index point (i, j, k) by the relation:

$$\begin{aligned} F_2(\Delta x, t)_{i,j,k} = \frac{1}{6} \big(& |\mathbf{u}_{i,j,k} - \mathbf{u}_{i+1,j,k}|^2 + |\mathbf{u}_{i,j,k} - \mathbf{u}_{i-1,j,k}|^2 \\ + & |\mathbf{u}_{i,j,k} - \mathbf{u}_{i,j+1,k}|^2 + |\mathbf{u}_{i,j,k} - \mathbf{u}_{i,j-1,k}|^2 \\ + & |\mathbf{u}_{i,j,k} - \mathbf{u}_{i,j,k+1}|^2 + |\mathbf{u}_{i,j,k} - \mathbf{u}_{i,j,k-1}|^2 \big) \quad . \end{aligned} \tag{10.19}$$

When the grid is non-uniform or when $\Delta x \neq r$, an interpolation technique has to be used to compute the integral. Rather than use a linear interpolation, it is recommended that the interpolation method be based on physical knowledge. So in the isotropic homogeneous turbulence case, when we see that we have:

$$\begin{aligned} F_2(\mathbf{x}, r, t) &= 4.82 K_0 (\varepsilon r)^{2/3} \quad , \\ F_2(\mathbf{x}, r', t) &= 4.82 K_0 (\varepsilon r')^{2/3} \quad , \end{aligned}$$

we deduce the proportionality relation:

$$F_2(\mathbf{x}, r, t) = F_2(\mathbf{x}, r', t) \left(\frac{r}{r'}\right)^{2/3} \quad . \tag{10.20}$$

Relation (10.19) is thus generalized to the form:

$$F_2(\mathbf{x}, r, t) = \frac{1}{n} \sum_{i=1}^{n} |\mathbf{u}(\mathbf{x}) - \mathbf{u}(\mathbf{x} + \Delta_i)|^2 \left(\frac{r}{\Delta_i}\right)^{2/3} \quad , \tag{10.21}$$

where n is the number of neighboring points retained for computing the structure function and Δ_i the distance of the ith point to the point where this function is evaluated.

It has already been said that the Structure Function model in its original form exhibits defects similar to those of the Smagorinsky model because of the uncertainty relation that prevents any good frequency localization of the information. One way of at least partly remedying this program is to look for the structure function evaluation information only in the directions of statistical homogeneity of the solution. This is done by evaluating the structure function only from points located in the directions of periodicity of the solution. This way, the mean gradient of the solution is not taken into account in the evaluation of the subgrid viscosity. We again find here an idea similar to the one on which the splitting technique is based, in Sect. 5.3.2.

11. Examples of Applications

This chapter gives a few examples of large-eddy simulation applications that are representative of their accomplishments in the sense that they correspond either to flows that are very frequently treated or to configurations that stretch the technique of today to its limits.

11.1 Homogeneous Turbulence

11.1.1 Isotropic Homogeneous Turbulence

Problem Description. Isotropic homogeneous turbulence is the simplest turbulent flow on which subgrid models can be validated. The physical description of this flow is precisely the one on which the very great majority of these models are constructed. Moreover, the flow's statistical homogeneity makes it possible to use periodicity conditions for the computation, and high-accuracy numerical methods: pseudo-spectral methods can be used, optimally reducing the effect of the numerical error on the solution.

Because of the great simplicity of this flow, most subgrid models yield very satisfactory results in terms of the statistical moments of the velocity field and the integral scales, which reduces the discriminatory range of this test case. It is nonetheless widely used for fundamental type studies of turbulence and modeling.

Two types of such flow are considered:

- Freely decaying isotropic homogeneous turbulence in which the energy is initially distributed in a narrow spectral band and then, as the energy cascade sets in, is directed toward the small scales and finally dissipated at the cutoff by the subgrid model. During the time the cascade is setting in, the kinetic energy remains constant, and later declines. The computation can be validated by comparison with decay laws developed by analytical theories (see [189]) or by comparison with experimental data.
- Sustained isotropic homogeneous turbulence, in which total dissipation of the kinetic energy is prevented by injecting energy at each time step, for example by maintaining a constant energy level in the wave vectors of a given norm. After a transitory phase, an equilibrium solution is established

including an inertial range. The computation is validated by comparison with theoretical or experimental data concerning the inertial region, and quantities associated with the large scales.

A few Realizations. The first large-eddy simulations of the free-decaying type were performed at the end of the seventies and early eighties [61] with resolutions of the order of 16^3 and 32^3. Self-similar solutions could not be obtained with these resolutions because the integral scale becomes larger than the computational domain. However, the comparison with filtered experimental data turns out to be satisfactory [13]. More recent simulations (for example [191, 235]) performed with different subgrid models on grids of 128^3 points have yielded data in agreement analytical theories for the kinetic energy decay. Higher-resolution simulations have been performed.

In the sustained case, Chasnov [54] is an example of achieving self-similar solutions in agreement with theory for resolutions of 64^3 and 128^3, though with an over-evaluation of the Kolmogorov constant. More recently, Fureby *et al.* [106] have tested six subgrid models and a case of implicit numerical diffusion on a 32^3 grid. The conclusions of this work are that the different realizations, including the one based on artificial dissipation, are nearly indiscernable in terms of the quantities linked to the resolved field, and are in good agreement with data yielded by a direct numerical simulation.

Though isotropic homogeneous turbulence is statistically the simplest case of turbulent flow, it possesses a complex dynamics resulting from the interactions of very many elongated vortex structures called "worms". These structures are illustrated in Fig. 11.1, which comes from a large-eddy simulation of freely decaying isotropic homogeneous turbulence on a 128^3 grid. Obtaining good results therefore implies that the simulation is capable of reflecting the dynamics of these structures correctly. We clearly see here the difference with the RANS approach (see Chap. 1), for which isotropic homogeneous turbulence is a zero-dimension problem: for the large-eddy simulation, this problem is fully three-dimensional and reveals all the aspects of this technique (modeling errors, filter competition, and so forth).

11.1.2 Anisotropic Homogeneous Turbulence

Anisotropic homogeneous turbulence allows a better analysis of the subgrid models because the dynamics is more complex, while optimum numerical methods are retained. So it can be expected that this type of flow offers more discriminatory test cases for the subgrid models than do isotropic flows.

Bardina *et al.* [13] performed a set of simulations corresponding to the following three cases in the early eighties:

- Homogeneous turbulence subjected to a solid-body rotation. Good agreement is measured with experimental data using a de-filtering technique, on a 32^3 grid with a Smagorinsky model (4.90). The effects of rotation on the turbulence are confirmed, *i.e.* a reduction in the dissipation of the kinetic energy.
- Homogeneous turbulence subjected to pure strain: still a 32^3 grid, with results in good agreement with experimental data concerning the turbulent intensity, using the Smagorinsky model and mixed Smagorinsky–Bardina model (6.118). The best results are obtained with the latter.
- Homogeneous turbulence subjected to a deformation and rotation: simulations are performed on a 32^3 grid with the two previously mentioned models. No validation is presented, for lack of reference data.

Simulations of homogeneous turbulence subjected to sequential shearing have also been performed by Dang [73] on a 16^3 grid with several effective viscosity models, yielding good results concerning the prediction of the anisotropy of the resolved scales. Similar computations have also been performed by Aupoix [6].

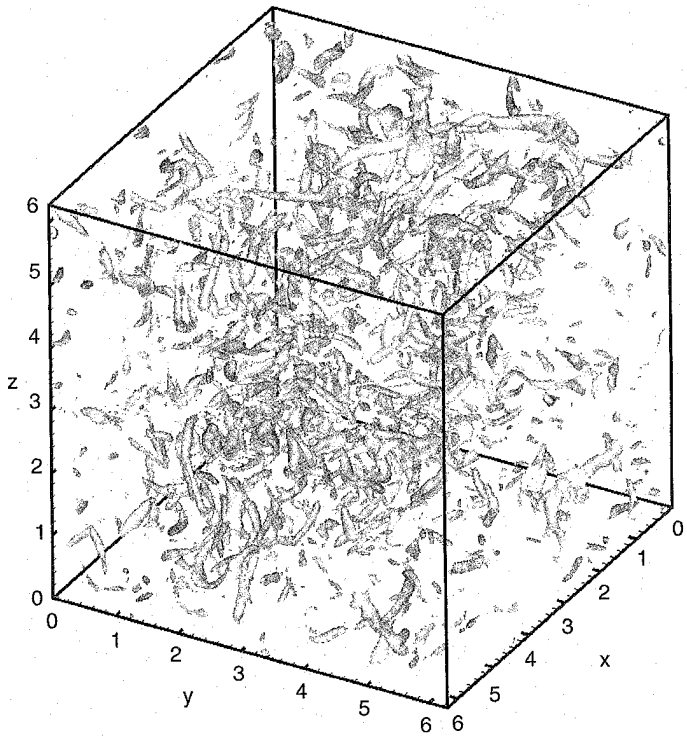

Fig. 11.1. Isotropic homogeneous turbulence. Instantaneous view of vortices (illustrated by an iso-value surface of the vorticity). With the permission of E. Garnier, ONERA.

11.2 Flows Possessing a Direction of Inhomogeneity

These flows represent the next level of complexity. The presence of a direction of inhomogeneity prompts the use of lower-order numerical methods, at least for this inhomogeneity, and boundary conditions. Also, more complex physical mechanisms are at play that can exceed the possibilities of the subgrid models.

11.2.1 Time-Evolving Plane Channel

Problem Description. The time-evolving plane channel flow is a flow between two infinite parallel flat plates having the same velocity. The time character is due to the fact that we consider the velocity field as being periodic in both directions parallel to the plates. Since the pressure is not periodic, a forcing term corresponding to the mean pressure gradient is added in the form of a source term in the momentum equations. The flow is characterized by the fluid viscosity, the distance between the plates, and the fluid velocity. This case study configuration is used for investigating the properties of a turbulent flow in the presence of solid walls, and is a widely used test case. Turbulence is generated within the boundary layers that develop along each solid wall (see Sect. 9.2.1). It is the driving mechanism here, which must imperatively be simulated with accuracy to obtain reliable results. To do so, the grid has to be refined near the surfaces, which raises numerical problems with respect to the homogeneous turbulence. Moreover, the subgrid models must be able to preserve these driving mechanisms.

The flow topology is illustrated in the iso-value surface plot of the vorticity in Fig. 11.2.

A Few Realizations. There are dozens of numerical realizations of plane channel flows. The first are from Deardorff [76] in 1970. The first landmark results obtained by solving the dynamics of the near-wall region are due to Moin

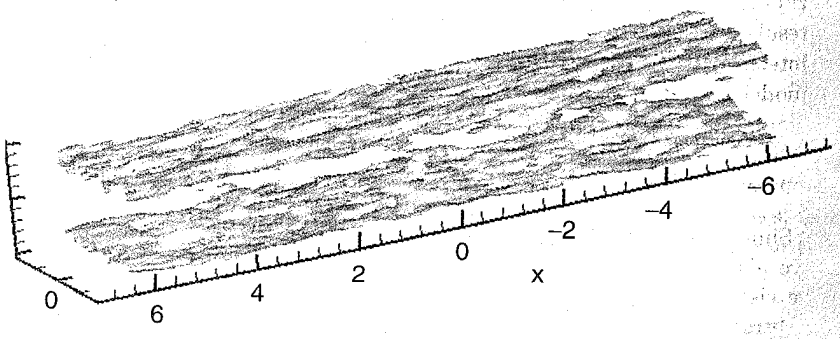

Fig. 11.2. Plane channel flow. Iso-surface of instantaneous vorticity. With the permission of E. Montreuil, ONERA.

Table 11.1. Characteristics of time-evolving plane channel flow computations.

Ref.	[245]	[264]	[298]	[171]
Re_c	13800	47100	$\approx 1,5.10^5$	$1,09.10^5$
$Lx \times Ly \times Lz$	$2\pi \times \pi \times 2$	$5\pi/2 \times \pi/2 \times 2$	$4 \times 2 \times 1$	$2\pi \times \pi/2 \times 2$
$Nx \times Ny \times Nz$	$64 \times 64 \times 128$	$64 \times 81 \times 80$	$64 \times 32 \times 32$	$\simeq 2.10^6$+H
SGS Model	Sc	Dyn	Sc	Dyn
Wall	-	-	MSc	-
$O(\Delta x^\alpha)$	S/2	S/T	2	S/Gsp
$O(\Delta t^\beta)$	2	3	2	3

and Kim [245] in 1982. The characteristics of the computations presented in the four reference works [171, 245, 264, 298] are reported in Table 11.1. These computations are representative of the various techniques employed by most authors. The Table summarizes the following information:

- The Reynolds number Re_c referenced to the channel mid-height and mean velocity at the center of the channel.
- The dimensions of the computational domain expressed as a function of the channel mid-height. The domain dimensions must be greater than those of the driving mechanisms in the near-wall region (see Sect. 9.2.1).
- The number of grid points. Simulations generally include few points because the solution is bi-periodical. The computations at high Reynolds number without wall model presented [171] use a hierarchic grid technique with nine grid levels (symbol "+H").
- The subgrid model used ("Sc"is the Schumann subgrid viscosity model (5.70) and "Dyn"the dynamic Smagorinsky model (4.137)). Only two models are used in the computations presented, but most existing models have been applied to this configuration.
- The treatment of the solid walls ("-"is the no-slip condition, "MSc"the Schumann wall model (9.19) to (9.21)). A single computation based on a wall model is presented, knowing that nearly all the models mentioned in Chap. 9 have been used for dealing with this flow.
- The accuracy of the space discretization schemes. Since the directions of statistical homogeneity are linked to directions of periodicity in the solution, pseudo-spectral methods are often used for processing them. This is true of all the computations presented, identified by an "S", except for reference [298], which presents a second-order accurate finite volume method. In the normal direction, three cases are presented here: use of second-order accurate schemes (identified by a "2"), of a Chebyshev method ("T"), and a Galerkin method based on B-splines ("Gsp"). The effect of the numerical error on the solution can be reduced by using higher-order methods, which are consequently recommended by many authors.

– The accuracy of the time integration. The convection term is usually treated explicitly (Runge-Kutta or Adams-Bashforth scheme) and the diffusion terms implicitly (Crank-Nicolson or second-order backward Euler scheme). Nearly all the computations are performed with second- or third-order accuracy.

The results obtained on this configuration are usually in good agreement with experimental data, and especially as concerns the first-order (mean field) and second-order (Reynolds stresses) statistical moments. Examples of data for these quantities are shown in Figs. 11.3 and 11.4. The mean longitudinal velocity profile is compared here with a theoretical turbulent boundary layer solution, and very good agreement with it is observed. It should be noted that the logarithmic region is relatively small, which is due to the fact that the Reynolds number for the computation is low ($Re_\tau = 180$). The profiles of the three main Reynolds stresses are compared with those obtained by direct numerical simulation on a grid including about twenty times more degrees of freedom. Although these stresses are calculated only from the resolved field, such that the contribution of the subgrid scales is not included, we observe that the agreement with the reference solution is very satisfactory. This illustrates the fact that data obtained by large-eddy simulation can be used directly in practice without recourse to a de-filtering technique. In the present case, the very good quality of the results can be explained by the fact that a large part of the kinetic energy of the exact solution is contained in the resolved scales.

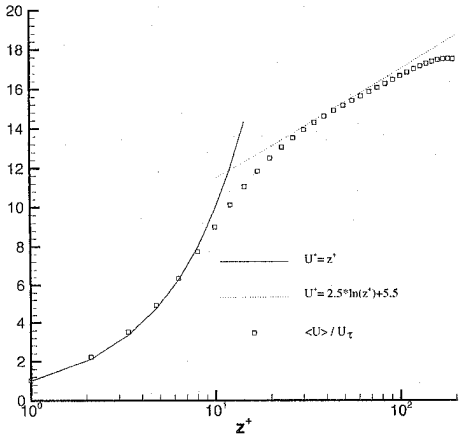

Fig. 11.3. Plane channel flow. Mean longitudinal velocity profile referenced to the friction velocity, compared with a theoretical turbulent boundary layer profile. Small circle symbols: LES computation. Lines: theoretical profile. With the permission of E. Montreuil, ONERA.

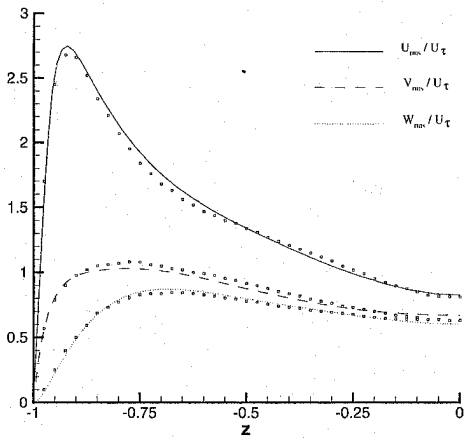

Fig. 11.4. Plane channel flow. Profiles of solved Reynolds stresses with respect to the friction velocity, compared with data from a direct numerical simulation computation. Dot symbols: direct numerical simulation. Lines: LES computation. With the permission of E. Montreuil, ONERA.

The quality of the results is essentially due to the resolution of the dynamics in the near-wall region ($z^+ < 100$). This implies that, if a wall model is not used, the computational grid is fine enough to represent the dynamics of the vortex structures present, and that the subgrid models employed do not alter this dynamics. Because of the necessary volumes of the grids, this resolution constraint limits the possible Reynolds number. The largest friction Reynolds number achieved to date, using a hierarchic grid generation method, is $Re_\tau = 4000$ [171]. The standard subgrid viscosity models (Smagorinsky, Structure Function, and so forth) are generally too dissipative and have to be used with caution (modification of the value of the model constant, wall damping function, and so forth) [292]. Results concerning the transition to turbulence in the configuration are available in reference [271]. Lastly, the results obtained for this flow have been found to be very sensitive to numerical errors induced either by the discrete numerical scheme or by the continuous form of the convection term [172, 257].

11.2.2 Other Flows

Other examples of shear flows treated in the framework of the time-evolution approximation can be found for:

– plane mixing layer, in [310];
– boundary layers, in [167, 221, 223, 243];
– round jet, in [96];

- plane wake, in [124];
- rotating plane channel, in [176, 177, 240, 241, 268, 324];
- plane jet, in [182].

As in the case of the plane channel flows described above, periodicity conditions are used in the directions of statistical homogeneity. The numerical methods are generally dedicated to the particular configuration being treated (with spectral methods used in certain directions) and are therefore optimum. A forcing term is added in the momentum equations to take the driving pressure gradient into account or avoid diffusion of the base profile.

Transitional flows are more sensitive to the subgrid model and to the numerical errors, as an inhibition of the transition or re-laminarization of the flow are possible. This is more especially true of flows (for example boundary layers) for which there exists a critical Reynolds number: the effective Reynolds number of the simulation must remain above the threshold within which the flow is laminar.

It should be noted that the boundary conditions in the inhomogeneous direction raises little difficulty for the flow configurations mentioned above. These are either solid walls that are easily included numerically (except for the procedure of including the dynamics), or outflow conditions in regions where the flow is potential. In the latter case, the computation domain boundary is generally pushed back as far as possible from the region being studied, which reduces any spurious effects.

The types of results obtained, and their quality, are comparable to what has already been presented for the plane channel flow.

11.3 Flows Having at Most One Direction of Homogeneity

This type of flow introduces several additional difficulties compared with the previous cases. The limited number or total absence of directions of homogeneity makes it necessary in practice to use numerical methods of moderate order of accuracy (generally two, rarely more than four), and highly anisotropic grids. The effect of the numerical error will therefore be high. Moreover, most of these flows are in spatial expansion and the problems related to the definition of the inflow and outflow conditions then appear. Lastly, the flow dynamics becomes very complex, which accentuates the modeling problems.

11.3.1 Round Jet

Problem Description. The example of the round jet flow in spatial expansion is representative of the category of free shear flows in spatial expansion. The case is restricted here to an isothermal, isochoric round jet flow piped

into a uniform, steady outer flow in a direction parallel to that of the jet. Two main regions can be identified:

- First, we find a region at the pipe exit where the flow consists of a laminar core called a potential cone, which is surrounded by an annular mixing layer. The mixing layer is created by the inflectional instability associated with the deficit velocity profile of the boundary layer on the wall of the circular pipe. As the mixing layer thickens while moving away from the pipe exit section, it reduces the diameter of the potential cone and also induces an increase in the jet diameter.
- After the potential cone disappears, we have a "pure jet" region where the flow gradually reaches a regime corresponding to a similarity solution.

The first region can be decomposed into two: a "transition" region where the mixing layer has not yet reached its self-similar regime, and the similarity region where it has. This organization is illustrated in Figs. 11.5 and 11.6, representing respectively the iso-surfaces of vorticity and pressure obtained from large-eddy simulation results. The vorticity field very clearly shows the transition of the annular mixing layer. The topology of the pressure field shows the existence of coherent structures.

Experimental and numerical analyses have shown that this flow is strongly dependent on many parameters, which makes it highly discriminatory.

A Few Realizations. There are far fewer round jet simulations in the literature than there are plane channel flows. This is mainly due to the increased difficulty. Four of these realizations are described in the following, with their characteristics listed in Table 11.2, which gives:

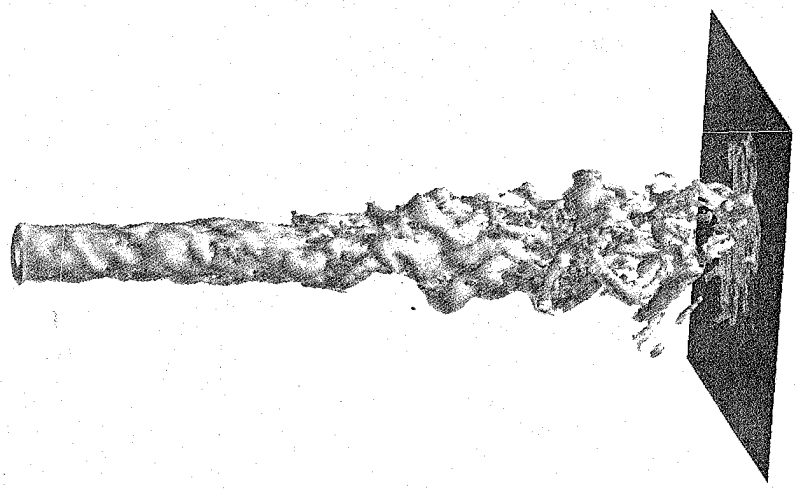

Fig. 11.5. Round jet. Iso-surface of instantaneous vorticity (LES computation). Exit plane in black. With the permission of P. Comte, LEGI.

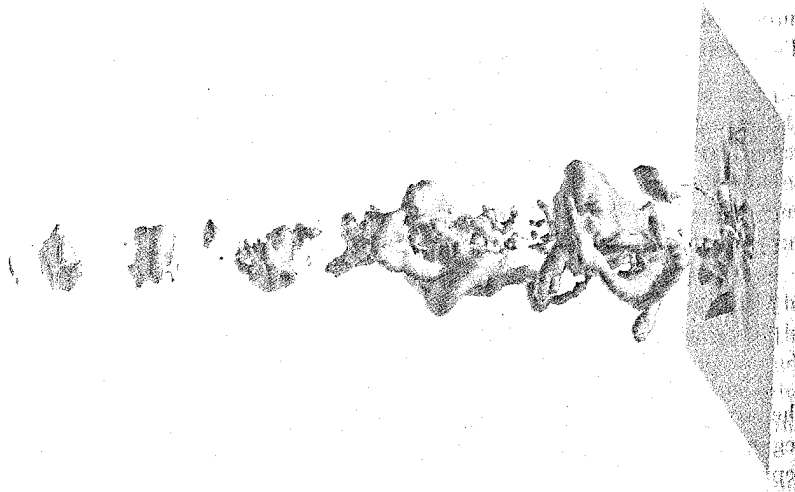

Fig. 11.6. Round jet. Iso-surface of instantaneous vorticity (LES computation). With the permission of P. Comte, LEGI.

- the Reynolds number Re_D referenced to the initial jet diameter D and the maximum of the mean initial velocity profile;
- the computational domain dimensions referenced to the length D;
- the number of grid points. All the grids used by the authors mentioned are Cartesian. The symbol H designates the use of embedded grids (four grid levels for [260]).
- the subgrid model ("MSM" standing for the Mixed Scale Model (4.116); "Dyn" the dynamic model (4.137); "FSF" the filtered Structure Function model (4.225)). It should be noted that, for all the known realizations of this flow, only the subgrid viscosity models have been used.
- the freestream condition generation mode. The symbol $U + b$ indicates that the non- steady inflow condition was generated by superimposing an average steady profile and a random noise, as indicated in Sect. 9.3.2.

Table 11.2. Characteristics of the round jet computations.

Ref.	[291]	[260]	[37]
Re_D	21000	50.10^4	21000
$Lx \times Ly \times Lz$	$10 \times 11 \times 11$	$12 \times 8 \times 8$	$10 \times 11 \times 11$
$Nx \times Ny \times Nz$	$101 \times 121 \times 121$	≈ 270000+H	$101 \times 288 \times 288$
SGS Model	MSM	Dyn	FSF
Inflow	U+b	U+b	U+b
$O(\Delta x^\alpha)$	2+up3	3+up3	S/6
$O(\Delta t^\beta)$	2	2	3

- the overall order of accuracy of accuracy in space of the numerical method. The symbol $+up3$ indicates that a third-order accurate upwind scheme is used for the convection term to ensure computation stability. The computations presented in [37] rely on spectral schemes in the directions normal to that of the jet.
- the time accuracy of the method employed.

Examples of results obtained on this configuration are compared with experimental data in Figs. 11.7 to 11.11. The axial evolution of the location of the point where the mean velocity is equal to half the maximum velocity is represented in Fig. 11.7. This quantity, which gives some indication concerning the development of the annular mixing layer, remains constant during the first phases of evolution of the jet, which confirms the existence of a potential cone. After the cone disappears, this quantity increases, which indicates the beginning of the pure jet region. It is observed that the length of the potential cone predicted by the computation is less than is observed experimentally. Similar conclusions can be drawn from the axial evolution of the average longitudinal velocity, which is presented in Fig. 11.8. The too-rapid expansion of the pure jet region is accompanied by a strong decay of the mean velocity[1]. These symptoms are observed on all known large-eddy simulation computations on this configuration and still have no precise explanation. Several hypotheses have been formulated concerning the

[1] This results from the conservation of the mass.

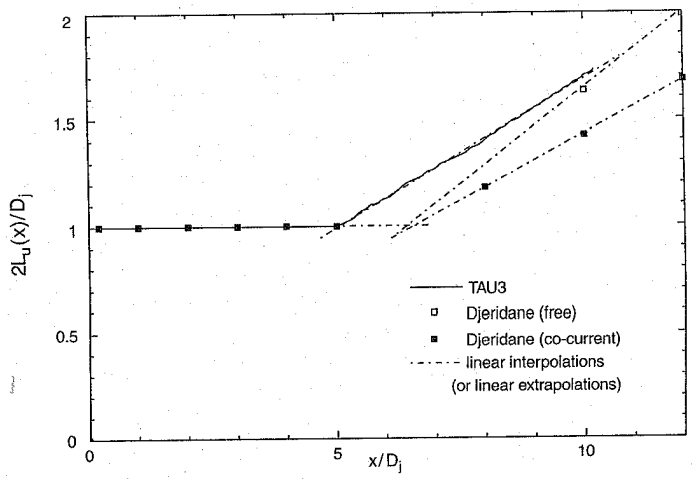

Fig. 11.7. Round jet. Axial evolution of the radial position of the point where the mean velocity is half the maximum velocity. Dots: experimental data. Dot-dashed lines: extrapolation of this data. Solid line: LES computation. With the permission of P. Comte, LEGI.

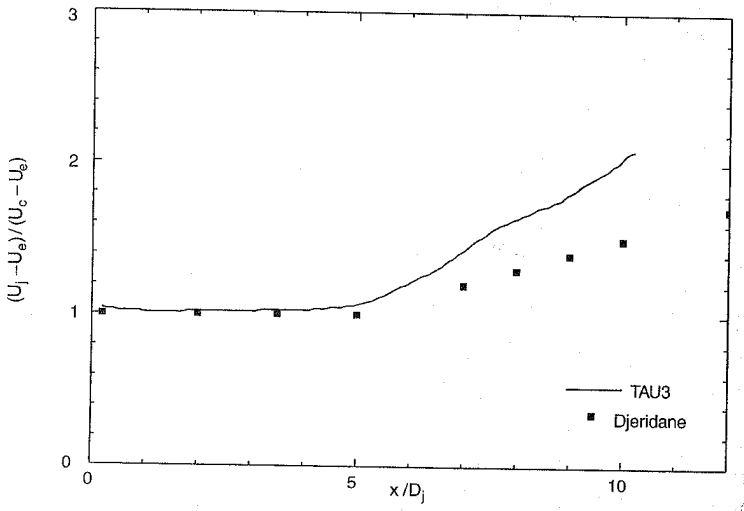

Fig. 11.8. Round jet. Axial evolution of the mean longitudinal velocity. Dots: experimental data. Line: LES computation. With the permission of P. Comte, LEGI.

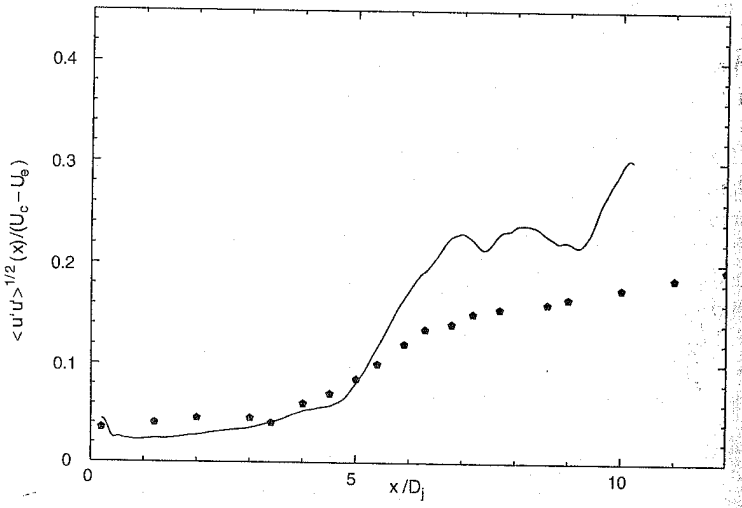

Fig. 11.9. Round jet. Axial evolution of the normalized longitudinal turbulent intensity. Dots: experimental data. Line: LES computation. With the permission of P. Comte, LEGI.

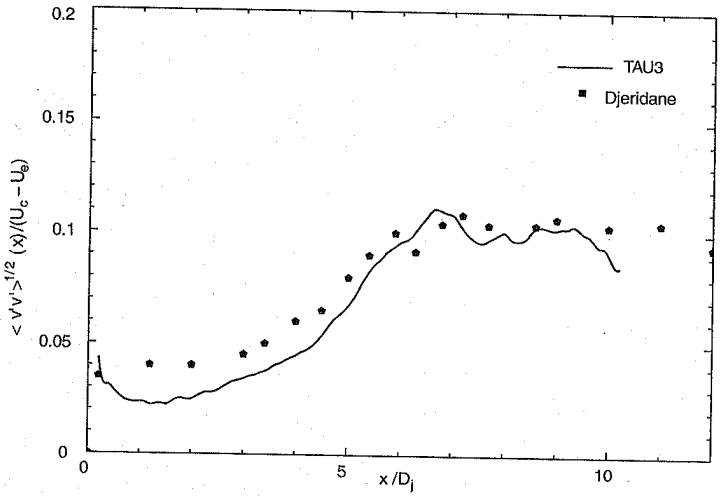

Fig. 11.10. Round jet. Axial evolution of the normal turbulent intensity. Dots: experimental data. Line: LES computation. With the permission of P. Comte, LEGI.

dependency on the initial perturbation, on the boundary conditions, or on the computational grid. The axial profiles of two main Reynolds stresses are presented in Figs. 11.9 and 11.10. These results are qualitatively correct. The Reynolds stresses increase along the axis and exhibit a maximum in a region close to the tip of the potential cone, which is in agreement with the experimental observations. It is noted that the level of the longitudinal stress predicted by the computation is higher than the experimental level in the pure jet region. The peak observed on the downstream boundary of the computational domain is a spurious effect that is no doubt related to the outflow condition. Generally, it is noticed that the quality of the results is not as good as in the case of the plane channel flow, which illustrates the fact that this flow is a more complicated case for large-eddy simulation.

Lastly, the velocity spectra generated from the computation are presented in Fig. 11.11. Over a decade, the computations recover a slope close to the -5/3 predicted by theory, and which is the foundation of the theoretical analyses presented in the previous chapters. This indicates that the resolved turbulent scales have "physical" behavior.

More generally, the conclusions given by the various authors are the following.

– The dynamics of the numerical solution is consistent, *i.e.* the values produced are located within the bounds fixed by the collected set of experimental measurements and the topology of the simulated flow exhibits the expected characteristics (potential cone, annular mixing layer, and so forth).

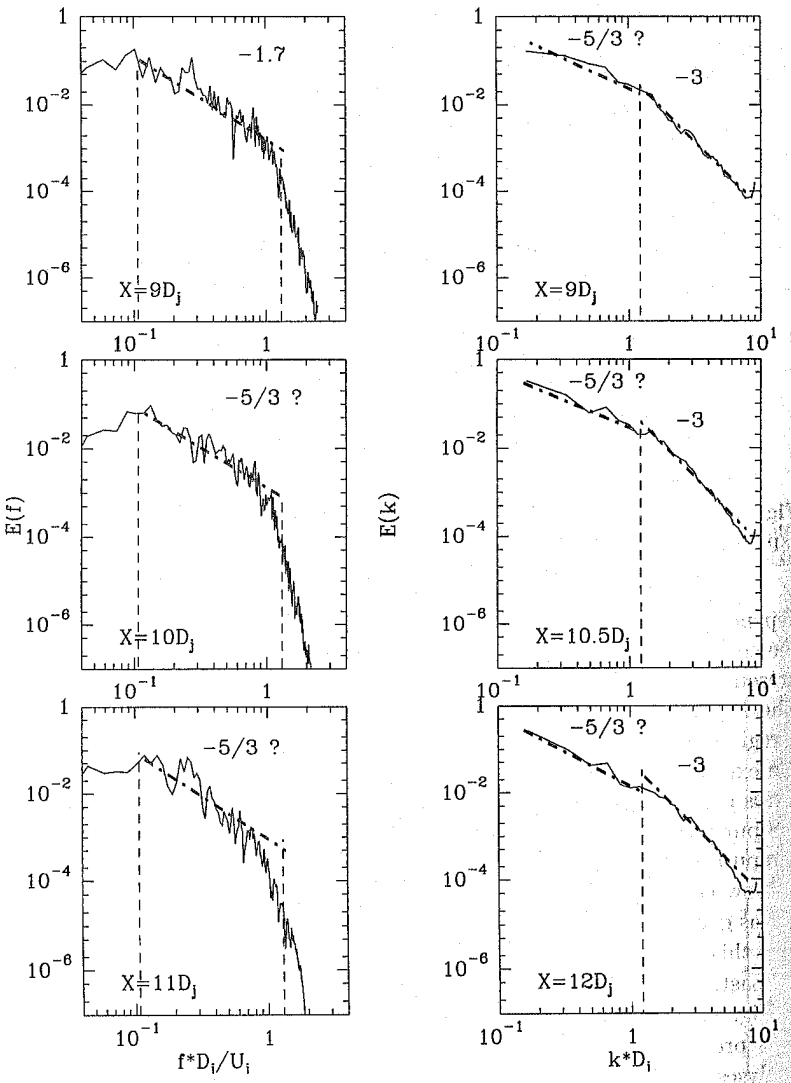

Fig. 11.11. Round jet. Time (left) and space (right) spectra of solved turbulent kinetic energy at different positions along the axis. With the permission of P. Comte, LEGI.

- While the dynamics is consistent, it is nonetheless very difficult to reproduce a particular realization (for example with fixed potential cone length and maximum turbulent intensity).

- The numerical solution exhibits a strong dependency on many parameters, among which we find:
  - the subgrid model, which allows a more or less rapid transition of the annular mixing layer are consequently influences the length of the potential cone and the turbulent intensity by modifying the effective Reynolds number in the simulation. More dissipative models delay the development of the mixing layer, inducing the existence of a very long potential cone.
  - the inflow condition: the mixing layer transition is also strongly dependent on the amplitude and shape of the perturbations.
  - the numerical error, which can affect the turbulent of the annular mixing layer and of the developed jet, especially during the transition phases. Here it is a matter of an error controlled by the computational grid and the numerical method. A dispersive error will have a tendency to accelerate the transition and thereby shorten the potential cone. A dissipative error will have the inverse effect. With too coarse a grid, the annular mixing layer cannot be represented correctly, which can induce it to thicken too quickly and thereby decrease the length of the potential cone.
  - the size of the computational domain. The computation is sensitive to the size of the computational domain, which modulates the effect of the boundary conditions, especially the outflow condition.
- All the computations predict the dominant time frequency of the jet correctly, which is therefore not a pertinent parameter for analyzing the models finely.
- The quality of the simulation is not a global character. Certain parameters can be correctly predicted while others are not. This diversity in the robustness of the results with respect to the simulation parameters sometimes makes it difficult to define discriminatory parameters.

Other Examples of Free Shear Flows. Other examples of free shear flows in spatial expansion have been simulated:

- plane mixing layer (see [310]);
- planar jet (see [70]);
- plane wake (see [109, 125, 339]).

The conclusions drawn from the analysis of these different cases corroborate those explained previously for the round jet as concerns the quality of the results and their dependency as a function of the computation parameters (subgrid model, grid, inflow condition, computational domain, and so forth). These conclusions are therefore valid for all free shear flows in spatial expansion.

11.3.2 Backward Facing Step

Problem Description. The flow over a backward facing step of infinite span is a generic example for understanding separated internal flows. It involves most of the physical mechanisms encountered in this type of flow and is doubtless the best documented, both experimentally and numerically, of the flows in this category. Its dynamics can be decomposed as follows. The boundary layer that develops upstream of the step separates at the step corner, becoming a free shear layer. This layer expands in the recirculation region, thereby entraining turbulent fluid volumes. This entrainment phenomenon may influence the development of the shear layer, which curves inward toward the wall in the reattachment region and impacts with it. After the reattachment, the boundary layer re-develops while relaxing toward a profile in equilibrium. The topology of this flow is illustrated in Fig. 11.12, which is developed from large-eddy simulation data. We observe first the transition of the separated shear layer, the formation of vortex structures in the impact area, and then of hairpin structures in the boundary layer after the reattachment.

This flow brings out difficulties in addition to those of the round jet, because it adds the dynamics both of the free shear layers and of the near wall region.

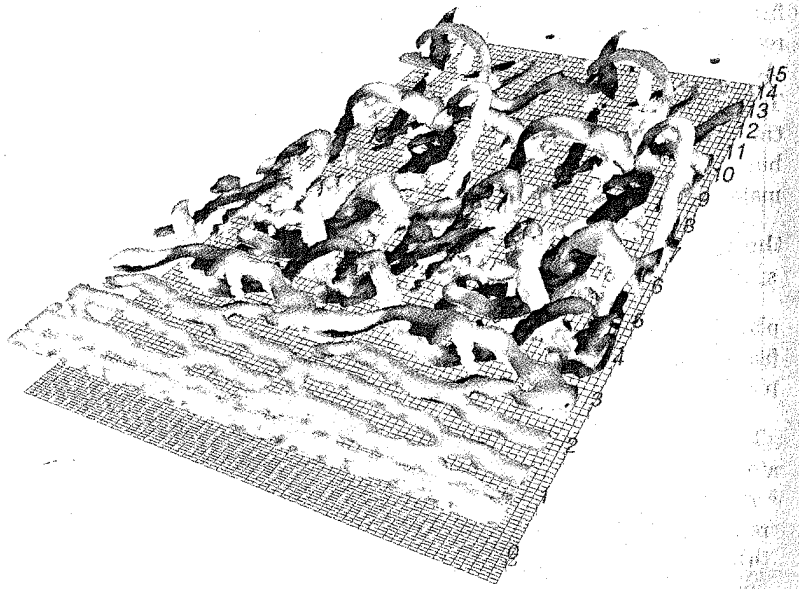

Fig. 11.12. Backward Facing Step. Iso-surface of instantaneous vorticity. With the permission of F. Delcayre, LEGI.

Table 11.3. Backward facing step computation characteristics.

Ref.	[103]	[294]	[309]	[122]
Re_H	$1,65.10^5$	11200	38000	28 000
$Lx \times Ly \times Lz$	$16 \times 4 \times 2$	$20 \times 4 \times 2,5$	$30 \times 5 \times 2,5$	$30 \times 3 \times 4$
$Nx \times Ny \times Nz$	$128 \times 32 \times 32$	$201 \times 31 \times 51$	$200 \times 30 \times 30$	$244 \times 96 \times 96$
SGS Model	Sc	MSM	FS	DynLoc
Inflow	P	U+b	U+b	U+b,Ca
Wall	MSc	-	MLog	-
$O(\Delta x^\alpha)$	2	2+up3	2+up3	2
$O(\Delta t^\beta)$	2	2	2	3

A Few Realizations. The methods used for simulating this flow are illustrated by four computations presented in Table 11.3. The parameters indicated are.

- Reynolds number Re_H, referenced to the step height H and the inflow velocity profile;
- the dimensions of the computational domain, referenced to the length H;
- the number of grid points used;
- subgrid model used ("Sc"means the Schumann model (5.70); "MSM"the Mixed Scale Model (4.116); "SF"the Structure Function model (4.102); "DynLoc"the constrained localized dynamic model (4.188)). As before for the round jet, only subgrid viscosity models have been used in the configuration.
- upstream condition generation mode: $U+b$ means the same thing as before, while P designates the use of a precursor, which in this case is a large-eddy simulation of a plane channel flow in [103]; Ca indicates the use of an inflow channel to allow the development of a "realistic"turbulence upstream of the separation. Depending on the author, the length of this channel is between four and ten H.
- treatment of the solid walls: "-"is the no-slip condition; MSc the Schumann wall model, (9.19) to (9.21); MGz the Grötzbach wall model (9.22). It can be seen that the use of wall models reduces the number of points considerably and makes it possible to simulate flows with high Reynolds numbers.
- spatial accuracy of the numerical method;
- time accuracy of the numerical method.

The results the various authors have obtained are generally in good qualitative agreement with experimental data: the flow topology is recovered and the realizations show the existence of coherent structures similar to those observed in the laboratory. On the other hand, there is much more difficulty obtaining quantitative agreement whenever this is possible at all (only ref-

erence [122] produces results in satisfactory agreement on the mean velocity field and turbulent intensity). This is due to the very high sensitivity of the result to the computation parameters. For example, variations of the order of 100 % of the average length of the recirculation region have been recorded when the inflow boundary condition or subgrid model are manipulated. This sensitivity stems from the fact that the flow dynamics is governed by that of the separated shear layer, so the problems mentioned before concerning free shear flows crop up here. We also note a tendency to under-estimate the value of the mean velocity in the recirculation area. However, as in the case of the round jet, the simulated physics does correspond to that of a backward facing step flow. This is illustrated by the mean velocity profiles and resolved Reynolds stresses in Fig. 11.13, and the pressure spectra in Fig. 11.14. The good agreement with experimental data in the prediction of the mean field and Reynolds stresses proves the theoretical consistency of the computation. This agreement is even clearer if we analyze the spectra. Near the step, the mixing layer dynamics is dominated by frequencies associated with the Kelvin-Helmholtz instability. The predicted value of the dominant frequency is in very good agreement with experimental observations. The double peak at the second measurement point shows that the simulation is capable of reflecting the low-frequency flapping mechanism of the separated region, and still remain in good agreement with experimental observations.

Also, it seems that the use of wall models does not affect the dynamics of this shear layer greatly. It becomes possible to deal with higher Reynolds numbers, but at the price of losing some of the quality of the results as concerns the wall surface terms (friction, pressure coefficient) in the recirculation zone [39]. Solutions for this configuration turn out to be highly dependent on the subgrid model: too dissipative a model will retard the development of the separated shear layer, pushing away the position of the reattachment point.

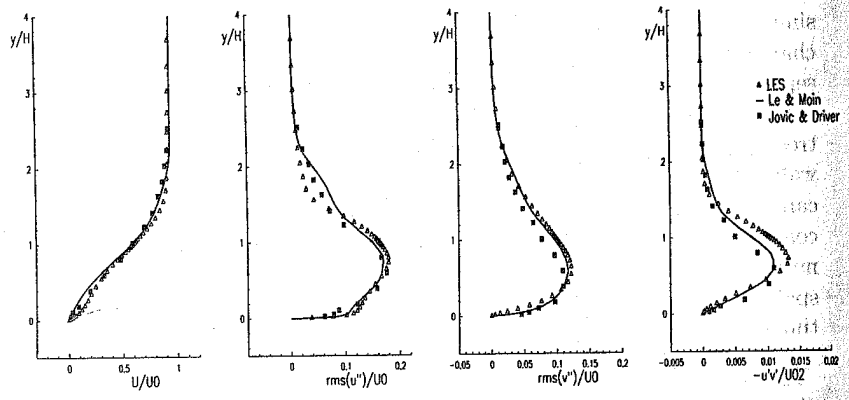

Fig. 11.13. Backward Facing Step. Mean velocity and Reynolds stresses profiles at the reattachment point. Triangles and solid line: LES computations. Squares: experimental data. With the permission of F. Delcayre, LEGI.

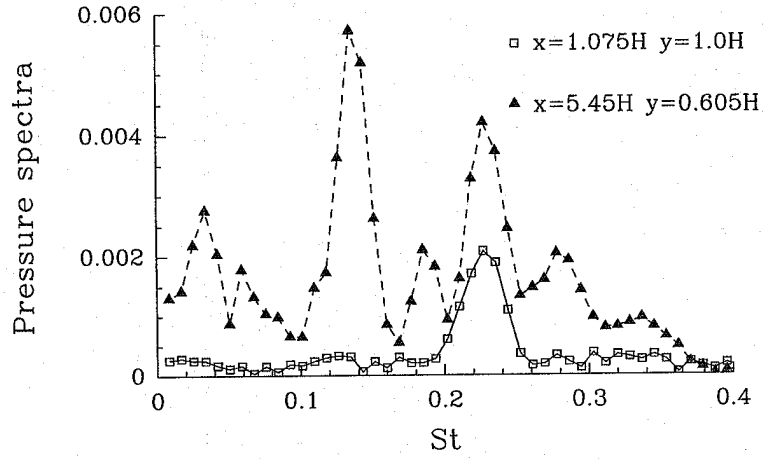

Fig. 11.14. Backward Facing Step. Pressure spectra. Squares: in the free shear layer near the step corner. Triangles: in the separated region near the reattachment point. With the permission of F. Delcayre, LEGI.

The results are also found to be dependent on the size of the domain and the fineness of the mesh in the spanwise direction, because these parameters affect the development of the mixing layer emanating from the step corner. A spanwise domain width of 4 to 6 H is considered to be a minimum in order to be able to capture the three-dimensional mechanisms at low frequencies. Lastly, the time frequencies associated with the separated zone dynamics are robust parameters in the sense that they are often predicted with precision.

11.3.3 Square-Section Cylinder

Problem Description. The square-section infinite-span cylinder is a good example of separated external flows around bluff bodies. This type of configuration involves phenomena as diversified as the impact of the flow on a body, its separation (and possible reattachment) on the body surface, the formation of a near-wake region, and alternating vortex street, and the development of the wake up to a self-similar solution. Each of these phenomena poses its own particular numerical and modeling problems.

Realizations. This flow was chosen as an international test case for large-eddy simulation, and has consequently served as a basis for many computations, which are mostly summarized in [279] (see also [254, 333, 334] for a

discussion of this test case). The test case parameters are: a Reynolds number Re_D, referenced to the length D of the cylinder edge and the freestream velocity, equal to 22,000, and a computational domain of $20D \times 4D \times 14D$. The span is assumed to be infinite and a periodicity condition is used in this direction.

None of the sixteen computations collected in [279] produces an overall good agreement with experimental data, *i.e.* is capable of predicting all of the following parameters with an error of less than 30 %: average lift and drag; drag and lift variances; main vortex shedding frequency; and average length of the separated region behind the cylinder. Average lift and drag, as well as the vortex shedding frequency, are very often predicted very satisfactorily. This is due to the fact that these quantities do not depend on the small scale turbulence and are governed by Von Karman structures, which are very large in size. The length of the recirculation region behind the cylinder is very often under-estimated, as is the amplitude of the mean velocity in this region. Also, the mean velocity in the wake is only very rarely in agreement the experimental data.

The numerical methods used are of moderate order of accuracy (at most second-order in space and third-order in time), and third-order upstream upwind schemes are often used for the convection term. Only subgrid viscosity models have been used (Smagorinsky model, various dynamic models, Mixed Scale Model). Certain authors use wall models at the cylinder surface.

The lack of agreement with experimental data is explained by the very high sensitivity of the different driving mechanisms to the numerical errors and to the diffusion introduced by the models. So we again find here the problems mentioned above for the case of the backward facing step, but now they are amplified by the fact that, in order to master the impact phenomenon numerically, the numerical diffusion introduced is much stronger than in the former case. Also, as most of the grids used are Cartesian and monodomain, the resolution near the cylinder is too weak to allow a satisfactory representation of the boundary layers.

11.3.4 Other Examples

Many other flows have been examined by large-eddy simulation.

Among wall-bounded flows without separation, we may mention: flat plate boundary layer [92, 109, 206]; boundary layer on a curved surface in the presence of Görtler vortices [203]; flow in a circular-section toric pipe [298]; three-dimensional boundary layer in equilibrium [349]; juncture flow [316].

Examples of recirculating flows are: confined coaxial round jets [3]; flow around a wing section of infinite span at incidence [151–153, 161, 180] (see Fig. 11.15); flow in a planar asymmetric diffuser [95, 158, 160, 162]; flow around a cube mounted on a flat plate [219, 255, 279, 345]; flow around a circular-section cylinder [18, 36, 155, 237, 238]; flow in a lid-driven cavity [366]; flow in

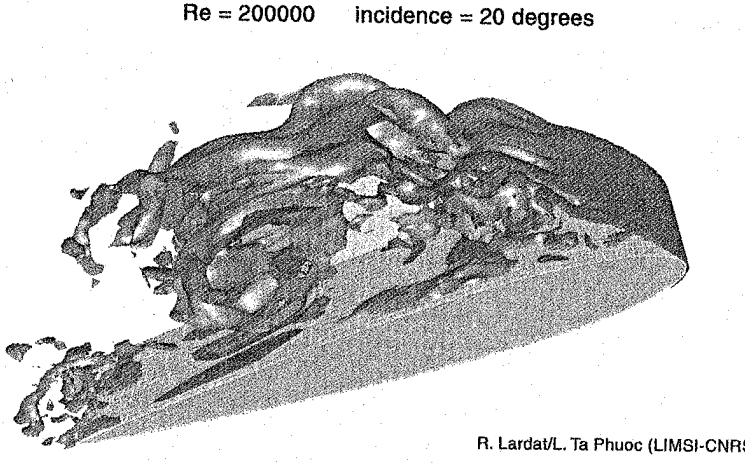

Fig. 11.15. Flow around a wing at high incidence: iso-surface of instantaneous vorticity. With the permission of R. Lardat and L. Ta Phuoc, LIMSI.

a ribbed channel [64, 354]; jet impacting a flat plate [261, 277, 338]; boundary layer on a wavy surface or a bump [88, 135, 173, 350–352]; flow over a swept wedge [144]; flow past a blunt trailing edge [217]; separated boundary layer [40, 346].

11.4 Lessons

11.4.1 General Lessons

We can draw the following lessons concerning the large-eddy simulation technique from the computations mentioned above:

- When the technique is used for dealing with the ideal case in which it was derived (homogeneous turbulence, optimum numerical method), it yields very good results. The vast majority of subgrid models produce results that are indiscernable from reality, which removes any discriminatory character from this type of test case, which in fact can only be used to assess the consistency of the method.
- Extending the technique to inhomogeneous cases brings up many other problems, concerning both the physical modeling (subgrid models) and the numerical method. The latter point becomes crucial because the use of numerical methods of moderate order of accuracy (generally two) greatly increases the effect of the numerical error. This is accentuated by the use of artificial dissipations for stabilizing the simulation in "stiff"cases (strong under-resolution, strong gradients). This error seems to be reducable by

refining the computational grid, which is done more and more by using adaptive grids (local adaptation or enrichment).
- Shear flows show themselves to be very strongly dependent on the inflow condition when this is unsteady. Generating these conditions is still an open problem.
- The quality of the results is variable but, for each configuration, robust, correctly predicted parameters exist. The physics simulated is often consistent in that it exhibits the generic features that are observed experimentally but does not necessarily correspond to a desired target realization. This is due to the dependency on the many simulation parameters.
- The quality of the results is subordinate to the correct representation of the flow driving mechanisms (transition, near-wall dynamics, and so forth). Low numerical error and consistent modeling are therefore mandatory in those regions where these mechanisms occur. The other regions of the flow where the energy cascade is the dominant mechanism are of lesser importance.
- When the flow dynamics becomes complex, subgrid viscosity models are often used. This is because they provide a clear kinetic energy dissipation and therefore stabilize the simulation. This stabilizing character seems to become predominant compared with the physical quality of the modeling insofar as the numerical difficulties increase (with the presence of strong highly heterogeneous grids, and so forth).
- There is a consensus today that the numerical method used must be accurate to at least the second order in space and time. First-order accurate numerical dissipations are totally proscribed. Third-order accurate methods in time are rarely used. As concerns the spatial accuracy, satisfactory results are obtained by certain authors with second-order accurate methods, but higher-order accurate schemes are often used. Numerical stabilization methods (upwind scheme, artificial dissipation, smoothing, and so forth) should be used only when absolutely necessary.

11.4.2 Subgrid Model Efficiency

Here we will try to draw some conclusions concerning the efficiency of the subgrid models for processing a few generic flows. These conclusions should be taken with caution. As we have seen all through this book, very many factors (numerical method, grid, subgrid model, and others) are involved and are almost indissociable, so it is very difficult to try to isolate the effect of a model in a simulation. The conclusions presented are statistical in the sense that they are the fruit of an analysis of simulations performed on similar (at least geometrically) flow configurations with different methods. A "deterministic" analysis could lead to contradictory conclusions, depending on the other. Also, there is no question of ranking the models, as the available information is too spotty to draw up a reliable list. Lastly, very many factors like the discretization of the subgrid models still remain to be studied.

We may, however, sketch out the following conclusions.

1. To simulate a homogeneous flow:
   a) All subgrid models including a subgrid viscosity yield similar results.
   b) Scale similarity models do not yield good results if used alone. This is also true for all the other types of flows.
2. To simulate a free shear flow (mixing layer, jet, wake):
   a) Subgrid viscosity models based on the large scales can delay the transition. This problem can be remedied by using a dynamic procedure, a selection function, or an accentuation technique. The other subgrid viscosity models seem to allow the transition without any harmful effects.
   b) Using a mixed structural/functional model improves the results obtained with a subgrid viscosity model based on the large scales.
3. To simulate a boundary layer or plane channel flow:
   a) Subgrid viscosity models based on the resolved scales may inhibit the driving mechanisms and re-laminarize the flow. As before, this problem is resolved by using a dynamic procedure, selection function, or accentuation technique. The other subgrid viscosity models do not seem to exhibit this defect.
   b) Using a mixed functional/structural model can improve the results by taking the driving mechanisms better into account.
   c) Using a model for the backward cascade can also improve the results.
4. For separated flows (backward facing step, for example), use a model that can yield good data on a free shear flow (to capture the dynamics of the recirculating area) and on a boundary layer (to represent the dynamics after the reattachment point).
5. For transitional flows:
   a) Subgrid viscosity models based on the gradients of the resolved scales generally yield poor results because they are too dissipative and damp the phenomena. This problem can be remedied by using a dynamic procedure, a selection function, or the accentuation technique.
   b) Anisotropic tensorial models can inhibit the growth of certain three-dimensional modes and lead to unexpected scenarios of transition to turbulence.
6. For fully developed turbulent flows, the problems with subgrid viscosity models based on the large scales are less pronounced than in the previous cases. Because these flows have a marked dissipative character, they produce results that are sometimes better than the other models because they ensure numerical stability properties in the simulation.

A. Statistical and Spectral Analysis of Turbulence

A.1 Turbulence Properties

Flows qualified as "turbulent" can be found in most fields that make use of fluid mechanics. These flows posses a very complex dynamics whose intimate mechanisms and repercussions on some of their characteristics of interest to the engineer should be understood in order to be able to control them. The criteria for defining a turbulent flow are varied and nebulous because there is no true definition of turbulence. Among the criteria most often retained, we may mention [68]:

- the random character of the spatial and time fluctuations of the velocities, which reflect the existence of finite characteristic scales of statistical correlation (in space and time);
- the velocity field is three-dimensional and rotational;
- the various modes are strongly coupled, which is reflected in the non-linearity of the mathematical model retained (Navier–Stokes equations);
- the large mixing capacity due to the agitation induced by the various scales;
- the chaotic character of the solution, which exhibits a very strong dependency on the initial condition and boundary conditions.

A.2 Foundations of the Statistical Analysis of Turbulence

A.2.1 Motivations

The very great dynamical complexity of turbulent flows makes for a very lengthy deterministic description of them. To analyze and model them, we usually refer to a statistical representation of the fluctuations. This reduces the description to that of the various statistical moments in the solution, which sharply reduces the volume of information. Moreover, the random character of the fluctuations make this approach natural.

A.2.2 Statistical Average: Definition and Properties

We use $\langle\phi\rangle$ to denote the stochastic mean (or statistical average, or mathematical expectation, or ensemble average) of a random variable ϕ calculated from n independent realizations of the same phenomenon $\{\phi_l\}$:

$$\langle\phi\rangle = \lim_{n\to\infty} \frac{1}{n}\sum_{l=1}^{n} \phi_l \quad . \tag{A.1}$$

The turbulent fluctuation ϕ'_l associated with the realization ϕ_l is defined as its deviation from the mathematical expectation:

$$\phi'_l = \phi_l - \langle\phi\rangle \quad . \tag{A.2}$$

By construction, we have the property:

$$\langle\phi'\rangle \equiv 0 \quad . \tag{A.3}$$

On the other hand, fluctuation moments of second or higher order are not necessarily zero. The standard deviation σ can be defined as:

$$\sigma^2 = \langle\phi'^2\rangle \quad . \tag{A.4}$$

We define the *turbulence intensity* as $\sigma/\langle\phi\rangle$.

The correlation at two points in space and two times, $(\mathbf{x},\mathbf{x}')$ and (t,t') of the two random variables ϕ and ψ, denoted $R_{\phi\psi}(\mathbf{x},\mathbf{x}',t,t')$ is:

$$R_{\phi\psi}(\mathbf{x},\mathbf{x}',t,t') = \langle\phi(\mathbf{x},t)\psi(\mathbf{x}',t')\rangle \quad . \tag{A.5}$$

A.2.3 Ergodicity Principle

When ϕ is a random steady function in time (*i.e.* its probability density function is independent of time), we can apply the ergodicity principle according to which it is equivalent, statistically speaking, to consider indefinitely repeated experiments with a single drawing or a single experiment with an infinite number of drawings. We will therefore admit that a single experiment of infinite duration can be considered as representative of all possible scenarios.

The theorem of ergodicity says that the quadratic mean of the random function $\phi_T(t)$ defined by:

$$\phi_T(t) = \frac{1}{T}\int_t^{t+T} \phi(t')dt' \quad , \tag{A.6}$$

converges to a non-random limit equal to the stochastic mean $\langle\phi\rangle$ as $T\to\infty$ only on the condition that:

$$\lim_{T\to\infty} \frac{1}{T}\int_0^T R_{\phi'\phi'}(t)dt = 0 \quad , \tag{A.7}$$

where $R_{\phi'\phi'}(t)$ is the time autocorrelation (or covariance) of the fluctuations of ϕ over time interval t:

$$R_{\phi'\phi'}(t) = \langle(\phi(t') - \langle\phi\rangle)(\phi(t'+t) - \langle\phi\rangle)\rangle \quad . \tag{A.8}$$

For turbulent fluctuations, the random character reflects the fact that $R_{\phi'\phi'}(t)\to 0$ as $t\to 0$. So if we define the mean in time $\overline{\phi}$ as the limit of ϕ_T as $T\to\infty$, *i.e.*:

$$\overline{\phi} = \lim_{T\to\infty} \frac{1}{T}\int_0^T \phi(t)dt \quad , \tag{A.9}$$

we get the equality:

$$\overline{\phi} = \langle\phi\rangle \quad . \tag{A.10}$$

We establish that the standard error varies as $1/\sqrt{T}$ for sufficiently large T. Another way of estimating $\langle\phi\rangle$ is to construct the "experimental" average ϕ_n defined as the arithmetic mean from experiments:

$$\phi_n(t) = \frac{1}{n}\sum_{i=1}^{n} \phi_i(t) \quad , \tag{A.11}$$

where the time t is arbitrary since the flow is assumed to be statistically steady. We show that the standard error decreases as $1/\sqrt{n}$ if the experiments ϕ_l are independent.

Let ϕ and ψ be two random variables. The operator $\langle\,\rangle$ thus defined verifies the following properties, sometimes called Reynolds rules:

$$\langle\phi+\psi\rangle = \langle\phi\rangle + \langle\psi\rangle \quad , \tag{A.12}$$

$$\langle a\phi\rangle = a\langle\phi\rangle \quad \text{a= const.} \quad , \tag{A.13}$$

$$\langle\langle\phi\rangle\psi\rangle = \langle\phi\rangle\langle\psi\rangle \quad , \tag{A.14}$$

$$\langle\frac{\partial\phi}{\partial s}\rangle = \frac{\partial\langle\phi\rangle}{\partial s} \qquad s = \mathbf{x}, t \quad , \tag{A.15}$$

$$\langle\int \phi(\mathbf{x},t)d^3\mathbf{x}dt\rangle = \int\langle\phi(\mathbf{x},t)\rangle d^3\mathbf{x}dt \quad . \tag{A.16}$$

Any operator that verifies these properties is called a Reynolds operator. We deduce from these relations the properties:

$$\langle\langle\phi\rangle\rangle = \langle\phi\rangle \quad , \tag{A.17}$$

$$\langle\phi'\rangle = 0 \quad . \tag{A.18}$$

A.2.4 Decomposition of a Turbulent Field

Decomposition Principle. One technique very commonly used for describing a turbulent field is statistical representation. The velocity field at time t and position $\mathbf{x}$ splits into:

$$\mathbf{u}(\mathbf{x},t) = \langle \mathbf{u}(\mathbf{x},t) \rangle + \mathbf{u}'(\mathbf{x},t) \quad . \tag{A.19}$$

Using this decomposition and the stochastic mean, we define an evolution equation for the quantity $\langle \mathbf{u}(\mathbf{x},t) \rangle$. To recover all the information contained in the $\mathbf{u}(\mathbf{x},t)$ field, we have to handle an infinite set of equations for the statistical moments of it. The quadratic non-linearity of the Navier–Stokes equations induces an intrinsic coupling among the various moments of the solution: the evolution equation of the moment of order n in the solution uses the moment of order $(n+1)$. To recover all the information in the exact solution, it is thus necessary to solve an infinite hierarchy of coupled equations. As this is impossible in practice, this hierarchy is truncated at an arbitrarily chosen level so as to obtain a finite number of equations. This truncation brings out an unknown term that will be modeled using closure hypotheses. If the degree of precision of the information obtained theoretically increases with the number of equations retained, the consequences of the truncation and of the hypotheses used are difficult to predict.

Equations of the Stochastic Moments. The evolution equations of the mean field are obtained by applying the averaging operator to the Navier–Stokes equations. By applying the rules of commutation with the derivation in the case of an incompressible Newtonian fluid and with no external forces, we get

$$\frac{\partial \langle u_i \rangle}{\partial t} + \frac{\partial}{\partial x_j} \langle u_i u_j \rangle = -\frac{\partial \langle p \rangle}{\partial x_i} + \nu \frac{\partial^2 \langle u \rangle}{\partial x_j \partial x_j} \quad , \tag{A.20}$$

$$\frac{\partial \langle u_i \rangle}{\partial x_i} = 0 \quad , \tag{A.21}$$

where ν is the kinematic viscosity. The non-linear term $\langle u_i u_j \rangle$ is unknown and has to be decomposed as a function of $\langle \mathbf{u} \rangle$ and $\mathbf{u}'$. By introducing relation (A.19) and considering the properties (A.12) to (A.18), we get:

$$\langle u_i u_j \rangle = \langle u_i \rangle \langle u_j \rangle + \langle u_i' u_j' \rangle \quad . \tag{A.22}$$

The last term of the right-hand side, called the Reynolds tensor, is unknown and has to be evaluated. It represents the coupling between the fluctuations and the mean field. This evaluation can be made by solving the corresponding evolution equation, either by employing a model, called closure or turbulence model.

A.2.5 Isotropic Homogeneous Turbulence

Definitions. A field is said to be statistically homogeneous along the parameter x, or imprecisely just "homogeneous", if its statistical moments are independent of the value of x where the measurements are made. This is expressed:

$$\frac{\partial}{\partial x} \langle \phi_1 .... \phi_n \rangle = 0 \quad . \tag{A.23}$$

A homogeneous field is said to be statistically isotropic (in the Taylor sense), or more simply "isotropic", if all statistical moments relative to a set of points $(x_1, ..., x_n)$ at times $(t_1, ..., t_n)$ remains invariant when the set of n points and the coordinate axis are rotated, and if there is statistical invariance for symmetry about an arbitrary plane.

We may note that there exists an idea of quasi-isotropy introduced by Moffat, which does not require the invariance by symmetry.

A Few Properties. A turbulent field is said to be homogeneous (resp. homogeneous isotropic) if its velocity fluctuation $\mathbf{u}'$ is homogeneous (resp. homogeneous isotropic). One necessary condition for achieving homogeneity is that the mean velocity gradient be constant in space:

$$\frac{\partial \langle u_i \rangle}{\partial x_j} = \text{const.} \tag{A.24}$$

Isotropy requires that the mean field $\langle \mathbf{u} \rangle$ be zero. When the turbulence is isotropic, only the diagonal elements of the Reynolds tensor are non-zero. Moreover, these are mutually equal:

$$\langle u_i' u_j' \rangle = \frac{2}{3} K \delta_{ij} \quad , \tag{A.25}$$

where K is the turbulent kinetic energy.

A.3 Introduction to Spectral Analysis of the Isotropic Turbulent Fields

A.3.1 Definitions

The tensor of correlations at two points $R_{\alpha\beta}(\mathbf{r})$ of a statistically homogeneous vector field $\mathbf{u}$ defined as:

$$R_{\alpha\beta}(\mathbf{r}) = \langle u_\alpha(\mathbf{x}+\mathbf{r}) u_\beta(\mathbf{x}) \rangle \tag{A.26}$$

can be related to a spectral tensor $\Phi_{\alpha\beta}(\mathbf{k})$ by the following two relations:

$$R_{\alpha\beta}(\mathbf{r}) = \int \Phi_{\alpha\beta}(\mathbf{k}) e^{\mathrm{i}k_j r_j} d^3\mathbf{k} \quad , \tag{A.27}$$

$$\Phi_{\alpha\beta}(\mathbf{k}) = \frac{1}{(2\pi)^3} \int R_{\alpha\beta}(\mathbf{r}) e^{-\mathrm{i}k_j r_j} d^3\mathbf{k} \quad , \tag{A.28}$$

where $\mathrm{i}^2 = -1$. The tensor at the origin, $R_{\alpha\beta}(0)$, is the Reynolds tensor. In the case of an isotropic field, the general form of the correlation tensor becomes:

$$R_{\alpha\beta}(r) = K\left([f(r) - g(r)] \frac{r_\alpha r_\beta}{r^2} + g(r)\delta_{\alpha\beta} \right) \quad , \tag{A.29}$$

where $f(r)$ and $g(r)$ are two real scalar functions. When the velocity field is solenoidal, these two functions are related by:

$$g(r) = f(r) + \frac{r}{2}\frac{\partial f(r)}{\partial r} \quad . \tag{A.30}$$

The incompressibility constraint also allows us to establish the following relation for the tensor $\Phi_{\alpha\beta}(\mathbf{k})$:

$$\Phi_{\alpha\beta}(\mathbf{k}) = \frac{E(\mathbf{k})}{4\pi k^2}\left(\delta_{\alpha\beta} - \frac{k_\alpha k_\beta}{k^2} \right) \quad , \tag{A.31}$$

where the scalar function $E(\mathbf{k})$ is called a three-dimensional spectrum. It represents the contribution of the wave vectors of k to the turbulent kinetic energy, *i.e.* wave vectors whose tips are included in the region located between two spheres of radius k and $k+dk$. The spectral energy density, denoted $A(\mathbf{k})$, is therefore equal to $E(\mathbf{k})/4\pi k^2$. The three-dimensional spectrum is computed from the spectral tensor by integration over the sphere of radius k:

$$E(k) = \frac{1}{2}\int \Phi_{ii}(\mathbf{k}) dS(\mathbf{k}) \quad , \tag{A.32}$$

where $dS(\mathbf{k})$ is the integration element on the sphere of radius k. This quantity can also be related to the function $f(r)$ by the relation:

$$E(k) = \frac{K}{\pi}\int_0^\infty kr\left(\sin(kr) - kr\cos(kr)\right) f(r) dr \quad . \tag{A.33}$$

The turbulent kinetic energy, K, is found by summation over the entire spectrum:

$$K \equiv \frac{\langle u_i' u_i' \rangle}{2} = \int_0^\infty E(\mathbf{k}) d^3\mathbf{k} \quad . \tag{A.34}$$

By construction, the spectral tensor has the property:

$$\Phi_{ij}(-\mathbf{k}) = \Phi_{ij}^*(\mathbf{k}) \quad , \tag{A.35}$$

where the asterisk indicates the complex conjugate number. The homogeneity property of the turbulent field implies:

$$\Phi_{ij}(\mathbf{k}) = \Phi_{ji}^*(\mathbf{k}) \quad . \tag{A.36}$$

The spectral tensor can also be related to the velocity fluctuation $\mathbf{u}'$ and to its Fourier transform $\widehat{\mathbf{u}}'$ defined as:

$$\widehat{\mathbf{u}}_i'(\mathbf{k}) = \frac{1}{(2\pi)^3}\int \mathbf{u}'(\mathbf{x}) e^{-\mathrm{i}k_j x_j} d^3\mathbf{x} \quad . \tag{A.37}$$

Simple expansions lead to the equality:

$$\langle \widehat{u}_i'(\mathbf{k}')\widehat{u}_j'(\mathbf{k}) \rangle = \delta(\mathbf{k}+\mathbf{k}')\Phi_{ij}(\mathbf{k}) \quad . \tag{A.38}$$

So we see that the two modes are correlated statistically only if $\mathbf{k}+\mathbf{k}' = 0$. An equivalent definition of the spectral tensor is:

$$\Phi_{ij}(\mathbf{k}) = \int \langle \widehat{u}_i'^*(\mathbf{k})\widehat{u}_j'(\mathbf{k}') \rangle d^3\mathbf{k}' \quad . \tag{A.39}$$

A.3.2 Modal Interactions

The nature of the interactions among the various modes can be brought out by analyzing the non-linear term that appears in the evolution equation associated with them. This equation, for the mode associated with the wave vector $\mathbf{k}$ (the dependency on $\mathbf{k}$ is not expressed, for the sake of simplicity) is:

$$\frac{\partial \widehat{u}_i}{\partial t} + \mathrm{i}k_j \widehat{a}_{ij} = -\mathrm{i}k_i \widehat{p} - \nu k^2 \widehat{u}_i \quad . \tag{A.40}$$

The two quantities $\widehat{a}_{ij}$ and $\widehat{p}$ are related to $u_i u_j$ and the pressure p by the relations:

$$u_i(\mathbf{x})u_j(\mathbf{x}) = \int \widehat{a}_{ij}(\mathbf{k}) e^{\mathrm{i}k_l x_l} d^3\mathbf{k} \quad , \tag{A.41}$$

$$\frac{1}{\rho}p(\mathbf{x}) = \int \widehat{p}(\mathbf{k}) e^{\mathrm{i}k_l x_l} d^3\mathbf{k} \quad . \tag{A.42}$$

By introducing the spectral decompositions:

$$u_i(\mathbf{x}) = \int \widehat{u}_i(\mathbf{k}') e^{\mathrm{i}k_l' x_l} d^3\mathbf{k}' \quad , \tag{A.43}$$

$$u_j(\mathbf{x}) = \int \widehat{u}_j(\mathbf{k}'') e^{\mathrm{i}k_l'' x_l} d^3\mathbf{k}'' \quad , \tag{A.44}$$

the non-linear term becomes:

$$u_i(\mathbf{x})u_j(\mathbf{x}) = \int \underbrace{\int \widehat{u}_i(\mathbf{k}')\widehat{u}_j(\mathbf{k}-\mathbf{k}')d^3\mathbf{k}'}_{\widehat{a}_{ij}(\mathbf{k})} e^{\mathrm{i}k_l x_l} d^3\mathbf{k} \quad , \tag{A.45}$$

where we have performed the variable change $\mathbf{k} = \mathbf{k}' + \mathbf{k}''$. The pressure term is computed by the Poisson equation:

$$\frac{1}{\rho}\frac{\partial^2 p}{\partial x_i \partial x_i} = -\frac{\partial^2 u_i u_j}{\partial x_i \partial x_j} \quad , \tag{A.46}$$

or, in the spectral space:

$$k^2 \widehat{p} = -k_l k_m \widehat{a}_{lm} \quad . \tag{A.47}$$

The momentum equation therefore takes the form:

$$\left[\frac{\partial}{\partial t} + \nu k^2\right] \widehat{u}_i(\mathbf{k}) = M_{ijm}(\mathbf{k}) \int \widehat{u}_m(\mathbf{k}')\widehat{u}_j(\mathbf{k}-\mathbf{k}')d^3\mathbf{k}' \quad , \tag{A.48}$$

in which

$$M_{ijm}(\mathbf{k}) = -\frac{\mathrm{i}}{2}\left(k_m P_{ij}(\mathbf{k}) + k_j P_{im}(\mathbf{k})\right) \quad , \tag{A.49}$$

where $P_{ij}(\mathbf{k})$ is the projection operator on the plane orthogonal to the vector $\mathbf{k}$. This operator is expressed:

$$P_{ij}(\mathbf{k}) = \left(\delta_{ij} - \frac{k_i k_j}{k^2}\right) \quad . \tag{A.50}$$

The linear terms are grouped into the left-hand side and the non-linear terms in the right. The first linear term represents the time dependency and the second the viscous effects. The non-linear term represents the effect of convection and pressure. We can see that the mode $\mathbf{k}$ interacts with the modes $\mathbf{p} = \mathbf{k}'$ and $\mathbf{q} = (\mathbf{k} - \mathbf{k}')$ such that $\mathbf{k} + \mathbf{p} = \mathbf{q}$. This triadic nature of the non-linear interactions is intrinsically related to the mathematical structure of the Navier–Stokes equations.

A.3.3 Spectral Equations

The equations for the spectral tensor components Φ_{ij} are obtained by applying an inverse Fourier transform to the transport equations of the two-point double correlations. After computation, we get:

$$\frac{\partial \Phi_{ij}}{\partial t} - \lambda_{lm} k_l \frac{\partial \Phi_{ij}}{\partial k_m} + \lambda_{il}\Phi_{lj} + \lambda_{jl}\Phi_{il} + 2\nu k^2 \Phi_{ij} = \left(k_l \Theta_{ilj} + k_l \Theta^*_{jli}\right) + \left(k_i \Sigma_j + k_j \Sigma^*_j\right) \quad , \tag{A.51}$$

where:

$$\Theta_{ilj} = \frac{\mathrm{i}}{(2\pi)^3}\int \langle u_i'(\mathbf{x})u_l'(\mathbf{x})u_j'(\mathbf{x}+\mathbf{r})\rangle e^{-\mathrm{i}k_n r_n} d^3\mathbf{r} \quad , \tag{A.52}$$

$$\Sigma_j = \frac{\mathrm{i}}{(2\pi)^3}\int \frac{1}{\rho}\langle p'(\mathbf{x})u_j'(\mathbf{x}+\mathbf{r})\rangle e^{-\mathrm{i}k_n r_n} d^3\mathbf{r} \tag{A.53}$$

$$= 2\lambda_{lm}\frac{k_l}{k^2}\Phi_{mj} - \frac{k_l k_m}{k^2}\Theta_{mlj} \quad , \tag{A.54}$$

$$\lambda_{ij} = \frac{\partial \langle u\rangle_i}{\partial x_j} \quad . \tag{A.55}$$

By expanding the terms (A.52) and (A.54), equation (A.51) takes the form:

$$\left(\frac{\partial}{\partial t} + 2\nu k^2\right)\Phi_{ij}(\mathbf{k}) + \frac{\partial \langle u_i\rangle}{\partial x_l}\Phi_{jl}(\mathbf{k}) + \frac{\partial \langle u_j\rangle}{\partial x_l}\Phi_{il}(\mathbf{k}) - 2\frac{\partial \langle u_l\rangle}{\partial x_m}\left(k_i \Phi_{jm}(\mathbf{k}) + k_j \Phi_{mi}(\mathbf{k})\right) - \frac{\partial \langle u_l\rangle}{\partial x_m}\frac{\partial}{\partial k_m}\left(k_l \Phi_{ij}(\mathbf{k})\right) = P_{il}(\mathbf{k})T_{lj}(\mathbf{k}) + P_{jl}(\mathbf{k})T^*_{li}(\mathbf{k}) \quad , \tag{A.56}$$

where

$$T_{ij}(\mathbf{k}) = k_l \int\int\int \langle u_i(\mathbf{k})u_l(\mathbf{p})u_j(-\mathbf{k}-\mathbf{p})\rangle d^3\mathbf{p} \quad . \tag{A.57}$$

The evolution equation for the energy spectrum $E(k)$, derived from (A.51) by integration over the sphere of radius k, is:

$$\frac{\partial E(k)}{\partial t} = P(k) + T(k) + D(k) \quad , \tag{A.58}$$

where the kinetic energy production term $P(k)$ by interaction with the mean field, the transfer term $T(k)$ and the dissipation term $D(k)$ are given by:

$$P(k) = -\lambda_{ij}\phi_{ij}(k) \quad , \tag{A.59}$$

$$T(k) = \frac{1}{2}\int \left(k_l(\Theta_{ili} + \Theta^*_{ili}) + \lambda_{lm}\frac{\partial(k_l \phi_{ii})}{\partial k_m}\right) dS(\mathbf{k}) \quad , \tag{A.60}$$

$$D(k) = -2\nu k^2 E(k) \quad , \tag{A.61}$$

where the tensor $\phi_{ij}(k)$ is defined as the integral of $\Phi_{ij}(\mathbf{k})$ over the sphere of radius k:

$$\phi_{ij}(k) = \int \Phi_{ij}(\mathbf{k}) dS(\mathbf{k}) \quad . \tag{A.62}$$

The kinetic energy conservation property for ideal fluid is expressed by:

$$\int_0^\infty T(k)dk = 0 \quad . \tag{A.63}$$

We come up with the kinetic energy evolution equation in the physical space by integrating the equation (A.58) over the entire spectrum:

$$\frac{\partial K}{\partial t} = \int_0^\infty \frac{\partial E(k)}{\partial t} dk = \int_0^\infty P(k)dk + \int_0^\infty T(k)dk + \int_0^\infty D(k)dk \; . \tag{A.64}$$

In the isotropic homogeneous case, production is zero and we get:

$$\frac{\partial K}{\partial t} = -\varepsilon \quad , \tag{A.65}$$

where the kinetic energy dissipation rate ε is given by:

$$\varepsilon = \int_0^\infty 2\nu k^2 E(k)dk \quad . \tag{A.66}$$

A.4 Characteristic Scales of Turbulence

Several characteristic scales of turbulence can be defined. We define the integral scale L_{ij}^l as:

$$L_{ij}^l = \int_{-\infty}^{+\infty} R_{ij}(r)dr \quad . \tag{A.67}$$

This scale is representative of the length over which the turbulent fluctuations are mutually correlated, so it is directly related to the size of the structures that form the turbulent field. Another scale, called the Taylor microscale, is denoted λ_τ and is defined as:

$$\frac{\langle u'^2 \rangle}{\lambda_\tau^2} = \langle \left(\frac{\partial u'}{\partial x} \right)^2 \rangle \quad . \tag{A.68}$$

While the first scale is associated with all the turbulent structures, this latter scale is related directly to the small scales of the turbulence. Considering that the dissipation , can be written as:

$$\varepsilon = 2\nu \langle \left(\frac{\partial u'}{\partial x} \right)^2 \rangle \quad , \tag{A.69}$$

we get the relation:

$$\varepsilon = 2\nu \frac{\langle u'^2 \rangle}{\lambda_\tau^2} \quad . \tag{A.70}$$

The Taylor microscale thus appears as characteristic of the dissipative phenomena.

A.5 Spectral Dynamics of Isotropic Homogeneous Turbulence

A.5.1 Energy Cascade and Local Isotropy

Analyses on the basis of equation (A.58) show that the dynamical mechanism associated with the term $T(k)$ is a kinetic energy transfer from the small wave numbers to the large. This process is called the energy cascade. It is relatively local in frequency: the transfers are negligible among wave numbers separated by more than two decades. It repeats itself until such time as the structures are so small that the viscous mechanisms, represented by the $D(k)$ term, become preponderant.

The local isotropy hypothesis formalized by Kolmogorov assumes statistical homogeneity and isotropy in a small space-time domain and not throughout the flow. This is equivalent to the hypothesis that the flow scales, while sufficiently small, are governed by a dynamics similar to that of isotropic homogeneous turbulence. They are thus independent of the large scales and their statistical structure acquires a universal character.

Kolmogorov's first hypothesis is that the statistical moments of the scales located in such a domain depend only on the separation distance r, the total dissipation by viscosity per unit mass ε, and the viscosity ν.

The second hypothesis is that the statistical moments for large separation distances become independent of the viscosity and are no longer a function of r and ε.

A.5.2 Equilibrium Spectrum

With the hypothesis of local isotropy, we find three distinct regions in the energy spectrum $E(k)$:

- the large scale region where the turbulence associated with the $P(k)$ term is produced. These scales are coupled with the mean field and are affected by the boundary conditions, so they possess no universal character. However, following arguments related to the finite character of the energy spectral density $A(k)$, we can say that:

$$E(k) \simeq k^4 \text{ or } E(k) \simeq k^2 \text{ for } k \ll 1 \tag{A.71}$$

- the inertial range, associated with the intermediate scales, in which the energy is transferred by non-linear interaction with no action by viscosity or production. The energy spectrum depends only on k and ε. Since the energy is transferred without loss, ε remains constant. Assuming that there exists a self-similar form of the power-law spectrum, by dimensional arguments we get:

$$E(k) = K_0 \varepsilon^{2/3} k^{-5/3} \quad , \tag{A.72}$$

where the constant K_0 called the Kolmogorov constant, is close to 1.5.

– The dissipation region, which comprises the smallest scales where the kinetic energy is dissipated by the viscous effects. In this area, the relaxation time τ_d associated with the viscous effects is at least equal to that of the non-linear transfers, denoted τ_c. For a length scale l, these two times are evaluated as:

$$\tau_d \approx l^2/\nu, \quad \tau_c \approx \nu^2/\varepsilon \quad . \tag{A.73}$$

The dissipation region is characterized by the relation:

$$\tau_d \leq \tau_c \Longrightarrow l \leq \sqrt{\nu^3/\varepsilon} \quad . \tag{A.74}$$

We call the Kolmogorov scale, which is denoted η_K, the scale for which these two times are equal and which marks the beginning of the dissipation region:

$$\eta_K = \sqrt{\nu^3/\varepsilon} \quad . \tag{A.75}$$

The characteristic velocity associated with this scale is:

$$v_K = (\nu\varepsilon)^{1/4} \quad . \tag{A.76}$$

The energy spectrum depends explicitly only on k, ν and ε, or equivalently on k, the Kolmogorov scales η_K, and v_K. The dimensional arguments do not lead to a unique form $E(k)$, and several solutions have been proposed. Arguments concerning the regularity of the velocity field and these gradients suggest an exponential decay of $E(k)$ in this region.

B. EDQNM Modeling

The EDQNM model is briefly described here in its isotropic and anisotropic versions. For more details concerning the isotropic version, the reader may refer to the work of Lesieur [189].

B.1 Isotropic EDQNM Model

Starting with the Navier–Stokes equations written in symbolic form:

$$\left(\frac{\partial}{\partial t} + \nu k^2\right) u = uu \quad , \tag{B.1}$$

we derive an infinite hierarchical set of evolution equations as usual for the statistical moments of the velocity u:

$$\left(\frac{\partial}{\partial t} + \nu k^2\right) \langle uu \rangle = \langle uuu \rangle \quad , \tag{B.2}$$

$$\left(\frac{\partial}{\partial t} + \nu(k^2+p^2+q^2)\right) \langle uuu \rangle = \langle uuuu \rangle \quad , \tag{B.3}$$

$$\ldots = \ldots \quad ,$$

where the symbol $\langle\rangle$ designates a statistical average. We then adopt the following hypothesis.

Hypothesis B.1 (Quasi-normality Hypothesis). *The velocity distribution law is close to the Gaussian bell curve and its fourth-order cumulant, denoted $\langle uuuu \rangle_c$ is zero.*

The evolution equation of the triple correlations then become:

$$\left(\frac{\partial}{\partial t} + \nu(k^2+p^2+q^2)\right) \langle uuu \rangle = \sum \langle uu \rangle \langle uu \rangle \quad . \tag{B.4}$$

The quasi-normal approximation does not provide the realizability condition, *i.e.* the spectrum $E(k)$ can take negative values. To recover this property, Orszag proposes introducing a triple-correlation damping term and then gets:

$$\left(\frac{\partial}{\partial t}+\nu(k^2+p^2+q^2)\right)\langle uuu\rangle=\sum\langle uu\rangle\langle uu\rangle-(\eta_k+\eta_p+\eta_q)\langle uuu\rangle\ . \quad \text{(B.5)}$$

The solution to this equation is:

$$\langle uuu\rangle(t)=\int_0^t\sum\langle uu\rangle\langle uu\rangle e^{-(\mu_k+\mu_p+\mu_q)t}dt \quad , \quad \text{(B.6)}$$

with

$$\mu_k=\eta_k+\nu k^2 \quad . \quad \text{(B.7)}$$

To get a solution that is easier to calculate, we adopt the following hypothesis:

Hypothesis B.2. *The relaxation time of the triple correlations is small compared with the relaxation time of the double correlations (which is also that of the energy spectrum).*

With this hypothesis, we can "Markovianize" equation (B.6), which leads to:

$$\begin{aligned}\langle uuu\rangle(t) &= \sum\langle uu\rangle\langle uu\rangle\int_0^t e^{-(\mu_k+\mu_p+\mu_q)t}dt\\ &= \sum\langle uu\rangle\langle uu\rangle\frac{1-e^{-(\mu_k+\mu_p+\mu_q)t}}{\mu_k+\mu_p+\mu_q} \quad . \end{aligned} \quad \text{(B.8)}$$

This relation closes the derivation equation of the second-order moments. This closure is equivalent to replacing the solution of the Navier–Stokes equations with that of the following Langevin-type stochastic model:

$$\left(\frac{\partial}{\partial t}+(\nu+\eta(k,t))k^2\right)u=f(k,t) \quad , \quad \text{(B.9)}$$

in which

$$\eta(k,t)=\frac{1}{2}\int\int\Theta_{kpq}(t)\frac{p}{kq}b_{kpq}E(q,t)dpdq \quad . \quad \text{(B.10)}$$

The forcing term f is such that:

$$\begin{aligned}F(k,t) &\equiv 4\pi k^2\int_0^t\langle f(k,t)f(k,s)\rangle_{|k|=cste}ds\\ &= \int\int\Theta_{kpq}(t)\frac{k^3}{pq}a_{kpq}E(p,t)E(q,t)dpdq \quad , \end{aligned} \quad \text{(B.11)}$$

where a_{kpq} and b_{kpq} are coefficients linked to the geometry of the triad $(\mathbf{k},\mathbf{p},\mathbf{q})$, defined as:

$$a_{kpq}=\frac{1}{2}(1-xyz-2y^2z^2),\ b_{kpq}=\frac{p}{k}(xy+z^3) \quad , \quad \text{(B.12)}$$

where x, y and z are the cosines of the angles of the triangle formed by the wave vectors $(\mathbf{k},\mathbf{p},\mathbf{q})$, opposed respectively to $\mathbf{k}$, $\mathbf{p}$ and $\mathbf{q}$. The relaxation time $\Theta_{kpq}(t)$ is evaluated as:

$$\Theta_{kpq}(t)=\frac{1-e^{-(\mu_k+\mu_p+\mu_q)t}}{\mu_k+\mu_p+\mu_q} \quad , \quad \text{(B.13)}$$

where the damping factor μ_k is chosen as follows:

$$\mu_k=\nu k^2+0,36\sqrt{\int_0^k p^2E(p)dp} \quad . \quad \text{(B.14)}$$

B.2 Cambon's Anisotropic EDQNM Model

To study anisotropic homogeneous flows, we define the following two spectral tensors [44] (see Appendix A):

$$\Phi_{ij}(\mathbf{k})\simeq\langle\widehat{u}_i'^*(\mathbf{k})\widehat{u}_j'(\mathbf{k})\rangle \quad , \quad \text{(B.15)}$$

$$\phi_{ij}(k)=\int\Phi_{ij}(\mathbf{k})dA(\mathbf{k}) \quad . \quad \text{(B.16)}$$

The evolution equation for the quantities $\phi_{ij}(k)$ in the presence of mean velocity gradients is:

$$\begin{aligned}\left(\frac{\partial}{\partial t}+2\nu k^2\right)\phi_{ij}(k) &= -\frac{\partial\langle u\rangle_i}{\partial x_k}\phi_{jl}(k)-\frac{\partial\langle u\rangle_j}{\partial x_l}\phi_{il}(k)\\ &+ P_{ij}^{\mathrm{l}}(k)+S_{ij}^{\mathrm{l}}(k)\\ &+ P_{ij}^{\mathrm{nl}}(k)+S_{ij}^{\mathrm{nl}}(k) \quad , \end{aligned} \quad \text{(B.17)}$$

where

$$P_{ij}^{\mathrm{l}}(k)=2\frac{\partial\langle u\rangle_l}{\partial x_m}\int\frac{k_l}{k^2}\left[k_i\Phi_{mj}(\mathbf{k})+k_j\Phi_{mi}(\mathbf{k})\right]dA(\mathbf{k}) \quad , \quad \text{(B.18)}$$

$$S_{ij}^{\mathrm{l}}(k)=\frac{\partial\langle u\rangle_l}{\partial x_m}\int\frac{\partial}{\partial k_m}\left(k_l\Phi_{ij}(\mathbf{k})\right)dA(\mathbf{k}) \quad , \quad \text{(B.19)}$$

$$P_{ij}^{\mathrm{nl}}(k) = -\int \frac{k_l}{k^2}\left[k_i T_{lj}(\mathbf{k}) + k_j T_{li}^*(\mathbf{k})\right] dA(\mathbf{k}) \quad , \tag{B.20}$$

$$S_{ij}^{\mathrm{nl}}(k) = \int \left[T_{ij}(\mathbf{k}) + T_{ij}^*(\mathbf{k})\right] dA(\mathbf{k}) \quad . \tag{B.21}$$

Equation (B.17) is closed by replacing $\Phi(\mathbf{k})$ with a modeled form as a function of $\phi(k)$, where the direction of k is controlled in the integrals (B.18) to (B.21):

$$\begin{aligned} P_{ij}^{\mathrm{l}}(k) \;=\; & 2E(k)\left[\frac{2}{5}\langle S\rangle_{ij}\right. \\ & - 3D\left(\langle S\rangle_{lj}H_{li}(k) + \langle S\rangle_{li}H_{lj}(k) - \frac{2}{3}\delta_{ij}\langle S\rangle_{lm}H_{lm}(k)\right) \\ & \left. + \frac{14}{3}\left(D+\frac{4}{7}\right)(\rangle\Omega\langle_{il}H_{lj}(k) + \langle\Omega\rangle_{jl}H_{li}(k))\right] \quad , \end{aligned} \tag{B.22}$$

$$\begin{aligned} S_{ij}^{\mathrm{l}}(k) \;=\; & -\frac{2}{15}\langle S\rangle_{ij}\frac{\partial}{\partial k}\left(kE(k)\right) + 2\langle S\rangle_{il}\frac{\partial}{\partial k}\left(kDE(k)H_{jl}(k)\right) \\ & + 2\langle S\rangle_{jl}\frac{\partial}{\partial k}\left(kDE(k)H_{il}(k)\right) \\ & - \frac{1}{3}\delta_{ij}\langle S\rangle_{lm}\frac{\partial}{\partial k}\left(\left[2+11D\right]kE(k)H_{lm}(k)\right) \quad , \end{aligned} \tag{B.23}$$

$$\begin{aligned} P_{ij}^{\mathrm{nl}}(k) \;=\; & \int\int \Theta_{kpq}\frac{2}{pq}(x+yz)H_{ij}(q)\left[k^1 pE(p)E(q)\left(y(z^2-y^2)(a(q)+3)\right.\right. \\ & \left.\left. + (y+xz)\frac{a(q)}{5}\right) - p^3E(k)E(q)y(z^2-x^2)(a(q)+3)\right] dpdq\,, \end{aligned} \tag{B.24}$$

$$\begin{aligned} S_{ij}^{\mathrm{nl}}(k) \;=\; & \int\int \Theta_{kpq}\frac{2}{pq}\left[(xy+z^3)\left(k^2pE(p)E(q)\left\{\frac{1}{3}\delta_{ij} + H_{ij}(p)\right.\right.\right. \\ & \left.\left. + H_{ij}(q)\right\} - p^3E(k)E(q)\left\{\frac{1}{3}\delta_{ij} + H_{ij}(k) + H_{ij}(q)\right\}\right) \\ & \left. + H_{ij}(q)\left(k^2pE(p)E(q)c_{kpq} - p^3E(k)E(q)c_{pkq}\right)\right] dpdq\,, \end{aligned} \tag{B.25}$$

where

$$\langle S\rangle = \frac{1}{2}\left(\nabla\langle\mathbf{u}\rangle + \nabla^T\langle\mathbf{u}\rangle\right), \quad \langle\Omega\rangle = \frac{1}{2}\left(\nabla\langle\mathbf{u}\rangle - \nabla^T\langle\mathbf{u}\rangle\right) \quad ,$$

and x, y and z are the cosines of the interior angles opposite the wave vectors $\mathbf{k}$, $\mathbf{p}$ and $\mathbf{q}$, respectively, in the triangle formed by these vectors. The anisotropy parameter $a(k)$ is optimized by the Rapid Distortion Theory. The factor D is defined as:

$$D = \frac{2}{7}\left(1 + \frac{4}{5}a\right) \quad . \tag{B.26}$$

The energy and anisotropy spectra, denoted respectively $E(k)$ and $H_{ij}(k)$, are given by the relations:

$$E(k) = \frac{1}{2}\phi_{ll}(k) \quad , \tag{B.27}$$

$$H_{ij}(k) = \frac{\phi_{ij}(k)}{2E(k)} - \frac{1}{3}\delta_{ij} \quad . \tag{B.28}$$

The geometric factor c_{kpq} is defined as:

$$c_{kpq} = \frac{1}{2}(xy+z)\left[(y^2-z^2)(a(q)+3) + \frac{2}{5}a(q)(1+z^2)\right] \quad . \tag{B.29}$$

The relaxation time $\Theta_{kpq}(t)$ is evaluated as:

$$\Theta_{kpq}(t) = \frac{1-e^{-(\mu_k+\mu_p+\mu_q)t}}{\mu_k+\mu_p+\mu_q} \quad , \tag{B.30}$$

where the damping term μ_k is:

$$\mu_k = \nu k^2 + 0,36\left(\int_0^k p^2E(p)dp + \langle\Omega\rangle_{ij}\langle\Omega\rangle_{ij}\right)^{1/2} \quad . \tag{B.31}$$

It should be noted that fully anisotropic versions, which call for no angular parameter setting, have been proposed and compared with simulations for the case of pure rotation and stable stratification [56].

References

1. Abba, A., Bucci, R., Cercignani, C., Valdettaro, L. (1996): A new approach to the dynamic subgrid scale model. Unpublished
2. Adrian, J. (1990): Stochastic estimation of subgrid-scale motions. Appl. Mech. Rev. **43**(5), 214–218
3. Akselvoll, K., Moin, P. (1996): Large-eddy simulation of turbulent confined coannular jets. J. Fluid Mech. **315**, 387–411
4. Antonopoulos-Domis, M. (1981): Aspects of large-eddy simulation of homogeneous isotropic turbulence. Int. J. Numer. Meth. Fluids **1**, 273–290
5. Arandiga, F., Donat, R., Harten, A. (1999): Multiresolution based on weighted averages of the hat function II: nonlinear reconstruction techniques. SIAM J. Sci. Comput. **20**(3), 1053–1093
6. Aupoix, B. (1984): Eddy viscosity subgrid models for homogeneous turbulence. (Proceedings of "Macroscopic modelling of turbulent flows, Lecture notes in physics, Vol. 230), Springer-Verlag, 45–64
7. Aupoix, B. (1985): Subgrid scale models for homogeneous anisotropic turbulence. (Proceedings of the Euromech Colloquium 199, "Direct and large eddy simulation of turbulence", Notes on numerical fluid mechanics, Vol. 15) Vieweg, 36–66
8. Aupoix, B. (1989): Application of two-point closures to subgrid scale modelling for homogeneous 3D turbulence. (Turbulent shear flows, von Karman Institute for Fluid Dynamics, Lecture Series 1989-03)
9. Aupoix, B., Cousteix, J. (1982): Modèles simples de tensions de sous-maille en turbulence homogène isotrope (in french). Rech. Aéro. **4**, 273–283
10. Bagget, J.S., Jimenez, J., Kravchenko, A.G. (1997): Resolution requirements in large-eddy simulations of shear flows. Annual Research Briefs - Center for Turbulence Research, 51–66
11. Balaras, E., Benocci, C., Piomelli, U. (1996): Two-layer approximate boundary conditions for large-eddy simulations. AIAA Journal **34**(6), 1111–1119
12. Bardina, J., Ferziger, J.H., Reynolds, W.C. (1980): Improved subgrid scale models for large eddy simulation. AIAA Paper 80-1357
13. Bardina, J., Ferziger, J.H., Reynolds, W.C. (1983): Improved turbulence models based on large eddy simulation of homogeneous, incompressible, turbulent flows. Report TF-19, Thermosciences Division, Dept. Mechanical Engineering, Stanford University
14. Basdevant, C., Lesieur, M., Sadourny, R. (1978): Subgrid-scale modeling of enstrophy transfer in two-dimensional turbulence. J. Atmos. Sci. **35**, 1028–1042
15. Basdevant, C., Sadourny, R. (1983): Modélisation des échelles virtuelles dans la modélisation numérique des écoulements turbulents bidimensionnels (in french). J. Mech. Théor. Appl., numéro spécial, 243–269

16. Bastin, F., Lafon, P., Candel, S. (1997): Computation of jet mixing noise due to coherent structures: the plane jet case. J. Fluid Mech. **335**, 261–304
17. Batchelor, G.K. (1953): The theory of homogeneous turbulence. Cambridge University Press
18. Beaudan, P., Moin, P. (1994): Numerical experiments on the flow past a circular cylinder at subcritical Reynolds number. Report TF-62, Thermosciences Division, Dept. Mechanical Engineering, Stanford University
19. Berkooz, G. (1994): An observation on probability density equations, or, when do simulations reproduce statistics ? Nonlinearity **7**, 313–328
20. Berkooz, G., Holmes, P., Lumley, J.L. (1993): The proper othogonal decomposition in the analysis of turbulent flows. Ann. Rev. Fluid Mech. **25**, 539–575
21. Bertoglio, J.P. (1984): A stochastic subgrid model for sheared turbulence. (Proceedings of "Macroscopic modelling of turbulent flows, Lecture notes in physics, Vol. 230) Springer-Verlag, 100–119
22. Bertoglio, J.P., Mathieu, J. (1984): A stochastic subgrid model for large-eddy simulation: general formulation. C. R. Acad. Sc. Paris **299**, série II, (12), 751–754
23. Bertoglio, J.P., Mathieu, J. (1984): A stochastic subgrid model for large-eddy simulation: generation of a stochastic process. C. R. Acad. Sc. Paris **299**, série II, (13), 835–838
24. Biringen, S., Reynolds, W.C. (1981): Large-eddy simulation of the shear-free turbulent boundary-layer. J. Fluid Mech. **103**, 53–63
25. Boersma, B.J., Kooper, M.N., Nieuwstadt, F.T.M., Wesseling, P. (1997): Local grid refinement in large-eddy simulation. J. Engng. Math.**32**, 161–175
26. Bonnet, J.P., Delville, J., Druault, P., Sagaut, P., Grohens, R. (1997): Linear stochastic estimation of LES inflow conditions. (Advances in DNS/LES, C. Liu, Z. Liu eds.) Greyden Press, 341–348
27. Boris, J.P., Book, D.L. (1973): Flux-Corrected Transport.I. SHASTA, a fluid transport algorithm that works. J. Comput. Phys. **11**, 38–69
28. Boris, J.P., Grinstein, F.F., Oran, E.S., Kolbe, R.L. (1992): New insights into large-eddy simulation. Fluid Dyn. Res. **10**, 199–228
29. Borue, V., Orszag, S.A. (1995): Forced three-dimensional homogeneous turbulence with hyperviscosity. Europhys. Lett.. **29**, 687–692
30. Borue, V., Orszag, S.A. (1995): Self-similar decay of three-dimensional turbulence with hyperviscosity. Phys. Rev. E. **52**, R856–859
31. Borue, V., Orszag, S.A. (1996): Numerical study of Kolmogorov flow at high Reynolds numbers. J. Fluid Mech. **306**, 293–323
32. Borue, V., Orszag, S.A. (1996): Kolmogorov's refined similarity hypothesis for hyperviscous turbulence. Phys. Rev. E. **366**, R21–24
33. Borue, V., Orszag, S.A. (1998): Local energy flux and subgrid-scale statistics in three-dimensional turbulence. J. Fluid Mech. **366**, 1–31
34. Bouchon, F., Dubois, T. (1999): Incremental Unknowns: a tool for large-eddy simulations ?. (Direct and Large Eddy Simulation III, Voke, Sandham and Kleiser eds) Kluwer, 275–286
35. Brasseur, J.G., Wei, C.H. (1994): Interscale dynamics and local isotropy in high Reynolds number turbulence within triadic interactions. Phys. Fluids A **6**(2), 842–870
36. Breuer, M. (1998): Large eddy simulation of the subcritical flow past a circular cylinder: numerical and modeling aspects. Int. J. Numer. Meth. Fluids **28**, 1281–1302
37. Brun, C., Kessler, P., Comte, P., Lesieur, M. (1997): Simulation des grandes échelles de jets ronds (in french). Rapport de synthèse, Contrat DGA/DRET 95-2557 A

38. Cabot, W. (1995): Large-eddy simulations with wall models. Annual Research Briefs - Center for Turbulence Research, 41–49
39. Cabot, W. (1996): Near-wall models in large-eddy simulations of flow behind a backward-facing step. Annual Research Briefs - Center for Turbulence Research, 199–210
40. Cabot, W. (1998): Large-eddy simulation of a separated boundary layer. Annual Research Briefs - Center for Turbulence Research, 279–288
41. Calgaro, C., Debussche, A., Laminie, J. (1998): On a multilevel approach for the two-dimensional Navier-Stokes equations with finite elements. Int. J. Numer. Meth. Fluids **27**, 241–258
42. Calmet, I., Magnaudet, J. (1997): Large-eddy simulation of high-Schmidt number mass transfer in a turbulent channel flow. Phys. Fluids **9**(2), 438–455
43. Cantekin, M.E., Westerink, J.J., Luettich, R.A. (1994): Low and moderate Reynolds number transient flow simulations using space filtered Navier-Stokes equations. Numer. Meth. Partial Diff. Eq. **10**, 491–524
44. Cambon, C., Jeandel, D., Mathieu, J. (1981): Spectral modelling of homogeneous non-isotropic turbulence. J. Fluid Mech. **104**, 247–262
45. Cambon, C., Mansour, N.N., Godeferd, F.S. (1997): Energy transfer in rotating turbulence. J. Fluid Mech. **337**, 303–332
46. Carati, D., Cabot, W. (1996): Anisotropic eddy viscosity models. Proceedings of the Summer Program - Center for Turbulence Research, 249–259
47. Carati, D., Ghosal, S., Moin, P. (1995): On the representation of backscatter in dynamic localization models. Phys. Fluids **7**(3), 606–616
48. Carati, D., Rogers, M.M. (1998): Ensemble-averaged LES of time-evolving plane wake. Proceedings of the Summer Program - Center for Turbulence Research, 325–336
49. Carati, D., Vanden Eijnden, E. (1997): On the self-similarity assumption in dynamic models for large-eddy simulations. Phys. Fluids **9** (7), 2165–2167
50. Carati, D., Winckelmans, G.S., Jeanmart, H. (1999): Exact expansions for filtered-scales modelling with a wide class of LES filters. (Direct and Large Eddy Simulation III, Voke, Sandham and Kleiser eds) Kluwer, 213–224
51. Carati, D., Wray, A., Cabot, W. (1996): Ensemble-averaged dynamic modeling. Proceedings of the Summer Program - Center for Turbulence Research, 237–248
52. Cerutti, S., Meneveau, G. (1998): Intermittency and relative scaling of subgrid-scale energy dissipation in isotropic turbulence. Phys. Fluids **10** (4), 928–937
53. Chapman, D.R. (1979): Computational aerodynamics development and outlook. AIAA Journal **17**(12), 1293–1313
54. Chasnov, J.R. (1990): Simulation of the Kolmogorov inertial subrange using an improved subgrid model. Phys. Fluids A **3**(1), 188–200
55. Chen, M., Temam, R. (1991): Incremental unknowns for solving partial differential equations. Numer. Math. **59**, 255–271
56. Choi, H., Moin, P. (1994): Effects of the computational time step on numerical solutions of turbulent flow. J. Comput. Phys. **113**, 1–4
57. Chollet, J.P. (1983): Two-point closures as a subgrid modelling for large-eddy simulations. (Fourth Symposium on Turbulent Shear Flows, Karlsruhe, Allemagne)
58. Chollet, J.P. (1984): Spectral closures to derive a subgrid scale modelling for large eddy simulation. (Proceedings of "Macroscopic modelling of turbulent flows, Lecture notes in physics, Vol. 230), Springer-Verlag, 161–176
59. Chollet, J.P. (1984): Turbulence tridimensionnelle isotrope: modélisation statistique des petites échelles et simulation numérique des grandes échelles (in french). Thèse de Doctorat es-sciences, Grenoble, France

60. Chollet, J.P. (1992): LES and subgrid models for reactive flows and combustion. ERCOFTAC Summer School/Workshop on modelling turbulent flows, Lyon, France
61. Chollet, J.P., Lesieur, M. (1981): Parametrization of small scales of three-dimensional isotropic turbulence utilizing spectral closures. J. Atmos. Sci. **38**, 2747–2757
62. Chorin, A., Kast, A., Kupferman, R. (1998): Optimal prediction of underresolved dynamics. Proc. Natl. Acad. Sci. USA, Applied Mathematics **95**, 4094–5098
63. Chung, Y.M., Sung, H.J. (1997): Comparative study of inflow conditions for spatially evolving simulation. AIAA Journal **35**(2), 269–274
64. Ciofalo, M., Collins, M.W. (1992): Large-eddy simulation of a turbulent flow and heat transfer in plane and rib-roughened channels. Int. J. Numer. Meth. Fluids **15**, 453–489
65. Clark, R.A., Ferziger, J.H., Reynolds, W.C. (1979): Evaluation of subgrid-scale models using an accurately simulated turbulent flow. J. Fluid Mech. **91**(1), 1–16
66. Colella, P., Woodward, P.R. (1984): The Piecewise Parabolic Method (PPM) for gas-dynamical simulations. J. Comput. Phys. **54**, 174–201
67. Cook, A.W. (1997): Determination of the constant coefficient in the scale similarity models of turbulence. Phys. Fluids **9**(5), 1485–1487
68. Cousteix, J. (1989): Turbulence et couche limite (in french). CEPADUES - Editions, France
69. Cziesla, T., Biswas, G., Mitra, N.K. (1999): Large eddy simulation in a turbulent channel flow using exit boundary conditions. Int. J. Numer. Meth. Fluids **30**, 763–773
70. Dai, Y., Kobayashi, T., Taniguchi, N. (1994): Large eddy simulation of plane turbulent jet flow using a new outflow velocity boundary condition. JSME International Journal Series B **37**(2), 242–253
71. Dakhoul, Y.M., Bedford, K.W. (1986): Improved averaging method for turbulent flow simulation. Part 1: theoretical development and application to Burger's transport equation. Int. J. Numer. Meth. Fluids **6**, 49–64
72. Dakhoul, Y.M., Bedford, K.W. (1986): Improved averaging method for turbulent flow simulation. Part 2: calculations and verification. Int. J. Numer. Meth. Fluids **6**, 65–82
73. Dang, K.T. (1985): Evaluation of simple subgrid-scale models for the numerical simulation of homogeneous turbulence. AIAA Journal **23**(2), 221–227
74. David, E. (1993): Modélisation des écoulements compressibles et hypersoniques (in french). Thèse de Doctorat de l'INPG, Grenoble, France
75. De Stefano, G., Denaro, F.M., Riccardi, G. (1998): Analysis of 3D backward-facing step incompressible flows via a local averaged-based numerical procedure. Int. J. Numer. Meth. Fluids **28**, 1073–1091
76. Deardorff, J.W. (1970): A numerical study of three-dimensional turbulent channel flow at large Reynolds numbers. J. Fluid Mech. **41**, 453–465
77. Deardorff, J.W. (1973): The use of subgrid transport equations in a three-dimensional model of atmospheric turbulence. ASME J. Fluids Engng., 429–438
78. Debussche, A., Dubois, T., Temam, R. (1995): The nonlinear Galerkin method: a multiscale method applied to simulation of homogeneous turbulent flows. Theoret. Comp. Fluid Dynamics **7**, 279–315
79. Denaro, F.M. (1996): Towards a new model-free simulation of high-Reynolds-number flows: local average direct numerical simulation. Int. J. Numer. Methods Fluids**23**, 125–142

80. Deschamps, V. (1988): Simulation numérique de la turbulence homogène incompressible dans un écoulement de canal plan (in french). ONERA, Note technique 1988-5
81. Domaradzki, J.A., Liu, W. (1995): Approximation of subgrid-scale energy transfer based on the dynamics of the resolved scales of turbulence. Phys. Fluids **7**(8), 2025–2035
82. Domaradzki, J.A., Liu, W., Brachet, M.E. (1993): An analysis of subgrid-scale interactions in numerically simulated isotropic turbulence. Phys. Fluids **5**(7), 1747–1759
83. Domaradzki, J.A., Loh, K.C. (1999): The subgrid-scale estimation model in the physical space representation. Phys. Fluids **11** (8), 2330–2342
84. Domaradzki, J.A., Metcalfe, R.W., Rogallo, R.S., Riley, J.J. (1987): Analysis of subgrid-scale eddy viscosity with the use of results from direct numerical simulations. Phys. Rev. Letter **58**(6), 546–550
85. Domaradzki, J.A., Saiki, E.M. (1997): A subgrid-scale model based on the estimation of unresolved scales of turbulence. Phys. Fluids **9** (7), 2148–2164
86. Domaradzki, J.A., Saiki, E. (1997): Backscatter models for large-eddy simulations. Theoret. Comput. Fluid Dynamics **9**, 75–83
87. Domaradzki, J.A., Yee, P.P. (2000): The subgrid-scale estimation model for high Reynolds number turbulence. Phys. Fluids **12**(1), 193–196
88. Dornbrack, A., Schumann, U. (1993): Numerical simulation of turbulent convective flow over a wavy terrain. Boundary-Layer Meteorol. **65**, 323–355
89. Dubois, T., Bouchon, F. (1998): Subgrid-scale models based on incremental unknowns for large eddy simulations.. Annual Research Briefs - Center for Turbulence Research, 221–235
90. Dubois, T., Jauberteau, F., Temam, R. (1999): Dynamic multilevel methods and the numerical simulation of turbulence. Cambridge University Press.
91. Ducros, F. (1995): Simulations numériques directes et des grandes échelles de couches limites compressibles (in french). Thèse de Doctorat de l'INPG, Grenoble, France
92. Ducros, F., Comte, P., Lesieur, M. (1996): Large-eddy simulation of transition to turbulence in a boundary layer developing spatially over a flat plate. J. Fluid Mech. **326**, 1–36
93. Engquist, B., Lötstedt, P., Sjögreen, B. (1989): Nonlinear filters for efficient shock computation. Math. Comput. **52**(186), 509–537
94. Fabignon, Y., Beddini, R.A., Lee, Y. (1995): Analytic evaluation of finite difference methods for compressible direct and large eddy simulations. ONERA, TP 1995-128
95. Fatica, M., Mittal, R. (1996): Progress in the large-eddy simulation of flow through an asymmetric plane diffuser. Annual Research Briefs - Center for Turbulence Research, 249–257
96. Fatica, M., Orlandi, P., Verzicco, R. (1994): Direct and large-eddy simulations of round jets. (Direct and Large Eddy Simulation I, Voke, C-hollet & Kleiser eds.) Kluwer, 49–61
97. Ferziger, J.H. (1977): Large eddy simulations of turbulent flows. AIAA Journal **15**(9), 1261–1267
98. Ferziger, J.H. (1997): Large eddy simulation: an introduction and perspective. (New tools in turbulence modelling, O. Métais and J. Ferziger eds.) Les éditions de physique, Springer, 29–48
99. Ferziger, J.H., Leslie, D.C. (1979): Large eddy simulation: A predictive approach to turbulent flow computation. (AIAA Comput. Fluid Conf., Williamsburg, USA)

147. Hughes, T.J.R., Stewart, J. (1996): A space-time formulation for multiscale phenomena. J. Comput. Appl. Math. **74**, 217–229
148. Hylin, E.C., McDonough, J.M.(1996): Theoretical development of a stochastic model for small-scale turbulence in an additive decomposition of the Navier-Stokes equations. ME Report No CFD-02-96, Dept. of Mechanical Engineering, University of Kentucky
149. Iliescu, T., Layton, W.J. Approximating the larger eddies in fluid motion III: the Boussinesq model for turbulent fluctuations. To be published
150. Jameson, A., Schmidt, W., Turkel, E. (1981): Numerical solutions of the Euler equations by finite volume methods using Runge-Kutta time stepping schemes. AIAA Paper 81-1259
151. Jansen, K. (1994): Unstructured-grid large-eddy simulation of flow over an airfoil. Annual Research Briefs - Center for Turbulence Research, 161–175
152. Jansen, K. (1995): Preliminary large-eddy simulations of flow around a NACA 4412 airfoil using unstructured meshes. Annual Research Briefs - Center for Turbulence Research, 61–73
153. Jansen, K. (1996): Large-eddy simulations of flow around a NACA 4412 airfoil using unstructured grids. Annual Research Briefs - Center for Turbulence Research, 225–233
154. Jordan, S.A. (1999): A large-eddy simulation methodology in generalized curvilinear coordinates. J. Comput. Phys. **148**, 322–340
155. Jordan, S.A., Ragab, S.A. (1998): A large eddy simulation of the near wake of a circular cylinder. Journal of Fluids Engineering **120**, 243–252
156. Juneja, A., Brasseur, J.G. (1999): Characterictics of subgrid-resolved-scale dynamics in anisotropic turbulence, with application to rough-wall boundary layers. Phys Fluids **11** (10), 3054–3068
157. Juneja, A., Lathrop, D.P., Sreenivasan, K.R., Stolovitzky, G. (1994): Synthetic turbulence. Phys. Rev. E. **49**(6), 5179–5194
158. Kaltenbach, H.J. (1994): Large-eddy simulation of flow through a plane, asymmetric diffuser. Annual Research Briefs - Center for Turbulence Research, 175–185
159. Kaltenbach, H.J. (1997): Cell aspect ratio dependence of anisotropy measures for resolved and subgrid scale stresses. J. Comput. Phys. **136**, 399–410
160. Kaltenbach, H.J. (1998): Towards a near-wall model for LES of a separated diffuser flow. Annual Research Briefs - Center for Turbulence Research, 255–265
161. Kaltenbach, H.J., Choi, H. (1995): Large-eddy simulation of flow around an airfoil on structured mesh. Annual Research Briefs - Center for Turbulence Research, 51–61
162. Kaltenbach, H.J., Fatica, M., Mittal, R., Lund, T.S., Moin, P. (1999): Study of flow in a planar asymmetric diffuser using large-eddy simulation. J. Fluid Mech. **390**, 151–185
163. Kaneda, Y., Leslie, D.C. (1983): Tests of subgrid models in the near-wall region using represented velocity fields. J. Fluid Mech. **132**, 349–373
164. Kanna, S., Brasseur, J.G. (1997): Analysis of Monin-Obukhov similarity from large-eddy simulation. J. Fluid Mech. **345**, 251–286
165. Kawamura, T., Kuwahara, K. (1984): Computation of high Reynolds number flow around a circular cylinder with surface roughness. AIAA Paper 84-0340
166. Kerr, R.M., Domaradzki, J.A., Barbier, G. (1996): Small-scale properties of nonlinear interactions and subgrid-scale energy transfer in isotropic turbulence. Phys. Fluids **8**(1), 197–208
167. Kosovic, B. (1997): Subgrid-scale modelling for the large-eddy simulation of high-Reynolds number boundary layers. J. Fluid Mech. **336**, 151–182

168. Kraichnan, R.H. (1967): Inertial ranges in two-dimensional turbulence. J. Fluid Mech. **10**(7), 1417–1423
169. Kraichnan, R.H. (1971): Inertial-range transfer in two- and three-dimensional turbulence. J. Fluid Mech. **47**(3), 525–535
170. Kraichnan, R.H. (1976): Eddy viscosity in two and three dimensions. J. Atmos. Sci. **33**, 1521–1536
171. Kravchenko, A.G., Moin, P., Moser, R. (1996): Zonal embedded grids for numerical simulations of wall-bounded turbulent flows. J. Comput. Phys. **127**, 412–423
172. Kravchenko, A.G., Moin, P. (1997): On the effect of numerical errors in large-eddy simulations of turbulent flows. J. Comput. Phys. **131**, 310–322
173. Krettenauer, K., Schumann, U. (1992): Numerical simulation of turbulent convection over a wavy terrain. J. Fluid Mech. **237**, 261–299
174. Kuerten, J.M.G., Geurts, B.J., Vreman, A.W., Germano, M. (1999): Dynamic inverse modeling and its testing in large-eddy simulations of the mixing layer. Phys. Fluids **11** (12), 3778–3785
175. Langford, J., Moser, R. (2000): Optimal LES formulations for isotropic turbulence. J. Fluid Mech. **398**, 321–346
176. Lamballais, E. (1996): Simulations numériques de la turbulence dans un canal plan tournant (in french). Thèse de Doctorat de l'INPG, Grenoble, France
177. Lamballais, E., Métais, O., Lesieur, M. (1998): Spectral-dynamic model for large-eddy simulations of turbulent rotating channel flow. Theoret. Comput. Fluid Dynamics **12**, 149-177
178. Landau, L., Lifchitz, E. (1967): Fluid Mechanics. MIR, Moscou
179. Launder, B.E, Spalding, D.B. (1972): Mathematical models of turbulence. Academic Press, Londres
180. Lardat, R. (1997): Simulation numériques d'écoulements externes instationnaires décollés autour d'une aile avec des modèles de sous-maille (in french). Notes et documents du LIMSI **97-12**
181. Layton, W.J. (1996): A nonlinear, subgridscale model for incompressible viscous flow problems. SIAM J. Sci. Comput. **17** (2), 347–357
182. Le Ribault, C., Sarkar, S., Stanley, S.A. (1999): Large eddy simulation of a plane jet. Phys. Fluids **11**(10), 3069–3083
183. Lee, S., Lele, S.K., Moin, P. (1992): Simulation of spatially evolving turbulence and the application of Taylor's hypothesis in compressible flow. Phys. Fluids A **4**(7), 1521–1530
184. Leith, C.E. (1990): Stochastic backscatter in a subgrid-scale model: Plane shear mixing layer. Phys. Fluids A **2**(3), 297–299
185. Lele, S.K. (1994): Compressibility effects on turbulence. Ann. Rev. Fluid. Mech. **26**, 211–254
186. Leonard, A. (1974): Energy cascade in large-eddy simulations of turbulent fluid flows. Adv. in Geophys. A **18**, 237–248
187. Leonard, B.P. (1979): A stable and accurate convective modelling procedure based on quadratic upstream interpolation. Comp. Meth. Appl. Mech. Eng. **19**, 59–98
188. Lesieur, M. (1983): Introduction à la turbulence bidimensionnelle (in french). J. Méc. Théor. Appl., numéro spécial, 5–20
189. Lesieur, M. (1997): Turbulence in fluids, 3rd edition. Kluwer
190. Lesieur, M., Métais, O. (1996): New trends in large-eddy simulations of turbulence. Ann. Rev. Fluid Mech. **28**, 45–82
191. Lesieur, M., Rogallo, R.S. (1989): Large-eddy simulation of passive scalar diffusion in isotropic turbulence. Phys. Fluids A **1**(4), 718–722

100. Foias, C., Manley, O., Temam, R. (1987): Sur l'interaction des petits et grands tourbillons dans des écoulements turbulents (in french). C.R. Acad. Sci. Paris t. **305**, série I, 497–500
101. Foias, C., Manley, O., Temam, R. (1988): Modelling of the interaction of small and large eddies in two dimensional turbulent flows. MMAN **22**(1), 93–114
102. Foias, C., Manley, O., Temam, R. (1991): Approximate inertial manifolds and effective viscosity in turbulent flows. Phys. Fluids A **3**(5), 898–911
103. Friedrich, R., Arnal, M. (1990): Analysing turbulent backward-facing step flow with the lowpass-filtered Navier-Stokes equations. J. Wind Eng. Ind. Aerodyn. **35**, 101–128
104. Fureby, C., Grinstein, F.F. (1999): Monotonically Integrated large eddy simulation of free shear flows. AIAA Journal **37**(5), 544–556
105. Fureby, C., Tabor, G. (1997): Mathematical and physical constraints on large-eddy simulations. Theoret. Comput. Fluid Dynamics **9**, 85–102
106. Fureby, C., Tabor, G., Weller, H.G., Gosman, A.D. (1997): A comparative study of subgrid scale models in homogeneous isotropic turbulence. Phys. Fluids **9**(5), 1416–1429
107. Fureby, C., Tabor, G., Weller, H.G., Gosman, A.D. (1997): Differential subgrid stress models in large eddy simulations. Phys. Fluids **9** (11), 3578–3580
108. Galdi, G.P., Layton, W.J. (2000): Approximating the larger eddies in fluid motion II: a model for space-filtered flow. Math. Models and Meth. in Appl. Sciences **10**(3), 343–350
109. Gao S., Voke, P., Gough, T. (1997): Turbulent simulation of flat plate boundary layer and near wake. (Direct and Large Eddy Simulation II, Chollet, Voke and Kleiser eds) Kluwer, 115–124
110. Garnier, E., Mossi, M., Sagaut, P., Deville, M., Comte, P. (1999): On the use of shock-capturing schemes for large-eddy simulation. J. Comput. Phys. **153**, 273–311
111. Germano, M. (1986): Differential filters for the large eddy numerical simulation of turbulent flows. Phys. Fluids **29**(6), 1755–1757
112. Germano, M. (1986): Differential filters of elliptic type. Phys. Fluids **29**(6), 1757–1758
113. Germano, M. (1986): A proposal for a redefinition of the turbulent stresses in the filtered Navier-Stokes equations. Phys. Fluids **29**(7), 2323–2324
114. Germano, M. (1987): On the non-Reynolds averages in turbulence. AIAA Paper 87-1297
115. Germano, M. (1992): Turbulence: The filtering approach. J. Fluid Mech. **238**, 325–336
116. Germano, M. (1996):A statistical formulation of the dynamic model. Phys. Fluids **8** (2), 565–570
117. Germano, M. (1998): Fundamentals of large-eddy simulation. Unpublished
118. Germano, M., Piomelli, U., Moin, P., Cabot, W.H. (1991): A dynamic subgrid-scale eddy viscosity model. Phys. Fluids A **3**(7), 1760–1765
119. Geurts, B. (1997): Inverse modeling for large-eddy simulation. Phys. Fluids **9** (12), 3585–3587
120. Ghosal, S. (1996): An analysis of numerical errors in large-eddy simulations of turbulence. J. Comput. Phys. **125**, 187–206
121. Ghosal, S. (1999):): Mathematical and physical constraints on large-eddy simulation of turbulence. AIAA J. **37** (4), 425–433
122. Ghosal, S., Lund, T.S., Moin, P., Akselvoll, K. (1995): A dynamic localization model for large-eddy simulation of turbulent flows. J. Fluid Mech. **286**, 229–255

123. Ghosal, S., Moin, P. (1995): The basic equations for the large-eddy simulation of turbulent flows in complex geometry. J. Comput. Phys. **118**, 24–37
124. Ghosal, S., Rogers, M. (1997): A numerical study of self-similarity in a turbulent plane wake using large-eddy simulation. Phys. Fluids **9**(6), 1729–1739
125. Gonze, M.A. (1993): Simulation numérique des sillages en transition à la turbulence (in french). Thèse de Doctorat de l'INPG, Grenoble, France
126. Grinstein, F.F., Guirguis, R.H. (1992): Effective viscosity in the simulation of spatially evolving shear flows with monotonic FCT models. J. Comput. Phys. **101**, 165–175
127. Grötzbach, G. (1987): in Encyclopedia of Fluid Mechanics, édité par N.P. Chereminisoff (Gulf, West Orange, NJ), Vol. 6
128. Härtel, C., Kleiser, L. (1997): Galilean invariance and filtering dependence of near-wall grid-scale/subgrid-scale interactions in large-eddy simulation. Phys. Fluids **9**(2), 473–475
129. Härtel, C., Kleiser, L. (1998): Analysis and modelling of subgrid-scale motions in near-wall turbulence. J. Fluid Mech. **356**, 327–352
130. Härtel, C., Kleiser, L., Unger, F., Friedrich, R. (1994): Subgrid-scale energy transfer in the near-wall region of turbulent flows. Phys. Fluids **6**(9), 3130–3143
131. Harten, A. (1984): On a class of high resolution total-variation-stable finite-difference schemes. SIAM J. Numer. Anal. **21**, 1–23
132. Harten, A. (1993): Discrete multi-resolution analysis and generalized wavelets. Applied Numerical Mathematics **12**, 153–192
133. Harten, A. (1995): Multiresolution algorithms for the numerical solution of hyperbolic conservation laws. Communication on Pure and Applied Mathematics **XLVIII**, 1305–1342
134. Harten, A. (1996): Multiresolution representation of data: a general framework. SIAM J. Numer. Anal. **33**(3), 1205–1256
135. Henn, D.S., Sykes, R.I. (1999): Large-eddy simulation of flow over wavy surfaces. J. Fluid Mech. **383**, 75–112
136. Hirsch, C. (1987): Numerical computation of internal and external flows. John Wiley & Son
137. Horiuti, K. (1985): Large eddy simulation of turbulent channel flow by one-equation modeling. J. Phys. Soc. Japan **54**(8), 2855–2865
138. Horiuti, K. (1987): Comparison of conservative and rotational forms in large eddy simulation of turbulent channel flow. J. Comput. Phys. **71**, 343–370
139. Horiuti, K. (1989): The role of the Bardina model in large eddy simulation of turbulent channel flow. Phys. Fluids A **1**(2), 426–428
140. Horiuti, K. (1990): Higher-order terms in the anisotropic representation of Reynolds stresses. Phys. Fluids A **2**(10), 1708–1710
141. Horiuti, K. (1993): A proper velocity scale for modeling subgrid-scale eddy viscosities in large eddy simulation. Phys. Fluids A **5**(1), 146–157
142. Horiuti, K. (1997): Backward scatter of subgrid-scale energy in wall-bounded turbulence and free shear flow. J. Phys. Soc. Japan **66**(1), 91–107
143. Horiuti, K. (1997): A new dynamic two-parameter mixed model for large-eddy simulation. Phys. Fluids **9**(11), 3443–3464
144. Huai, X., Joslin, R.D., Piomelli, U. (1999): Large-eddy simulation of boundary-layer on a swept wedge. J. Fluid Mech. **381**, 357–380
145. Hughes, T.J.R. (1995): Multiscale phenomena: Green's function, the Dirichlet-to-Neumann formulation, subgrid scale models, bubbles and the origin of stabilized methods. Comput. Methods Appl. Mech. Engrg. **127**, 387–401
146. Hughes, T.J.R., Feijoo, G.R., Mazzei, L., Quincy, J.B. (1998): The variational multiscale method - a paradigm for computational mechanics. Comput. Methods Appl. Mech. Engrg. **166**, 2–24

236. Misra, A., Pullin, D.I. (1997): A vortex-based subgrid stress model for large-eddy simulation. Phys. Fluids **9**(8), 2443–2454
237. Mittal, R. (1995): Large-eddy simulation of flow past a circular cylinder. Annual Research Briefs - Center for Turbulence Research, 107–117
238. Mittal, R. (1996): Progress on LES of flow past a circular cylinder. Annual Research Briefs - Center for Turbulence Research, 233–243
239. Mittal, R., Moin, P. (1997): Suitability of upwind-biased finite-difference schemes for large-eddy simulation of turbulent flows. AIAA Journal **35**(8), 1415–1417
240. Miyake, Y., Kajishima, T. (1986): Numerical simulation of the effects of Coriolis force on the stucture of turbulence. Global effects. Bull. JSME **29**, 3341–3346
241. Miyake, Y., Kajishima, T. (1986): Numerical simulation of the effects of Coriolis force on the stucture of turbulence. Structure of turbulence. Bull. JSME **29**, 3347–3351
242. Moeng, C.H. (1984): A large-eddy simulation model for the study of planetary boundary-layer turbulence. J. Atmos. Sci. **41**(13), 2052–2062
243. Moeng, C.H., Wyngaard, J.C. (1988): Spectral analysis of large-eddy simulations of the convective boundary layer. J. Atmos. Sci. **45**(23), 3573–3587
244. Moin, P., Jimenez, J. (1993): Large eddy simulation of complex flows. (24th AIAA Fluid Dynamics Conference, Orlando, USA)
245. Moin, P., Kim, J. (1982): Numerical investigation of turbulent channel flow. J. Fluid Mech. **118**, 341–377
246. Morikawa, H., Maruyama, T. (1999): Theory of conditional random field and its application to wind engineering. Kyoto University Press
247. Morinishi, Y., Kobayashi, T. (1990): in (Engineering turbulence modelling and experiments, Rodi and Ganic eds.) Elsevier, New York, 279
248. Morinishi, Y., Vasilyev, O. (1998): Subgrid scale modeling taking the numerical error into consideration. Annual Research Briefs - Center for Turbulence Research, 237–253
249. Mossi, M. (1999): Simulation of benchmark and industrial unsteady compressible turbulent fluid flows. PhD Thesis No 1958, EPFL, Lausanne, Switzerland.
250. Muchinsky, A. (1996): A similarity theory of locally homogeneous anisotropic turbulence generated by a Smagorinsky-type LES. J. Fluid Mech. **325**, 239–260
251. Mukerji, S., McDonough, J.M., Menguc, M.P., Manickavasagam, S., Chung, S. (1998): Chaotic map models of soot fluctuations in turbulent diffusion flames. Int. J. Heat Mass Transfer **41**, 4095–4112
252. Mullen, J.S., Fischer, P.F. (1999): Filtering technique for complex geometries fluid flows. Commun. Numer. Meth. Engng. **15**, 9–18
253. Murakami, S. (1993): Comparison of various turbulence models applied to a bluff body. J. Wind Eng. Ind. Aerodyn. **46 & 47**, 21–36
254. Murakami, S., Izuka, S., Ooka, R. (1999): CFD analysis of turbulent flow past square cylinder using dynamic LES. Journal of Fluids and Structures. **13**, 1097–1112
255. Murakami, S., Mochida, A., Hibi, K. (1987): Three-dimensional numerical simulation of air flow around a cubic model by means of large-eddy simulation. J. Wind Eng. Ind. Aerodyn. **25**, 291–305
256. Murray, J.A., Piomelli, U., Wallace, J.M. (1996): Spatial and temporal filtering of experimental data for a priori studies of subgrid-scale stresses. Phys. Fluids **8**(7), 1978–1980
257. Najjar, F.M., Tafti, D.K. (1996): Study of discrete test filters and finite difference approximations for the dynamic subgrid-scale stress model. Phys. Fluids **8**(4), 1076–1088

258. O'Neil, J., Meneveau, C. (1997): Subgrid-scale stresses and their modelling in a turbulent plane wake. J. Fluid Mech. **349**, 253–293
259. Oberlack, M. (1997): Invariant modeling in large-eddy simulation of turbulence. Annual Research Briefs - Center for Turbulence Research, 3–22
260. Olsson, M., Fuchs, L. (1996): Large eddy simulation of the proximal region of a spatially developing circular jet. Phys. Fluids **8**(8), 2125–2137
261. Olsson, M., Fuchs, L. (1998): Large eddy simulations of a forced semiconfined circular impinging jet. Phys. Fluids **10**(2), 476–486
262. Pascal, F., Basdevant, C. (1992):. Nonlinear Galerkin method and subgrid-scale model for two-dimensional turbulent flows. Theoret. Comp. Fluid Dynamics **3**, 267–284
263. Perrier, P., Pironneau, O. (1981): Subgrid turbulence modelling by homogeneization. Mathematical Modelling **2**, 295–317
264. Piomelli, U. (1993): High Reynolds number calculations using the dynamic subgrid-scale stress model. Phys. Fluids A **5**(6), 1484–1490
265. Piomelli, U., Cabot, W.H., Moin, P., Lee, S. (1990): Subgrid-scale backscatter in transitional and turbulent flows. Proceedings of the Summer Program - Center for Turbulence Research, 19–30
266. Piomelli, U., Coleman, G.N., Kim, J. (1997): On the effects of nonequilibrium on the subgrid-scale stresses. Phys. Fluids **9**(9), 2740–2748
267. Piomelli, U., Ferziger, J.H., Moin, P., Kim, J. (1989): New approximate boundary conditions for large eddy simulations of wall-bounded flows. Phys. Fluids A **1**(6), 1061–1068
268. Piomelli, U., Liu, J. (1995):Large-eddy simulation of rotating channel flows using a localized dynamic model. Phys. Fluids **7** (4), 839–848
269. Piomelli, U., Moin, P., Ferziger, J.H. (1988): Model consistency in large eddy simulation of turbulent channel flows. Phys. Fluids **31**(7), 1884–1891
270. Piomelli, U., Yunfang, X., Adrian, R.J. (1996): Subgrid-scale energy transfer and near-wall turbulence structure. Phys. Fluids **8**(1), 215–224
271. Piomelli, U., Zang, T.A., Speziale, C.G., Hussaini, M.Y. (1990): On the large-eddy simulation of transitional wall-bounded flows. Phys. Fluids A **2**(2), 257–265
272. Porter, D.H., Pouquet, A., Woodward, P.R. (1994): Kolmogorov-like spectra in decaying three-dimensional supersonic flows. Phys. Fluids **6**(6), 2133–2142
273. Pullin, D.I., Saffman, P.G. (1994): Reynolds stresses and one-dimensional spectra for a vortex model of homogeneous anisotropic turbulence. Phys. Fluids **6**(5), 1787–1796
274. Quéméré, P., Sagaut, P., Couaillier, V. (2000): Une méthode multidomaine/multirésolution avec application à la simulation des grandes échelles. C. R. Acad. Sci. Paris, Série II.b **328**, 87–90
275. Quirk, J.J. (1991): An adaptative grid algorithm for computational shock hydrodynamics. PhD Thesis, College of Aeronautics
276. Rajagopalan, S., Antonia, R.A. (1979): Some properties of the large structure in a fully developed turbulent duct flow. Phys. Fluids **22**(4), 614–622
277. Rizk, M.H., Menon, S. (1988): Large-eddy simulations of axisymmetric excitation effects on a row of impinging jets. Phys. Fluids **31**(7), 1892–1903
278. Robinson, S.K. (1991): The kinematics of turbulent boundary layer structure. NASA, Tech. Memo. TM 103859
279. Rodi, W., Ferziger, J.H., Breuer, M., Pourquié, M. (1997): Status of large-eddy simulation: results of a Workshop. ASME J. Fluid Engng. **119**(2), 248–262
280. Rogallo, R.S., Moin, P. (1984): Numerical simulation of turbulent flows. Ann. Rev. Fluid Mech. **16**, 99–137

192. Lesieur, M., Schertzer, D. (1978): Amortissement autosimilaire d'une turbulence à grand nombre de Reynolds (in french). Journal de Mécanique **17**(4), 609–646
193. Leslie, D.C., Quarini, G.L. (1979): The application of turbulence theory to the formulation of subgrid modelling procedures. J. Fluid Mech. **91**(1), 65–91
194. Lilly, D.K. (1967): The representation of small-scale turbulence in numerical simulation experiments. (Proceedings of the IBM Scientific Computing Symposium on Environmental Sciences, Yorktown Heights, USA)
195. Lilly, D.K. (1992): A proposed modification of the Germano subgrid-scale closure method. Phys. Fluids A **4**(3), 633–635
196. Lin, C.C. (1999): Near-grid-scale energy transfer and coherent structures in the convective planetary boundary layer. Phys. Fluids **11** (11), 3482–3494
197. Liu, C., Liu, Z. (1994): Fourth order finite difference and multigrid methods for modeling instabilities in flat plate boundary layers - 2D and 3D approaches. Computers Fluids **23**(7), 955–982
198. Liu, C., Liu, Z. (1995): Multigrid mapping in box relaxation for simulation of the whole process of flow transition in 3D boundary layers. J. Comput. Phys. **119**, 325–341
199. Liu, S., Katz, J., Meneveau, C. (1999): Evolution and modelling of subgrid scales during rapid straining of turbulence. J. Fluid Mech. **387**, 281–320
200. Liu, S., Meneveau, C., Katz, J. (1994): On the properties of similarity subgrid-scale models as deduced from measurements in a turbulent jet. J. Fluid Mech. **275**, 83–119
201. Loh, K.C., Domaradzki, J.A. (1999): The subgrid-scale estimation model on nonuniform grids. Phys. Fluids **11** (12), 3786–3792
202. Love, M.D. (1980): Subgrid modelling studies with Burgers equation. J. Fluid Mech. **100**(1), 87–110
203. Lund, T.S. (1994): Large-eddy simulation of a boundary layer with concave streamwise curvature. Annual Research Briefs - Center for Turbulence Research, 185–197
204. Lund, T.S. (1997): On the use of discrete filters for large eddy simulation. Annual Research Briefs - Center for Turbulence Research, 83–95
205. Lund, T.S., Novikov, E.A. (1992): Parametrization of subgrid-scale stress by the velocity gradient tensor. Annual Research Briefs - Center for Turbulence Research, 27–43
206. Lund, T.S., Wu, X., Squires, K.D. (1998): On the generation of turbulent inflow conditions for boundary-layer simulations. J. Comput. Phys. **140**, 233–258
207. McComb, W.D. (1990): The physics of fluid turbulence. Clarendon Press, Oxford
208. McDonough, J.M., Bywater (1985): Effects of local large-scale parameters on the small-scale chaotic solutions to Burgers' equation. AIAA Paper 85-1653
209. McDonough, J.M., Bywater (1986): Large-scale effects on local small-scale chaotic solutions to Burgers' equation. AIAA J. **24** (12), 1924–1930
210. McDonough, J.M., Bywater, R.J., Buell, J.C. (1984): An investigation of strange attractor theory and small-scale turbulence. AIAA Paper 84-1674
211. McDonough, J.M., Mukerji, S., Chung, S. (1998): A data-fitting procedure for chaotic time series. Appl. Math. and Comput. **95**, 219–243
212. McDonough, J.M., Saito, K. (1994): Local, small-scale interaction of turbulence with chemical reactions in H2-O2 combustion. Fire Science and Technology **14** (1), 1–18
213. McDonough, J.M., Wang, D. (1995): Additive turbulent decomposition: a highly parallelizable turbulence simulation technique. (New algorithms ans applications, Satofuka, Periaux, Ecer eds) Elsevier, 129–136

214. McRae, G.J., Goodin, W.R,, Seinfeld, J. (1982): Numerical solution of the atmospheric diffusion equation for chemically reacting flows. J. Comput. Phys. **45**, 1–42
215. Magnient, J.C., Sagaut, P., Deville, M. (1999): Analysis of mesh-independent subfilter-scale models for turbulent flows. (Direct and Large Eddy Simulation III, Voke, Sandham and Kleiser eds) Kluwer, 263–274
216. Maltrud, M.E., Vallis, G.K. (1993): Energy and enstrophy transfer in numerical simulations of two-dimensional turbulence. Phys. Fluids A **5**, 1760–1775
217. Manoha, E., Troff, B., Sagaut, P. (2000): Trailing edge noise prediction using large-eddy simulation and acoustic analogy. AIAA Journal **38**(8), 1340–1350
218. Mansour, N.N., Moin, P., Reynolds, W.C., Ferziger, J.H. (1977): Improved methods for large-eddy simulations of turbulence. (Symposium on Turbulent Shear Flow, Penn State, USA)
219. Maruyama, T., Rodi, W., Maruyama, Y., Hiroaka, H. (1999): Large eddy simulation of the turbulent boundary layer behind roughness elements using an artificially generated inflow. J. Wind Eng. Ind. Aerodyn. **83**, 381–392
220. Mason, P.J. (1994): Large-eddy simulation: A critical review of the technique. Q. J. R. Meteorol. Soc. **120**, 1–26
221. Mason, P.J., Brown, A.R. (1994): The sensitivity of large-eddy simulations of turbulent shear flow to subgrid models. Boundary Layer Meteorol. **70**, 133–150
222. Mason, P.J., Callen, N.S. (1986): On the magnitude of the subgrid-scale eddy coefficient in large-eddy simulations of turbulent channel flow. J. Fluid Mech. **162**, 439–462
223. Mason, P.J., Thomson, D.J. (1992): Stochastic backscatter in large-eddy simulations of boundary layers. J. Fluid Mech. **242**, 51–78
224. Maurer, J., Fey, M. (1999): A scale-residual model for large-eddy simulation. (Direct and Large Eddy Simulation III, Voke, Sandham and Kleiser eds) Kluwer, 237–248
225. Meneveau, C. (1994): Statistics of turbulence subgrid-scale stresses: Necessary conditions and experimental tests. Phys. Fluids **6**(2), 815–833
226. Meneveau, C., Katz, J. (1999): Conditional subgrid force and dissipation in locally isotropic and rapidly strained turbulence. Phys Fluids **11** (8), 2317–2329
227. Meneveau, C., Katz, J. (1999): Dynamic testing of subgrid models in large-eddy simulation based on the Germano identity. Phys. Fluids **11** (2), 245–247
228. Meneveau, C., Katz, J. (2000): Scale-invariance and turbulence models for large-eddy simulation. Ann. Rev. Fluid Mech. **32**, 1–32
229. Meneveau, C., Lund, T.S. (1997): The dynamic Smagorinsky model and scale-dependent coefficients in the viscous range of turbulence. Phys. Fluids **9**(12), 3932–3934
230. Meneveau, C., Lund, T.S., Cabot, W.H. (1996): A Lagrangian dynamic subgrid-scale model of turbulence. J. Fluid Mech. **319**, 353–385
231. Meneveau, C., Lund, T.S., Moin, P. (1992): Search for subgrid scale parametrization by projection pursuit regression. Proceedings of the Summer Program - Center for Turbulence Research, 61–81
232. Meneveau, C., O'Neil, J. (1994): Scaling laws of the dissipation rate of turbulent subgrid-scale kinetic energy. Phys. Rev. E. **49**(4), 2866–2874
233. Menon, S., Yeung, P.K., Kim, W.W. (1996): Effect of subgrid models on the computed interscale energy transfer in isotropic turbulence. Computer and Fluids **25**(2), 165–180
234. Mestayer, P. (1982): Local isotropy and anisotropy in high-Reynolds-number turbulent boundary layer. J. Fluid Mech. **125**, 475–503
235. Métais, O., Lesieur, M. (1992): Spectral large-eddy simulation of isotropic and stably stratified turbulence. J. Fluid Mech. **256**, 157–194

281. Ronchi, C., Ypma, M., Canuto, V.M. (1992): On the application of the Germano identity to subgrid-scale modeling. Phys. Fluids A **4**(12), 2927–2929
282. Sadourny, R., Basdevant, C. (1981): Une classe d'opérateurs adaptés à la modélisation de la diffusion turbulente en dimension deux (in french). C. R. Acad. Sc. Paris **292**, 1061–1064
283. Sadourny, R., Basdevant, C. (1985): Parametrization of subgrid-scale barotropic and baroclinic eddies in quasi-geostrophic models: anticipated potential vorticity method. J. Atmos. Sci. **42**, 1353–1363
284. Sagaut, P. (1996): Numerical simulations of separated flows with subgrid models. Rech. Aéro. **1**, 51–63
285. Sagaut, P. (1998): Introduction à la simulation des grandes échelles pour les écoulements de fluide incompressible (in french). Springer-Verlag, Berlin.
286. Sagaut, P., Comte, P., Ducros, F. (2000): Filtered subgrid-scale models. Phys. Fluids **12**(1), 233–236
287. Sagaut, P., Garnier, E., Séror, C. (1999): Généralisation de l'identité de Germano et application à la modélisation sous-maille (in french). C. R. Acad. Sci. Paris, Série II.b, t. **327**, 463–466
288. Sagaut, P., Garnier, E., Terracol, M. (2000): A general algebraic formulation for multi-parameter dynamic subgrid-scale modeling. International Journal of Computational Fluid Dynamics **13**, 251–257
289. Sagaut, P., Grohens, R. (1999): Discrete filters for large-eddy simulation. Int. J. Numer. Methods Fluids **31**, 1195–1220
290. Sagaut, P., Labourasse, E., Quéméré, P., Terracol, M. (2000): Multiscale approaches for unsteady simulation of turbulent flows. Int. J. Nonlinear Sciences and Numerical Simulation **1**(4)
291. Sagaut, P., Lê, T.H. (1997): Some investigations on the sensitivity of large-eddy simulation. (Direct and Large Eddy Simulation II, Chollet, Voke and Kleiser eds.) Kluwer, 81–92
292. Sagaut, P., Montreuil, E., Labbé, O. (1999): Assessment of some self-adaptive SGS models for wall bounded flows. Aerospace Science & Technology **3**(6), 335–344
293. Sagaut, P., Troff, B. (1997): Subgrid-scale improvements for non-homogeneous flows. . (Advances in DNS/LES, C. Liu, Z. Liu eds.) Greyden Press,
294. Sagaut, P., Troff, B., Lê, T.H., Ta, P.L. (1996): Large eddy simulation of turbulent flow past a backward facing step with a new mixed scale SGS model. (Computation of three-dimensional complex flows, Notes on Numerical Fluid Mechanics 53, Deville, Gavrilakis and Rhyming eds.) Vieweg, 271–278
295. Sarghini, F., Piomelli, U., Balaras, E. (1999): Scale-similar models for large-eddy simulations. Phys. Fluids **11** (6), 1596–1607
296. Salvetti, M.V., Banerjee, S. (1994): A priori tests of a new dynamic subgrid-scale model for finite-difference large-eddy simulations. Phys. Fluids **7**(11), 2831–2847
297. Salvetti, M.V., Zang, Y., Street, R.L., Banerjee, S. (1997): Large-eddy simulation of free-surface decaying turbulence with dynamic subgrid-scale models. Phys. Fluids **9**(8), 2405–2419
298. Schumann, U. (1975): Subgrid scale model for finite difference simulations of turbulent flows in plane channels and annuli. J. Comput. Phys. **18**, 376–404
299. Schumann, U. (1995): Stochastic backscatter of turbulence energy and scalar variance by random subgrid-scale fluxes. Proc. R. Soc. Lond. A **451**, 293–318
300. Schumann, U. (1995): Boundary conditions at walls - The unsolved problem. Non publié
301. Schwarz, K.W. (1990): Evidence for organized small-scale structure in fully developed turbulence. Phys. Rev. Letters **64**(4), 415–418

302. Scotti, A., Meneveau, C. (1997): Fractal model for coarse-grained nonlinear partial differential equations. Phys. Rev. Lett. **78** (5), 867–870
303. Scotti, A., Meneveau, C. (1999 A fractal model for large-eddy simulation of turbulent flow. Physica D **127**, 198–232
304. Scotti, A., Meneveau, C., Fatica, M. (1997): Dynamic Smagorinsky model on anisotropic grids. Phys. Fluids **9** (6), 1856–1858
305. Scotti, A., Meneveau, C., Lilly, D.K. (1993): Generalized Smagorinsky model for anisotropic grids. Phys. Fluids A **5**(9), 2306–2308
306. Sengupta, T.K., Nair, M.T. (1999): Upwind schemes and large-eddy simulation. Int. J. Numer. Meth. Fluids **31**, 879–889
307. Shah, K.B., Ferziger, J.H. (1995): A new non-eddy viscosity subgrid-scale model and its application to channel flow. Annual Research Briefs - Center for Turbulence Research, 73–91
308. Shao, L., Sarkar, S., Pantano, C. (1999): On the relationship between the mean flow and subgrid stresses in large eddy simulation of turbulent shear flows. Phys. Fluids **11** (5), 1229–1248
309. Silveira Neto, A., Grand, D., Métais, O., Lesieur, M. (1993): A numerical investigation of the coherent vortices in turbulence behind a backward facing step. J. Fluid Mech. **256**, 1–25
310. Silvestrini, J. (1996): Simulation des grandes échelles des zones de mélange - Application à la propulsion solide des lanceurs spatiaux (in french). Thèse de Doctorat de l'INPG, Grenoble, France
311. Silvestrini, J.H., Lamballais, E., Lesieur, M. (1998): Spectral-dynamic model for LES of free and wall shear flows. Int. J. Heat and Fluid Flow **19**, 492–504
312. Smagorinsky, J. (1963): General circulation experiments with the primitive equations. I: The basic experiment. Month. Weath. Rev. **91**(3), 99–165
313. Speziale, C.G. (1985): Galilean invariance of subgrid-scale stress models in the large-eddy simulation of turbulence. J. Fluid Mech. **156**, 55–62
314. Speziale, C.G. (1987): On nonlinear K-l and K-ϵ models of turbulence. J. Fluid Mech. **178**, 459–475
315. Speziale, C.G. (1991): Analytical methods for the development of Reynolds-stress closures in turbulence. Ann. Rev. Fluid Mech. **23**, 107–157
316. Sreedhar, M., Stern, F. (1998): Large eddy simulation of temporally developing juncture flows. Int. J. Numer. Meth. Fluids **28**, 47–72
317. Stanisic, M.M. (1985): The mathematical theory of turbulence. Springer-Verlag, Berlin
318. Stevens, B., Moeng, C.H., Sullivan, P. (1999): Large-eddy simulations of radiatively driven convection: sensitivities to the representation of small scales. J. Atmos. Sci. **56**, 3963–3984
319. Stolz, S., Adams, N.A. (1999): An approximate deconvolution procedure for large-eddy simulation. Phys Fluids **11** (7), 1699–1701
320. Stolz, S., Adams, N.A., Kleiser, L. (1999): The approximate deconvolution model applied to LES of turbulent channel flow. (Direct and Large Eddy Simulation III, Voke, Sandham and Kleiser eds) Kluwer, 163–174
321. Sullivan, P.P., McWilliams, J.C., Moeng, C.H. (1994): A subgrid-scale model for large-eddy simulation of planetary boundary-layer flows. Boundary-Layer Meteorol. **71**, 247–276
322. Sullivan, P., McWilliams, J.C., Moeng, C.H. (1996): A grid nesting method for large-eddy simulation of planetary boundary-layer flows. Boundary-Layer Meteorology **80**, 167–202
323. Tafti, D. (1996): Comparison of some upwind-biased high-order formulations with a second-order central-difference scheme for time integration of the incompressible Navier-Stokes equations. Computers & Fluids **25**(7), 647–665

324. Tafti, D., Vanka, S.P. (1991): A numerical study of the effects of spanwise rotation on turbulent channel flow. Phys. Fluids A **3**, 642–656
325. Temam, R. (1991): Approximation of attractors, large eddy simulations and multiscale methods. Proc. R. Soc. Lond. A **434**, 23–39
326. Tennekes, H., Lumley, J.L. (1972): A first course in turbulence. MIT Press
327. Terracol, M., Sagaut, P., Basdevant, C. (2000): Une méthode multiniveau pour la simulation des grandes échelles des écoulements turbulents compressibles (in french). *C. R. Acad. Sci. Paris, Série II.b* **328**, 81–86
328. Troff, B., Lê, T.H., Loc, T.P. (1991): A numerical method for the three-dimensional unsteady incompressible Navier-Stokes equations. J. Comput. Appl. Math. **35**, 311–318
329. Tziperman, E., Yavneh, I., Ta'asan, S. (1993): Multilevel turbulence simulations. Europhys. Lett. **24**(4), 239–244
330. van der Ven, H. (1995): A family of large eddy simulation (LES) filters with nonuniform filter widths. Phys. Fluids **7**(5), 1171–1172
331. Vandromme, D., Haminh, H. (1991): The compressible mixing layer. (Turbulence and coherent structures, O. Métais, M. Lesieur eds) Kluwer Academic Press, 508–523
332. Vasilyev, O., Lund, T.S., Moin, P. (1998): A general class of commutative filters for LES in complex geometries. J. Comput. Phys. **146**, 82–104
333. Verstappen, R., Veldman, E. (1997): Direct numerical simulation of turbulence at lower costs. J. Engng. Math.**32**, 143–159
334. Verstappen, R., Veldman, E. (1998): Spectro-consistent discretization of Navier-Stokes: a challenge to RANS and LES. J. Engng. Math.**34**, 163–179
335. Vinokur, M. (1989): An analysis of finite-difference and finite-volume formulations of conservation laws. J. Comput. Phys **81**, 1–52
336. Voke, P.R. (1990): Multiple Mesh simulation of turbulent flow. Technical report QMW EP-1082, Queen Mary and Westfield College, University of London, London, U.K.
337. Voke, P.R. (1996): Subgrid-scale modelling at low mesh Reynolds number. Theoret. Comput. Fluid Dynamics **8**, 131–143
338. Voke, P.R., Gao, S., Leslie, D. (1995): Large-eddy simulations of plane impinging jets. Int. J. Numer. Meth. Fluids **38**, 489–507
339. Voke, P.R., Potamitis, S.G. (1994): Numerical simulation of a low-Reynolds-number turbulent wake behind a flate plate. Int. J. Numer. Meth. Fluids **19**, 377–393
340. Vreman, B., Geurts, B., Kuerten, H. (1994): Realizability conditions for the turbulent stress tensor in large-eddy simulation. J. Fluid Mech. **278**, 351–362
341. Vreman, B., Geurts, B., Kuerten, H. (1994): On the formulation of the dynamic mixed subgrid-scale model. Phys. Fluids **6**(12), 4057–4059
342. Waleffe, F. (1992): The nature of triad interactions in homogeneous turbulence. Phys. Fluids A **4**(2), 350–363
343. Waleffe, F. (1993): Inertial transfer in the helical decomposition. Phys. Fluids A **5**(3), 677–685
344. Weinan, E., Shu, C.W. (1994): A numerical resolution study of high order essentially non-oscillatory schemes applied to incompressible flow. J. Comput. Phys. **110**, 39–46
345. Werner, H., Wengle, H. (1991): Large-eddy simulation of turbulent flow over and around a cube in a plate channel. (8th Symposium on Turbulent Shear Flows, Munich, Germany)
346. Wilson, P.G., Pauley, L.L. (1998): Two- and three-dimensional large-eddy simulations of a transitional separation bubble. Phys. Fluids **10**(11), 2932–2940

347. Winckelmans, G.S., Lund, T.S., Carati, D., Wray, A. (1996): A priori testing of subgrid-scale models for the velocity-pressure and vorticity-velocity formulations. Proceedings of the Summer Program - Center for Turbulence Research, Stanford, 309–329
348. Wong, V.C. (1992): A proposed statistical-dynamic closure method for the linear or nonlinear subgrid-scale stresses. Phys. Fluids A **4**(5), 1080–1082
349. Wu, X., Squires, K.D. (1997): Large eddy simulation of an equilibrium three-dimensional turbulent boundary layer. AIAA Journal **35**(1), 67–74
350. Wu, X., Squires, K.D. (1998): Prediction of the three-dimensional turbulent boundary layer over a swept bump.. AIAA Journal **36**(4), 505–514
351. Wu, X., Squires, K.D. (1998): Prediction of the high-Reynolds-number flow over a two-dimensional bump. AIAA Journal **36**(4), 505–514
352. Wu, X., Squires, K.D. (1998): Numerical investigation of the turbulent boundary layer over a bump. J. Fluid Mech. **362**, 229–271
353. Yakhot, V., Orszag, S.A. (1986): Renormalization group analysis of turbulence. I. Basic Theory. J. Sci. Comput. **1**, 3–51
354. Yang, K.S., Ferziger, J.H. (1993): Large-eddy simulation of turbulent obstacle flow using a dynamic subgrid-scale model. AIAA Journal **31**(8), 1406–1413
355. Yeung, P.K., Brasseur, J.G. (1991): The response of isotropic turbulence to isotropic and anisotropic forcing at large scales. Phys. Fluids A **3**(5), 884–897
356. Yeung, P.K., Brasseur, J.G., Wang, Q. (1995): Dynamics of direct large-small scale couplings in coherently forced turbulence: concurrent physical- and Fourier-space views. J. Fluid Mech. **283**, 43–95
357. Yoshizawa, A. (1979): A statistical investigation upon the eddy viscosity in incompressible turbulence. J. Phys. Soc. Japan **47**(5), 1665–1669
358. Yoshizawa, A. (1982): Eddy-viscosity-type subgrid-scale model with a variable Smagorinsky coefficient and its relationship with the one-equation model in large eddy simulation. Phys. Fluids **25**(9), 1532–1538
359. Yoshizawa, A. (1984): Statistical analysis of the deviation of the Reynolds stress from its eddy-viscosity representation. Phys. Fluids **27**(6), 1377–1387
360. Yoshizawa, A. (1989): Subgrid-scale modeling with a variable length scale Phys. Fluids A **1**(7), 1293–1295
361. Yoshizawa, A. (1991): A statistically-derived subgrid model for the large-eddy simulation of turbulence. Phys. Fluids A **3**(8), 2007–2009
362. Yoshizawa, A., Horiuti, K. (1985): A statistically-derived subgrid-scale kinetic energy model for the large-eddy simulation of turbulent flows. J. Phys. Soc. Japan **54**(8), 2834–2839
363. Yoshizawa, A., Tsubokura, M., Kobayashi, T., Taniguchi, N. (1996): Modeling of the dynamic subgrid-scale viscosity in large-eddy simulation. Phys. Fluids **8**(8), 2254–2256
364. Zahrai, S., Bark, F.H., Karlsson, R.I. (1995): On anisotropic subgrid modeling. Eur. J. Mech. B/Fluids **14**(4), 459–486
365. Zang, T.A. (1991): Numerical simulation of the dynamics of turbulent boundary layers: Perspectives of a transition simulator. Philos. Trans. R. Soc. Lond. Ser. A **336**, 95–102
366. Zang, Y., Street, R.L., Koseff, J.R. (1993): A dynamic mixed subgrid-scale model and its application to turbulent recirulating flows. Phys. Fluids A **5**(12), 3186–3196
367. Zhao, H., Voke, P.R. (1996): A dynamic subgrid-scale model for low-Reynolds-number channel flow. Int. J. Numer. Meth. Fluids **23**, 19–27
368. Zhou, Y. (1993): Degrees of locality of energy transfer in the inertial range. Phys. Fluids A **5**(5), 1092–1094

369. Zhou, Y. (1993): Interacting scales and energy transfer in isotropic turbulence. Phys. Fluids A **5**(10), 2511–2524
370. Zhou, Y., Vahala, G., Hossain, M. (1989): Renormalized eddy viscosity and Kolmogorov's constant in forced Navier-Stokes turbulence. Phys. Rev. A **40**(10), 5865–5874

Subject Index

also reflects the local effects at the cutoff. The other basic assumptions underlying the Chollet–Lesieur model are maintained.

4. The Lesieur–Rogallo model (p.79), which computes the intensity of the transfers by a dynamic procedure. This is an extension of the Chollet–Lesieur model for flows in spectral disequilibrium, as modifications in the nature of the transfers to the subgrid scales can be considered. The dynamic procedure consists in including in the model information relative to the energy transfers at play with the highest resolved frequencies. The assumptions concerning the filter are not relaxed, though.
5. Models based on the analytical theories of turbulence (p.80), which compute the effective viscosity without assuming anything about the spectrum shape of the resolved scales, are thus very general. On the other hand, the spectrum shape of the subgrid scales is assumed to be that of a canonical inertial range. These models, which are capable of including very complex physical phenomena, require very much more implementation and computation effort than the previous models. The assumptions concerning the filter are the same as for the previous models.

Chollet–Lesieur Model. Subsequent to Kraichnan's investigations, Chollet and Lesieur [61] proposed an effective viscosity model using the results of the EDQNM closure on the canonical case. The full subgrid transfer term including the backward cascade is written:

$$T^{e}_{sgs}(k|k_c) = -2k^2 E(k)\nu_e(k|k_c) \quad , \tag{4.15}$$

in which the effective viscosity $\nu_e(k|k_c)$ is defined as the product

$$\nu_e(k|k_c) = \nu_e^+(k|k_c)\nu_e^\infty \quad . \tag{4.16}$$

The constant term ν_e^∞, independent of k, corresponds the asymptotic value of the effective viscosity for wave numbers that are small compared with the cutoff wave number k_c. This value is evaluated using the cutoff energy $E(k_c)$:

$$\nu_e^\infty = 0.441 K_0^{-3/2}\sqrt{\frac{E(k_c)}{k_c}} \quad . \tag{4.17}$$

The function $\nu_e(k|k_c)$ reflects the variations of the effective viscosity in the proximity of the cutoff. The authors propose the following form, which is obtained by approximating the exact solution with a law of exponential form:

$$\nu_e^+(k|k_c) = 1 + \frac{K_0^{3/2}}{\nu_e^\infty} 15.2\exp(-3.03k_c/k) \quad . \tag{4.18}$$

This form makes it possible to obtain an effective viscosity that is nearly independent of k for wave numbers that are small compa with k_c, with a

finite increase near the cutoff. There is a limited inclusion of the backward cascade with this model: the effective viscosity remains strictly positive for all wave numbers, while the backward cascade is dominant for very small wave numbers, which would correspond to negative values of the effective viscosity.

Constant Effective Viscosity Model. A simplified form of the effective viscosity of (4.16) can be derived independently of the wave number k [190]. By averaging the effective viscosity along k and assuming that the subgrid modes are in a state of energy balance, we get:

$$\nu_e(k|k_c) = \nu_e = \frac{2}{3}K_0^{-3/2}\sqrt{\frac{E(k_c)}{k_c}} \quad . \tag{4.19}$$

Dynamic Spectral Model. The asymptotic value of the effective viscosity (4.17) has been extended to the case of spectra of slope $-m$ by Métais and Lesieur [235] using the EDQNM closure. For a spectrum proportional to $k^{-m}, m \leq 3$, we get:

$$\nu_e^\infty(m) = 0.31\frac{5-m}{m+1}\sqrt{3-m}K_0^{-3/2}\sqrt{\frac{E(k_c)}{k_c}} \quad . \tag{4.20}$$

For $m > 3$, the energy transfer cancels out, inducing zero effective viscosity. Here, we find a behavior similar to that of two-dimensional turbulence. Extension of this idea in physical space has been derived by Lamballais and his coworkers [177, 311].

Lesieur–Rogallo Model. By introducing a new filtering level corresponding to the wave number $k_m < k_c$, Lesieur and Rogallo [191] propose a dynamic algorithm for adapting the Chollet–Lesieur model. The contribution to the transfer $T(\mathbf{k}), k < k_c$, corresponding to the $(\mathbf{k}, \mathbf{p}, \mathbf{q})$ triads such that p and/or q are in the interval $[k_m, k_c]$, can be computed explicitly by Fourier transforms. This contribution is denoted $T_{sub}(k|k_m, k_c)$ and is associated with the effective viscosity:

$$\nu_e(k|k_m, k_c) = -\frac{T_{sub}(k|k_m, k_c)}{2k^2 E(k)} \quad . \tag{4.21}$$

The effective viscosity corresponding to the interactions with wave numbers located beyond k_m is the sum:

$$\nu_e(k|k_m) = \nu_e(k|k_m, k_c) + \nu_e(k|k_c) \quad . \tag{4.22}$$

This relation corresponds exactly to Germano's identity and was previously derived by the authors. The two terms $\nu_e(k|k_m)$ and $\nu_e(k|k_c)$ are then modeled by the Chollet–Lesieur model. We adopt the hypothesis that when $k < k_m$, then $k \ll k_c$, which leads to $\nu_e^+(k|k_m) = \nu_e^+(0)$. Relation (4.22) then leads to the equati